The dynamical stereochemistry of photon–initiated bimolecular reactions

A thesis submitted for the degree of Doctor of Philosophy

by

Andrew James Alexander

Magdalen College, University of Oxford 1997

Abstract

The product state specific stereodynamics of the photon–initiated reaction of $O(^1D_2)$ with H_2 has been investigated by polarised Doppler–resolved laser induced fluorescence, under room temperature bulb conditions. Product state resolved differential cross sections, excitation functions and rotational angular momentum alignments are reported for the following product channels,

$$O(^1D_2) + H_2(^1\Sigma_g^+,\, v = 0) \;\rightarrow\; OH(X^2\Pi; v' = 0, N' = 14, f) \;+\; H(^2S).$$

at a mean collision energy of 12 kJ mol^{-1}. The data are compared with extensive state resolved quasi–classical trajectory (QCT) calculations of the linear and angular momentum distributions and excitation functions conducted on the Schinke–Lester (SL1) and K *ab initio* ground state ($1^1A'$) potential energy surfaces. Overall, good agreement is obtained between the QCT calculated and experimentally determined stereodynamical features. The results are discussed in light of other recent work on this prototypical insertion reaction, and on the related systems of $O(^1D_2)$ + HD and CH_4.

Acknowledgements

I would like to begin by expressing my gratitude to my supervisor, Professor John Simons who has given me exceptional support: it has been a true pleasure to work for him. I am also very grateful to Dr. Mark Brouard who has been a tremendous source of friendly advice and has brought some order to an otherwise scattered mind.

I will not forget the unswerving enthusiasm and generosity of Professor Javier Aoiz who has devoted much of his time to my upbringing and who has been an admirable teacher. Many thanks also to Drs. Bañares, Herrero, and Sáez Rábanos for looking after me so well in Madrid.

I am deeply indebted to Steve Rayner, with whom I spent my first year in the lab, and who gave me a solid grounding in experimental science. After having survived the terrible O + HCl everything else was somewhat easier in comparison. Thanks also to Justin Short for sharing ideas, hours in the lab, and beers after hours.

There have been many friends in the lab who have made the real difference to research. In no particular order they are Steve Langford, John Dickinson, Rob Randall, Gavin Markillie, Dave Blunt, Stuart MacKenzie, Russell Low, Andrew James, Paul Joireman, Mark Lambert, Yo Fujimura, Itamar Burak, Caroline Russell, Evan Robertson, Matt Hockridge, Simon Gatenby, Rob Hamilton, Kostas Kalogerakis, Dom Hughes, Sam Greenland, Claire Vallance.

Outside of hours, I must thank the people who have contributed most to my experience of Oxford. Special merit goes to the boys of Rancho Diablo (our first year hovel): Mike Kelsen, Paul Bollyky and Alex Hartemink. Plus the irregulars: Len Shapiro and Dennis

Chua. Thanks to Georgie Hurst for being my pimp, to Markus Malkmus for wine, whisky and not necessarily all at once. Also to Jules, Karen, Brooke, the ex-residents of Cowley place (+Justin again!) for keeping me sane with the responsibilities of the MCR.

I must say I have been beaten up in style during my time here. Many thanks to Gary Miller (V dan) for his fine instruction and good humour. Thanks also to Tom and Lawrence for real friendship and, of course, beer and curry.

Finally, thanks and love go to my family: mum, dad, Mike and Jacqui, who have supported me through thick and thin, and without whom it is really true to say that none of this would have been possible.

Contents

Chapter 1 Introduction

The study of elementary chemical reactions at a fundamental molecular level presently constitutes a major field of research in chemistry. As chemists have concerned themselves with the transformation from one compound to another, so they have become involved in trying to understand the fundamental mechanisms of reactions.

The field of reaction dynamics involves the study of the motions of atoms as they interact and rearrange during a reactive encounter. The history of the field stretches back as far as the 1920s, when the unfolding of quantum mechanics and a growing understanding of the nature of the chemical bond fostered the concept of the reactive potential energy surface (PES) [1, 2]. The Born–Oppenheimer approximation assumes that the timescale for motion of the nuclei is sufficiently slow for the electrons to rearrange at each configuration. This concept made way for a microscopic picture of the rearrangement of atoms as motion over the potential energy surface. Indeed, the first classical trajectory study of the dynamics of a chemical reaction was carried out as long ago as 1936 by Hirschfelder, Eyring and Topley [3] on the hydrogen exchange reaction $H + H_2 \rightarrow H_2 + H$ using the potential energy surface of London [2]. Since then, the dynamics of many reactions have been interpreted using the concept of motion on electronically adiabatic potential surfaces, valid within the bounds of the Born–Oppenheimer approximation[1].

The PES represents the potential energy of the system as a function of nuclear configuration. The nuclear masses involved control the *kinematic* behaviour, and features of the

[1]The prefixes dia (from Greek "through") and adia ("not through") stem from the type of functions used to calculate potential energy surfaces and refer to the behaviour (crossing or non–crossing) of these surfaces.

surface, such as minimum pathways and energy barriers, control the *dynamic* behaviour of the nuclei: together these factors govern all aspects of a chemical reaction. The nature of the PES will strongly influence the reaction feasibility and rate, the microscopic mechanism of the reaction and the nature of the products formed. It will also determine the influence of reagent state on the reactivity. The study of reaction dynamics relies on stimulated interplay between theory and experiment. Novel experiments provide a testbed for theoretical calculations, whilst theory can indicate fruitful areas of experimental activity or can assist in the understanding of mechanism. All of these areas of activity contribute to the development of the potential energy surface.

This thesis presents the results of a combined theoretical and experimental study of the fundamental benchmark reaction (see section 1.9):

$$O(^1D_2) + H_2(^1\Sigma_g^+) \rightarrow OH(X^2\Pi) + H(^2S). \tag{1.1}$$

The experiments employed a novel strategy of laser initiation of the reaction in a flowing mixture of gases at low pressure and room temperature (*i.e.*, in a "bulb"), with optical detection of the diatomic products. The theoretical study involved integrating the classical equations of motion using previously developed ground state adiabatic potential energy surfaces. In this way the microscopic details of the reaction dynamics were studied, and the experimental data were compared directly with theoretical calculations.

The remainder of the thesis is divided as follows: the rest of this chapter gives a brief overview of the range of experimental and theoretical methods available to the dynamicist, and a selective review of previous work on the $O(^1D_2) + H_2$ reaction is given. Chapter 2 reviews the theoretical basis for the analysis of the experimental and theoretical results, chapter 3 gives a detailed description of the experimental method and the corresponding

data analysis, along with data analysis methods relevant to the theoretical quasiclassical trajectory (QCT) study. Chapter 4 presents results of a QCT study of the reaction of $O(^1D_2)$ + HD and sets the scene for the results of the experimental study. Experimental determination of the product translational (linear momentum) distribution of a particular OH product channel ($v' = 0, N' = 14$) is presented in chapter 5. Finally, in chapter 6, results of the experimental determination of product OH($v' = 0, N' = 14$) rotational polarisation is given along with a detailed QCT study of angular momentum polarisation in the reaction and its role as an indicator of the reaction mechanism.

1.1 Dynamical stereochemistry: the chemical shape of a molecule

Dynamical stereochemistry, as defined by Levine [4], is concerned with the *chemical shape* of molecules. It seeks to determine and understand the dependence of reactivity as a function of distance and approach of the reagents. Chemical shape is dependent not only on the molecule itself, but on the other reagent: it describes the apparent size and shape of a molecule as "seen" by an attacking reagent atom or molecule during the course of a reactive (or non–reactive) collision. Chemical shape is intimately connected to the topology of the potential energy surface: the height and geometry of barriers, the position and depth of attractive wells.

A number of experimental and theoretical techniques to probe chemical shape have evolved over the course of the last thirty years and there has been a considerable increase in our understanding of the dynamics of chemical reactions [5, 6, 7]. Several reviews have been published [8] and various special issues have been been devoted to the field of dynamical stereochemistry [9]–[13]. The purpose of this Introduction is to give a flavour, if only brief, of some of the many varied efforts going on in this field.

The methods for experimental study of dynamical stereochemistry may be generally cate-

gorised in the following ways: techniques which involve manipulation or detection of either reagents or products, and techniques which employ either optical or mass based spectrometric methods, although the techniques are often intimately linked. We begin with one of the longest surviving experimental techniques: crossed molecular beam (CMB) methods.

1.2 Crossed Molecular Beam methods

The crossed molecular beam method was introduced in the early 1950s [14] and involved the creation of fast moving streams of atoms which could then react with target molecules. The techniques were widely applied in the 1960s to reactions of alkali metals using hot wire surface–ionisation detection (the "alkali era") [15]. The method reached maturity in the 1970s with the development of universal machines [16] which used a mass spectrometer as a detector making the method generally applicable. The technique had its second birth in the 1980s with the study of the F + $H_2(D_2)$ reaction by Y. T. Lee and co–workers [17] who were able to vibrationally resolve the angular scattering of the products.

The CMB method allows the observation of single reactive collisions of well defined reagents [18]. The experiments allow the internal states and the velocities of the reagents to be selected, usually by supersonic expansion and seeding techniques, the initial relative velocity vector is well defined in magnitude and direction and so the measured distributions of the scattered products can be directly related to the collision process. The generality of the mass spectrometric detection is the key to its continued successful competition with other, predominantly laser based, methods. Some recent studies, however, have employed the CMB technique with optical product detection [19, 20].

The experimental observables in a CMB experiment are usually the angular and velocity distributions (together, the doubly differential cross section) of reaction products (or reagents for nonreactive scattering). Although most of the measured DCS in CMB experiments are

unavoidably averaged over initial impact parameters and final product state quantum distributions, in favourable cases product vibrational resolution has been achieved, *e.g.* the study of F + H_2 by Lee and co–workers [17]. In recent state of the art experiments, Faubel *et al.* [21, 22] have reported studies on the F + D_2 reaction in a high resolution crossed molecular beam apparatus which is capable of clearly resolving the vibrational character of the DF fragment and of extracting rotational product distributions in these manifolds. The experiments were performed at a range of collision energies with data collected at various scattering angles, and the results show the same general trends as the negative ion photodetachment experiments of Neumark and co–workers (see later). These experimental studies have been augmented by extensive quasiclassical trajectory calculations [23, 24].

Casavecchia and co–workers [25] have studied the four atom reactions,

$$OH + D_2 \rightarrow HOD + D \tag{1.2}$$

$$OH + CO \rightarrow CO_2 + H \tag{1.3}$$

For these experiments an intense supersonic beam source of OH radicals was developed by application of an RF discharge to a rare gas carrier which had been bubbled through water; the OH radicals so produced were in the lowest ($^2\Pi$) electronic state, and predominantly in $v = 0$, low j. The apparatus used could measure the products' time of flight to better than 1%, and had an angular range of 145° with a resolution of 1°. The angular distributions of the HOD and CO_2 products from the above reactions revealed markedly different dynamics; the HOD is sharply backward scattered, whereas the CO_2 exhibits a broad forward–backward structure with a preference for the forward direction. From these scattering data it was concluded that OH + D_2 is a direct reaction dominated by an abstractive mechanism, while OH + CO goes *via* a long lived intermediate (HOCO) complex with a range of lifetimes comparable to the mean rotational period of the intermediate. The CMB results are providing an experimental benchmark for theoretical studies of four atom

systems [25, 26].

1.3 Methods for Alignment and Orientation of Reagents

Controlling the orientation of reagent molecules provides an intuitive way of studying directly the angular dependence of reactivity. There are two common approaches to achieve such alignment or orientation[2]: optical excitation and the use of electric fields. The reader is directed to refs. [8, 28] for more recent reviews of these topics. Ideally, to orient molecules, they must first be isolated in some way, and molecular beam methods are commonly used. There are two major ways of achieving electric field orientation: the *brute force* method, or by *hexapole focussing*.

1.3.1 Brute force method

The brute force method uses a homogeneous electric field to orient molecules with a permanent electric dipole moment *via* the second order Stark effect. When the field is applied, the molecule will tend to assume the direction of minimal energy with respect to the field. The molecules tend to perform a pendular motion once they have damped down into the lowest energy state according to their initial rotational angular momentum. If the molecule has enough rotational angular momentum, however, the electric field strength may be insufficient to trap the molecules in these pendular states and the net orientation will be negligible. A big disadvantage of this method is the large electric field strengths required to achieve orientation [29, 30].

The idea is illustrated in the experiments of Loesch an Möller [31, 32] who studied the reaction of oriented ICl with potassium atoms. The ICl was oriented using a field of 20 kV cm^{-1}, and the average axis orientation achieved was quantified in terms of the angle,

[2]For an explanation of the distinction between *alignment* and *orientation*,

see section 2.3 or reference [27].

θ, between the molecular bond axis and the electric field direction, as $\langle\cos\theta\rangle = 0.63$ for $J = M = 0$, and $\langle\cos\theta\rangle = 0.19$ for $J = 1$ with M averaged over ±1 and 0. The sense of the orienting field could be inverted so that reactivity with either the I or the Cl atom pointing in the direction of the K atom approach could be compared. For both orientations, the KCl or KI products were forward scattered (parallel to the incoming K atom), and the KCl products exhibited both fast and slow components with a significant steric effect. The results were interpreted in terms of a "harpoon" mechanism [7]. First the K atom transfers an electron to the ICl molecule, which subsequently falls apart, and the K^+ ion collects the halide ion produced by a subsequent strong ionic attraction as it passes through the interaction region. Transfer of an electron from K to ICl on the ground $^2\Sigma^+$ surface of the anionic species results in the formation of Cl^- and I without significant kinetic energy release, yielding the slow KCl product. Electron transfer to the repulsive $^2\Pi$ surface which also correlates with production of I + Cl^-, gives substantial translational energy release, and the two ions combine to give the fast KCl product. A second $^2\Pi$ surface correlates with the production of Cl + I^-, and thus electron transfer onto this surface followed by the ion combination gives a KI product with just one speed component. Loesch and Möller used model calculations to quantify the observed steric data in terms of cones of reaction. For attack of K at the Cl end to form KI, a cone with apex angle *ca.* 80° was proposed. Attack at the I end leading to KCl formation gave a much wider acceptance angle, $\approx$ 200°.

1.3.2 Electrostatic Hexapole Focussing

As its name suggests, the electrostatic hexapole method makes use of a hexapolar arrangement of rods with alternating positive and negative fields to generate an inhomogeneous electric field. The inhomogeneous field both state–selects molecules travelling parallel to the hexapole axis, and orients them with respect to the local field within the hexapole. Spatial orientation with respect to the laboratory frame is then obtained by use of a uniform

electric field region outside the hexapole.

An example of this method is provided by the study of the reaction Rb + $CH_3I \rightarrow CH_3$ + RbI [33, 34]. A hexapole focussing field was used to state select methyl iodide molecules before they passed into a region of linear electric field. It was then possible to orient the methyl iodide, *i.e.*, to choose the value of $\langle \cos\gamma \rangle = KM/(J^2 + J)$, where γ is the angle of the C–I bond with respect to the relative velocity between Rb and CH_3I. As one may intuitively expect, the reaction producing RbI was found to be much more probable for CH_3I oriented with the I end pointed toward the Rb. In this way a "cone of nonreaction", centred on the methyl group, with an apex angle of about 53°, was estimated.

1.3.3 Laser Methods for Reagent Alignment

The optical excitation methods for alignment of reagents make use of the properties of polarised light. As a simple example, linearly polarised light excites transitions with $\Delta m_J = 0$, so that excitation of a rovibrational transition from, *e.g.*, $J = 0$ to $J = 1$ with linearly polarised light would produce a preferential population of $m_J = 0$ in the upper state, with no population in the $m_J = \pm 1$ levels. The alignment originates from the fact that the classical probability of absorption of a photon to excite a molecule from state $|i\rangle$ to state $|f\rangle$ depends upon the angle θ between the transition dipole moment, $\boldsymbol{\mu}_{if}$ and the polarisation vector of the laser radiation, $\boldsymbol{\varepsilon}$, according to the following equation [27],

$$P(i \rightarrow f) \;\propto\; |\boldsymbol{\mu}_{if} \cdot \boldsymbol{\varepsilon}|^2 \;\propto\; \cos^2\theta \tag{1.4}$$

The location of the transition moment within the molecular frame is well defined with respect to the direction of the rotational angular momentum vector. Therefore, since the excitation process favours those molecules for which $\boldsymbol{\mu}_{if}$ is aligned parallel to $\boldsymbol{\varepsilon}$, this anisotropy is carried over into the distribution of upper state angular momentum vectors. For linearly

polarised light only even (symmetric with respect to θ) moments of the angular momentum distribution can be excited, and so the molecular axes may be aligned, but not oriented. To obtain orientation, it is possible to use elliptically polarised light.

Most studies employing laser alignment have focussed on alignment of reagent diatomics [8], although many examples using polarised light to align atomic orbitals have been reported [35]. A recent example of laser induced reagent anisotropy is the study of the reactions of chlorine with methane and its deuterated analogues [36]–[39],

$$\mathrm{Cl}(^2\mathrm{P}_{3/2}) \ + \ \mathrm{CH_4}(\nu_3 = 1, J) \ \rightarrow \ \mathrm{HCl}(v', J') \ + \ \mathrm{CH_3} \tag{1.5}$$

$$\mathrm{Cl}(^2\mathrm{P}_{3/2}) \ + \ \mathrm{CD_3H}(\nu_1 = 1, J) \ \rightarrow \ \mathrm{HCl}(v', J') \ + \ \mathrm{CD_3} \tag{1.6}$$

In order to do these experiments, it was necessary to reduce the spread in velocities and quantum states of the reagents by co–expansion of molecular chlorine and methane into a high vacuum. The detection stage included a linear time–of–flight (TOF) tube which was used to detect HCl molecules after ionisation by (2+1) REMPI. By use of a thin strip mask in the TOF tube, it was possible to detect only those fragments with velocity along the TOF axis, a technique which has been nicknamed "core extraction" [37]. Chlorine atoms are produced by linearly polarised photolysis at 355 nm producing almost exclusively $\mathrm{Cl}(^2\mathrm{P}_{3/2})$ with a well defined spread not more than about 20° off the TOF axis.

Polarised Infra–Red (IR) pumping of the CH_4 causes the vibrational amplitude of the ν_3 mode to be aligned in space, and excitation of the ν_1 mode of CD_3H can lead to spatial alignment of the vibrating C–H bond. Experiments were performed with the polarisation of the IR excitation laser alternately polarised perpendicular and parallel to the TOF detection axis. In the case of CD_3H this means that the Cl atom will approach along a direction either parallel or perpendicular to the C–H bond. The experiments indicated a forward scattered component that was substantially larger for side–on approach than for end–on approach. This preference was explained in terms of a peripheral mechanism in which the approach

of the Cl atom is roughly perpendicular to the C–H bond [38, 40]. The backward scattered component of the reaction is enhanced for parallel alignment, suggesting that a collinear mechanism leads to the formation of the backward scattered products [38].

1.4 Doppler Measurement of Product Velocities

Doppler absorption spectroscopy is a powerful tool for the study of elementary reaction dynamics. The technique takes its name from the effect discovered in 1842 by Christian Doppler. Born on November 29th, 1803, Christian Doppler (figure 1.1) grew up in Salzburg. At the age of 19 he was sent to the Polytechnic Institute in Vienna and completed his studies of science and philosophy in 1928. For the next years he was an assistant in higher mathematics at the the Polytechnic in Vienna and in 1835 accepted the position of Professor of Elementary Mathematics at Prague State Secondary School. In 1841 he became full Professor of Mathematics and Practical Geometry at the Technical Institute in Prague. It was at this time, inspired by observations by the English astronomer James Bradly (1693–1762), he presented the paper "On the Coloured Light of the Double Stars and Certain other stars of the Heavens" before a meeting of the Royal Bohemian Society of Science. It was in 1845 that Buy Ballot (1818–1890), a Dutch scientist, was able to confirm Doppler's theory in experiments he conducted using the Dutch railroad with horn players as a source of sound waves. In 1850, Doppler was appointed to the chair of Experimental Physics at the University of Vienna. On March 17th, 1853, at the age of 49 years, during a holiday in Venice, Doppler died from his deteriorating pulmonary tuberculosis.

The Doppler effect allows us to determine the velocity distribution of an atomic or molecular fragment, and this, as we shall see in later chapters, forms a sensitive probe of the products of a reactive encounter. If a particle moving with velocity v absorbs a photon, the absorption frequency is shifted by an amount $\Delta\nu$,

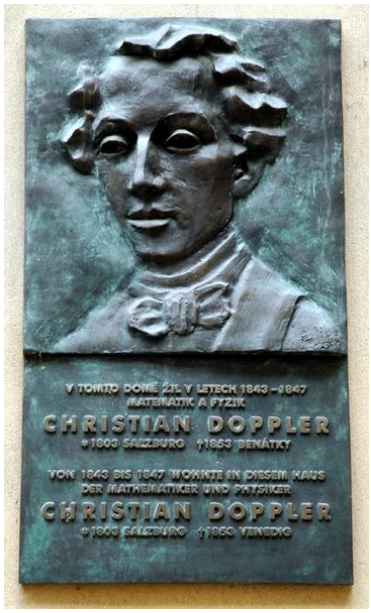

Figure 1.1 Christian Doppler (1803–1853)
[Photograph by Ulrichulrich, reproduced under Creative Commons Attribution-Share Alike 3.0 Unported license.]

$$\frac{\Delta\nu}{\nu_0} = \frac{v_p}{c} \tag{1.7}$$

where ν_0 is the absorption frequency of the stationary particle, v_p is the component of the particles velocity along the direction of travel of the photon (the "line of sight") and c is the speed of light. For an ensemble of particles with a three dimensional distribution of velocities the theoretical limiting absorption line at ν_0 will be broadened to give a Doppler profile covering a range of frequencies. From a careful analysis of this profile (or rather of several profiles taken under selected conditions) it is possible to extract the three dimensional product velocity distribution function. At first it may seem surprising that it is possible to extract a three dimensional function from a one dimensional projection. However, an impressive arsenal of analytical techniques have been developed which make this possible under a range of experimental situations.

1.4.1 Doppler Spectroscopy of Photofragments

Zare and Herschbach [41] were the first to show that the angular distribution of atomic fragments produced in photodissociation of a diatomic molecule may be deduced from the Doppler lineshape of the fragment. Angular distributions of photoproducts were first verified in the classic "photolysis mapping" experiment of Solomon [42]. Linearly polarised visible light was used to photolyse bromine or iodine within a hemispheric bulb whose inside surface had been coated with a thin film of tellurium. The pressure in the bulb was held sufficiently low such that the mean free path of the atomic fragments was larger than the radius of the bulb and so the fragments were able to etch the film of tellurium. Shortly after that Busch *et al.* [43] and Diesen *et al.* [44] made quantitative measurements of the recoil velocity distribution using linearly polarised ruby laser light and mass spectrometric detection.

The first use of Doppler profiles to measure directional anisotropy were made by Welge *et al.* [45]. They used Lyman–α spectroscopy to measure Doppler profiles of (ground state) H atoms from the 266 nm photodissociation of HI and were able to distinguish two dissociation channels, producing the two spin orbit states of chlorine, by virtue of the different H atom speeds.

As experimental attention turned to molecular fragments, it soon became clear that Doppler spectra were dependent not only on fragment velocity, but also on rotational polarisation and its correlation with recoil velocity. The reader is directed elsewhere for several excellent reviews of photodissociation [46].

1.4.2 Doppler Spectroscopy of Bimolecular Reactions

In 1977 Kinsey published a landmark paper on "Fourier Transform Doppler Spectroscopy: a new means of obtaining quantum state resolved velocity–angle distributions" [47]. The new strategy was rapidly exploited in studies of reactive and inelastic scattering by Kinsey and

co–workers [48], and was subsequently used in many studies of molecular photodissociation which all but diverted attention attention away from the study of bimolecular reactions by Doppler methods. Such a broad study of photodissociation has paid off, however, since this forms the basis for the (fully characterised) reagent sources which are utilised in the following scheme:

$$\begin{aligned} \mathrm{AD} + h\nu &\rightarrow \mathrm{A_t} + \mathrm{D}, \\ \mathrm{A_t} + \mathrm{BC} &\rightarrow \mathrm{AB} + \mathrm{C}. \end{aligned}$$

Bersohn and co–workers [49], were the first to exploit the anisotropy of molecular photodissociation to probe the dynamics of a subsequent secondary reaction. They used fast H atoms to study their reaction with deuterated alkenes and alkynes. H atoms were generated by polarised photodissociation of the precursor molecule H_2S,

$$\mathrm{H_2S} + h\nu(193\mathrm{nm}) \rightarrow \mathrm{H} + \mathrm{SH} \tag{1.8}$$

Deuterium atoms recoiling from their subsequent collision with target molecules, e.g. SiD_4, were observed by LIF using sub–Doppler excitation,

$$\mathrm{H} + \mathrm{SiD_4} \rightarrow \mathrm{HSiD_3} + \mathrm{D} \tag{1.9}$$

The H atoms were generated with very high translational energy, in excess of *ca.* 1.5 eV, and their velocity was aligned perpendicular to the polarisation vector $\boldsymbol{\varepsilon}$ of the absorbed photons (since the transition is polarised perpendicular to the molecular plane). H atoms recoiling perpendicular to $\boldsymbol{\varepsilon}$ present a double peaked Doppler contour, reflecting their motion towards or away from the 'observer'; when the probe laser was directed parallel to $\boldsymbol{\varepsilon}$, the Doppler profiles narrowed and presented only a single, central peak. Since measured Doppler

contours of the product D atom were similar to those of the H atom, Bersohn and co–workers inferred that the D atoms tend to emerge from reaction with velocities parallel to those of the incident H atom. In this case the product's relative velocity, $\boldsymbol{k'}$, is parallel to the reagent relative velocity vector, $\boldsymbol{k}$. This result was interpreted in terms of a displacement mechanism proceeding *via* a transition state structure approximating a trigonal bipyramid, reminiscent of an S_N2 inversion mechanism.

The experiments of Bersohn *et al.* probed atomic fragments, and were therefore limited to measurement of the linear momentum ($\boldsymbol{k}$,$\boldsymbol{k'}$) correlation or differential cross section. As in previous studies of molecular photodissociation, the state resolved probing of molecular fragments by Doppler methods was found to be sensitive to the product angular momentum polarisation [50]. Simons *et al.* [51, 52] employed polarised photodissociation of N_2O molecules at 193 nm to produce an anisotropic distribution of $O(^1D_2)$ atoms which they used to study the important stratospheric reaction,

$$O(^1D) + N_2O \rightarrow NO|f\rangle + NO|f'\rangle. \tag{1.10}$$

A broad spectrum of NO products was observed, populating all accessible vibrational levels up to $v' = 18$. NO fragments in the highest levels are, necessarily, partnered by NO in the lowest vibrational levels; their Doppler contours indicated slow NO($v' = 0$) and fast NO($v' = 16$ - 18). In the molecular centre of mass (CM) frame, the excited NO molecules were scattered forwards, while the NO ($v' = 0$) molecules were backward scattered. Initially this was interpreted in terms of a 'stripping' mechanism, in which the fast attacking $O(^1D_2)$ atoms snatched the terminal nitrogen atom from the target molecule, leaving 'cold' NO as an undisturbed spectator. The rotational angular momentum of the cold NO molecule was found to be strongly polarised, however, with a tendency for $\boldsymbol{j'}$ to lie perpendicular to the reagent velocity $\boldsymbol{k}$. Subsequent QCT calculations by Levine *et al.* [40], on a model

potential energy surface, identified a rather different mechanism. The mechanism involved a series of momentum transfers between the attacking $O(^1D_2)$ atom and the atoms in the N_2O molecule promoted by a strong, long range attraction between the terminal N atom and the $O(^1D_2)$. The 'chattering' collisions were initiated as the $O(^1D_2)$ flew *outside* the target molecule and the new NO molecule was scattered in the forward direction, *i.e.*, in the same sense as the attacking atom. The newly identified mechanism was described as a 'peripheral abstraction'.

Hancock et al. [53, 54] studied the reaction $O(^3P) + CS \rightarrow CO + S$ by using NO_2 photolysis with 355 nm polarised light and probing the CO products with sub–Doppler LIF. They found good agreement with QCT calculations carried out on a semi–empirical (London–Eyring–Polanyi–Sato) PES, giving a nearly isotropic distribution of $\boldsymbol{k'}$ with respect to $\boldsymbol{k}$. Similarly they found a near zero alignment of the product rotational angular momentum with respect to the reagent relative velocity vector.

Sub–Doppler spectroscopy has also been applied to the field of inelastic scattering by McCaffery and co–workers [55] who have developed techniques which use optical double resonance and sub–Doppler circular dichroism to obtain information on vector correlations and differential cross sections.

The most recent studies using Doppler resolved product probing have been able to extract full state–to–state differential cross sections [36]–[39], and can resolve the scattering angle dependence of the angular momentum alignment of the products [56]–[61].

1.5 Time–of–Flight Measurement of Product Velocities

Measurement of the time of flight of a product between two points in space is perhaps the most direct method for determining the velocity. Typically, the spatial region over which the time of flight is measured is from the reaction region to some region of detection. TOF

methods have been used in conjunction with many of the other methods mentioned here, *e.g.*, the F+H_2 reaction of Lee and co–workers [17], and the state–to–state measurements of Zare and co–workers [36]–[39].

Welge and co–workers have recently developed a sophisticated method of TOF detection which provides very high resolution for determining the energy distribution of products [62, 63, 64]. This is well illustrated by the case of H_2O photodissociation [65]. Laser photons at 121.6 nm were used to both dissociate the molecular beam of H_2O and to excite the H atom products from principal shell, $n = 1$ to $n = 2$. The atoms were further excited to levels with $n \approx 80$ by a second pulsed laser operating at around 365 nm. A small electric field repels any ions that are formed. The Rydberg states then travel along a field free flight tube where they are relatively gently ionised by an electric field. This "tagging" of H atoms by exciting them to high Rydberg levels eliminates any spread in velocities due to ionic repulsion during creation and flight–time. A review of photodissociation applications of this technique may be found elsewhere [66].

These methods have also been recently applied to the reaction of H + D_2 [67, 68, 69] which have allowed the measurement of vibrationally and rotationally resolved differential cross sections. These have been compared with extensive QCT and QM calculations [69].

1.6 Imaging Methods for Measurement of Product Velocities

As mentioned above, one dimensional imaging of velocity distributions provides not only information about the speed and direction of the products, but also about their angular momentum alignment. However, recovering this information often requires several different experimental arrangements of the apparatus to untangle all of the correlations in the Doppler profiles.

Two dimensional imaging techniques, while somewhat harder to set up, typically require

fewer experimental geometries to determine the population and low order alignment moments. The techniques can be broadly classified into two main categories: *noncoincidence* measurements, where data for one product is measured whilst integrating over the states and identities of the co–products [70], and *coincidence* experiments for which data on a *pair* of co–incident product fragments is recorded one pair at a time [71].

In a simple overview of the method, state selective ionisation of products may be achieved by REMPI, and the fly–out ions are detected by accelerating them onto a position sensitive detector consisting of one or more microchannel plates. Electrons are produced by ion impact in the channels of these plates and are accelerated to a phosphorescent screen. A digitising camera then records the image for averaging and analysis. Although the image is a two–dimensional projection of a three–dimensional velocity distribution, the full three–dimensional information can be obtained by mathematical transformation. The reader is directed to recent reviews for a full discussion of the technique [72, 73].

1.7 Methods for Impact Parameter Control

The impact parameter defines the distance of the collision from the centre of the target molecule, *c.f.* the concentric rings of a dartboard. The previously discussed techniques, except by coincidence, provide no method for controlling this parameter, which can have a huge effect on the reaction dynamics. One method which provides some ability to control the initial geometry of approach is to start the reagents in the equilibrium geometry of a van der Waals cluster. Several reviews of the field have appeared [74, 75] and only one example of the method will be given here.

A number of groups have investigated photodissociation of $HX{\cdot}CO_2$ complexes, where X=Br or I, as a way of studying the reaction $H + CO_2 \rightarrow OH + CO$ [75]. The general idea of the experiment is to photodissociate the HX species in a complex that holds the HX in

a restricted geometry relative to the partner, CO_2 in this case. The H atom will then be directed toward a limited range of locations on the CO_2 molecule. It is known for the $HBr{\cdot}CO_2$ complex, and assumed for the HI complex, that the H atom is roughly adjacent to the C atom in a T–shaped geometry [76, 77], although the zero–point amplitude is very large. It was originally assumed that the differences observed between the bulk (non complex) and the complex reactions might stem from the limited range of impact parameters and approach angles in the precursor complex. It is now generally accepted that the resulting HOCO complex decomposes statistically, but that less energy is imparted to HOCO when the reaction starts from a van der Waals complex. The X atom takes away more energy in translation, leaving less for HOCO, because it pushes off from the whole complex rather than just the H atom [75]. Further evidence for the statistical mechanism came from time–domain experiments (see below).

1.8 Transition State Spectroscopy

The first experiments which claimed to be studies of the transition state were performed by Polanyi and co–workers [78] and Hering *et al.* [79], and since then a variety of frequency and time–domain techniques have been developed which have unequivocally demonstrated that direct information may be obtained, despite the considerable experimental challenge of probing molecular configurations which may exist for only a few tens of femtoseconds. Reviews of the field have been numerous, the reader is directed to recent articles by Polanyi and Zewail [80] and Zewail [81].

1.8.1 The Time Domain

Advances in laser technology mean that it is now possible to generate ultra–short pulses, with temporal widths down to picosecond and even femtosecond timescales, approximately the same order of magnitude as the time it takes for a chemical reaction to occur. This

has led to a new form of spectroscopy in which it is possible to probe bimolecular reactions initiated by the photolysis of a van der Waals complex (see previous section). The photolysis of the precursor complex establishes the zero of time and a femtosecond probe pulse interrogates the evolving species at a well defined time delay. As part of their dynamical investigation of $HX{\cdot}CO_2$ complexes, Wittig and co–workers have carried out time resolved experiments at a range of photolysis wavelengths [82, 83, 84, 85]. The characteristic rise times of OH product, which are associated with the lifetime of the HOCO complex, varied between 250 and 1500 fs, making this a good limiting test of RRKM and other statistical theories. The OH appearance rate was found to be in good accord with the predictions of RRKM theory [82, 85].

1.8.2 The Frequency Domain

One of the newest forms of transition state spectroscopy has been pioneered by Neumark and co–workers [86] and termed negative ion photodetachment. The technique involves accessing the region around the transition state of a bimolecular reaction through optical dissociative excitation of an electron out of a stable negative ion. The spectrum of electron binding energies should provide a map of the potential over the so–called Franck–Condon region of the PES which, for certain anions, corresponds to the A + BC transition region. The first reaction considered with this technique was the hydrogen exchange reaction I + HI, initiated from IHI^- [86, 87], although the technique has had a considerable impact on the understanding of the F + H_2 reaction, through photodetachment experiments of the FH_2^- anion [88, 89]. The outstanding agreement between the experimental photodetachment spectrum and three dimensional quantum mechanical calculations on a new *ab initio* PES served to establish that the transition state for this reaction was not collinear [24].

1.9 The reaction of $O(^1D_2)$ with H_2

The work of this thesis deals exclusively with the reaction,

$$O(^1D_2) + H_2(^1\Sigma_g^+) \rightarrow OH(X^2\Pi) + H(^2S), \tag{1.11}$$

and its isotopic variants (reaction with HD and D_2), although it is hoped that the results may provide more general insight into similar bimolecular systems.

As will become clear from the following discussion, a considerable amount of effort, both theoretical and experimental, has been channeled into reaction (1.11) to determine the details of the mechanism. The reaction has been well studied for a number of reasons:

- It is theoretically amenable to calculations of the PES - both semi-empirical and *ab-initio* [90, 91],
- It involves the reaction of an excited state atom $O(^1D_2)$,
- The reaction may proceed over one of a number of surfaces, with the possibility of involvement of surface seams (conical intersections) and possibly non–adiabatic pathways [92],
- The reaction is known to proceed at low collision energies, preferentially *via* a deep intermediate potential well (~ 7 eV from reagents and ~ 5 eV to products as above) correlating with the ground state of water $\tilde{X}(^1A_1)$ [91],
- It is generally accepted that the mechanism proceeds preferentially by insertion, in contrast with the benchmark abstraction reaction, F + H_2 which has been more thoroughly investigated [24],
- The reaction is important in atmospheric chemistry since it involves the singlet oxygen atom [93], and produces the stratospherically important OH radical [94]. The reaction is also one of the fundamental processes of the H_2/O_2 combustion reaction scheme [95].

In order to place the present work in its proper context, the following section will briefly discuss previous work on the reaction of $O(^1D_2)$ with H_2. In the discussion that follows, it must be borne in mind, that a number of reagent collision energies have been employed, both in the experimental and theoretical work. The collision energy will inevitably affect the details of the product distributions, both scalar and vectorial, and in general experimental and theoretical collision energies previously studied range from thermal (≈ 2.5 kJ mol^{-1}) to hot atom (≈ 21 kJ mol^{-1}).

1.9.1 Computed Potential Energy Surfaces

It will be convenient in the following discussion to begin with an introduction to the potential energy surfaces which have been developed to date for the HOH system, although the following list will be limited to those surfaces which have been used for dynamical calculations of the $O(^1D_2)$ + H_2 reaction. The reader is directed to figure (3.6) for a simple correlation diagram of the system.

1. Sorbie Murrell (SM) [90]. A ground state surface principally derived to reproduce rovibrational spectroscopic data for the ground state of H_2O. There is no barrier to collinear approach of $O(^1D_2)$ towards H_2. A cusp is obtained in the H-H potential due to crossing of the $O(^3P)/O(^1D_2)$ potential curves.
2. Schinke–Lester (SL) [96]. These surfaces are fits to *ab-initio* data of Howard, McLean and Lester [91]. There are 3 surfaces (SL1 – 3) which differ in the relative barrier heights for collinear and perpendicular attack. SL2 presents a barrier to insertion. SL1 has a small shoulder to insertion and a small barrier to collinear attack while SL3 has no barriers; more recently both were modified (M) to correct the exoergicity which led to an over-estimate of product vibration (SL1M and SL3M) [97]. A smoothing (S) polynomial was also developed to correct a discontinuity in the entrance channel [98]. The fully modified surfaces are hereafter referred to as SL1MS and SL3MS.

3. Murrell Carter Mills and Guest (MCMG) [99]. Ab-initio calculations on both the $\tilde{X}(1^1A')$ and $\tilde{B}(2^1A')$ surfaces were fitted using a 2-valued adiabatic representation.
4. Whitlock Muckerman and Fisher (WMF) [100]. Two ground-state surfaces were created using the VB-DIM (valence bond diatomics in molecules) semi-empirical method. WMF1 contains a small barrier to insertion, and was thus excluded from further calculation. WMF2 gives otherwise general ground-state features, with very good agreement in the asymptotic channels.
5. Murrell Carter (MC) [101]. Another ground state surface which was designed to fit spectroscopic data, but which also included smoothing of the cusp encountered in SM.
6. Kuntz *et al.* [102, 103, 92, 104] have used the VB-DIM approach to model both ground and excited state potentials.
7. Rabitz, Harding and Schatz have developed the most recent *ab–initio* surfaces [105]. The K PES represents an analytical fit to the ground state surface ($1^1A'$) from high–level *ab-initio* calculations. The same authors have also developed a surface fitted to *ab-initio* points of the upper ($2^1A''$) surface [106].
8. Dobbyn and Knowles have also recently carried out high–level *ab-initio* calculations for the $\tilde{X}$, $\tilde{A}$ and $\tilde{B}$ states of this system. The results have yet to be published, however[107].

1.9.2 Rate constants and Total cross sections

Early work on the reaction of $O(^1D_2)$ with H_2 by Pavlyuchenko indicated an efficient reaction even at low temperatures, apparently with zero activation energy[108]. The study of the reaction dynamics began to flourish with the introduction of *flash photolysis* techniques when Basco and Norrish observed vibrational excitation of OH as a result of the reaction [109]. Ultraviolet photolysis of ozone was employed to produce the highly reactive $O(^1D_2)$ species, which reacts with H_2 to initiate the subsequent OH catalysed chain decomposition

of the O_3.

The work of DeMore [110] confirmed that the reaction proceeded with zero activation energy, with reaction to produce OH + H as the dominant mechanism for removal of $O(^1D_2)$.

Absolute thermal rate constants were first reported by Husain [111], using time resolved atomic absorption spectroscopy. More recent works by Wolfrum et al. [112, 113] have used laser techniques (UV photolysis of N_2O and VUV LIF of the product atom) to estimate the absolute reactive cross-sections and rate-constants for each of the isotopic variations of reaction (1.11). The photolytically produced reagents were superthermal, however, although Wolfrum's results agree quite well with previous (thermal) results. Most recently Talukdar and Ravishankara [114] made a further measurement of the thermal rate coefficient using pulsed photolysis of ozone at high reagent pressures and by monitoring the atomic resonance fluorescence (vacuum ultraviolet resonance fluorescence VUV-RF). The most recent results of the measurement of the rate coefficient for reaction (1.11) are collected in table (1.1).

1.9.3 Product Rotational Distributions

The first measurements on the scalar rotational distributions were made using LIF by Luntz *et al.* [120] and also by Smith, Butler and Lin [121, 122], who employed 266 nm photolysis of O_3 followed by UV LIF of the product OH. The results indicated rotationally hot product $OH(N')$ distributions, peaking at $N' = 25$ ($v' = 0$) and $N' = 17$ ($v' = 1$) with nearly equal populations in $v' = 0$ and $v' = 1$.

The early measurements of the rotational distributions were closely matched by QCT calculations performed on an *ab-initio* surface calculated by Howard, McLean and Lester [91] and subsequently fitted by Schinke and Lester (SL surface)[96]. Both the measurements and calculations indicated a highly nonstatistical product N' distribution. This was at variance, however, with the QCT calculated differential cross sections which indicated near forward-

Rate coefficient (10^{-10} cm^3 molecule^{-1} s^{-1})	Source
Experimental	
2.7 ± 0.6	VUV LIF [112][(a)]
1.0 ± 0.2	NASA/JPL recommended [115]
1.20 ± 0.10	VUV RF [114][(b)]
1.30 ± 0.10	VUV RF [114][(c)]
Theoretical	
1.73	SM [116]
1.3 ± 0.14	MCMG [117]
1.74	SL3 [118]
1.75	MC [118]
0.92	WMF2 [100]
1.3	K [A′+2(A″)] [106]
0.84	SL1 [119]
0.78	SL1MS [119]

(a) Measured at a mean collision energy of 12 kJ mol^{-1},

(b) Monitoring the O atom, (c) Monitoring the H atom.

Table 1.1 Thermal (300 K) rate coefficients, both theoretical and experimental, for reaction (1.11). For the HD/D_2 equivalents, consult the references cited above.

backward symmetry; trajectories were observed to last, on average for several vibrational periods. Luntz *et al.* [120] suggested that the hot N' distribution resulted from an insertion mechanism, causing excitation of the bending mode of H_2O.

Hot rotational distributions were also observed in QCT calculations by Whitlock *et al.* [123, 100], although these authors preferred to describe the reaction as a combination of abstractive and insertive mechanisms on the basis of a bimodal vibrational distribution. They attributed the vibrationally cold products ($v' = 0$) to an insertion mechanism, and the hotter products (peaking at $v' = 2$) to an abstraction mechanism. This was despite the observation of solely *unimodal* rotational distributions (both experimental and theoretical). Ransome and Wright [124] made a study of the question of abstraction *vs.* insertion using QCT calculations on the Schinke and Lester surface (SL3), which was observed to give vibrational distribution peaking at ($v' = 3$). By observing the passage of trajectories into the potential well, they attributed no more than 4% of successful reactions to an abstractive mechanism, at variance with the mechanism proposed by Whitlock *et al.* [123, 100].

Further LIF studies of the rotational populations of higher vibrational states by Butler, Wiesenfeld and coworkers [125, 126, 127], plus an infrared absorption study by Sears *et al.* [128] confirmed that *all* vibrational levels were rotationally hot with apparently unimodal distributions. Vibrational level $v' = 2$ was found to peak at $N' = 18$ with $v' = 3$ peaking at $N' = 13$. No preference for the $\Pi_{1/2}$ or $\Pi_{3/2}$ spin-orbit states of OH was found. A preferential population of the $\Pi(A')$ Λ-doublet was observed, however (see figure A.2). This preference in electronic symmetry (with respect to the rotational plane of the OH) is generally taken to indicate the dominance of an insertion mechanism [129], although the mechanism for population of the Λ-doublet states is still open to question [130].

Rynefors, Elofson and Holmlid [131] carried out Monte Carlo RRKM simulations which included angular momentum constraints. Their purely statistical algorithm reproduced the

observed rotational distributions exceedingly well, implying that the overall contribution to the hot rotational distribution is *angular momentum conservation* over and above any specific dynamical effects.

1.9.4 Product Vibrational Distribution

In an early work, Basco and Norrish observed that the $O(^1D_2)$–H_2 reaction gave product OH excited at least up to the second vibrational level [109]. Since then the characterisation of the product vibrational distribution and the mechanism for its production has remained a key issue: experimental and theoretical results are summarised in figures (1.2) and (1.3), and table (1.2). LIF studies began with Smith and Butler [122] who observed almost equal populations in $v' = 1$ and $v' = 0$. LIF experiments are difficult, however, due to the onset of predissociation for rovibrationally excited OH in the $A^2\Sigma^+$ state *via* the repulsive $^4\Sigma^-$ state. Infrared chemiluminescence (IR-CL) on the other hand is able to probe all vibrational levels, except $v' = 0$ (there can be no emission from this state). Using IR-CL Butler, Sloan and co-workers determined that the vibrational distribution was inverted, probably peaking in $v' = 2$, although combined with the LIF data, a bimodal distribution was inferred [132, 133]. They interpreted this as evidence for two dynamically different channels; one preferentially exciting rotation, the other vibration.

An alternative method for determining the vibrational distribution is to use a chemical laser with grating selection. In this way Huang *et al.* [138] found no evidence for vibrational inversion, but quite a flat vibrational distribution, dropping at $v' = 4$ - see figure (1.2). Unfortunately, their experimental conditions were estimated to have caused relaxation and secondary reaction effects of up to 20% [138], making it difficult to estimate the true nascent population distribution.

Unfortunately the IR-CL data is left carrying the brunt of responsibility for the question

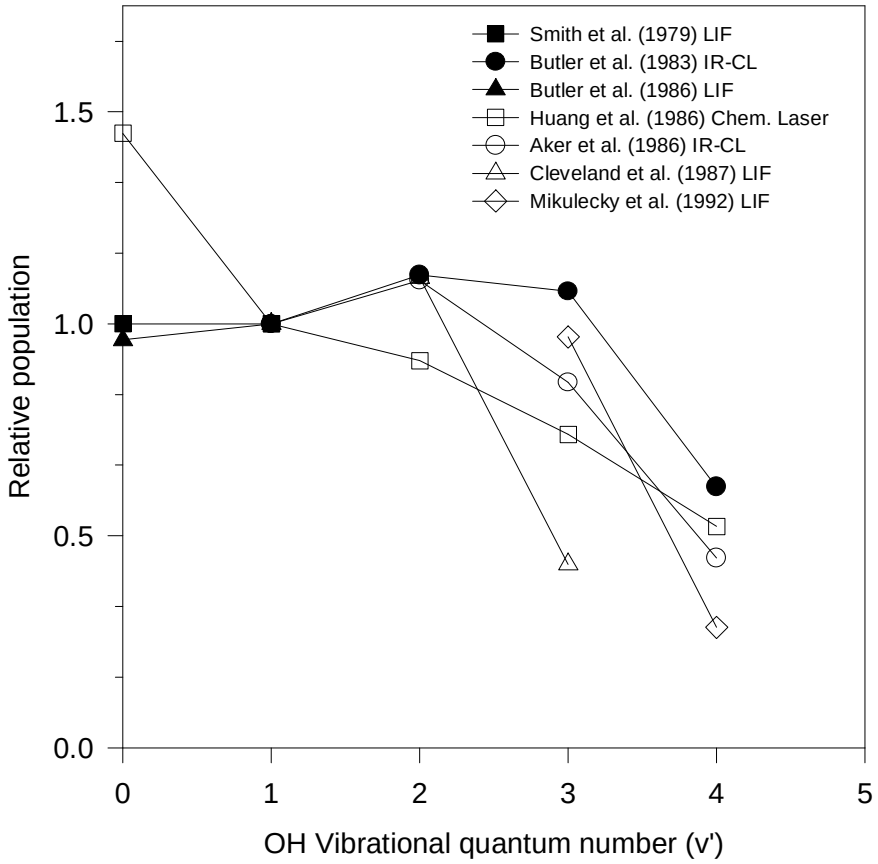

Figure 1.2 Experimentally determined product vibrational distributions for the reaction of $O(^1D_2)$ with H_2. All data are scaled to unit population in $v' = 1$. The $v' = 3/v' = 2$ data of Cleveland *et al.* [127] has been placed with $v' = 2$ at the mean $v' = 2$ of the two IR–CL results. The $v' = 4/v' = 3$ data of Mikulecky *et al.* [134] has been similarly placed such that $v' = 3$ coincides with the mean $v' = 3$ value for the two IR–CL studies.

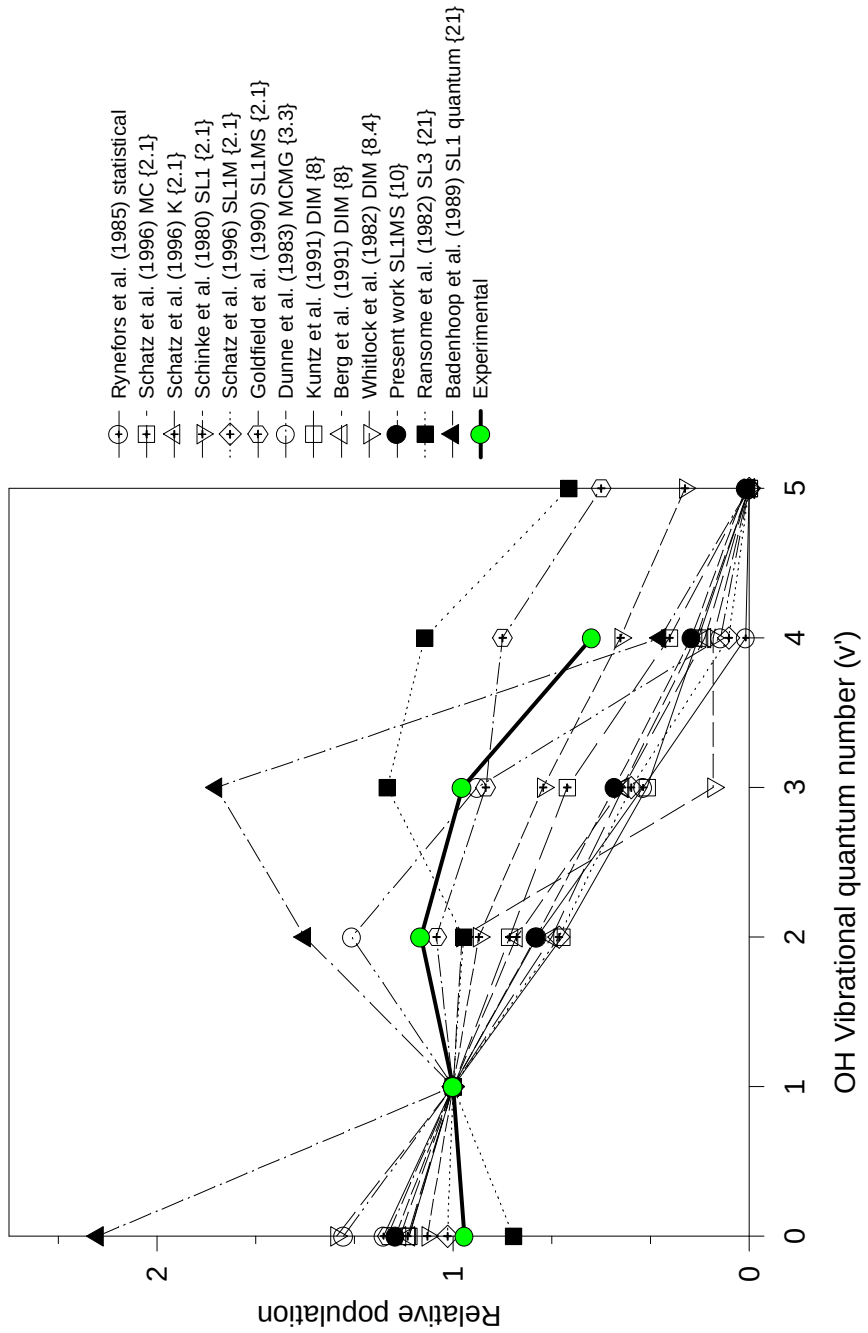

Figure 1.3 Theoretical product vibrational distributions for the reaction of $O(^1D_2)$ with H_2, as determined by various authors. The data are scaled to unit population in $v' = 1$. The data are tabulated in table (1.2). The experimental results shown are the average of the IR-CL results of Butler *et al.* [126] and Aker *et al.* [133] and using the LIF results of Butler *et al.* for $v' = 0$ and $v' = 1$ [126].

	Vibrational populations						Energy /
Reference / surface	$v' = 0$	$v' = 1$	$v' = 2$	$v' = 3$	$v' = 4$	$v' = 5$	kJ mol^{-1}
Rynefors [131] Statistical	0.372	0.301	0.216	0.108	0.004	0.000	—
Schatz [105] MC	0.300	0.260	0.210	0.160	0.070	0.000	2.1
Schatz [105] K	0.330	0.280	0.220	0.120	0.050	0.000	2.1
Schinke [96] SL1	0.250	0.230	0.210	0.160	0.100	0.050	2.1
Schatz [105] SL1M	0.326	0.320	0.205	0.128	0.022	0.000	2.1
Goldfield [98] SL1MS	0.222	0.182	0.192	0.162	0.152	0.091	2.1
Dunne [117] MCMG	0.290	0.212	0.284	0.194	0.020	0.000	3.3
Kuntz [135] DIM	0.348	0.303	0.192	0.105	0.052	0.000	8
Kuntz [136] DIM	0.339	0.295	0.197	0.125	0.044	0.000	8
Whitlock [100] DIM	0.387	0.277	0.269	0.034	0.034	0.000	8.4
Present work, SL1MS	0.334	0.280	0.210	0.127	0.054	0.003	10
Ransome [124] SL3	0.140	0.176	0.170	0.215	0.193	0.107	21
Badenhoop [137] SL1 (QM)	0.324	0.147	0.221	0.265	0.044	0.000	21

Table 1.2 Raw data for theoretical OH product vibrational distributions from the literature. See also figure (1.3) and text for details.

of the peak at $v' = 2$. No LIF work which compares $v' = 2$ to $v' = 1$ directly has been published, although the ratio $v' = 1/v' = 0$ appears to be very close to unity. What is certainly clear is that the reaction produces OH vibration up to the limit of available energy. At this time the IR-CL must be taken as the most reliable measurement of the vibrational distribution.

Theoretical calculations of the product vibrational distribution have been very sensitive to the PES. The preferential production of vibration in a simple bimolecular reaction is generally ascribed to an abstractive type mechanism, although this is dependent on the nature of the intermediate potential energy surface [7]. We need only look at the kinematically similar, but direct abstractive F + H_2 reaction which shows an inverted vibrational distribution. In the present reaction, it has been unclear whether or not there is some branching between two identifiable mechanisms (abstraction and insertion), and what effect this has on the product vibrational distribution. Park and Wiesenfeld studied the the product fractional vibrational energy release, $\langle f'_v \rangle$, for a number of reactions – see Table (1.3) [139]. The results show a range of $\langle f'_v \rangle$ indicating a relatively high value for F + H_2, but only a nominally lower value for $O(^1D_2)$ + H_2 highlighting a stark difference between these two reactions.

The results of theoretical attempts to model the vibrational distribution are summarised in figure (1.3). Some of the surfaces produce a bimodal or inverted vibrational distribution, others produce a monotonically decreasing distribution. In general, however, no statistical modelling leads to an inverted distribution, particularly the model of Rynefors *et al.* [131] which was successful at reproducing the rotational distribution. Many authors have ascribed the population of higher vibrational states to an abstraction mechanism. An immediate observation, however, is that the more *attractive* PESs, e.g. SL3, produce vibrational peaks at $v' = 2/3$, with the exception of the MC which has no barriers and does not produce an

Reaction	$\langle f'_v \rangle$	$\langle f'_r \rangle$	$\langle f'_t \rangle$
F + H_2	0.66	0.08	0.26
F + HCl	0.56	0.21	0.23
O(^{3}P) + HBr	0.51	0.24	0.25
O(^{1}D) + H_2	0.40	0.31	0.29
O(^{1}D) + HCl	0.58	0.18	0.24

Table 1.3 Disposal of available energy in XH (X=O,F) product of selected elementary bimolecular reactions [139].

inverted vibrational distribution [101].

The effects of the higher surfaces were investigated by Kuntz *et al.* [103, 92] who used DIM models of the three lowest surfaces (two ^{1}A′ and one ^{1}A″). Surface hopping was included in their QCT study by using Landau–Zener probabilities to jump between diabatic surfaces in the regions of crossing. Trajectories were started on either of the two lowest surfaces, and vastly different dynamics were observed. In particular it was observed that those trajectories starting on the lowest surface led to a monotonically decreasing vibrational distribution, peaking at $v' = 0$. Trajectories started on the first excited surface, on the other hand, were observed to produce a unimodal vibrational distribution peaking at $v' = 2$. These trajectories first encounter a small barrier to reagent approach, followed by a strong repulsive energy release into the exit channel.

In the early work of Schinke and Lester [96] it was observed that an increase in reagent translational energy caused an inversion of the product vibrational distribution. Aker, Sloan and Wright [140] made an investigation of the effects of reagent collision energy using QCT methods on the SL1S surface. They found that the vibrational distribution became inverted at higher translational energies, although the overall partitioning of energy (f'_v,

f'_r, f'_t) indicated only a slightly lower fraction into rotation. By monitoring the lowest attained potential energy of the trajectories they were able to ascribe no more than 5.4% of trajectories to an abstractive mechanism. By making a more detailed study of individual trajectories, Aker *et al.* discovered that higher translational energy collision caused the trajectory to collide with the inner wall of the insertion potential before the HH bond could relax [140]. This type of collision results in excitation of the symmetric and anti-symmetric stretches in favour of the bending mode. Conversely, lower energy collisions were found to follow the minimum energy path more closely, leading to more bending than stretch. The degree of attractiveness in the entrance channel will also affect the degree of vibrational excitation; a more attractive potential will cause trajectories to be accelerated into the hard collision described above, leading to an inverted vibrational distribution – as is observed for the SL3 potential (see section 3.11.1).

Schatz and coworkers developed a 2D quantum study with a bending sudden approximation to remove the bending degree of freedom [137]. A bimodal vibrational distribution was found. They observed that the drop off in the high v' tail from the quantum results was in very good agreement with (3D) classical trajectory results, implying a similar mechanism. The QCT results, which peak at larger v', were observed to avoid the deepest part of the well, but were still clearly insertive, in agreement with the study by Aker *et al.*[140]. A shift towards higher product v' with higher reagent translational energy was also observed, in agreement with other studies using quasi-classical methods.

Finally, it is worth noting that the most recent ground state PES, the K PES by Rabitz *et al.* lies somewhere between the SL1 and SL3 potentials in terms of attractiveness, and (at 5.0 kcal mol^{-1}) leads to a unimodal vibrational distribution [105].

1.9.5 Reagent Excitation

In the previous section we discussed the striking effect of reagent translational energy on the product vibrational distribution, as determined by Aker *et al.* [140]. It was found that the exact structure of the entrance channel, particularly the attractiveness, was found to be very important. Excitation of reagents to higher states is a fruitful method for the determination of subtle effects in scattering experiments, and this has been applied a number of times to study of the O + H_2 reaction.

Mikulecky and Gericke used photolytic production of O($^1D_2$) from ozone at low pressures to probe the O-H_2 reaction at superthermal oxygen velocities [134, 141]. They found that the excess translational energy makes a significant contribution to production of the highest rotational states of OH. They attributed this to a greater excitation of the bending vibration in the H_2O intermediate with a faster transfer of this energy into the asymmetric stretch and finally increased rotation in the product. A marginal drop in the Λ-doublet specificity led the authors to speculate an increase in abstraction. The mechanism behind Λ-doublet production may reflect non-adiabatic effects in the exit channel, however, and so no firm conclusions should be made. Gericke also studied the effect of reagent vibrational excitation by using stimulated Raman pumping (SRP) of the H_2. Molecular hydrogen in $v = 1$ was found to change the product vibrational ratio $v' = 3/v' = 4$ from 3.5, in the case of unexcited reagents, to 3.0 – a shift towards more $v' = 4$ product. This is evidently not a large effect, but Schinke [96] observed such a trend in his QCT calculations on the SL surface; vibrational excitation of the H_2 led to a highly inverted vibrational distribution.

Berg, Sloan and Kuntz made a comprehensive study of reagent vibrational, translational and rotational energy using QCT calculations [136]. They used a VB-DIM (valence bond diatomics-in-molecules) surface which included non-adiabatic surface hopping effects (using Landau-Zener probabilities). Each of the modes was excited at approximately the same

energy. Increased translational energy was found to decrease the cross-section, leading to a more forward peaking angular distribution; the faster reagent velocity increases the centrifugal barrier, and makes it more difficult for the potential to "capture" the O atom. It is tempting to ascribe the increase in forward scattering to a more direct mechanism like "stripping", where the O just captures an H atom and continues. This is not consistent with the underlying mechanism observed for this reaction, and it will be shown later that this effect is more likely a result of residence time in the well, coupled with angular momentum effects.

Increased reagent rotational excitation produced little effect on the product distributions[136]; the fractional partitioning of energy is almost exactly that for ground state reagents. Not even the total cross section was affected, although this may result from a combination of effects. Frustration of the insertion would be expected to occur at higher j levels, since the potential can no longer orient to its favoured C_{2v} geometry. On the other hand, the effective bond length of the molecule would be increased by its increased rotation (an effect not reproduced by the QCT calculations), or the molecule could act like a "baseball bat", colliding sharply with the incoming atomic reagent. In any case it would appear that the extra reagent energy is distributed fairly in the products, with little specificity.

Increased reagent vibrational energy decreases the number of traversals of the H_2O minimum, and this was found to lead to higher product vibrational quantum numbers, $OH(v')$. The reagent vibrational energy was also found to increase the likelihood of non-adiabatic crossings to excited surfaces in the reaction; other types of reagent energy were not efficient at doing this. Infact for H_2 in $v = 4$ a bimodal vibrational distribution, peaking in $v' = 2$ and $v' = 9$ was observed. The crossing seam allows for two effects: some trajectories are "rejected" by making a recrossing back to the reagent channel, those that are successful in reacting have had more time to relax during their time on the upper surface, and result in

Reaction	$\Gamma_{H/D}$
$O(^1D)/HD$	1.13 ± 0.08
$S(^1D)/HD$	1.91 ± 0.10
$F(^2P)/HD$	0.66 ± 0.10

Table 1.4 Product branching ratios for the reaction of HD with selected hot–atoms from the study by Tsukiyama *et al.* [142] — see text for details.

lower v'. Trajectories reacting directly on the ground state have the full energy immediately available to them and populate higher v'. In addition, the shape of the effective $v = 4$ potential, with a slightly higher mean H_2 bond length encourages reorientation to collinear geometries [136].

In all cases Berg, Sloan and Kuntz found that the product rotational distributions were much less sensitive to reagent excitation; the distributions retain their inverted nature, extending out to high product j'. This may be, once again, a signature of the underlying angular momentum constraints, in conjunction with some lesser specific dynamical effects.

1.9.6 Isotopic branching ratios

Whitlock *et al.* [123] were the first to use the $O(^1D_2)/HD$ isotopic variant to probe the details of their potential energy surface. They found an isotopic branching ratio $\Gamma_{H/D} = 5.6 \pm 0.2$ in favour of the H + OD products. This is highly nonstatistical when compared with the prior distribution value of $\Gamma_{H/D} = 1.00$. Tsukiyama *et al.* [142] made an experimental study of the reactions of $O(^1D)$, $S(^1D)$ and $F(^2P)$ with HD by producing hot atom precursors followed by VUV LIF of the product atoms – the results are shown in table (1.4).

As can be seen from table (1.4) the results of Tsukiyama *et al.* clearly differentiate between

traditional abstraction, F(^{2}P)/HD, and insertion of the ^{1}D atoms. The result for O(^{1}D) is only marginally larger than the prior distribution value, which is close to unity. The abstraction results are consistent with a classical picture where, in the rotating HD molecule, the H atom sweeps out a larger circle and is therefore more likely to be attacked (favouring the D atom product). In the case of an insertion complex, the same forces act on both the H and the D, and so the exit of the lighter H atom would be favoured [142].

Experimental and theoretical branching ratios from a number of studies at various collision energies are listed in table (1.5). Recent results on the SL1MS and K surfaces will be presented later in chapters 4 and 5. Table (1.5) clearly shows quite a wide spread in values from different surfaces.

1.9.7 Product angular distributions

The first *cross molecular beam* (CMB) study of the O(^{1}D$_2$)/H$_2$ reaction, carried out by Y. T. Lee and co-workers at a collision energy of 2.7 kcal mol^{-1}, indicated a symmetric forward-backward product angular distribution [145]. The results also indicated essentially no coupling between the product translational energy release and the angular distribution. Similar results were obtained at the higher collision energy of 4.0 kcal mol^{-1}, and the authors attributed this behaviour to an intermediate complex mechanism. At that time the experiment was not trivial, however, and their results must now be re–evaluated in the light of more recent CMB studies [20, 146] which indicate a tendency towards slightly more backward scattering, with a notable coupling between the product scattering angle and energy, as will be discussed in chapter 4.

The O(^{1}D$_2$)/H$_2$ system has recently become highly popular. Recent cross molecular beam studies by Cassavecchia *et al.* [147], and by Suits *et al.* [148] (using imaging detection) all indicate a preference for backward scattering which increases with reagent translational

Collision energy / kJ mol^{-1}	Branching ratio $\Gamma_{H/D}$	Technique/Surface	Reference
	Experimental		
10.0	1.13 ± 0.08	VUV LIF	[142]
10.0	1.5 ± 0.2	REMPI	[143]
10.0	1.3 ± 0.1	VUV LIF	[143]
10.0	1.33 ± 0.07	VUV RF	[114]
14.2	1.4 ± 0.2	REMPI	[143]
14.2	1.35 ± 0.20	VUV LIF	[113]
	Theoretical		
2.1	1.09 ± 0.08	MC	[118]
2.1	1.85 ± 0.24	SL1	[118]
2.1	1.79 ± 0.18	SL3	[118]
2.4	2.6 ± 0.4	MCMG	[144]
8.4	5.6 ± 0.2	WMF2	[123]
20.9	1.09 ± 0.06	MC	[118]
20.9	1.43 ± 0.18	SL1	[118]
24.1	2.0 ± 0.3	MCMG	[144]
10.0	1.000	RRHO	[142]

Table 1.5 Theoretical and Experimental isotopic branching ratios for the reaction of O(^{1}D) + HD. See text for abbreviations of surfaces and techniques.

energy. These observations are upheld by QCT calculations which allow for non-adiabatic crossings [104]. The results of measurement of the product angular distributions will be discussed further in the light of the results to be presented in the later chapters.

References

[1] M. Born and J. R. Oppenheimer, *Ann. Physik*, **84** (1927) 457.

[2] F. London, *Z. Elektrochem.*, **35** (1929) 552.

[3] J. O. Hirschfelder, H. Eyring and B. Topley, *J. Chem. Phys.*, **4** (1936) 170.

[4] R. D. Levine, *J. Phys. Chem.*, **94** (1990) 8872.

[5] J. C. Polanyi, *Science*, **236** (1987) 680.

[6] Y. T. Lee, *Science*, **236** (1987) 793.

[7] R. D. Levine and R. B. Bernstein, *Molecular Reaction Dynamics and Chemical Reactivity*, Oxford University Press, 1987.

[8] A. J. Orr–Ewing, *J. Chem. Soc. Faraday Trans.*, **92** (1996) 881, and references therein.

[9] *J. Phys. Chem.*, **91** (1987) 5365.

[10] *J. Chem. Soc. Faraday Trans.*, **85** (1989) 925.

[11] *J. Chem. Soc. Faraday Trans.*, **89** (1993) 1401.

[12] *J. Phys. Chem.*, **99** (1995) 13569.

[13] *J. Phys. Chem.*, **101** (1997) 7461.

[14] (a) T. H. Bull and P. B. Moon, *Discuss. Far. Soc.*, **17** (1954) 54.

(b) E. H. Taylor and S. Datz, *J. Chem. Phys.*, **23** (1955) 1711.

[15] (a) D. R. Herschbach, *Adv. Chem. Phys.*, **10** (1966) 319, and references therein.

(b) D. R. Herschbach, *Chem. Scr.*, **27** (1987) 327.

[16] Y. T. Lee, J. D. McDonald, P. R. Le Breton and D. R. Herschbach, *Rev. Sci. Instr.*, **40** (1969) 1402.

[17] (a) D. M. Neumark, A. M. Wodtke, G. N. Robinson, C. C. Hayden and Y. T. Lee, *J. Chem. Phys.*, **82** (1985) 3045.

(b) D. M. Neumark, A. M. Wodtke, G. N. Robinson, C. C. Hayden, K. Shobatake, R. K. Sparks, T. P. Shafer and Y. T. Lee, *J. Chem. Phys.*, **82** (1985) 3067, and references therein.

[18] Y. T. Lee, in *Atomic and Molecular Beam Methods*, ed. G. Scoles, Oxford University Press, 1987, vol. 1.

[19] G. Hall, K. Liu, M. J. McAuliffe, C. F. Giese and W. R. Gentry, *J. Chem. Phys.*, **81** (1984) 5577.

[20] K. Liu and D-. C. Che, *J. Chem. Phys.*, **103** (1995) 5164.

[21] (a) M. Faubel, L. Y. Rusin, S. Schlemmer, F. Sondermann, U. Tappe and J. P. Toennies, *J. Chem. Phys.*, **101** (1994) 2106.

(b) M. Faubel, B. Martinezhaya, L. Y. Rusin, U. Tappe and J. P. Toennies, *Chem. Phys. Lett.*, **232** (1995) 197.

[22] M. Faubel, B. Martinezhaya, L. Y. Rusin, U. Tappe and J. P. Toennies, F. J. Aoiz and L. Bañares, *Chem. Phys.*, **207** (1996) 227.

[23] F. J. Aoiz, L. Bañares, M. Faubel, B. Martinezhaya, L. Y. Rusin, U. Tappe and J. P. Toennies, *Chem. Phys.*, **207** (1996) 245.

[24] For a recent review of the F + H_2 system, see D. E. Manolopoulos, *J. Chem. Soc. Faraday Trans*, **93** (1997) 673.

[25] M. Alagia, N. Balucani, P. Casavecchia, D. Stranges and G. G. Volpi, *J. Chem. Soc. Faraday Trans.*, **91** (1995) 575.

[26] D. C. Clary, *J. Phys. Chem.*, **98** (1994) 10678.

[27] A. J. Orr–Ewing and R. N. Zare, in *The Chemical Dynamics and Kinetics of Small Radicals*, ed. K. Liu and A. Wagner, World Scientific, Singapore 1995.

[28] K. Kuwata and T. Kasai, in *The Chemical Dynamics and Kinetics of Small Radicals*, eds. K. Liu and A. Wagner, World Scientific, Singapore 1995.

[29] P. R. Brooks, *Science*, **193** 11.

[30] H. J. Loesch and A. Remscheid, *J. Chem. Phys.*, **93** (1990) 4779.

[31] H. J. Loesch and J. Möller, *J. Chem. Phys.*, **97** (1992) 9016.

[32] H. J. Loesch and J. Möller, *J. Phys. Chem.*, **97** (1993) 2158.

[33] S. E. Choi and R. B. Bernstein, *J. Chem. Phys.*, **83** (1985) 4463.

[34] D. H. Parker and R. B. Bernstein, *Annu. Rev Phys. Chem.*, **40** (1989) 561.

[35] S. R. Leone, *Acc. Chem. Res.*, **25** (1992) 71.

[36] W. R. Simpson, A. J. Orr–Ewing and R. N. Zare, *Chem. Phys. Lett.*, **212** (1993) 163.

[37] W. R. Simpson, A. J. Orr–Ewing, T. P. Rakitzis, S. A. Kandel, and R. N. Zare, *J. Chem. Phys.*, **103** (1995) 7299.

[38] W. R. Simpson, T. P. Rakitzis, S. A. Kandel, A. J. Orr–Ewing and R. N. Zare, *J. Chem. Phys.*, **103** (1995) 7313.

[39] A. J. Orr–Ewing, W. R. Simpson, T. P. Rakitzis, S. A. Kandel and R. N. Zare, *J. Chem. Phys.*, **106** (1997) 5961.

[40] M. Ben–Nun, M. Brouard, J. P. Simons and R. D. Levine, *Chem. Phys. Lett.*, **210** (1993) 423.

[41] R. N. Zare and D. R. Herschbach, *Proc. IEEE*, **51** (1963) 173.

[42] J. Solomon, *J. Chem. Phys.*, **47** (1967) 889.

[43] (a) G. E. Busch, R. T. Mahoney, R. I. Morse and K. R. Wilson, *J. Chem. Phys.*, **51** (1969) 837.

(b) G. E. Busch and K. E. Wilson, *J. Chem. Phys.*, **56** (1972) 3638.

[44] R. W. Diesen, J. C. Wahr and S. E. Adler, *J. Chem. Phys.*, **50** (1969) 3635.

[45] R. Schmiedl, H. Dugan, W. Meier and K. Welge, *Z. Phys. A*, **304** (1982) 137.

[46] (a) J. P. Simons, *J. Phys. Chem.*, **91** (1987) 5378.

(b) P. L. Houston, *J. Phys. Chem.*, **91** (1987) 5388.

(c) M. P. Docker, A. Hodgson and J. P. Simons, in *Molecular Photodissociation Dynamics*, eds. M. N. R. Ashfold and J. E. Baggott, Royal Society of Chemistry, London, 1987.

(d) P. L. Houston and G. E. Hall, *Annu. Rev. Phys. Chem.*, **40** (1989) 375.

(e) L. J. Butler and D. M. Neumark, *J. Phys. Chem.* **100** (1996) 12801.

[47] J. L. Kinsey, *J. Chem. Phys*, **66** (1977) 2560.

[48] (a) W. D. Phillips, J. A. Serri, D. J. Ely, D. E. Pritchard, K. R. Way and J. L. Kinsey, *Phys. Rev. Lett.*, **41** (1978) 937.

(b) E. J. Murphy, J. H. Brophy, G. S. Arnold, W. L. Dimpfl and J. L. Kinsey, *J. Chem. Phys.*, **70** (1979) 5910.

(c) E. J. Murphy, J. H. Brophy and J. L. Kinsey, *J. Chem. Phys.*, **74** (1981) 331.

(d) J. A. Serri, C. H. Becker, M. B. Evel, J. L. Kinsey, W. P. Moskowitz and D. E.

Pritchard, *J. Chem. Phys.*, **74** (1981) 5116.

(e) J. A. Serri, J. L. Kinsey and D. E. Pritchard, *J. Chem. Phys.*, **75** (1981) 663.

[49] (a) G. W. Johnson, S. Satyapal, R. Bersohn and B. Katz, *J. Chem. Phys.*, **92** (1990) 206. (b) A. Chattopadhyay, S. Tasaki, R. Bersohn and M. Kawasaki, *J. Chem. Phys.*, **95** (1991) 1033.

(c) B. Katz, J. Park, S. Satyapal, S. Tasake, A. Chattopadhyay, W. Yi and R. Bersohn, *Faraday Discuss. Chem. Soc.*, **91** (1991) 73.

(d) R. Bersohn and M. Kawasaki, *Isr. J. Chem.*, **34** (1994) 19.

[50] F. Green, G. Hancock, A. J. Orr-Ewing, M. Brouard, S. P. Duxon, P. A. Enriquez, R. Sayos and J. P. Simons, *Chem. Phys. Lett.*, **182** (1991) 568.

[51] M. Brouard, S. P. Duxon, P. A. Enriquez, R. Sayos and J. P. Simons, *J. Phys. Chem.*, **95** (1991) 8169.

[52] M. Brouard, S. P. Duxon, P. A. Enriquez and J. P. Simons, *J. Chem. Phys.*, **97** (1992) 7414.

[53] F. Green, G. Hancock and A. J. Orr-Ewing, *Faraday Discuss. Chem. Soc.*, **91** (1991) 79.

[54] M. L. Costen, G. Hancock, A. J. Orr-Ewing and D. Summerfield, *J. Chem. Phys.*, **100** (1994) 2754.

[55] (a) T. L. D. Collins, A. J. McCaffery and M. J. Wynn, *Phys. Rev. Lett.*, **66** (1991) 137.

(b) T. L. D. Collins, A. J. McCaffery, J. P. Richardson and M. J. Wynn, *Phys. Rev. Lett.*, **70** (1993) 3393.

(c) T. L. D. Collins, A. J. McCaffery, J. P. Richardson, R. J. Wilson and M. J. Wynn, *J. Chem. Phys.*, **102** (1995) 4419.

[56] W. R. Simpson, T. P. Rakitzis, S. A. Kandel, T. Lev–On and R. N. Zare, *J. Phys. Chem.*, **100** (1996) 7938.

[57] S. A. Kandel, T. P. Rakitzis, T. Lev–On and R. N. Zare, *J. Chem. Phys.*, **105** (1996) 7550.

[58] S. A. Kandel, T. P. Rakitzis, T. Lev–On and R. N. Zare, *Chem. Phys. Lett.*, **265** (1997) 121.

[59] F. J. Aoiz, M. Brouard and P. A. Enriquez, *J. Chem. Phys.*, **105** (1996) 4964.

[60] M. Brouard, H. M. Lambert, S. P. Rayner and J. P. Simons, *Mol. Phys.*, **89** (1996) 403.

[61] A. J. Alexander, F. J. Aoiz, L. Bañares, M. Brouard, J. Short and J. P. Simons, *J. Phys. Chem. A*, **101** (1997) 7544.

[62] J. Biesner, L. Schnieder, J. Schmeer, G. Ahlers, X. Xie, K. H. Welge, M. N. R. Ashfold and R. N. Dixon, *J. Chem. Phys.*, **88** (1988) 3607.

[63] J. Biesner, L. Schnieder, G. Ahlers, X. Xie, K. H. Welge, M. N. R. Ashfold and R. N. Dixon, *J. Chem. Phys.*, **91** (1989) 2901.

[64] X. Xie, L. Schnieder, H. Wallmeier, R. Boettner, K. H. Welge and M. N. R. Ashfold, *J. Chem. Phys.*, **92** (1990) 1608.

[65] D. H. Mordaunt, M. N. R. Ashfold and R. N. Dixon, *J. Chem. Phys.*, **100** (1994) 7360.

[66] M. N. R. Ashfold, D. H. Mordaunt and S. H. S. Wilson, in *Advances in Photochemistry*, D. Neckers, D. Volman and G. von Bunau, eds., Wiley, New York, 1996.

[67] L. Schnieder, K. Seekamp-Rahn, F. Liedeker, H. Steuwe and K. H. Welge, *Faraday Discuss. Chem. Soc.*, **91** (1991) 259.

[68] F. J. Aoiz, L. Bañares, M. J. D' Mello, V. J. Herrero, V. J. Sáez Rábanos, L. Schnieder and R. E. Wyatt, *J. Chem. Phys.*, **101** (1994) 5781.

[69] L. Schnieder, K. Seekamp-Rahn, J. Borkowski, E. Wrede, K. H. Welge, F. J. Aoiz, L. Bañares, M. J. D' Mello, V. J. Herrero, V. J. Sáez Rábanos and R. E. Wyatt, *Science*, **269** (1995) 207.

[70] D. W. Chandler and P. L. Houston, *J. Chem. Phys.*, **87** 1445.

[71] D. P. de Bruijn and J. Los, *Rev. Sci. Instrum.*, **53** (1982) 1020.

[72] A. J. R. Heck and D. W. Chandler, *Annu. Rev. Phys. Chem.*, **46** (1995) 335.

[73] P. L. Houston, *Acc. Chem. Res.*, **28** (1995) 453.

[74] See, for example, R. Miller and Z. Bačić, *J. Phys. Chem.*, **100** (1996) 12945, and references therein.

[75] C. Wittig and A. H. Zewail, in *Chemical Reactions in Clusters*, ed. E. R. Bernstein, Oxford University Press, 1996.

[76] S. W. Sharpe, Y. P. Zeng, C. Wittig and R. A. Beaudet, *J. Chem. Phys.*, **92** (1990) 943.

[77] Y. P. Zeng, S. W. Sharpe, S. K. Shin, C. Wittig, and R. A. Beaudet, *J. Chem. Phys.*, **97** (1992) 5392.

[78] P. Arrowsmith, F. E. Bartoszek, S. H. P. Bly, T. Carrington, P. E. Charters and J. C. Polanyi, *J. Chem. Phys.*, **73** (1980) 5895.

[79] P. Hering, P. R. Brooks, R. F. Curl, R. S. Judson and R. S. Lowe, *Phys. Rev. Lett.*, **44** (1980) 687.

[80] J. C. Polanyi and A. H. Zewail, *Annu. Rev. Phys. Chem.*, **28** (1995) 119.

[81] A. H. Zewail, *J. Phys. Chem.*, **100** (1996) 12701, and references therein.

[82] S.I. Ionov, G.A. Brucker, C. Jaques, L. Valachovic and C. Wittig, *J. Chem. Phys.*, **97** (1992) 9486.

[83] E. Bohmer, K. Mikhaylichenko and C. Wittig, *J. Chem. Phys.*, **99** (1993) 6545.

[84] C. Jaques, L. Valachovic, S. Ionov, E. Bohmer, Y. Wen, J. Segall and C. Wittig, *J. Chem. Soc. Faraday Trans.*, **89** (1993) 1419.

[85] S.I. Ionov, G.A. Brucker, C. Jaques, L. Valachovic and C. Wittig, *J. Chem. Phys.*, **99** (1993) 6553.

[86] (a) A. Weaver, R. B. Metz, S. E. Bradforth and D. M. Neumark, *J. Phys. Chem.*, **92** (1988) 5558.

(b) D. M. Neumark, *Acc. Chem. Res.*, **25** (1993) 33.

[87] I. M. Waller, T. N. Kitsopoulous, A. Weaver and D. M. Neumark, *J. Phys. Chem.*, **94** (1990) 2240.

[88] S. E. Bradforth, D. W. Arnold, D. M. Neumark and D. E. Manolopoulos, *J. Chem. Phys.*, **99** (1993) 6345.

[89] D. E. Manolopoulos, K. Stark, H. –J. Werner, D. W. Arnold, S. E. Bradforth and D. M. Neumark, *Science*, **262** (1993) 1852.

[90] K. S. Sorbie and J. N. Murrell, *Mol. Phys.*, **29** (1975) 1387.

[91] R. E. Howard, A. D. McLean and W. A. Lester Jr., *J. Chem. Phys.*, **71** (1979) 2412.

[92] P. J. Kuntz, B. I. Niefer and J. J. Sloan, *J. Chem. Phys.*, **88** (1988) 3629.

[93] J. R. Wiesenfeld, *Acc. Chem. Res.*, **15** (1982) 110.

[94] R. P. Wayne, *Chemistry of Atmospheres*, 2nd edn., Oxford University Press, 1992.

[95] M. J. Pilling and P. W. Seakins, *Reaction Kinetics*, Oxford University Press, 1995.

[96] R. Schinke and W. A. Lester Jr., *J. Chem. Phys.*, **72** (1980) 3754.

[97] R. Schinke, *J. Chem. Phys.*, **80** (1984) 5510.

[98] E. M. Goldfield and J. R. Wiesenfeld, *J. Chem. Phys.*, **93** (1990) 1030.

[99] J. N. Murrell, S. Carter, I. M. Mills and M. F. Guest, *Mol. Phys.*, **42** (1981) 605.

[100] P. A. Whitlock, J. T. Muckerman and E. R. Fisher, *J. Chem. Phys.*, **76** (1982) 4468.

[101] J. N. Murrell and S. Carter, *J. Phys. Chem.*, **88** (1984) 4887.

[102] R. Polák, I. Paidarová and P. J. Kuntz, *J. Chem. Phys.*, **82** (1985) 2352.

[103] R. Polák, I. Paidarová and P. J. Kuntz, *J. Chem. Phys.*, **87** (1987) 2863.

[104] G. C. Schatz, L. A. Pederson and P. J. Kuntz, *Faraday Discuss. Chem. Soc.*, *submitted.*

[105] T-. S. Ho, T. Hollebeek, H. Rabitz, L. B. Harding and G. C. Schatz, *J. Chem. Phys.*, **105** (1996) 10472.

[106] G. C. Schatz, A. Papaioannou, L. A. Pederson, L. B. Harding, T. Hollebeek, T. -S. Ho, and H. Rabitz, *J. Chem. Phys.*, **107** (1997) 2340.

[107] A. Dobbyn, *personal communication.*

[108] M. Pavlyuchenko, *J. Phys. Chem. USSR*, **14** (1940) 877; *Chem. Abs.*, **35** (1941) 3879.

[109] N. Basco and R. G. W. Norrish, *Can. J. Chem.*, **38** (1960) 1769; *Proc. Roy. Soc. A*, **260** 293.

[110] W. B. DeMore, *J. Chem. Phys.*, **47** (1967) 2777.

[111] R. F. Heidner and D. Husain, *Int. J. Chem. Kin.*, **5** (1973) 819.

[112] S. Koppe, T. Laurent, P. D. Naik, H.-R. Volpp, J. Wolfrum, T. Arusi-Parpar, I. Bar and S. Rosenwaks, *Chem. Phys. Lett.*, **214** (1993) 546.

[113] T. Laurent, P. D. Naik, H.-R. Volpp, J. Wolfrum, T. Arusi-Parpar, I. Bar and S. Rosenwaks, *Chem. Phys. Lett.*, **236** (1995) 336.

[114] R. K. Talukdar and A. R. Ravishankara, *Chem. Phys. Lett.*, **253** (1996) 177.

[115] W. B. DeMore, S. P. Sander, D. M. Golden, R.F. Hampson, M. J. Kurylo, C. J. Howard, A. R. Ravishankara, C. E. Kolb and M. J. Molina, *Chemical kinetics and photochemical data for use in stratospheric modelling*, JPL publication 94-26 (Jet Propulsion Laboratory, 1994).

[116] K. S. Sorbie and J. N. Murrell, *Mol. Phys.*, **31** (1976) 905.

[117] L. J. Dunne and J. N. Murrell, *Mol. Phys.*, **50** (1983) 635.

[118] M. S. Fitzcharles and G. C. Schatz, *J. Phys. Chem.*, **90** (1986) 3634.

[119] A. J. Alexander, F. J. Aoiz, L. Bañares, M. Brouard, V. J. Herrero and J. P. Simons, *Chem. Phys. Lett.*, *in press.*

[120] A. C. Luntz, R. Schinke, W. A. Lester Jr. and Hs. H. Günthard, *J. Chem. Phys.*, **70** (1979) 5908.

[121] G. K. Smith, J. E. Butler and M. C. Lin, *Chem. Phys. Lett.*, **65** (1979) 115.

[122] G. K. Smith and J. E. Butler, *J. Chem. Phys.*, **73** (1980) 2243.

[123] P. A. Whitlock, J. T. Muckerman and P. M. Kroger, in *Potential Energy Surfaces and Dynamics Calculations*, ed. D. G. Truhlar, (Plenum, New York, 1981), pp 551–586

[124] S. W. Ransome and J.S. Wright, *J. Chem. Phys.*, **77** (1982) 6346.

[125] G. M. Jursich and J. R. Wiesenfeld, *Chem. Phys. Lett.*, **119** (1985) 511.

[126] J. E. Butler, G. M. Jursich, I. A. Watson and J. R. Wiesenfeld, *J. Chem. Phys.*, **5365** (1986) 5365.

[127] C. B. Cleveland, G. M. Jursich, M. Trolier and J. R. Wiesenfeld, *J. Chem. Phys.*, **86** (1987) 3253.

[128] T. J. Sears, G. E. Hall and J. J. F. McAndrew, *J. Chem. Phys.*, **91** (1989) 5201.

[129] P. Andresen and E. W. Rothe, *J. Chem. Phys.*, **82** (1985) 3634.

[130] M. H. Alexander, *personal communication.*

[131] K. Rynefors, P. A. Elofson, and L. Holmlid, *Chem. Phys.*, **100** (1985) 53.

[132] J. E. Butler, R. G. MacDonald, D. J. Donaldson and J. J. Sloan, *Chem. Phys. Lett.*, **95** (1983) 183.

[133] P. M. Aker and J. J. Sloan, *J. Chem. Phys.*, **85** (1986) 1412.

[134] K. Mikuleky and K. -H. Gericke, *J. Chem. Phys.*, **96** (1992) 7490.

[135] P. J. Kuntz, B. I. Niefer and J. J. Sloan, *Chem. Phys.*, **151** (1991) 77.

[136] P. A. Berg, J. J. Sloan and P. J. Kuntz, *J. Chem. Phys.*, **95** (1991) 8038.

[137] J. K. Badenhoop, H. Koizumi and G. C. Schatz, *J. Chem. Phys.*, **91** (1989) 142.

[138] Y. Huang, Y. Gu, C. Liu, X. Yang and Y. Tao, *Chem. Phys. Lett.*, **127** (1986) 432.

[139] C. R. Park and J. R. Wiesenfeld, *Chem. Phys. Lett.*, **163** (1989) 230.

[140] P. M. Aker, J. J. Sloan and J. S. Wright, *Chem. Phys.*, **110** (1986) 275.

[141] K. Mikuleky and K. H-. Gericke, *Chem. Phys.*, **175** (1993) 13.

[142] K. Tsukiyama, B. Katz and R. Bersohn, *J. Chem. Phys.*, **83** (1985) 2889.

[143] Y. Matsumi, K. Tonokura, M. Kawasaki and H. L. Kim, *J. Phys. Chem.*, **96** (1992) 10622.

[144] L. J. Dunne, *Chem. Phys. Lett.*, **158** (1989) 535.

[145] R. J. Buss, P. Casavecchia, T. Hirooka, S. J. Sibener and Y. T. Lee, *Chem. Phys. Lett.*, **82** (1981) 386.

[146] Y-. T. Hsu and K. Liu, *J. Chem. Phys.*, (1997) *in press.*

[147] M. Alagia, N. Balucani, L. Cartechini, P. Casavecchia, E. H. van Kleef, G. G. Volpi, P. J. Kuntz and J. J. Sloan, *J. Chem. Phys., submitted.*

[148] M. Ahmed, D. S. Peterka and A. G. Suits, *Abstracts of the 1997 conference on the dynamics of molecular collisions* (Gull Lake, Minnesota).

Chapter 2 Theoretical considerations

2.1 Introduction

In this chapter the theory behind measurement of stereodynamical properties by Doppler methods will be discussed. The chapter begins with a discussion of kinematic considerations and the frames of reference employed. The moment expansion of the CM product distribution is detailed, both in the Bipolar formalism of Dixon [1], and the more recent Polarisation Dependent Differential Cross Sections (PDDCS) of Shafer *et al.* [2]. Equations for the relationship between these two formalisms are given. The dependence of the Doppler lineshape on the bipolar moments of Dixon, and their relationship to the PDDCS is discussed.

2.2 Kinematic Considerations

2.2.1 Photoinitiation sequence

We begin with a discussion of the kinematic considerations involved in the present work. The 'hot atom' reaction involves the photolysis of a suitable precursor molecule, AD, in the presence of a target molecule, BC, either in a bulb (low pressure gas), or in a molecular beam. The translationally fast atomic fragments may then undergo reaction with the target molecules:

$$\mathrm{AD} + h\nu \rightarrow \mathrm{A_t} + \mathrm{D}, \tag{2.1}$$

$$\mathrm{A_t} + \mathrm{BC} \rightarrow \mathrm{AB}|\mathrm{f}\rangle + \mathrm{C}, \tag{2.2}$$

where the product AB is born in a range of quantum states $|f\rangle$ and may be probed (state–selectively) *via* Doppler resolved laser excitation. If linearly polarised photolysis radiation is used in the photolysis step (equation 2.1), then the atomic fragments will, in general, be aligned relative to the electric vector of the photolysis radiation, $\boldsymbol{\varepsilon_{ph}}$. The LAB angular distribution of recoil velocities is given by[3],

$$P(\hat{\boldsymbol{u}}_{\mathbf{A}}) \;=\; \frac{1}{4\pi}\left[1 \;+\; \beta\,\mathrm{P}_2(\cos\Theta)\right] \tag{2.3}$$

where P_2 is the second Legendre polynomial, and Θ is the angle between the photolysis vector and the fragment recoil velocity unit vectors: $\cos\Theta = \hat{\boldsymbol{\varepsilon}}_{\boldsymbol{ph}} \cdot \hat{\boldsymbol{u}}_{\mathbf{A}}$. The anisotropy parameter, β, defines the shape of the distribution with respect to the transition dipole moment of the precursor, $\boldsymbol{\mu}_{\mathbf{AD}}$,

$$\beta \;=\; 2\,\langle \mathrm{P}_2(\hat{\boldsymbol{\mu}} \cdot \hat{\boldsymbol{u}}_{\mathbf{A}})\rangle \;=\; 5\,\langle \mathrm{P}_2(\hat{\boldsymbol{\varepsilon}}_{\boldsymbol{ph}} \cdot \hat{\boldsymbol{u}}_{\mathbf{A}})\rangle \tag{2.4}$$

where the brackets $\langle \ldots \rangle$ indicate an average over the angle implied by the scalar product. As can be seen from equation (2.3), the distribution is azimuthally symmetric, the polar symmetry axis being the direction of $\boldsymbol{\varepsilon_{ph}}$ (i.e., the Z axis of our laboratory (LAB) frame). For prompt recoil (relative to the motion of the precursor) β takes the limiting values of -1 for recoil perpendicular to the transition moment, and $+2$, corresponding to recoil along the transition moment.

The anisotropic distribution of the atomic precursor is carried over into the distribution of reagent relative velocity vectors $P(\boldsymbol{k})$ for A...BC. Of course the actual form of $P(\boldsymbol{k})$ will

also include an average over the motions of the precursor molecule AD, the target molecule BC, and the range, if any, of dissociation channels available to the photolysis.

We begin by establishing an idealised relationship between the product's speed and its angular distribution.

2.2.2 The idealised photoinitiated reaction

We aim to establish relationships between the speed distribution of a product, as could be measured by time–of–flight or Doppler methods, and the angular distribution of that product in the centre of mass frame. Following Shafer *et al.* [4] we begin with a discussion of the limiting case for the photoinitiated reaction under a number of simplifying assumptions:

- The precursor and target molecule are assumed to be stationary with respect to each other, this is well approximated by an effusive co–expansion of AD and BC.
- We also assume that the photodissociation occurs by a single channel (perhaps using monochromatic linearly polarised radiation) giving atoms with a single velocity characterised by the anisotropy parameter β.
- Finally, it is assumed that the product partner fragment, C, is structureless (i.e. it has no energetically accessible excited states).

The internal states of the reagents and products in our idealised reaction are uniquely defined such that the speed distribution of the AB product in the A...BC CM frame may be deduced by conservation of energy and momentum [4],

$$w \;=\; \frac{m_{\mathrm{C}}}{M}\left(\frac{2\left(\mu E_t/m_{\mathrm{A}} - \Delta E\right)}{\mu'}\right)^{1/2}. \tag{2.5}$$

In this equation m_{X} is the mass of the fragment X, μ and μ' are the reduced masses of the reagents and products respectively, and M is the total mass. E_t is the collision energy,

and ΔE is the reaction exoergicity. Since the hot atom is monoenergetic, the motion of the centre of mass, v_{cm}, is given simply by,

$$v_{cm} \;=\; \frac{m_{\mathrm{A}}}{M}\left(\frac{2E_t}{m_{\mathrm{A}}}\right)^{1/2}. \tag{2.6}$$

The speed of the AB product in the LAB frame, v, is determined from the CM speed v_{cm}, the speed of AB in the CM frame (w, given above) and the cosine of the CM scattering angle, $\cos\theta_t$ according to the law of cosines: see figure (2.1),

$$v^2 \;=\; v_{cm}^2 \;+\; w^2 \;+\; 2wv_{cm}\cos\theta_t. \tag{2.7}$$

The range of product lab speeds, v, must obey the triangular relation for the three vectors:

$$|v_{cm} - w| \;\leq\; v \;\leq\; |v_{cm} + w| \tag{2.8}$$

The probability distribution of AB product lab speeds, $P(v)$, is then simply related to the product angular distribution, $P(\cos\theta_t)$:

$$P(v)\,\mathrm{d}v \;=\; P(\cos\theta_t)\,\mathrm{d}(\cos\theta_t). \tag{2.9}$$

The product angular distribution is more commonly written as the CM differential cross section (DCS) such that,

$$P(\cos\theta_t) \;=\; \frac{2\pi}{\sigma}\frac{\mathrm{d}\sigma}{\mathrm{d}\omega_t} \tag{2.10}$$

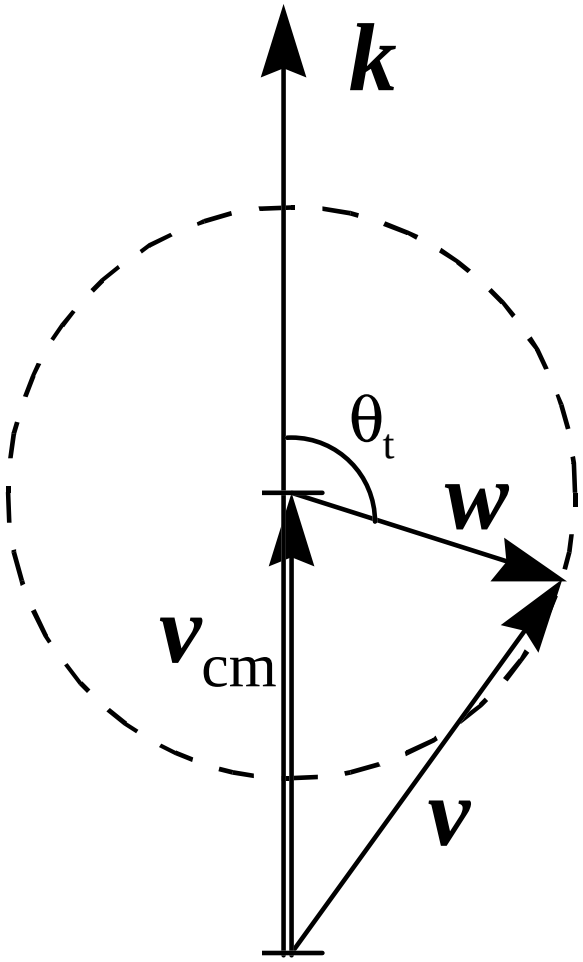

Figure 2.1 Simplified ('collapsed') Newton diagram showing the idealised photoinitiated A + BC reaction referred to in the text. The velocity of the centre of mass, $\boldsymbol{v_{cm}}$ lies parallel to the velocity of A.

where σ is the total reaction cross section, as mentioned in chapter 1. The probability distribution is normalised to unity,

$$\int_{-1}^{+1} P(\cos\theta_t)\,\mathrm{d}(\cos\theta_t) \;=\; 1, \tag{2.11}$$

and the solid angle, $\mathrm{d}\omega_t \;=\; \mathrm{d}(\cos\theta_t)\mathrm{d}\phi_t$. In equation (2.10), σ is the reactive cross section, in units of area, and the DCS ($d\sigma/\mathrm{d}\omega_t$) is therefore also in units of area over a given solid angle (area/steradian).

Combining equations (2.9) and (2.10) we obtain,

$$P(v) \;=\; \frac{2\pi}{\sigma}\,\frac{\mathrm{d}\sigma}{\mathrm{d}\omega_t}\,\frac{\mathrm{d}(\cos\theta_t)}{\mathrm{d}v} \tag{2.12}$$

and,

$$P(v) \;=\; \frac{2\pi}{\sigma}\,\frac{\mathrm{d}\sigma}{\mathrm{d}\omega_t}\,\frac{v}{wv_{cm}} \tag{2.13}$$

where we have used equation (2.7) to obtain the Jacobian transformation between $\cos\theta_t$ and v. This result is significant: it shows that the LAB speed distribution and CM angular distribution may be simply related by a simple speed dependent factor. Thus, for this idealised bimolecular reaction, determination of the speed distribution is equivalent to determination of the normalised differential cross section. In practice, however, the kinematics or energetics may make the range of observable speeds too small to be measured. For example, if m_{B} is much greater than the masses of the other fragments, most of the kinetic energy will be transferred to the C product, and the AB product velocity will be too small to measure practically. The full range of situations has been quantified by Shafer *et al.* who used the quotient γ,

$$\gamma = \frac{w}{v_{cm}} = \frac{m_{\mathrm{C}}}{m_{\mathrm{A}}}\left(\frac{\mu E_{\mathrm{A}} - m_{\mathrm{A}}\Delta E}{\mu' E_{\mathrm{A}}}\right)^{1/2}, \tag{2.14}$$

which, for $\Delta E = 0$, reduces to:

$$\gamma = \left(\frac{m_{\mathrm{C}}\, m_{\mathrm{BC}}}{m_{\mathrm{A}}\, m_{\mathrm{AB}}}\right)^{1/2}. \tag{2.15}$$

There are three clearly identifiable cases:

1. Case 1: $w \ll v_{cm} (\gamma \ll 1)$. This case applies to the reaction of a heavy hot atom A with a light target BC. the centre of mass velocity dominates the triangular relationship and makes the relative difference between forward scattered and backward scattered LAB velocities, v, very small.
2. Case 2: $w \gg v_{cm} (\gamma \gg 1)$. When a light A atom reacts with a heavy target BC molecule, γ is large. In this case the LAB velocity of the product v is close to that of the CM value w. The only dynamically significant component of the product velocity is its angular anisotropy, and for a photoinitiated bulb reaction, this will be dependent on the angular anisotropy of the hot atom, β.
3. Case 3: $w \approx v_{cm} (\gamma \approx 1)$. This is the optimal situation for photoinitiated bulb reactions, and occurs for $\Delta E \approx 0$ when $m_{\mathrm{A}} \approx m_{\mathrm{C}}$. The range of product speeds as a function of scattering angle is broad. Unlike the case of $\gamma \gg 1$, the measurable information is no longer limited by the hot atom anisotropy, but is limited by the sharpness of the distribution of hot atom speeds.

For the reaction of O + H_2, using the simplified kinematic relationship (equation 2.15), we find $\gamma = 0.086$ which is small, and approximates to case 1 above. We are saved, however, by the large exoergicity of the reaction and using the full expression (equation 2.14) in the limit of no product internal energy, we obtain a revised estimate of $\gamma = 0.42$. Gamma

is very much dependent on the internal energy of the product fragment, and so only low rovibrational states will provide significant information. Furthermore, these estimates make a number of assumptions, especially regarding the target velocity, which for the relatively light H_2 will be significant.

2.3 Angular momentum polarisation

2.3.1 Classical description of rotational angular momentum distributions

Classically, in the limit of high angular momentum, a spatial distribution of angular momenta may be written as an expansion in spherical harmonics,

$$P(\boldsymbol{J}) \;=\; \frac{1}{4\pi}\sum_k\sum_q c_{kq}\mathrm{Y}_{kq}(\theta_r,\phi_r), \tag{2.16}$$

where (θ_r,ϕ_r) are the continuously distributed polar co–ordinates in some fixed (xyz) frame. For an azimuthally symmetric system, $q\equiv 0$ and, provided that we choose the symmetry axis as our z axis, we may rewrite equation (2.16) in terms of Legendre polynomials,

$$P(\boldsymbol{J}) \;=\; \frac{1}{4\pi}\sum_k a_k\mathrm{P}_k(\cos\theta_r). \tag{2.17}$$

The a_k coefficients of the expansion give the moments of the distribution,

$$a_k = (2k+1)\langle \mathrm{P}_k(\cos\theta_r)\rangle,$$

and the above equations may be recast in terms of the alignment parameters, $A_q^{(k)}(J)$ defined as[1],

$$A_0^{(0)}(J) \;=\; 1 \tag{2.18}$$

[1]Note that the quadrupolar alignment parameter is exceptional in its definition due to a factor of 2.

$$
\begin{aligned}
A_0^{(1)}(J) &= \langle \mathrm{P}_1(\cos\theta)\rangle \\
A_0^{(2)}(J) &= 2\langle \mathrm{P}_2(\cos\theta)\rangle \\
A_0^{(3)}(J) &= \langle \mathrm{P}_3(\cos\theta)\rangle \\
A_0^{(4)}(J) &= \langle \mathrm{P}_4(\cos\theta)\rangle, \quad \textit{etc.}
\end{aligned}
$$

The first moment represents the dipolar distribution of $\boldsymbol{J}$, i.e., the *orientation*. The second moment represents the *alignment*, see figure (2.2). This may be generalised to the expansion in terms of spherical harmonics, equation (2.16), although in this case alignment parameters with $q \neq 0$ can arise, and these describe the distribution of the projection of $\boldsymbol{J}$ onto the xy plane.

2.3.2 The multipole moments

The concept of alignment parameters in the case of small $\boldsymbol{J}$ requires a quantum formulation. The system is defined in terms of the *density–matrix*, $\boldsymbol{\rho} = \rho_{MM'}$, The diagonal elements of this matrix, ρ_{MM}, simply give the populations of the states $|JM)$. The off–diagonal elements describe the coherence terms that arise when cylindrical symmetry is broken and quantum mechanical phase relationships exist between $|JM)$ and $|JM')$ states.

In order to describe the angular momentum distribution, we require a set of operators whose expectation values will give us the moments of the distribution. One such set of operators are the *spherical tensor operators* $J_q^{(k)}$ which may be expanded in terms of the more familiar angular momentum operators, $J_\pm$ and J_z. The alignment parameters are given by,

$$
A_q^{(k)}(J) = \frac{c(k)}{\langle JM|\boldsymbol{J^2}|JM\rangle^{k/2}} \langle J_q^{(k)}\rangle, \tag{2.19}
$$

where $c(k)$ are normalisation parameters (see ref.[5]). The $\langle J_q^{(k)}\rangle$ are the multipole moments

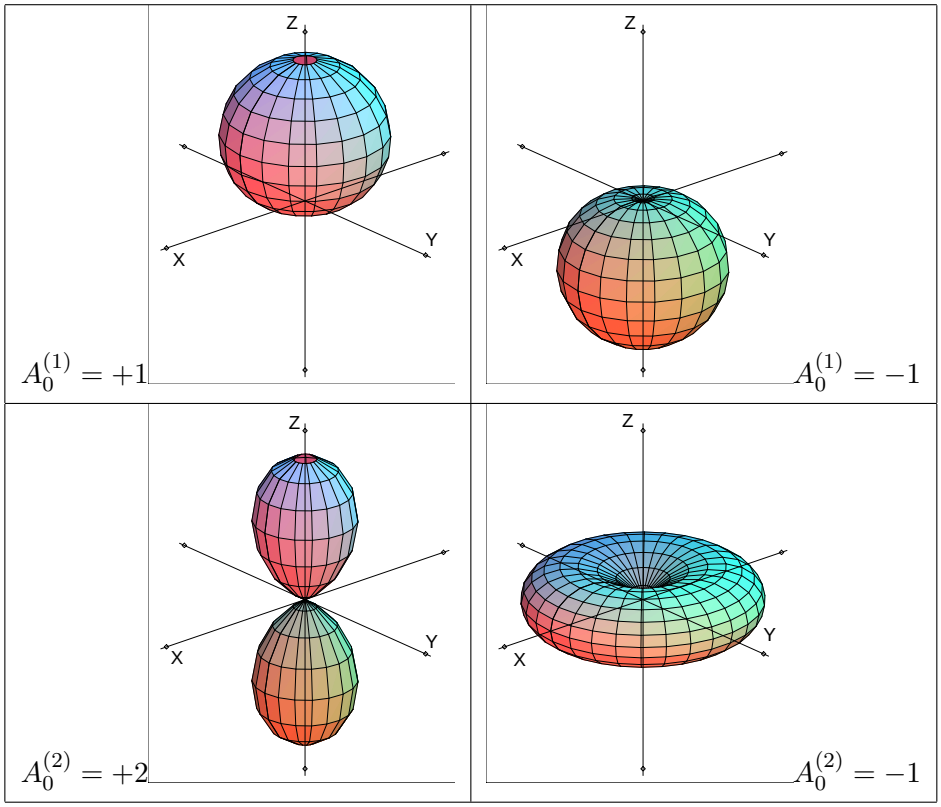

Figure 2.2 Polar plots of the $P(\boldsymbol{J})$ vector distribution illustrating the concepts of *orientation* and *alignment*: orientation (top panels) distinguishes the sense ($+z$ or $-z$) whereas alignment is only a measure of the degree of polarisation along the z axis or in the xy plane. Alignment parameters corresponding to the situations pictured are given, with $A_0^{(0)} \equiv 1$ and all other alignment parameters set to zero.

of the spherical tensor operators,

$$\langle J_q^{(k)} \rangle \;=\; \langle (J|J_q^{(k)}|J) \rangle \;=\; \sum_M \sum_{M'} \rho_{MM'} \langle JM'|J_q^{(k)}|JM \rangle \tag{2.20}$$

where $\rho_{MM'}$ are the density matrix elements. These spherical tensor operators are very useful since they transform under rotation in the same way as the angular momentum vectors, enabling easy transfer between frames. They also couple in the same way as angular momenta; for example an operator acting on orbital angular momentum space may be coupled to an operator acting on rotational angular momentum space to form an operator that acts on both spaces, or if the angular momenta are coupled, on the total angular momentum space. Finally, by use of the Wigner–Eckart theorem, the factoring of dynamical and geometrical (or selection rule) terms in the system is facilitated. As a simple example, for an axially symmetric system, the density matrix becomes diagonal and employing the Wigner–Eckart theorem,

$$\langle (J|J_q^{(k)}|J) \rangle \;=\; \sum_M \rho_{MM} (-1)^{J-M} \begin{pmatrix} J & k & J \\ -M & q & M \end{pmatrix} \langle J||J^{(k)}||J \rangle. \tag{2.21}$$

The 3J symbol ensures that $M + (-M) = q = 0$, thus a system with axial symmetry may only possess moments with $q = 0$ (provided we choose the symmetry axis as our z axis). The reduced matrix elements $\langle J||J^{(k)}||J \rangle$ are independent of the choice of frame, however, and are given simply by,

$$\begin{aligned} \langle J||J^{(0)}||J \rangle &= (2J+1)^{\frac{1}{2}}, \\ \langle J||J^{(1)}||J \rangle &= [J(J+1)(2J+1)]^{\frac{1}{2}}, \\ \langle J||J^{(2)}||J \rangle &= \left[\frac{J(J+1)(2J-1)(2J+1)(2J+3)}{6} \right]^{\frac{1}{2}}, \qquad \textit{etc.} \end{aligned} \tag{2.22}$$

2.3.3 The LIF intensity of a polarised ensemble

The intensity for a (1+1) LIF process involves a resonant absorption process followed by a spontaneous fluorescence:

$$I \;=\; C\sum_{M_f}\left\langle\left|\sum_{M_e}(f|\hat{\boldsymbol{\varepsilon}}_{\boldsymbol{d}}\cdot\boldsymbol{\mu}|e)(e|\hat{\boldsymbol{\varepsilon}}_{\boldsymbol{a}}\cdot\boldsymbol{\mu}|i)\right|^2\right\rangle \tag{2.23}$$

where $\hat{\boldsymbol{\varepsilon}}_{\boldsymbol{d}}$ and $\hat{\boldsymbol{\varepsilon}}_{\boldsymbol{a}}$ are the polarisation unit vectors of the detected and absorbed photons respectively, and $\boldsymbol{\mu}$ represents the dipole moment operator of the molecule. C is a normalisation constant which contains information regarding populations. The initial state is denoted $|i)$ and the sums in equation (2.23) run over the (e) intermediate and (f) final M quantum states, subject to the selection rules for these processes. Expanding out the summations, and following some recoupling of angular momenta, Greene and Zare [6] have shown that this expression may be written,

$$I \;=\; CS\sum_{k_d}\sum_{k_a}\sum_{k}\mathcal{A}_q^{(k)}(J_i)\;\epsilon'(k_d,k_a,k,q,\Omega)\;\gamma'_{k_dk_ak}(J_i,J_e,J_f). \tag{2.24}$$

In this equation, ϵ' are excitation–detection geometrical factors which are a function of the multipole indices of the detected and absorbed photons and of their propagation and polarisation angles denoted collectively by Ω. The $\gamma'_{k_dk_ak}$ are angular momentum coupling factors. C is a constant proportional to the population of the initial state, S is the product of the excitation and emission linestrengths and the $\mathcal{A}^{(k)}$ are the alignment parameters. The power of the Wigner–Eckart theorem in this case is quite clear – equation (2.23) has been reduced to a very convenient form keeping alignment and geometrical factors separate.

The ϵ' factors for twelve special orthogonal excitation–detection geometries involving linearly polarised light have been tabulated by Dixon [1] and the $\gamma'_{k_dk_ak}$ are simply functions

Line	$\overline{\gamma}'_{220}$	$\overline{\gamma}'_{202}$	$\overline{\gamma}'_{022}$	$\overline{\gamma}'_{222}$	$\overline{\gamma}'_{224}$
$Q_{22}(14)$	0.150079	−0.245353	−0.992347	0.107606	0.062920
${}^{Q}R_{12}(14)$	−0.083022	−0.247159	0.446556	−0.052963	−0.024631
$P_{22}(14)$	−0.066882	−0.246760	0.553424	−0.052877	−0.040658
${}^{P}Q_{12}(14)$	0.149793	−0.244886	−0.992347	0.107401	0.062800

Table 2.1 Angular momentum coupling factors for the OH A-X 1+1 LIF transitions used in this thesis.

of the rotational quantum numbers. For example γ'_{220} is given by,

$$\gamma'_{220} = (-1)^{J_i - J_f} \frac{9(2J_e+1)}{2} \left\{ \begin{array}{ccc} J_e & J_e & 2 \\ 1 & 1 & J_f \end{array} \right\} \left\{ \begin{array}{ccc} J_e & J_e & 2 \\ 1 & 1 & J_i \end{array} \right\}. \tag{2.25}$$

where $\{:::\}$ denotes a 6J symbol [7]. After accounting for the effects of hyperfine coupling and the detection of unresolved fluorescence, the γ' are denoted $\overline{\gamma}'_{k_d k_a k}$. The $\overline{\gamma}'_{k_d k_a k}$ for the OH LIF transitions used in this thesis are given in table (2.1).

Equation (2.24) accounts for the total intensity of the LIF. The $\mathcal{A}_q^{(k)}(J_i)$ may be written as functions of the Doppler resolved lineshape, however, and may be related to moments of the CM distribution of product linear and angular momenta [1].

2.4 The CM angular distribution

2.4.1 The CM frame

We begin by defining the centre–of–mass frame and co–ordinate system which will be used to characterise the product angular distribution. For the atom–diatom reaction (2.2), the reagent and product relative velocity vectors are $\boldsymbol{k} = \boldsymbol{v}_{\mathbf{A}} - \boldsymbol{v}_{\mathbf{BC}}$ and $\boldsymbol{k'} = \boldsymbol{v}_{\mathbf{AB}} - \boldsymbol{v}_{\mathbf{C}}$. These

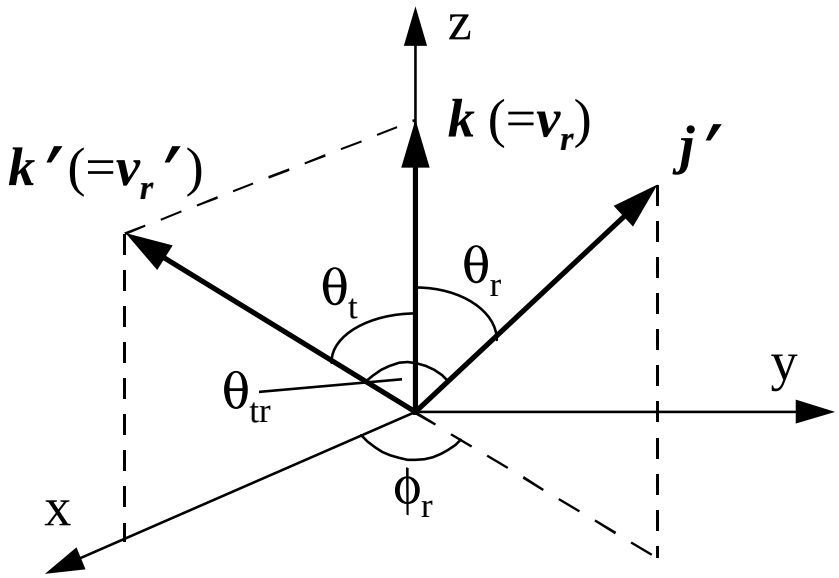

Figure 2.3 The centre–of–mass frame co–ordinate system used to characterise the $\boldsymbol{k}$,$\boldsymbol{k'}$,$\boldsymbol{j'}$ distribution.

vectors are independent of the motion of the centre–of–mass of the system [8]. The product molecule rotational angular momentum vector is denoted $\boldsymbol{j'}$. The variables $\omega_t = \{\theta_t, \phi_t\}$ and $\omega_r = \{\theta_r, \phi_r\}$ are the angular co–ordinates of the $\boldsymbol{k'}$ and $\boldsymbol{j'}$ vectors referenced to the CM frame, whose z axis lies in the direction of the relative velocity vector, $\boldsymbol{k}$, see figure (2.3).

2.4.2 The CM semiclassical angular distribution

For an atom–diatom reaction (equation 2.2), the CM semiclassical probability density function may be written,

$$P(\omega_t, \omega_r, w) \;=\; P(\omega_t, \omega_r)\,\delta(w - w_f) \;=\; \frac{1}{\sigma}\frac{\mathrm{d}^2\sigma}{\mathrm{d}\omega_t \mathrm{d}\omega_r}\,\delta(w - w_f), \tag{2.26}$$

where w is the CM product speed which, for state $|f\rangle$ at a given total energy, is constrained by energy conservation to w_f.

Following Dixon [1] the CM semiclassical angular distribution can be expanded in terms of bipolar harmonics,

$$P(\omega_t, \omega_r) \;=\; \frac{1}{16\pi^2} \sum_K \sum_Q \sum_{k_1} \sum_{k_2} [k_1][k_2] h_Q^K(k_1, k_2) B_Q^K(k_1, k_2; \omega_t, \omega_r) \tag{2.27}$$

where $[x]$ denotes $(2x+1)$. The bipolar harmonics, $B_Q^K(k_1, k_2; \omega_t, \omega_r)$, provide a closed set of orthogonal functions in the space spanned by two directions, given in this instance by the angular co–ordinates ω_t and ω_r. They are defined as [1, 9, 7],

$$B_Q^K(k_1, k_2; \omega_t, \omega_r) \;=\; \sum_{q_1} \sum_{q_2} (-1)^{K-Q} [K]^{\frac{1}{2}} \begin{pmatrix} k_1 & K & k_2 \\ q_1 & -Q & q_2 \end{pmatrix} C_{k_1\, q_1}(\theta_t, \phi_t) C_{k_2\, q_2}(\theta_r, \phi_r) \tag{2.28}$$

The expectation values of these bipolar harmonics are the CM frame *bipolar moments* and provide a complete description of the correlated distribution in the centre–of–mass frame,

$$h_Q^K(k_1, k_2) \;=\; \int\int\int\int B_Q^K(k_1, k_2; \omega_t, \omega_r)^* P(\omega_t, \omega_r)\, \mathrm{d}(\cos\theta_t)\, \mathrm{d}(\cos\theta_r)\, \mathrm{d}\phi_t\, \mathrm{d}\phi_r, \tag{2.29}$$

Since $\boldsymbol{k'}$ is defined as lying in the CM xz–plane, $\phi_t = 0$ (see figure 2.3). For $P(\omega_t, \omega_r)$ to be real, Q must therefore equal zero [10]. The expression for the angular distribution may then be written [1],

$$P(\omega_t, \omega_r) \;=\; \frac{1}{16\pi^2} \sum_K \sum_{k_1} \sum_{k_2} [k_1][k_2] h_0^K(k_1, k_2) B_0^K(k_1, k_2; \omega_t, \omega_r). \tag{2.30}$$

An alternative expansion in Biedenharn polynomials has been given by Case and Herschbach [11] and this is equivalent to equation (2.30).

Shafer–Ray *et al.* [2] employed a CM expansion in terms of (modified) spherical harmonics[2] [2],

$$P(\omega_t, \omega_r) \;=\; \sum_k \sum_q \frac{[k]}{4\pi}\; \frac{1}{\sigma}\frac{\mathrm{d}\sigma_{kq}}{\mathrm{d}\omega_t}\; C_{k\,q}(\theta_r, \phi_r)^* \tag{2.31}$$

and,

$$-k \;\leq\; q \;\leq\; +k \tag{2.32}$$

$$0 \;\leq\; k \;\leq\; 2j' \tag{2.33}$$

where j' is the rotational quantum number of the product molecule. The last relationship (2.33) restricts the range of k to make the classical distribution (2.31) consistent with quantum mechanics. The polarisation dependent differential cross–sections (PDDCS) are defined by,

$$\frac{1}{\sigma}\frac{\mathrm{d}\sigma_{kq}}{\mathrm{d}\omega_t} \;=\; \int\int C_{k\,q}(\theta_r, \phi_r) P(\omega_t, \omega_r)\, \mathrm{d}(\cos\theta_r)\, \mathrm{d}\phi_r \tag{2.34}$$

Note that the (kq) notation of the semiclassical PDDCS indicates a *spherical tensor density*, consistent with a fully quantum mechanical formulation where the PDDCS would be obtained from the density matrix [12].

Aoiz *et al.* [10] have shown that the Bipolar formalism of Dixon is entirely equivalent to the PDDCS formalism of Shafer–Ray *et al.*. Substitution of equation (2.30) into equation (2.34) gives the following relationship:

[2]Note that in ref.[2] the translational co–ordinates are denoted Ω_r and the rotational co–ordinates are $\Omega_{J'}$.

$$\frac{1}{\sigma}\frac{\mathrm{d}\sigma_{kq}}{\mathrm{d}\omega_t} \;=\; \frac{1}{4\pi}\sum_{k_1}[k_1]\, s^{k_1}_{kq}\, C_{k_1\,-q}(\theta_t, 0) \tag{2.35}$$

$$s^{k_1}_{kq} \;=\; \sum_{K}(-1)^K[K]^{\frac{1}{2}} \begin{pmatrix} k_1 & K & k \\ q & 0 & -q \end{pmatrix} h^K_0(k_1, k) \tag{2.36}$$

2.4.3 Consequences of symmetry for the CM angular distribution

Using equation (2.34) it can be shown that the PDDCS behave in the same way as the modified spherical harmonics with respect to complex conjugation:

$$\frac{1}{\sigma}\frac{\mathrm{d}\sigma^*_{kq}}{\mathrm{d}\omega_t} \;=\; (-1)^q \frac{1}{\sigma}\frac{\mathrm{d}\sigma_{k\,-q}}{\mathrm{d}\omega_t} \tag{2.37}$$

By considering the reaction sequence in the CM frame, we see that the distribution of AB internuclear axes must be invariant to reflection in the $\boldsymbol{k}$,$\boldsymbol{k'}$ (xz) plane (given that the reaction process is achiral). Since $\boldsymbol{j'}$ is a vector product of two vectors it is a *pseudovector*: the x and z components of $\boldsymbol{j'}$ will change sign, but the y component is invariant to reflection in the reaction plane. Therefore,

$$P(\omega_t, \theta_r, \phi_r) \;=\; P(\omega_t, \pi \;-\; \theta_r, \pi \;-\; \phi_r). \tag{2.38}$$

Combination of equations (2.31) and (2.38) leads to the following result,

$$\frac{1}{\sigma}\frac{\mathrm{d}\sigma_{kq}}{\mathrm{d}\omega_t} \;=\; (-1)^{k+q}\,\frac{1}{\sigma}\frac{\mathrm{d}\sigma_{k\,-q}}{\mathrm{d}\omega_t} \;=\; (-1)^k\,\frac{1}{\sigma}\frac{\mathrm{d}\sigma^*_{kq}}{\mathrm{d}\omega_t}. \tag{2.39}$$

Application of equations (2.37) and (2.39) yields

$$\frac{1}{\sigma}\frac{\mathrm{d}\sigma_{k0}}{\mathrm{d}\omega_t} \;=\; 0, \qquad \text{for } k \text{ odd}, \tag{2.40}$$

and,

$$\frac{1}{\sigma}\frac{\mathrm{d}\sigma_{kq+}}{\mathrm{d}\omega_t} = \frac{1}{\sigma}\frac{\mathrm{d}\sigma_{kq}}{\mathrm{d}\omega_t} + \frac{1}{\sigma}\frac{\mathrm{d}\sigma_{k\,-q}}{\mathrm{d}\omega_t} = 0, \qquad \begin{pmatrix} k \text{ even, } q \text{ odd} \\ k \text{ odd, } q \text{ even} \end{pmatrix} \tag{2.41}$$

$$\frac{1}{\sigma}\frac{\mathrm{d}\sigma_{kq-}}{\mathrm{d}\omega_t} = \frac{1}{\sigma}\frac{\mathrm{d}\sigma_{kq}}{\mathrm{d}\omega_t} - \frac{1}{\sigma}\frac{\mathrm{d}\sigma_{k\,-q}}{\mathrm{d}\omega_t} = 0, \qquad \begin{pmatrix} k \text{ even, } q \text{ odd} \\ k \text{ odd, } q \text{ even} \end{pmatrix} \tag{2.42}$$

These expressions ensure that the probability distribution $P(\omega_t, \omega_r)$ is real and symmetric with respect to the scattering plane. Note that the PDDCS are defined such that $(1/\sigma)(\mathrm{d}\sigma_{k0\pm}/\mathrm{d}\omega_t) = (1/\sigma)(\mathrm{d}\sigma_{k0}/\mathrm{d}\omega_t)$.

2.4.4 Moments of the k–k'–j' distribution

Integrating equation (2.27) over the angular co–ordinates of $\boldsymbol{j'}$ yields the moments of the $\boldsymbol{k}$–$\boldsymbol{k'}$ distribution. This gives the familiar differential cross section,

$$P(\omega_t) = \frac{1}{\sigma}\frac{\mathrm{d}\sigma_{00}}{\mathrm{d}\omega_t} = \frac{1}{4\pi}\sum_{k_1}[k_1]h_0^{k_1}(k_1,0)\mathrm{P}_{k_1}(\cos\theta_t) \tag{2.43}$$

where the $\mathrm{P}_{k_1}(\cos\theta_t)$ are Legendre polynomials of order k_1. Therefore, the bipolar moments $h_0^k(k,0)$ are the expectation values of the Legendre moments of the usual differential cross-section,

$$s_{00}^k = h_0^k(k,0) = \langle P_k(\cos\theta_t)\rangle. \tag{2.44}$$

These coefficients are readily calculated from QCT data, as will be shown in section (3.11.4).

Integration of the full $\boldsymbol{k}$–$\boldsymbol{k'}$–$\boldsymbol{j'}$ distribution over the translational degrees of freedom, i.e. over $\boldsymbol{k'}$, yields the rotational solid angle differential cross–section,

$$P(\omega_r) \;=\; \frac{1}{\sigma}\frac{\mathrm{d}\sigma}{\mathrm{d}\omega_r} \;=\; \frac{1}{2}\sum_k\sum_q [k]\, C_{kq}(\theta_r,\phi_r)^* \int_{-1}^{+1} \frac{1}{\sigma}\frac{\mathrm{d}\sigma_{kq}}{\mathrm{d}\omega_t}\,\mathrm{d}(\cos\theta_t) \tag{2.45}$$

This may be recast in terms of *polarisation parameters*, a_q^k, as defined by Shafer–Ray *et al.*[2],

$$a_q^k \;=\; 2\pi \int_{-1}^{+1} \frac{1}{\sigma}\frac{\mathrm{d}\sigma_{kq}}{\mathrm{d}\omega_t}\,\mathrm{d}(\cos\theta_t) \tag{2.46}$$

giving,

$$\begin{aligned}\frac{1}{\sigma}\frac{\mathrm{d}\sigma}{\mathrm{d}\omega_r} &= \frac{1}{4\pi}\sum_k\sum_q\; [k]\, a_q^k\, C_{kq}(\theta_r,\phi_r)^* \\ &= \sum_k\sum_{q\geq 0}\; [k]\,[a_{q\pm}^k \cos q\phi_r \;-\; i a_{q\mp}^k \sin q\phi_r]\, C_{kq}(\theta_r,0)\end{aligned} \tag{2.47}$$

where the upper sign is associated with even q and the lower sign with odd q. These polarisation parameters are obtained in the same way as the PDDCS (equations 2.41 and 2.42) and have the same properties,

$$a_{q+}^k \;=\; 0, \qquad \left(\begin{array}{c} k \text{ even, } q \text{ odd} \\ k \text{ odd, } q \text{ even}\end{array}\right), \tag{2.48}$$

$$a_{q-}^k \;=\; 0, \qquad \left(\begin{array}{c} k \text{ even, } q \text{ even} \\ k \text{ odd, } q \text{ odd}\end{array}\right), \tag{2.49}$$

$$a_0^k \;=\; 0, \qquad k \text{ odd}. \tag{2.50}$$

The rotational polar angle distribution, $P(\theta_r)$ is obtained by integrating equation (2.45) over ϕ_r,

$$P(\theta_r) \;=\; \frac{1}{2}\sum_k\; [k]\, a_0^k\, \mathrm{P}(\cos\theta_r). \tag{2.51}$$

the coefficients of this expansion are expectation values of the Legendre polynomial expansion in $\cos\theta_r$ (where $\cos\theta_r = \boldsymbol{k}\cdot\hat{\boldsymbol{j}}'$), and only the terms with even k are non–zero (see equation 2.50). Therefore, the distribution $P(\theta_r)$ is also even.

$$a_0^k \;=\; h_0^k(0,k) \;=\; \langle \mathrm{P}_k(\cos\theta_r)\rangle. \tag{2.52}$$

The rotational dihedral angular distribution, $P(\phi_r)$ is obtained by integrating equation (2.45) over all polar angles,

$$P(\phi_r) \;=\; \frac{1}{4\pi}\sum_k\sum_{q\geq 0}\; [k]\,[a_{q\pm}^k\cos q\phi_r \;-\; ia_{q\mp}^k\sin q\phi_r]\int_{-1}^{+1} C_{kq}(\theta_r,0)\mathrm{d}(\cos\theta_r), \tag{2.53}$$

Only terms involving a_{q+}^k are involved in the expansion and equation (2.53) can be re–written as a Fourier series in sines and cosines with only *odd* terms in sines and *even* terms in cosines:

$$P(\phi_r) \;=\; \frac{1}{2\pi}\left(1 \;+\; \sum_{\text{even } n\geq 2} a_n\,\cos(n\phi_r) \;+\; \sum_{\text{odd } n\geq 1} b_n\,\sin(n\phi_r)\right) \tag{2.54}$$

Moments of the $\boldsymbol{k'}-\boldsymbol{j'}$ distribution may be obtained by setting $K=0$ in equations (2.28) and (2.30) and by contracting the resulting summations, where $k_1 = k_2 = k$,

$$P(\theta_{tr}) \;=\; \frac{1}{2}\sum_k [k]^{\frac{3}{2}}\, h_0^0(k,k)\sum_q\, C_{kq}(\theta_t,0)C_{kq}(\theta_r,\phi_r)^*. \tag{2.55}$$

Application of the spherical harmonic addition theorem [9] yields,

$$P(\theta_{tr}) \;=\; \frac{1}{2}\sum_{k}[k]^{\frac{3}{2}}\, h_0^0(k,k)\mathrm{P}_k(\cos\theta_{tr}). \tag{2.56}$$

and it is clear that the CM bipolar moments, $h_0^0(k,k)$ are simply proportional to the expectation values of the corresponding Legendre polynomials:

$$h_0^0(k,k) \;=\; [k]^{-\frac{1}{2}}\,\langle \mathrm{P}_k(\cos\theta_{tr})\rangle \tag{2.57}$$

2.5 Polarisation Dependent Differential Cross Sections

The $a_{q\pm}^k$ polarisation parameters give a full description of the anisotropy of the $\boldsymbol{j'}$ angular momentum distribution. The relationship between the $a_{q\pm}^k$ polarisation parameters and the CM frame bipolar moments can be obtained by combining equations (2.35) and (2.46),

$$\begin{aligned} a_{q\pm}^k &= \sum_{k_1}\frac{[k1]}{2}\, s_{kq\pm}^{k_1}\int_{-1}^{+1} C_{k_1\,-q}(\theta_t,0)\,\mathrm{d}(\cos\theta_t) \\ &= \langle C_{kq}(\theta_r,0)\,[\mathrm{e}^{iq\phi_r}\pm(-1)^q\mathrm{e}^{-iq\phi_r}]\rangle. \end{aligned} \tag{2.58}$$

Therefore the polarisation parameters may be obtained simply as expectation values of the appropriate modified spherical harmonic.

Aoiz *et al.* have shown that the ratio of the PDDCS to the differential cross section gives the conditional expectation values at a given scattering angle ($\cos\theta_t$) [10],

$$\frac{\frac{1}{\sigma}\frac{\mathrm{d}\sigma_{kq\pm}}{\mathrm{d}\omega_t}}{\frac{1}{\sigma}\frac{\mathrm{d}\sigma_{00}}{\mathrm{d}\omega_t}} \;=\; \langle C_{kq}(\theta_r,0)[\mathrm{e}^{iq\phi_r}\pm(-1)^q\mathrm{e}^{-iq\phi_r}]\mid \cos\theta_t\rangle. \tag{2.59}$$

$k\,q\pm$	Argument	Limiting values (θ_r, ϕ_r)						
		0,0	0,90	45,0	45,90	45,180	90,0	90,90
0 0	1	1	1	1	1	1	1	1
2 0	$P_2(\cos\theta_r)$	1	1	$\frac{1}{4}$	$\frac{1}{4}$	$\frac{1}{4}$	$-\frac{1}{2}$	$-\frac{1}{2}$
2 1−	$2\,C_{21}(\theta_r, 0)\,\cos\phi_r$	0	0	$-\sqrt{\frac{3}{2}}$	0	$+\sqrt{\frac{3}{2}}$	0	0
2 2+	$2\,C_{22}(\theta_r, 0)\,\cos 2\phi_r$	0	0	$+\sqrt{\frac{3}{8}}$	$-\sqrt{\frac{3}{8}}$	$+\sqrt{\frac{3}{8}}$	$+\sqrt{\frac{3}{2}}$	$-\sqrt{\frac{3}{2}}$

Table 2.2 Arguments and limiting values of some of the alignment parameters and renormalised polarisation-dependent differential cross-sections (see text). The left hand column gives the kq index of the moment of interest and the limiting values are listed for the given (θ_r, ϕ_r) angles, expressed in degrees.

The above relationships show that the polarisation parameters and PDDCS must lie within the limits for the expectation values of the modified spherical harmonics. The present experiments, involving linearly polarised initiation and (1+1) LIF detection mean that only the low order moments are measurable, and more notably that these moments are *even*. The measurement of odd moments will be discussed later in chapter 6. The limiting values for the low order even moments of the polarisation parameters and renormalised PDDCS are given in table (2.5).

The (0 0) moment simply represents the regular DCS. The higher moments with $k = 2$ are perhaps not so generally interpretable. The (2 0) moment is the expectation value of the second Legendre moment in $\cos\theta_r$ and thus represents the alignment of the rotational angular momentum with respect to the polar z axis. The (2 1−) and (2 2+) moments are also dependent on the alignment, but also contain information regarding the *azimuthal* angular distribution, *i.e.,* with respect to the $\boldsymbol{k}$,$\boldsymbol{k'}$ (xz) scattering plane.

2.6 The LAB frame angular distribution

In the preceeding sections, results of the expansion of the semiclassical angular distribution in terms of CM frame harmonic functions have been given. As will be discussed later (chapter 3), however, the experiments are sensitive to moments of the angular distribution in the *laboratory* (LAB) frame. A procedure for the transformation from the CM to the LAB frame is required to facilitate the extraction of information referenced to the more useful CM frame. In this section, an overview of the method of transformation used is given, and is subject to certain simplifying conditions. A full treatment of this subject has been amply documented by Aoiz *et al.* (see refs. [13, 10] and references therein), however, and the reader is encouraged to look there for the details of the procedure.

2.6.1 Transformation to the intermediate v_1 moving frame

In order to simplify the discussion, it is assumed that the target molecular velocity, $\boldsymbol{v_2}$, is constrained to lie parallel to the hot atom velocity $\boldsymbol{v_1}$ so that $\boldsymbol{k} \,||\, \boldsymbol{v_1}$ and the relative speed, $v_r = |\boldsymbol{k}| = v_1 \pm v_2$. This 1D picture provides an adequate description of experiments involving co–expansion of precursor and reagent molecules combined with *in situ* photolysis of the precursor. It is also a reasonable approximation to the case of room temperature bulb conditions with a heavy target where $v_1 \gg v_2$.

We now introduce an intermediate frame, the v_1 *moving frame*, with $\boldsymbol{v_1}$ lying along the z axis, and with the product CM velocity, w lying in the xz plane – see figure (2.4). The product velocity in this frame also lies in the xz plane, and makes an angle θ_v with the polar (z) axis with $\phi_v = \phi_t = 0$. Note that in this unidimensional approximation, the co–ordinates of the rotational angular momentum $\boldsymbol{j'}$ are unaffected by transformation of the translational co–ordinates from the CM to the v_1 frames. The CM and v_1 frames are simply related by the following equations, employing the cosine law,

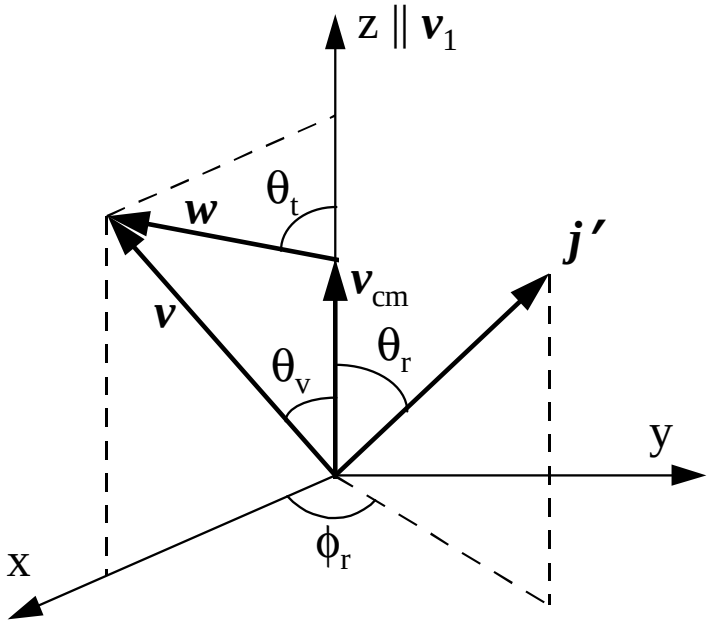

Figure 2.4 The v_1 moving frame co–ordinate system.

$$v^2 = w^2 + v_{cm}^2 + 2wv_{cm}\cos\theta_t, \tag{2.60}$$

$$w^2 = v_{cm}^2 + v^2 - 2vv_{cm}\cos\theta_v. \tag{2.61}$$

The LIF detection scheme is sensitive to the product molecule *number density*. Provided that the products are probed at a short (fixed) time delay after their creation, the differential flux into the product channel $|f\rangle$ will be proportional to the number density. This differential flux may be written,

$$I(\theta_v, \omega_r; v, v_1, v_2) = R\sigma v_r\, P(\omega_t, \omega_r)\delta(w - w_f)\,\frac{\partial(w, \theta_t)}{\partial(v, \theta_v)} \tag{2.62}$$

$$= R\sigma v_r\, P(\omega_t, \omega_r)\delta(w - w_f)\,\frac{v^2}{w_f^2} \tag{2.63}$$

$$= \quad R\sigma v_r \, P(\omega_t, \omega_r)\delta(\cos\theta_v \; - \; \cos\theta_v^f) \, \frac{v}{w_f v_{cm}} \tag{2.64}$$

where R takes accounts for the reaction volume probed and the number densities of the reagents. The $\frac{v^2}{w_f^2}$ factor in expression (2.63) represents a Jacobian transformation from the CM to the moving frame, and the following relationship has been used:

$$\frac{v^2}{w_f^2}\,\delta(w \; - \; w_f) \; = \; \delta(\cos\theta_v \; - \; \cos\theta_v^f) \, \frac{v}{w_f v_{cm}} \tag{2.65}$$

The flux can be alternatively expressed as an expansion in *moving frame bipolar harmonics*, $B_0^K(k_1, k_2; \theta_v, \omega_r)$:[3]

$$I(\theta_v, \omega_r; v, v_1, v_2) \; = \; \frac{1}{8\pi} \sum_K \sum_{k_1} \sum_{k_2} [k_1][k_2] \, b_0^K(k_1, k_2; v) B_0^K(k_1, k_2; \theta_v, \omega_r), \tag{2.66}$$

where the moving frame bipolar harmonics are given by

$$B_0^K(k_1, k_2; \theta_v, \omega_r) \; = \; \sum_q (-1)^K [K]^{\frac{1}{2}} \begin{pmatrix} k_1 & K & k_2 \\ q & 0 & -q \end{pmatrix} C_{k_1 q}(\theta_v, 0) \, C_{k_2 \, -q}(\theta_r, \phi_r), \tag{2.67}$$

and the moving frame bipolar moments by

$$\begin{aligned} b_0^K(k_1, k_2; v) \; &= \; \int B_0^K(k_1, k_2; \theta_v, \omega_r)^* \, I(\theta_v, \omega_r; v, v_1, v_2) \, \mathrm{d}(\cos\theta_v) \, \mathrm{d}\omega_r \\ &= \; R\sigma v_r \sum_{q \geq 0} (-1)^K [K]^{\frac{1}{2}} \begin{pmatrix} k_1 & K & k \\ q & 0 & -q \end{pmatrix} \\ &\times \; \frac{v}{w_i v_{cm}} \left(\frac{1}{\sigma} \frac{\mathrm{d}\sigma_{kq\pm}}{\mathrm{d}\omega_t} \right) C_{k_1 \, -q}(\theta_v^f, 0) \end{aligned} \tag{2.68}$$

[3] In the discussion that follows, a simplified notation for the moving frame bipolar moments is employed: $b_Q^K(k_1, k_2; v) \equiv b_Q^K(k_1, k_2; v, v_1, v_2)$

where the plus sign is associated with those cases when $K + k_1 + k + q$ is even, and the minus sign is associated when $K + k_1 + k + q$ is odd. The PDDCS $\left(\frac{1}{\sigma}\frac{\mathrm{d}\sigma_{kq\pm}}{\mathrm{d}\omega_t}\right)$ is evaluated at the value of θ_t which corresponds to given values of θ_v^f and v.

2.6.2 Transformation from the v_1 moving frame to the LAB frame

As detailed by Aoiz *et al.* [13, 10], the transformation of equation (2.66) from the v_1 frame to the LAB frame may be achieved by rotating the bipolar moments into the LAB frame (using rotation matrices), and multiplying by the probability that $\boldsymbol{v_1}$ (the z axis) has a specific orientation in the LAB frame (this probability being equivalent to the LAB frame velocity distribution of the reagent hot atom, equation 2.3). The resultant distribution is then integrated over all possible orientations of the $\boldsymbol{v_1}$ frame, and this may be written (for fixed v_1 and v_2):

$$\begin{aligned} I(v, \Omega_v, \Omega_j; v_1, v_2) &= \frac{1}{16\pi^2}\left[\sum_k [k]^2 b_0^0(k,k;v) B_0^0(k,k;\Omega_v,\Omega_j)\right. \\ &+ \left.\frac{\beta}{5}\sum_{k_1}\sum_{k_2}[k_1][k_2] b_0^2(k_1,k_2;v) B_0^2(k_1,k_2;\Omega_v,\Omega_j)\right], \end{aligned} \quad (2.69)$$

where β is the CM translational anisotropy of the atomic reagent produced by the photolysis step. The bipolar moments are those of equation (2.69), and $\Omega_v = \{\Theta_v, \Phi_v\}$ and $\Omega_j = \{\Theta_j, \Phi_j\}$ refer to the laboratory frame coordinates of $\boldsymbol{v}$ and $\boldsymbol{j'}$ in the LAB frame (see fig. 2.5). It is worth noting at this point that the form of equation (2.69) is very similar to that for molecular photodissociation [1], the only differences being the definition of the v_1 frame bipolar moments and the premultiplying factor of $\beta/2$ which results from referencing the moments to $\boldsymbol{v_1}$ rather than the electronic transition moment, $\boldsymbol{\mu}$.

Integration of equation (2.69) over all speeds, v_1 and v_2, gives the final expression for the LAB frame distribution,

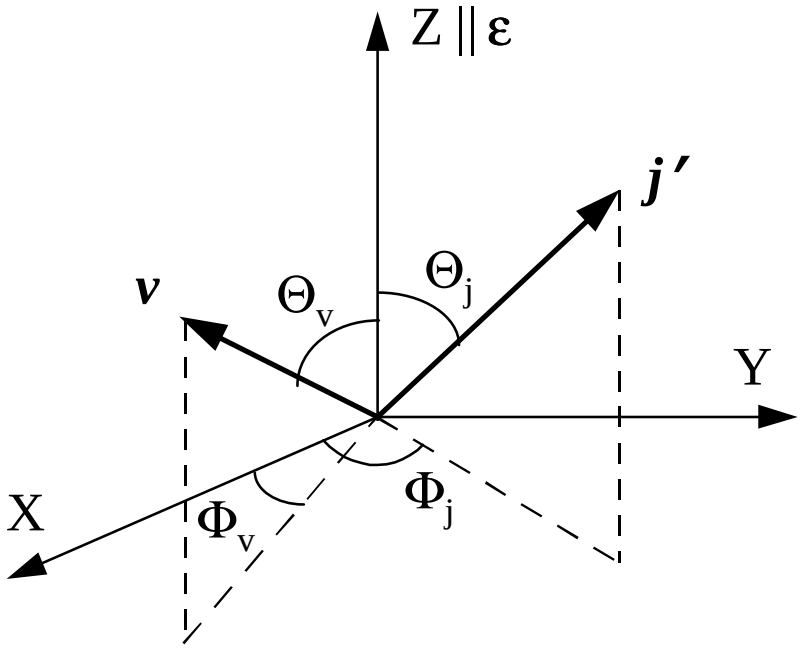

Figure 2.5 The LAB frame co–ordinate system.

$$I(v,\Omega_v,\Omega_j) = \frac{1}{16\pi^2}\left[\sum_k [k]^2\overline{b_0^0}(k,k;v)B_0^0(k,k;\Omega_v,\Omega_j) + \frac{\beta}{5}\sum_{k_1}\sum_{k_2}[k_1][k_2]\overline{b_0^2}(k_1,k_2;v)B_0^2(k_1,k_2;\Omega_v,\Omega_j)\right] \quad (2.70)$$

where the averaged LAB speed (v) dependent moments are given by,

$$\overline{b_0^K}(k_1,k_2;v) = \int\int f_K(v_1)g(v_2)b_0^K(k_1,k_2;v)v_1^2\,\mathrm{d}v_1\,\mathrm{d}v_2 \quad (2.71)$$

The LAB v_1 speed distribution, $f_K(v_1)$, is given by [13],

$$f_K(v_1) = \frac{\gamma}{2\pi}\int_0^\infty \frac{f(u)}{(uv_1)^{\frac{1}{2}}}\,\exp[-\gamma(u^2+v_1^2)]\,\mathrm{I}_{(2K+1)/2}(2\gamma v_1 u)\,4\pi u^2\mathrm{d}u \quad (2.72)$$

where $\gamma = m_{\mathrm{AD}}/2kT$, with m_{AD} being the mass of the precursor, $\mathrm{I}_{(2K+1)/2}$ are the modified spherical Bessel functions, and $f(u)$ is the speed distribution of the hot atom produced from a stationary precursor. This last equation includes a broadening effect in the precursor velocity as a result of thermal motion of the precursor and possible spread in recoil velocities associated with photodissociation of a polyatomic species. The distribution of v_2 is given in this case as a one dimensional Maxwell–Boltzmann speed distribution:

$$g(v_2) \;=\; \left(\frac{m_{\mathrm{BC}}}{2\pi kT}\right)^{\frac{1}{2}} \exp\left(-\frac{m_{\mathrm{BC}} v_2^2}{2kT}\right) \tag{2.73}$$

The LAB speed distribution of the product molecules is given simply by the zeroth moment, and in the literature is sometimes denoted $W(v)v^2$,

$$\overline{b_0^0}(0,0;v) \;=\; \int\int f_0(v_1) g(v_2)\; b_0^0(0,0;v)\; v_1^2\, dv_1\, dv_2 \;=\; W(v)v^2 \tag{2.74}$$

The sums over indices k, k_1 and k_2 are subject only to the triangle conditions of the 3J symbol (equation 2.69). For the simplified experimental case of achiral photoinitiation and detection *via* (1+1) LIF, the indices are restricted to the first ten even bipolar moments, $\overline{b_0^K}(k_1,k_2;v)$ [14]. Coefficients, for the six most dominant of these moments, as appearing in equation (2.69), are given in table (2.3), as are the normalisation factors relating the $\overline{b_0^K}(k_1,k_2;v)$ to the more commonly employed $\overline{\beta_0^K}(k_1,k_2;v)$ moments which will be used in chapter 3. The physical vector correlations to which these bipolar moments refer are shown in table (2.4).

Bipolar moment		Coefficients			
		$\frac{1}{\sigma}\frac{\mathrm{d}\sigma_{00}}{\mathrm{d}\omega_t}$	$\frac{1}{\sigma}\frac{\mathrm{d}\sigma_{20}}{\mathrm{d}\omega_t}$	$\frac{1}{\sigma}\frac{\mathrm{d}\sigma_{21-}}{\mathrm{d}\omega_t}$	$\frac{1}{\sigma}\frac{\mathrm{d}\sigma_{22+}}{\mathrm{d}\omega_t}$
$\beta_0^0(0,0)$	$b_0^0(0,0)$	1	0	0	0
$\beta_0^2(2,0)$	$b_0^2(2,0)$	$C_{20}(\theta_v^f,0)$	0	0	0
$\beta_0^2(0,2)$	$b_0^2(0,2)$	0	1	0	0
$\beta_0^0(2,2)$	$\sqrt{5}b_0^0(2,2)$	0	$C_{20}(\theta_v^f,0)$	$C_{21}(\theta_v^f,0)$	$C_{22}(\theta_v^f,0)$
$\beta_0^2(2,2)$	$\sqrt{\frac{7}{2}}b_0^2(2,2)$	0	$-C_{20}(\theta_v^f,0)$	$-\frac{1}{2}C_{21}(\theta_v^f,0)$	$C_{22}(\theta_v^f,0)$
$\beta_0^2(4,2)$	$\sqrt{\frac{7}{2}}b_0^2(4,2)$	0	$C_{40}(\theta_v^f,0)$	$\sqrt{\frac{5}{6}}C_{41}(\theta_v^f,0)$	$\sqrt{\frac{5}{12}}C_{42}(\theta_v^f,0)$

Table 2.3 The relationship between commonly determined one-dimensional moving frame bipolar moments and the polarisation-dependent differential cross-sections.

Bipolar Moment	LAB Vector Correlation
$\beta_0^0(0,0;v)$	$\boldsymbol{k},\boldsymbol{v'}$ speed distribution
$\beta_0^2(2,0;v)$	$\boldsymbol{k},\boldsymbol{v'}$ angular distribution
$\beta_0^2(0,2;v)$	$\boldsymbol{k},\boldsymbol{j'}$ rotational distribution
$\beta_0^0(2,2;v)$	$\boldsymbol{v'},\boldsymbol{j'}$ rotational distribution
$\beta_0^2(2,2;v)$	$\boldsymbol{k},\boldsymbol{v'},\boldsymbol{j'}$ triple vector correlation

Table 2.4 Vector correlations associated with the LAB frame bipolar moments. Note that here $\boldsymbol{v'}$ is labelled with a prime, whereas in the text the prime has been dropped. In the CM frame, correlations pertaining to $\boldsymbol{v'}$ transform to correlations involving $\boldsymbol{k'}$.

References

[1] R. N. Dixon, *J. Chem. Phys.*, **85** (1986) 1866.

[2] N. E. Shafer-Ray, A. J. Orr-Ewing and R. N. Zare, *J. Phys. Chem.*, **99** (1995) 7591.

[3] R. N. Zare, Mol. Phys., **4** (1972) 1.

[4] N. E. Shafer, A. J. Orr–Ewing, W. R. Simpson, H. Xu and R. N. Zare, Chem. Phys. Lett., **212** (1993) 155.

[5] A. J. Orr-Ewing and R. N. Zare, in *Chemical Dynamics and Kinetics of Small Free radicals*, eds. A. Wagner and K. Liu, World Scientific, Singapore 1995, p.936.

[6] C. H. Greene and R. N. Zare, *J. Chem. Phys.*, **78** (1983) 6741.

[7] R. N. Zare, *Angular Momentum, Understanding Spatial Aspects in Chemistry and Physics.*, John Wiley and Sons, 1983.

[8] R. D. Levine and R. B. Bernstein, *Molecular Reaction Dynamics and Chemical Reactivity*, Oxford University Press, 1987.

[9] D. M. Brink and G. R. Satchler, *Angular Momentum*, Oxford University Press, 1993.

[10] F. J. Aoiz, M. Brouard and P. A. Enriquez, *J. Chem. Phys.*, **105** (1996) 4964.

[11] D. A. Case and D. R. Herschbach, *Mol. Phys.*, **30** (1975) 1537.

[12] M. P. de Miranda and D. C. Clary, *J. Chem. Phys*, **106** (1997) 4515.

[13] F. J. Aoiz, M. Brouard, P. A. Enriquez and R. Sayos, *J. Chem. Soc. Faraday Trans.*, **89** (1993) 1427.

[14] M. P. Docker, *Chem. Phys.*, **135** (1989) 405.

Chapter 3 Methods and Analysis

This chapter includes a detailed description of the methods and equipment employed in the experiments. Procedures for analysing the raw experimental data are given, as are procedures for the running and analysis of the quasi-classical trajectory calculations.

The experiments make use of pulsed laser systems allowing the reaction initiation and subsequent product detection to be controlled on a nanosecond timescale. The use of tunable laser light provides the basis necessary for the Doppler-resolved measurements. Since the detection stage is optically based (as opposed to mass spectrometric) the method can be product quantum state selective, and this will prove an advantage as will be discussed in the following chapters.

A schematic of the experimental layout is shown in figure (3.1). Each of the key experimental features will be described in turn, and a discussion of the spectroscopy and measurements will be discussed later in this chapter.

3.1 Experimental apparatus

3.1.1 Experimental chamber

At the heart of the experiment is the reaction chamber. This is an enclosed steel shell which has been blackened on the interior with matt black paint. There are several exit ports including 4 steel arms at right angles fitted with spectrosil B windows. The arms contain blackened light baffles to collimate the laser light and reduce internal scattering.

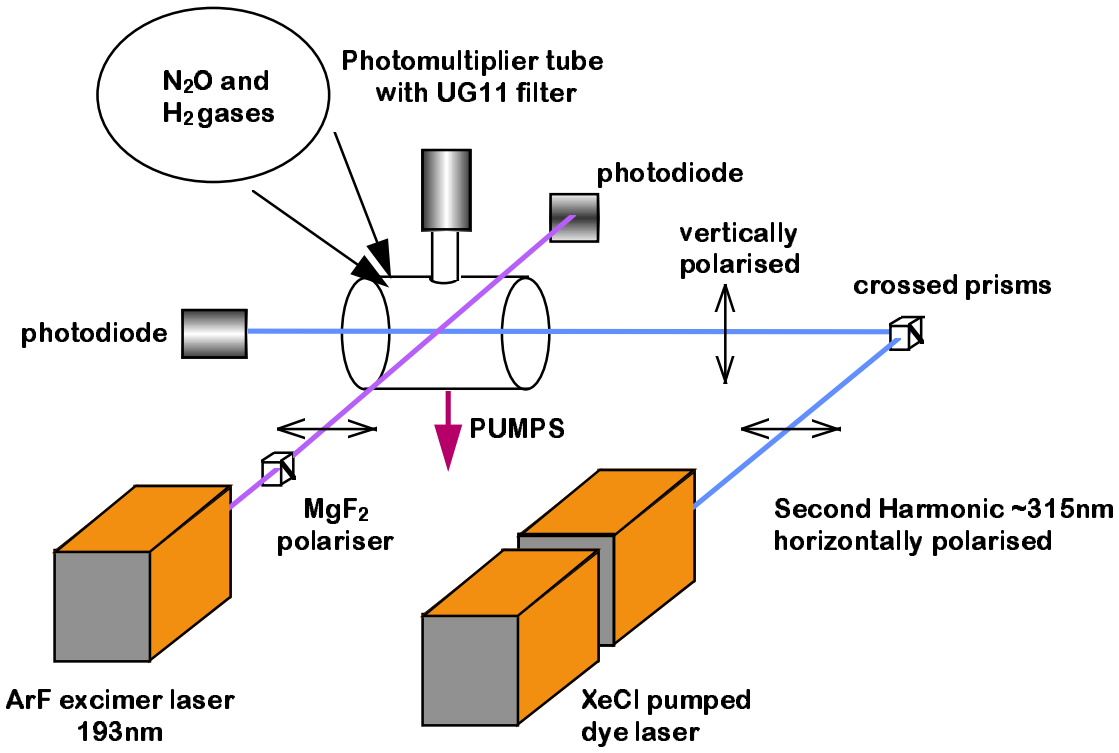

Figure 3.1 Schematic diagram of the experimental apparatus employed in the present work. See text for details of the apparatus.

Gas is introduced *via* a $1/4''$ stainless steel tube to which are attached the gas cylinders with needle valves to control the flow rate of each. The gases used were N_2O (BOC research grade 98.3%) and H_2 (BOC high purity grade 99.99%).

The cell is maintained under high vacuum (typically 10^{-6} Torr) by means of a diffusion pump (Edwards diffstak 160) backed by a rotary pump (Edwards Two stage) with a nominal capacity of 40 litres min^{-1}. The rotary pump was used to maintain the vacuum and ensure a continuous flow of the reagents during the experiment. A steady state flow rate was achieved by use of the needle valves to maintain a 1:1 mixture of the reagents at a total cell pressure of 83 mTorr (11.0 Pa). The cell pressure was measured using a calibrated capacitance manometer (Chell MK 1413 baratron).

3.1.2 Photolysis laser

The laser used to initiate the reaction was an ArF excimer laser (Lambda Physik Lextra 50). The 193 nm output beam was loosely focussed using a quartz lens and was passed through a MgF_2 Senarmont polariser. The polariser produces two beams with horizontal and vertical polarisations. A path length of approximately 1.5 m was required to allow satisfactory divergence of these beams before passing the required beam through an iris and then through the entrance window into the cell. Pulse energies measured at the entrance window were typically 2 to 3 mJ $pulse^{-1}$. The photolysis of N_2O will be discussed in section (3.2).

3.1.3 Probe laser

The probe laser system used for the detection stage of the experiment consisted of a dye laser (Lambda Physik FL3002) pumped using 308 nm radiation from a XeCl excimer laser (Lambda Physik EMG 201MSC). The laser medium consists of a fast flow of dye dissolved

in a suitable solvent. The dyes used were Rhodamine B dissolved in methanol, producing output at around 605 to 625 nm, and Rhodamine 101 in methanol, producing output from 620 nm to 640 nm. The dye laser included a precision tuned diffraction grating with prism expander system capable of producing polarised light with a nominal preference for 20:1 in favour of the vertical polarisation. The laser bandwidth is approximately 0.3 cm^{-1} (FWHM) in the fundamental. Use of a Fabry–Perot etalon (Lambda Physik FL337) which was mounted in the cavity and motor–tuned, served to reduce the operational bandwidth to approximately 0.06 cm^{-1} (fundamental). The measurement of the probe laser bandwidth will be discussed in section (3.7).

Ultraviolet light was produced by second harmonic generation in a motor tuned KDP crystal (Lambda Physik FL30), and this also served to improve the selectivity of polarisation. The fundamental radiation was blocked using a UG-5 filter, and the plane of polarisation was manipulated externally using a prism arrangement. The probe laser used a microprocessor controller to track the grating, etalon and crystal simultaneously. It also produced the triggering for the whole experiment which was in burst shots at 10 Hz.

3.1.4 Geometries and Detection

Three experimental geometries were used, conventionally known as cases A, B and D [1], and these are drawn schematically in fig. (3.2). As mentioned above, the plane of polarisation of the pump laser was controlled using an external polariser, and the probe laser plane of polarisation was controlled by prisms. The photomultiplier detector was fixed in the vertical direction, see fig. (3.2).

The reaction was initiated by a pulse from the photolysis laser, and the reactants were allowed to build up during a fixed delay (100 ± 20 ns) before a pulse from the probe laser was used to excite the OH products. After a further delay (10 ns) the undispersed fluorescence

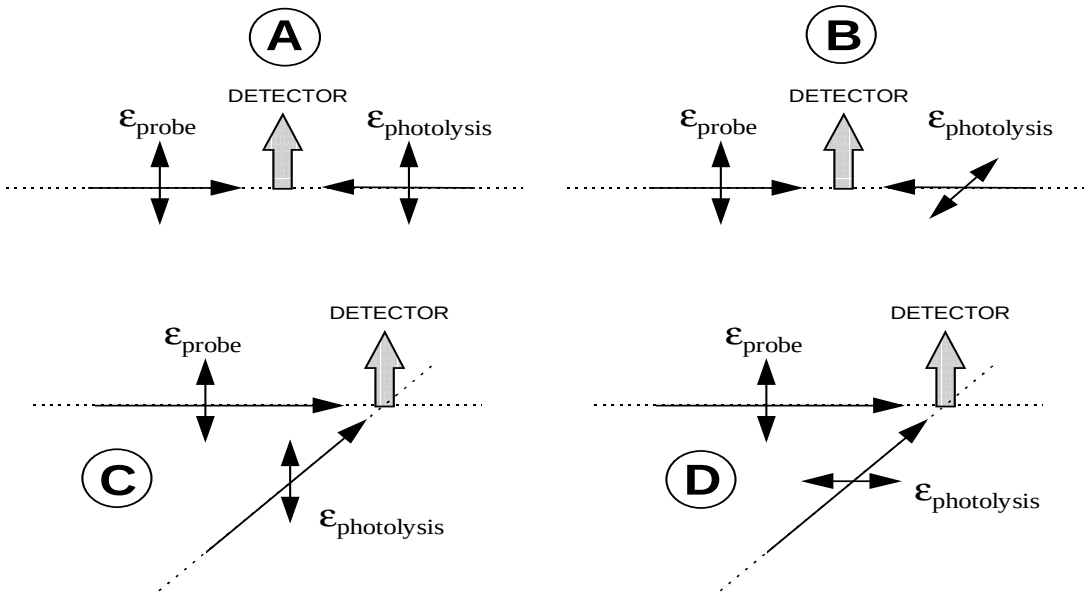

Figure 3.2 Schematic of the experimental geometries (cases) employed in the present work. Case C is also shown for completeness, although this geometry was not used in the present study. The electric vector is denoted by ε.

from these excited products was collected over a 300 ns period by a photomultiplier detection system. The delay between pump and probe lasers could be controlled using a home-made delay generator.

In the detection stage the undispersed fluorescence is collimated using a $f/1.3$ quartz lens and passed through a UG-11 broad band filter before being focussed onto a photomultiplier tube (PMT EMI 9831Q) using a matching lens. The filter serves to collect, preferentially, fluorescence arising from the OH (A→X) transition with a near linear transmission in this region. The filter also blocks much of the scattered light from the pump and probe lasers. The signal from the PMT is passed to a gated Boxcar integrator (SRS 250) and could be monitored using an oscilloscope (Tektronix 2225 50 MHz analogue scope) to enable tuning of the delays and gatewidths.

The power of the pump and probe lasers are also recorded on a shot-to-shot basis. A reflex from the entrance window of the probe laser is used to illuminate a saturated solution of Rhodamine 6G dye in a sealed quartz cuvette, the fluorescence is detected using a photodiode, amplified and passed to a boxcar integrator (SRS 250). A reflex from the pump laser is caught after the light has passed through the cell and is used to illuminate a cell filled with solid sodium salicylate. The resulting fluorescence is collected as for the probe laser. The pump laser was caught *after* passing through the cell to monitor the effects of the build up of an opaque film which was found to affect the pump beam cell windows. Fortunately the scans were short enough to be able to neglect this drop in power over each scan. The windows did require cleaning at the end of every day, however. The source of this build up was not clear, although pump oil and the black interior paint were prime suspects. Indeed even a liquid Nitrogen trap at the pump was unsuccessful at preventing or lessening this build-up.

Data from the boxcar integrators were collected and converted to digital form using an

analogue-to-digital interface (SRS 245) on a shot-to-shot basis and passed to a personal computer for processing and storage.

3.2 The photolysis of N_2O

The UV absorption spectrum of nitrous oxide (N_2O) starts near 200 nm and shows a first absorption band centered around 180 nm which consists of a broad peak with a superimposed diffuse structure [2]. The photodissociation at 193 nm has a small photoabsorption cross–section (9.0×10^{-20} cm^2), and produces ground state ($X^1\Sigma_g^+$) nitrogen molecules with predominantly ($> 90\%$) $O(^1D_2)$ - equation (3.1). The other channels, producing $O(^1S_0)$ and $O(^3P_J)$ account for less than 5% and 2% of the branching ratio respectively [3, 4].

$$N_2O + h\nu \;\rightarrow\; N_2(v,\; J) \;+\; O^* \tag{3.1}$$

The photodissociation of N_2O is particularly useful for hot–atom chemistry because the $O(^1D_2)$ is ejected at a high mean velocity (*ca.* 3 km s^{-1}) with a well defined angular distribution (see below, however) [5]. In addition, the N_2 partner fragment is chemically inert, and this reduces the effect of interference from secondary reactions. The product $O(^1D_2)$ atoms are born with a spread of translational energies corresponding to the spread in rotational levels of the partner N_2 fragment. The rotational distribution has been measured using REMPI of the N_2 molecule by Kummel [4] and more recently by Chandler *et al.* [6] and Teule [7], and is found to lie in the range $J = 60 - 85$, with a small percentage ($\sim 2\%$) of N_2 product in $v = 1$.

If the photolysis is carried out using linearly polarised light, the angular distribution of fragments (integrating over product speed) may be written [8]:

λ_{phot} / nm	$\langle E_t \rangle$ / kJ mol^{-1}	$\overline{\beta}$	Method (ref.)
193	112.13	0.48 ± 0.02	Time-Of-Flight [5]
193	114.22	0.50 ± 0.05	1D Doppler LIF [10]
203-205	106.27	—	REMPI of N_2 [4]
205	223.84	2.0	1D Doppler LIF [9]
205	114.22	0.60 ± 0.05	2D Imaging [11]

Table 3.1 Summary of the results of previous measurements of the mean anisotropy parameter for the UV photodissociation of N_2O.

$$I(\Theta) \;=\; [1 + \overline{\beta} P_2(\cos\Theta)]/4\pi \tag{3.2}$$

where $I(\Theta)$ is the distribution of the angle Θ between the photofragment velocity and the photolysis polarization vector, $\boldsymbol{\varepsilon_{ph}}$ – see chapter 2. The (product speed–averaged) translational anisotropy parameter, $\overline{\beta}$, has theoretical limiting values of +2, indicating prompt dissociation along the polarisation direction $\boldsymbol{\varepsilon_{ph}}$, and −1, indicating dissociation perpendicular to $\boldsymbol{\varepsilon_{ph}}$.

The mean anisotropy parameter, $\overline{\beta}$, and the translational energy release of the $O(^1D_2)$ have been measured by a number of groups, and the results are summarised in table (3.1). There appears to be some discrepancy in the results of ref. [9], however, and this suggests an erroneous analysis of the measured Doppler contours.

The results are consistent with a dissociation predominantly *via* a parallel transition to a bent excited state: $2^1A'(B^1\Delta) \leftarrow 1^1A'(\tilde{X}^1\Sigma^+)$ which must involve some bending of the ground state N_2O which is linear [13].

Recent studies of the rotational distribution of N_2 using REMPI have indicated a variation

in the angular anisotropy showing a trend for decreasing β with increasing J, *i.e.*, $\beta(J)$ [6, 7]. This result is in agreement with photofragment ion–imaging studies of the product atom using multiphoton ionisation [11, 6, 7]. The situation is further complicated, since the imaging studies indicate that the O atoms have an $|m_J|$ state dependent translational alignment, $\beta(J, m_J)$; there is a correlation between the recoil velocity and the electronic angular momentum of the O atom. It appears that, in general, there is no preferential population of any particular $|m_J|$ level [7].

At present it is not clear what effect, if any, electronic orbital alignment of the oxygen atoms would have on a bulb reaction. The present experiments, however, appear sensitive to the $O(^1D_2)$ speed dependence of β, and this will be discussed in chapters 5 and 6.

3.3 Exploratory analysis

The following reaction channel was chosen for experimental investigation:

$$O(^1D_2) \; + \; H_2 \; \rightarrow \; OH(v' = 0, N' = 14, f) \; + \; H. \tag{3.3}$$

The quantum state $OH(v' = 0, N' = 14)$ was picked for the following reasons:

- The low vibrational energy maximises the information available from the Doppler experiment because most of the exoergicity is released as product translation (see section 2.2.2).
- QCT calculations predict a strong dependence of angular distribution on product rotational state for $OH(v' = 0)$ [14]. An easy comparison may be made with previous experimental work on $OH(v' = 0,\ N' = 5)$ [15].
- The $OH(v' = 0)$ rotational distribution is hot, peaking at $N' \approx 25$ [16]: it is instructive to investigate the most populated channels.
- The electronic orbital angular momentum and nuclear rotation couple to give an energetic splitting of states known as lambda doubling (see appendix 1). The elec-

Line	Wavelength (λ)$^{(a)}$ / nm	Relative linestrength$^{(b)}$
$Q_{22}(14)$	311.7759	1412
$^{Q}R_{12}(14)$	311.7455	28
$P_{22}(14)$	316.1892	740
$^{P}Q_{12}(14)$	316.1598	44

$^{(a)}$ Dieke and Crosswhite [17]

$^{(b)}$ Chidsey and Crosley [18], normalised to $P_{11}(1)$=1000.

Table 3.2 Positions and relative linestrengths of OH LIF transitions studied experimentally (see text for details).

tronic symmetry of these states, A′/A″ with respect to the plane of rotation, becomes increasingly well defined with OH rotation. Each of these states may be accessed spectroscopically *via* main branch and satellite transitions in the LIF excitation spectrum. Unfortunately the linestrengths of the satellite transitions decrease with OH rotational quantum number, N'. The Doppler resolved measurement of $N' = 14$ satellite features is at the limit of present experimental capability.

- There are a set of Q and P lines (corresponding to A′ and A″ Λ–doublets respectively) which are uncontaminated by other transitions in the OH $(0-0)$ LIF spectrum.

The lines chosen were the P_{22}, Q_{22} and their respective satellites, $^{P}Q_{12}$ and $^{Q}R_{12}$. Figure (3.3) shows a portion of the OH LIF spectrum indicating the relative positions of the lines that were studied. The positions of the lines according to Dieke and Crosswhite [17], and relative linestrengths, as calculated by Chidsey and Crosley [18], are given in table (3.2).

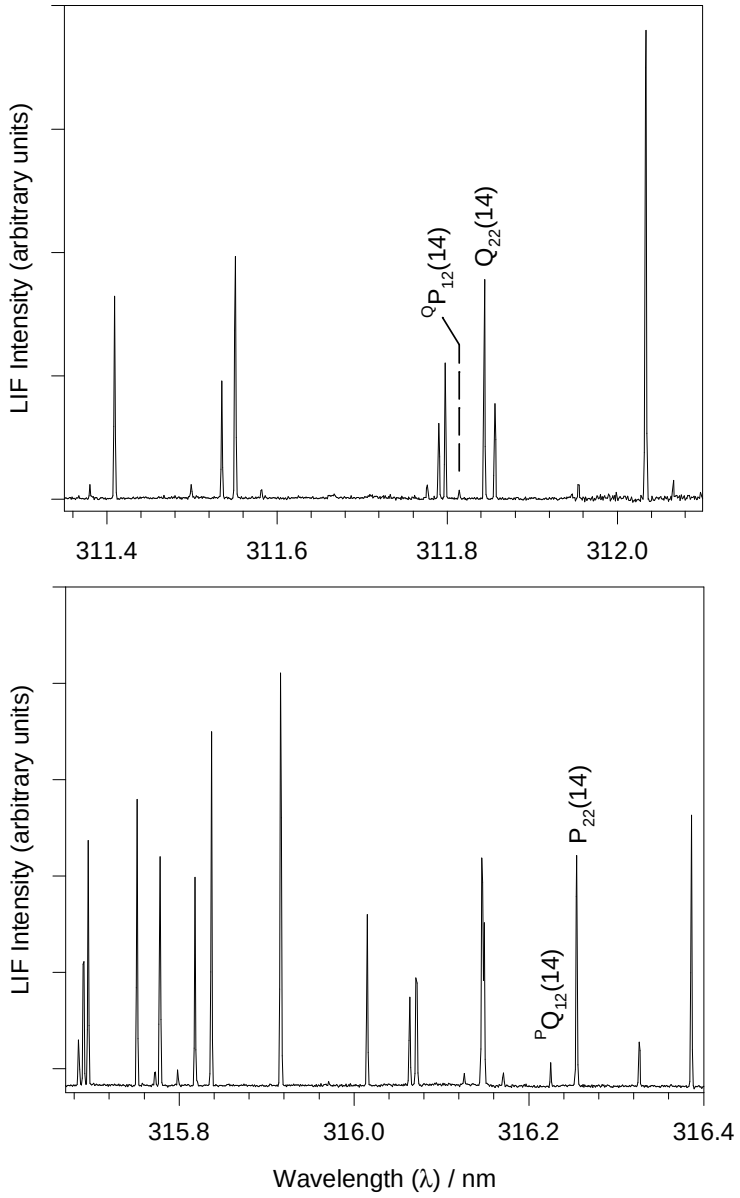

Figure 3.3 Part of the A–X LIF spectrum of OH showing the $v' = 0, N' = 14$ lines studied. Assignments were made using Dieke and Crosswhite [17]. There are no clear progressions in this part of the spectrum and so other lines are not labelled for clarity. See appendix A for details of assignments.

3.4 Measurement of laboratory frame Alignment

Measurement of the laboratory speed averaged alignment parameter, $\langle A_0^{(2)} \rangle$, is necessary to ensure the correct weighting of Q– and P/R–type transitions in the construction of the composite Doppler profiles.

The integrated intensity, I, of a rovibronic transition probed by 1+1 LIF using linearly polarised light and detecting undispersed fluorescence can be written [19]:

$$I \;=\; CS_{N'N''}(b_0 \;+\; \frac{5}{4} b_1 \langle A_0^{(2)} \rangle) \tag{3.4}$$

In this equation C is a constant, proportional to the population of the initial state, S is a product of linestrength factors for the transition of interest, b_0 and b_1 are angular momentum and geometrical factors. The factor b_0 depends solely on the rotational branch probed, and b_1 depends on the rotational branch and the experimental geometry (e.g. case A, B or D). The dependence of b_1 on experimental geometry is exploited to solve equation (3.4) for $\langle A_0^{(2)} \rangle$ using cases A and B; the constant b_1 changes sign between these cases, see table (3.3).

The change in experimental geometry requires the measurement of a ratio of integrated intensities. This provides a reference with which to determine the variation (if any) between the cases. In general, the experiment may be carried out by measuring both main line and satellite in cases A and B. Because of the small relative linestrength of the $N' = 14$ satellite lines, however, an alternative strategy is required.

The main line of each Λ-doublet was scanned under nascent conditions (section 3.1.4) and at low bandwidth resolution. In addition, the $^{\mathrm{P}}\mathrm{Q}_{12}(1)$ transition at 309.3722 nm was measured using a long (*ca.* 5 μs) pump-probe delay. Since the $^{\mathrm{P}}\mathrm{Q}_{12}(1)$ transition arises from a state

with $J = \frac{1}{2}$ and has zero alignment ($b_0 = 1$ and $b_1 = 0$) it provides a means of intensity normalisation.

We define the ratio,

$$X = \left(\frac{I_m}{I'}\right)_{\text{case A}} \cdot \left(\frac{I'}{I_m}\right)_{\text{case B}}, \tag{3.5}$$

where I_m is the intensity for either the $Q_{22}(14)$ or the $P_{22}(14)$ main line transitions and I' the intensity for the ${}^{P}Q_{12}(1)$ transition measured under as near identical conditions as possible. If we substitute the expressions for I (equation 3.4 and its analogues) we obtain,

$$\langle A_0^{(2)} \rangle \;=\; \frac{q_0^{(0)}}{q_0^{(2)}} \frac{(X-1)}{(\frac{X}{2} \;+\; 1)} \tag{3.6}$$

In practice, due to the large separation in the spectrum across the dye-range, great care was taken to ensure proper normalisation for laser intensity. Each line was recorded a number of times, fitted using Gaussian lineshapes, and the results averaged.

3.5 The Doppler lineshape

The Doppler effect in the case of electromagnetic radiation gives us a relationship for the frequency of light, ν_{obs}, as perceived by an observer travelling with a velocity v relative to the light source. Specifically,

$$\nu_{\text{obs}} = \nu_{\text{source}} \left(1 - \frac{v}{c}\right) \tag{3.7}$$

where ν_{source} is the limiting frequency in the absence of motion, v is the relative velocity between the source and the observer's frames, and c is the speed of light. It does not matter

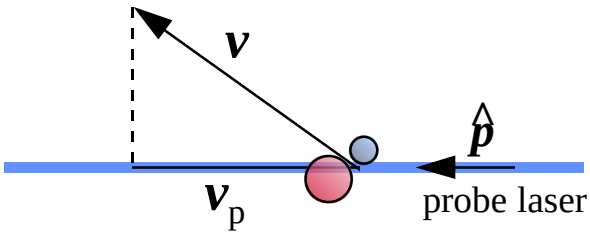

Figure 3.4 Schematic figure showing the projection of velocity onto the probe laser axis giving speed v_p.

whether the observer is stationary and the source is moving, only the *relative* velocity is of consequence.

It is clear that the interaction between a moving particle and an external light source will depend upon the velocity of the particle. We begin by considering this interaction to be the absorption stage of some arbitrary multiphoton process. For a probe laser with direction given by unit vector $\hat{\boldsymbol{p}}$, the Doppler shifted absorption frequency, ν_{D}, of a particle with velocity $\boldsymbol{v}$ will depend on the projection of this velocity on the probe laser axis,

$$v_p = \boldsymbol{v} \cdot \hat{\boldsymbol{p}}, \tag{3.8}$$

and,

$$\nu_{\mathrm{D}} = \nu_0 \left(1 - \frac{v_p}{c}\right), \tag{3.9}$$

where ν_0 is the resonant absorption frequency in the absence of relative motion, see figure (3.4). The Doppler shift is defined as:

$$\Delta\nu_{\mathrm{D}} \;=\; \nu_0 - \nu_{\mathrm{D}} \;=\; \frac{v_p}{c}\nu_0, \tag{3.10}$$

or, alternatively, we may use the fractional Doppler shift, x_{D}, defined as:

$$x_{\mathrm{D}} \;=\; \frac{v_p}{v} \;=\; \frac{\Delta\nu}{\Delta\nu_{\max}}, \tag{3.11}$$

where $\Delta\nu_{\max}$ would be the theoretical maximum shift if the directions of $\boldsymbol{v}$ and $\hat{\boldsymbol{p}}$ were coincident. The overall result for an ensemble of particles is a Doppler broadened lineshape function which represents the projection of their 3D velocity distribution onto the probe laser axis.

In general, however, the absorption of *polarised* light is an anisotropic process which is dependent on the moments of both the velocity and rotational angular momentum distributions - see chapter 2. We exploit this anisotropy in our experimental measurement of individual rotational features in the (1+1) LIF spectrum of product OH *via* absorption of linearly polarised light and subsequent detection of undispersed fluorescence. The resultant Doppler lineshape may be written [20],

$$D(v_p) = \int_{v=v_p}^{\infty} \frac{1}{2v} \left[\sum_L g_L(v) \mathrm{P}_L \left(\frac{v_p}{v} \right) \right] \mathrm{d}v, \tag{3.12}$$

where $L = 0, 2, 4$ and 6 and P_L is the Lth order Legendre polynomial. The dominant terms in the g_L factors are,

$$g_0(v) \;=\; b_0 \overline{\beta_0^0}(0,0;v) \;+\; b_1 \frac{\beta}{2} \overline{\beta_0^2}(0,2;v), \tag{3.13}$$

$$g_2(v) \;=\; b_2 \frac{\beta}{2} \overline{\beta_0^2}(2,0;v) \;+\; b_3 \overline{\beta_0^0}(2,2;v) \;+\; b_4 \frac{\beta}{2} \overline{\beta_0^2}(2,2;v), \tag{3.14}$$

$$g_4(v) \;=\; b_6 \frac{\beta}{2} \overline{\beta_0^2}(4,2;v). \tag{3.15}$$

In these equations the $\overline{\beta_0^K}(k_1,k_2;v)$ are the LAB frame bipolar moments as encountered in chapter 2; the bar denotes averaging over reagent velocities. The multiplicative factor $\frac{\beta}{2}$ appears in terms dependent on $\boldsymbol{k}$, the reagent relative velocity vector, where it reflects the anisotropy of the photolysis precursor. The b_i are the Dixon multipliers which are

dependent on experimental geometry and the rotational branch probed (i.e. Q↑ *vs.* P/R↑) [20]. The b_i are related to $q^{(k)}(j_i)$ coefficients (table 3.3), which are given by

$$q^{(0)} = 1 - \frac{2}{3}\overline{\gamma}'_{220}, \tag{3.16}$$

$$q^{(2)} = 1 - \frac{1}{2}\overline{\gamma}'_{202} - \frac{1}{2}\overline{\gamma}'_{022} - \frac{2}{3}\overline{\gamma}'_{222}, \tag{3.17}$$

$$q^{(4)} = -4\overline{\gamma}'_{224}. \tag{3.18}$$

The $\overline{\gamma}'_{k_d k_a k}$ are angular momentum coupling terms for 1+1 LIF, as given in section (2.3.3). The experimental geometries used are shown in figure (3.2), and are termed cases A, B and D after Docker [1] (see section 3.1.4). They differ in the directions of the pump and probe laser beams and their respective axes of polarisation. Table (2.4) lists the bipolar moments and the correlations of interest.

3.6 Composite Doppler profiles

Equation (3.12) represents a linear combination of the lab speed-dependent correlations of interest. There are 6 dominant terms, and these may be separated by solving a set of at least 6 simultaneous equations according to the variation in the b_i coefficients with experimental geometry and rotational branch. The b_i coefficients for the geometries used in the present study are given in table (3.3). To obtain the solutions we take weighted sums of the raw profiles from different experimental geometries/rotational branches – these are called *composite profiles* and depend on individual correlations of interest:

$$D_0^K(k_1, k_2; v_p) = \int_{v=|v_p|}^{\infty} \frac{1}{2v}\overline{\beta_0^K}(k_1, k_2; v)\mathrm{P}_{k_1}\left(\frac{v_p}{v}\right)\mathrm{d}v. \tag{3.19}$$

In the construction of the composite profiles, it is first necessary to weight each raw profile according to its correct relative integrated intensity which is given by,

	P_0		P_2			P_4
Geometry	b_0	b_1	b_2	b_3	b_4	b_6
A	$q^{(0)}$	$\frac{4}{5}q^{(2)}$	$-q^{(0)}$	$-q^{(2)}$	$\frac{4}{7}q^{(2)}$	$\frac{27}{35}q^{(2)}$
B	$q^{(0)}$	$-\frac{2}{5}q^{(2)}$	$-q^{(0)}$	$-q^{(2)}$	$-\frac{8}{7}q^{(2)}$	$\frac{9}{35}q^{(2)}$
D	$q^{(0)}$	$-\frac{2}{5}q^{(2)}$	$2q^{(0)}$	$-q^{(2)}$	$\frac{4}{7}q^{(2)}$	$-\frac{36}{35}q^{(2)}$
$\frac{1}{3}$(A+B+D)	$q^{(0)}$	0	0	$-q^{(2)}$	0	0
(A−D)	0	$\frac{6}{5}q^{(2)}$	$-3q^{(0)}$	0	0	$\frac{63}{35}q^{(2)}$
(D−B)	0	0	$3q^{(0)}$	0	$\frac{12}{7}q^{(2)}$	$-\frac{45}{35}q^{(2)}$

Table 3.3 Construction of composite Doppler profiles by weighting according to experimental geometry [1]. See text for definitions of the $q^{(i)}$ coefficients. Note that the $q^{(i)}$ have different values for Q and P/R branch lines and are dependent on rotational quantum number.

$$I \;=\; \int_{-\infty}^{\infty} D(x_{\mathrm{D}})\,\mathrm{d}x_{\mathrm{D}} \quad \propto \quad b_0 \;+\; b_1\langle\overline{\beta_0^2}(0,2)\rangle, \tag{3.20}$$

where $\langle\overline{\beta_0^2}(0,2)\rangle \;\equiv\; \frac{5}{4}\langle A_0^{(2)}\rangle$ [20]. The weights are dependent on the LAB speed-averaged alignment parameter, $\langle A_0^{(2)}\rangle$, which must be determined experimentally as detailed in section (3.4).

Solutions to equation (3.12) are then obtained by making the appropriate sum of profiles obtained in the different geometries as listed in table (3.3). Different P/R and Q rotational branch lines are used to separate the $q^{(0)}$ and $q^{(2)}$ contributions. For example, to retrieve the $\overline{\beta_0^0}(0,0;v)$ correlation for a given rovibrational (v',N') state we take the average of cases A, B and D for P–branch (or R–branch) lines. This gives an intermediate composite profile, $D_{\mathrm{P}}^{\frac{1}{3}(\mathrm{A+B+D})}$, which contains information from both the b_0 and b_3 terms. Similarly we make

a sum $D_{\rm Q}^{\frac{1}{3}({\rm A+B+D})}$ for the Q–branch lines. A weighted sum of these two intermediate composite profiles is then used to separate out the b_0 and b_3 terms yielding the final composite profile, in this case the $D_0^0(0,0;v_p)$ product speed–dependent profile:

$$q_{\rm Q}^{(2)} D_{\rm P}^{\frac{1}{3}({\rm A+B+D})} - q_{\rm P}^{(2)} D_{\rm Q}^{\frac{1}{3}({\rm A+B+D})} \;=\; (q_{\rm Q}^{(2)} q_{\rm P}^{(0)} - q_{\rm P}^{(2)} q_{\rm Q}^{(0)})\; D_0^0(0,0;v_p). \tag{3.21}$$

Some of the composite profiles still retain a contamination from the P_4 term — particularly the composite profiles $D_0^2(0,2;v)$ and $D_0^2(2,2;v)$. It is possible, however, to account for the residual $\overline{\beta_0^2}(4,2;v)$ moment due to its dependence on the same 3 PDDCS as the moments $\overline{\beta_0^2}(0,2;v)$, $\overline{\beta_0^0}(2,2;v)$ and $\overline{\beta_0^2}(2,2;v)$ — this is included in the simulation procedure detailed in chapter 2.

3.7 Estimation of laser linewidth

The experimentally measured Doppler lineshape function is actually a convolution of the limiting lineshape function, given in equation (3.12), with the probe laser lineshape function which has a finite width of frequencies [21],

$$D(x_{\rm D}) = \int_{-\infty}^{\infty} h(x_{\rm D} - x'_{\rm D})\; D(x'_{\rm D})\; {\rm d}x'_{\rm D}, \tag{3.22}$$

where

$$h(x_{\rm D} - x'_{\rm D}) \;\equiv\; h(x) \;=\; exp(-\epsilon x^2), \tag{3.23}$$

and

$$\epsilon = \frac{4\;\ln 2}{(\Delta x)^2}. \tag{3.24}$$

In this equation Δx represents the bandwidth (FWHM) of the laser lineshape which is assumed to be Gaussian. The factor $(4\;\ln 2)$ converts the FWHM factor to the standard

deviation of a normal distribution.

It can be seen that Doppler–resolved measurements rely on having a narrow probe–laser bandwidth. The manufacturer's specification for the bandwidth using an intracavity etalon was ≈0.08 cm^{-1} (2nd harmonic). In practice, the actual bandwidth will depend both on the dye and the laser light used to pump the dye. A precise measurement of the linewidth is necessary for generating the CM basis set of Doppler profiles (see section 3.8.2) which are convoluted with a laser Gaussian function. The measurement of lineshape is also a key diagnostic for the correct operation of the dye laser.

Rotational features (usually the main lines of the $N' = 14$ transition under investigation) were recorded at a long pump-probe delay (17 μs) and the usual pressure (11.0 Pa). The long delay ensures full translational relaxation, and improved signal-to-noise by increased build-up of lower (v',N') products. Interference from the scattered pump laser radiation is also reduced.

The 'relaxed' profiles may be considered as a convolution of a Maxwell-Boltzmann broadened lineshape with the probe-laser lineshape. The Maxwell-Boltzmann thermal distribution of products is a Gaussian function – we may estimate the FWHM of this from simple gas kinetic collision theory [22]:-

$$\Delta\nu_{\text{thermal}} = \frac{2\nu_0}{c}\sqrt{\frac{2RT\ \ln 2}{m}}. \tag{3.25}$$

Since the laser lineshape is assumed to be Gaussian, the problem reduces to a simple convolution of two Gaussians. The resultant linewidth will be given by:

$$\Delta\nu^2_{\text{observed}} \ = \ \Delta\nu^2_{\text{laser}} \ + \ \Delta\nu^2_{\text{thermal}}. \tag{3.26}$$

In practice this may be confirmed using a Fourier Transform method to deconvolute the thermal Gaussian from the observed lineshape [21, 23]. This involves expansion of the observed profile in terms of orthonormal harmonic oscillator wavefunctions (a product of a Gaussian with Hermite polynomials) and the use of analytical Fourier transforms followed by a numerical inverse transform once the thermal Gaussian has been divided out:

$$h_{\mathrm{laser}}(\nu) \;=\; \mathsf{FT}^{-1}\left\{\frac{\mathsf{FT}[D(\nu_{\mathrm{D}})]}{\mathsf{FT}[D_{\mathrm{thermal}}(\nu_{\mathrm{D}})]}\right\}, \tag{3.27}$$

where FT and FT^{-1} represent the Fourier and inverse Fourier transforms. The reader is directed to ref. [21] for a full discussion of this procedure.

3.8 Simulations in the Centre-of-Mass frame

Due to the averaging and symmetry involved in the experiments, it is not possible to effect a direct transformation from the laboratory (LAB) to the centre-of-mass (CM) frame; there is not a simple 1:1 mapping between the two frames. Instead, we must look to a simulation procedure to retrieve the CM parameters.

We begin by first balancing the energy books of our reaction,

$$\mathrm{O}(^1\mathrm{D}_2) \;+\; \mathrm{H}_2(^1\Sigma_g^+) \;\rightarrow\; \mathrm{OH}(\mathrm{X}^2\Pi_{1/2}, v', N') \;+\; \mathrm{H}(^2\mathrm{S}). \tag{3.28}$$

Given that the OH is state-selected, and that H is formed in its ground electronic state, we may write the following energy balance equation,

$$E_t \;+\; E_{\mathrm{int}}(\mathrm{H}_2) \;=\; \Delta H_0 \;+\; E_{\mathrm{int}}(\mathrm{OH}) \;+\; E_t'. \tag{3.29}$$

where E_t and E_t' are the reagent and product translational energies respectively, ΔH_0 is the reaction exothermicity (-182 kJ mol^{-1}) and $\mathrm{E_{int}}$ are the internal (rovibrational) energies. $E_{\mathrm{int}}(\mathrm{H_2}) \approx \langle E_{\mathrm{int}}(\mathrm{H_2})\rangle$, where the brackets denote an average over reagent internal states. The translational exoergicity, Q, is defined as [24],

$$Q = E_t' - E_t = -\Delta \mathrm{H_0} - E_{\mathrm{int}}(\mathrm{OH}) + E_{\mathrm{int}}(\mathrm{H_2}). \tag{3.30}$$

We may estimate $E_{\mathrm{int}}(\mathrm{H_2})$ at 300 K using Boltzmann statistics, and ΔH_0 and $E_{\mathrm{int}}(\mathrm{OH})$ are fixed. In general, however, E_t and E_t' will take a range of values. Q thus quantifies the excess energy available to the products as translational energy. For the O + $\mathrm{H_2}$ $\rightarrow$ OH($v' = 0$, $N' = 14$) + H reaction Q is estimated as 1.43 eV (138 kJ mol^{-1}).

3.8.1 The forward convolution procedure

It is possible to assume some product distribution in the CM frame, say the differential cross-section, and apply to this the necessary averaging over the reagent velocities and Newton triangles as described in chapter 2. We may also allow for some level of approximation in the averaging, perhaps constraining the reagent velocities to lie parallel or anti–parallel to each other. The simulated Doppler profiles are then obtained from the product speed and angular distributions projected onto the single dimension of our theoretical probe laser and a convolution procedure is applied to account for a finite laser linewidth.

This "*forward convolution*" was used successfully by Brouard, Simons and co-workers [21, 24, 25], but was limited in its accuracy, notwithstanding the level of approximation used in the simulation, due to the "trial–and–error" nature of this approach. It requires the subjective variation of parameters in an attempt to produce, effectively, a visually acceptable fit to the measured composite profiles.

3.8.2 Doppler profile basis functions

A more reasoned approach to the fitting of Doppler profiles, first employed by Hall and co-workers [26], is to write the simulated composite Doppler profile as an expansion in a set of basis profiles, and to determine the expansion coefficients by an optimisation procedure. This can be written:-

$$\mathcal{D}_0^K(k_1, k_2; v_p) \;=\; \sum_i \; a_i \, \mathcal{G}_0^K(k_1, k_2; v_p, \cos\,\theta_t^i), \tag{3.31}$$

where $\mathcal{D}_0^K(k_1, k_2; v_p)$ is the final simulated composite profile and $\mathcal{G}_0^K(k_1, k_2; v_p, \cos\,\theta_t^i)$ are a set of basis composite profiles which are parametrically dependent on a scattering angle or on a range of scattering angles θ_t of our choice. For example, a set of, say $i = 1 \ldots 10$ equally spaced bins over the range $\cos\theta_t = -1$ to $+1$, each with a midpoint $\cos\theta_t^i$, may be used. Some example basis functions are shown in figure (3.5).

For the simplified case where we are determining only the linear momentum distribution of the products, we can write equation (3.31) as,

$$\mathcal{D}_0^{k_1}(k_1, 0; v_p) \;=\; \sum_i \; a_i \, \mathcal{G}_0^{k_1}(k_1, 0; v_p, \cos\,\theta_t^i), \tag{3.32}$$

where $k_1 = 0$ or 2 for the speed–dependent or angular–dependent composite profiles respectively – see table (2.4).

It is possible to create Doppler profile basis functions for any of a range of centre-of-mass parameters of interest, e.g. f_t' – the fractional product translational energy release, or E_t – the reagent relative collision energy. However, it is essential that the measured data are sufficiently sensitive to the parameters of interest, and that we have a sufficient amount of data to allow a robust fit: this may be determined by simulation. Following the discussion

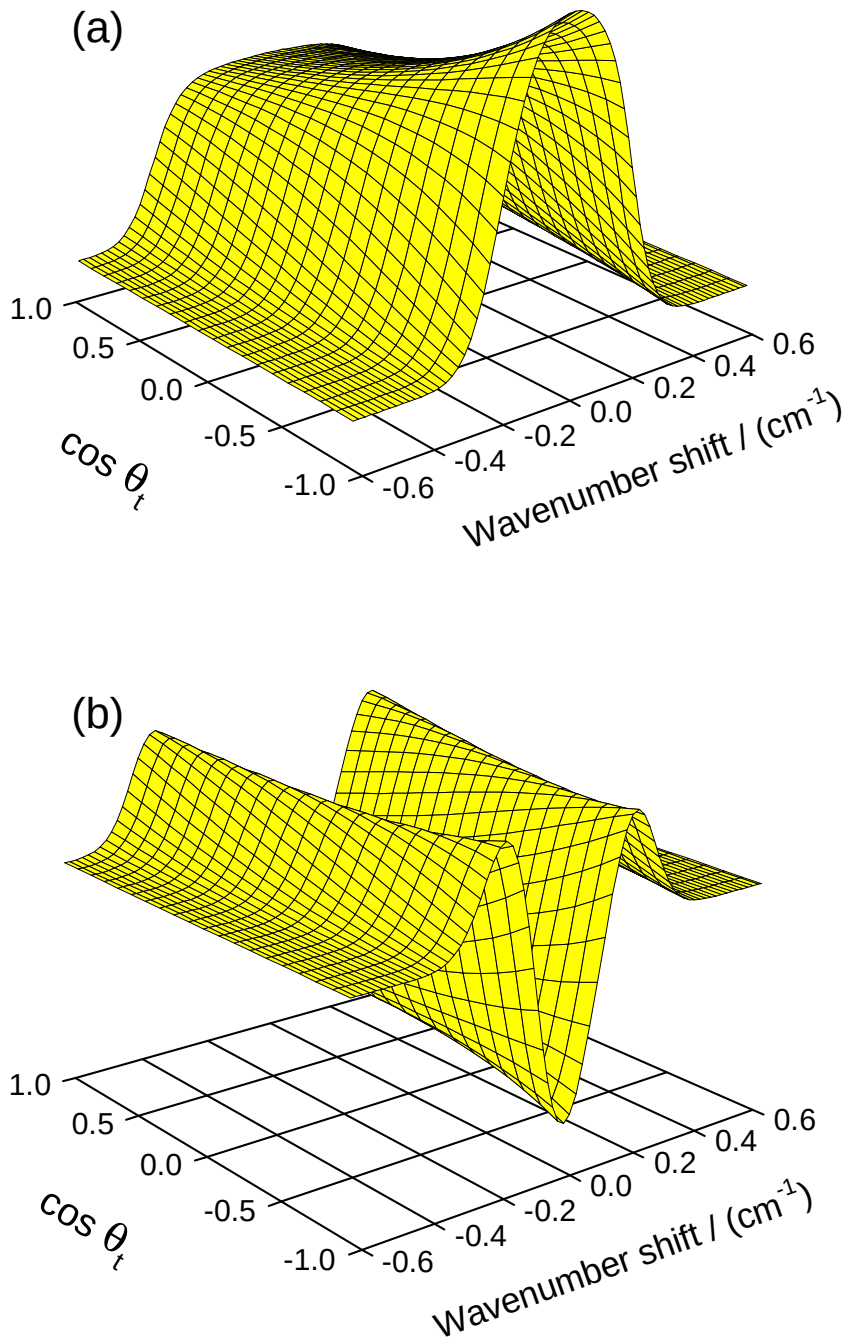

Figure 3.5 (a) Speed dependent, $\mathcal{D}_0^0(0,0;v_p)$, and (b) angular dependent $\mathcal{D}_0^2(2,0;v_p)$ simulated composite basis profiles for OH($v'=0, N'=14$) shown as a function of scattering angle, $\cos\theta_t$.

of energy balance given above, and from preliminary simulations for the O + H_2 system, it was found that it was necessary to include the reagent collision energy E_t in the simulated basis functions:-

$$\mathcal{D}_0^{k_1}(k_1, 0; v_p) \;=\; \sum_i \sum_j \; a_{ij}\, \mathcal{G}_0^{k_1}(k_1, 0; v_p, \cos\,\theta_t^i, E_t^j). \tag{3.33}$$

Finally, the a_{ij} which make up the weights of the bins in the final simulated composite profile, $\mathcal{D}_0^{k_1}(k_1, 0; v_p)$, will give us the product DCS and E_t distributions, e.g. the DCS may be written as a sum of delta functions [21]:

$$\frac{2\pi}{\sigma}\,\frac{\mathrm{d}\sigma}{\mathrm{d}\omega_t} \;=\; \sum_i \; a_i\, \delta(\cos\theta_t - \cos\theta_t^i). \tag{3.34}$$

3.8.3 Contraction of basis functions

As the number of parameters in the model is increased, it becomes more difficult to find the correct expansion coefficients; in fitting terminology, there is a risk of not finding the global minimum in the minimization procedure. There are minimization routines which are able to cope quite well with this increase in fitted parameters, but ultimately there will be an increased uncertainty in the results. In order to tackle this problem, we may effect a *contraction* procedure to exploit the orthogonal properties of the Legendre polynomials. The contracted basis set may be obtained by summing over all bins (i, j) with the Legendre polynomial functions, although the contraction procedure is actually included during the Monte Carlo integration procedure (see below).

$$\mathcal{F}_0^{k_1}(k_1, 0; v_p, l, m) \;=\; \sum_i \sum_j \; \mathrm{P}_l(\cos\,\theta_t^i)\mathrm{P}_m(E_t^j)\, \mathcal{G}_0^{k_1}(k_1, 0; v_p, \cos\,\theta_t^i, \epsilon_t^j), \tag{3.35}$$

where ϵ_t is the reduced variable $(2E_t - E_t^{\min} - E_t^{\max})/(E_t^{\max} - E_t^{\min})$ mapped from the range $[E_t^{\min}, E_t^{\max}]$ to $[-1, +1]$ to preserve the orthogonality properties of the Legendre functions. The $\mathcal{F}_0^K$ are the so–called *Legendre contracted basis profiles.*

The fitting procedure is as before, we must find the weights of the coefficients, a_{lm} required to make our simulated fit to the experimental profile this time using the $\mathcal{F}_0^{k_1}$ contracted basis set.

$$\mathcal{D}_0^{k_1}(k_1, 0; v_p) \;=\; \sum_l \sum_m \; a_{lm}\, \mathcal{F}_0^{k_1}(k_1, 0; v_p, l, m), \tag{3.36}$$

The relevant distribution may then be retrieved, trivially, as an expansion of these Legendre moments, see section (3.8.5).

3.8.4 Convergence

A potential cause for concern in the simulation procedures detailed here is the issue of convergence. The creation of simulated Doppler profiles requires a multidimensional integral over all of the reagent parameters, e.g. the $O(^1D_2)$ velocity. It is therefore necessary to include sufficient sample points for these integrals to converge. This was checked by making exhaustive simulations and trying to recover known differential cross sections [27]. Two alternative integration procedures were tested and were found to agree in the limit of large sample size. In order to exploit the contraction method a Monte Carlo integration procedure was used and Legendre contractions were made in both $\cos\theta_t$ and ϵ_t.

3.8.5 Separability *vs.* non-separability

When fitting a distribution function in two variables, the variables may be independent or inter–dependent. The distribution is termed *non–separable* when there is an inter–

dependence. In the present case this would mean a dependence of the DCS on the reagent collision energy,

$$f(\cos\theta_t, \epsilon_t) \;=\; \sum_l \sum_m \; a_{lm} \mathrm{P}_l(\cos\theta_t)\mathrm{P}_m(\epsilon_t) \;=\; \frac{2\pi}{\sigma}\left(\frac{\mathrm{d}\sigma}{\mathrm{d}\omega_t}\right)_{\epsilon_t}, \tag{3.37}$$

which results in $(l_{\max}+1)\times(m_{\max}+1)$ fitted coefficients $a_{00},\ldots,a_{l_{\max}m_{\max}}$.

In the *separable* model, the parameter distributions are independent, i.e. we have the same DCS for each reagent collision energy. We may write this as

$$f(\cos\theta_t, \epsilon_t) \;=\; \left(\sum_l \; a_l \mathrm{P}_l(\cos\theta_t)\right)\left(\sum_m \; b_m \mathrm{P}_m(\epsilon_t)\right) \;=\; \frac{2\pi}{\sigma}\frac{\mathrm{d}\sigma}{\mathrm{d}\omega_t}\cdot P(\epsilon_t), \tag{3.38}$$

with parameters $\{a_0 \ldots a_{l_{\max}}\}$ for the DCS, and parameters $\{b_0 \ldots b_{l_{\max}}\}$ for the excitation function. It was found that, although some simulations following a non–separable form returned reasonable fits, the increased number of parameters made the fitting unstable. This may reflect an insensitivity of the experimental data to such a precise functional form. As a result, the separable form was used to fit the data.

3.8.6 Polarisation dependent differential cross sections

As mentioned in chapter 2, the three bipolar moments $\overline{\beta_0^2}(0,2;v)$, $\overline{\beta_0^0}(2,2;v)$ and $\overline{\beta_0^2}(2,2;v)$ are each dependent on linear combinations of the three polarisation dependent differential cross sections (PDDCS) $\frac{1}{\sigma}\frac{d\sigma_{20}}{d\omega_t}$, $\frac{1}{\sigma}\frac{d\sigma_{21-}}{d\omega_t}$ and $\frac{1}{\sigma}\frac{d\sigma_{22+}}{d\omega_t}$ which reflect even moments of the full angular momentum distribution, $P(\boldsymbol{k},\boldsymbol{k'},\boldsymbol{j'})$. These three PDDCS may be extracted in an analogous manner to the DCS and excitation function as detailed above.

PDDCS basis sets are constructed, incorporating a full Monte Carlo integration over the

reagent distributions and including the estimated excitation function determined from fitting the $D_0^0(0,0;v_p)$ and $D_0^2(2,0;v_p)$ composite profiles. The basis functions may be written,

$$\mathcal{G}_0^K(k_1,k_2,q\pm;v_p,\cos\theta_t^i), \tag{3.39}$$

where,

$$\begin{aligned} k_2 &= 2 \\ k_1 &= 0 \text{ or } 2 \\ K &= 0 \text{ or } 2 \\ q &= 0,\ 1 \text{ or } 2. \end{aligned}$$

The indices (k_2,q) indicate which PDDCS the basis functions relate to:

$$(k_2,q) = 20 \quad \Rightarrow \quad \frac{1}{\sigma}\frac{d\sigma_{20}}{d\omega_t}, \tag{3.40}$$

$$(k_2,q) = 21- \quad \Rightarrow \quad \frac{1}{\sigma}\frac{d\sigma_{21-}}{d\omega_t}, \tag{3.41}$$

$$(k_2,q) = 22+ \quad \Rightarrow \quad \frac{1}{\sigma}\frac{d\sigma_{22+}}{d\omega_t}. \tag{3.42}$$

As discussed in section (3.8.3), the fitting of a large number of raw basis functions is an unreliable procedure. Another problem is that the PDDCS and alignment parameters have limiting values, as discussed in section (2.5). Aoiz *et al.* have shown that conditional expectation values may be obtained as a function of the scattering angle, $\cos\theta_t$. These are the *renormalised* PDDCS [28]:

$$\frac{\frac{1}{\sigma}\frac{\mathrm{d}\sigma_{kq\pm}}{\mathrm{d}\omega_t}}{\frac{1}{\sigma}\frac{\mathrm{d}\sigma_{00}}{\mathrm{d}\omega_t}} = \langle \mathrm{C}_{kq}(\theta_r,0)[\mathrm{e}^{iq\phi_r} \pm (-1)^q \mathrm{e}^{-iq\phi_r}] \mid \cos\theta_t \rangle. \tag{3.43}$$

For the O + H_2 system, the experimental differential cross sections were found to be zero or near zero at several points, particularly at sideways scattering. Potentially, this would cause

poles in the conditional expectation according to equation (3.43). In order to overcome the problems of large basis sets, and the possibility of poles in the renormalised PDDCS, a contraction procedure was employed. The raw basis are contracted with modified spherical harmonics and the contracted sets are adapted to the estimated DCS (see section 3.8.5 above),

$$\mathcal{H}_0^K(k_1, k_2, q\pm; v_p, k') \;=\; \sum_i \mathrm{C}_{k'+q}(\theta_t^i, 0)\mathcal{G}_0^K(k_1, k_2, q\pm; v_p, \cos\theta_t^i) f(\cos\theta_t^i), \tag{3.44}$$

where the sum runs over a range of scattering angles, θ_t^i, and $f(\cos\theta_t^i)$ is the fitted differential cross section at these scattering angles.

The contracted basis set, $\mathcal{H}_0^K(k_1, k_2, q\pm; v_p, k')$ are used to fit the experimental composite profiles according to the equation,

$$\mathcal{D}_0^K(k_1 k_2; v_p) \;=\; \sum_{k'} \sum_{q\geq 0} m_{k_2 q\pm}^{k'} \mathcal{H}_0^K(k_1, k_2, q\pm; v_p, k'), \tag{3.45}$$

where $\mathcal{D}_0^K(k_1 k_2; v_p)$ is the final simulated composite profile. Each experimental profile is dependent on three PDDCS, as can be seen from the sum over q. The expansion coefficients, $m_{k_2 q\pm}^{k'}$ are determined by least squares fitting simultaneously to the three polarisation dependent experimental profiles (see the following section).

The renormalised PDDCS may be obtained from the expansion coefficients $m_{k_2 q\pm}^{k'}$:

$$\frac{\frac{1}{\sigma}\frac{\mathrm{d}\sigma_{k_2 q\pm}}{\mathrm{d}\omega_t}}{\frac{1}{\sigma}\frac{\mathrm{d}\sigma_{00}}{\mathrm{d}\omega_t}} \;=\; \sum_{k'} m_{k_2 q\pm}^{k'} \mathrm{C}_{k'|q|}(\theta_t, 0). \tag{3.46}$$

The final PDDCS is retrieved by multiplying the renormalised PDDCS by the fitted differential cross section, $f(\cos\theta_t)$. Integrating the PDDCS over $\cos\theta_t$ yields the alignment

parameters $a_{q\pm}^{k_2}$ which represent the average polarisation for the product ensemble.

3.9 The fitting of experimental data

3.9.1 Choice of merit function

The experimental data are fitted according to the following criterion in which the sum of square residuals, commonly known as "chi–squared", is minimised [29]:

$$\chi^2 \;=\; \sum_{x=1}^{N} \Big[D_0^K(k_1, k_2; v_p^x) \;-\; \mathcal{D}_0^K(k_1, k_2; v_p^x) \Big]^2 \tag{3.47}$$

where $D_0^K(k_1, k_2; v_p)$ is the experimental composite profile, and $\mathcal{D}_0^K(k_1, k_2; v_p)$ is the simulated composite profile, which is written as a sum over basis functions (equation 3.36). In this equation, x runs over all N points of the experimental profile. The a_{lm} weights making up the simulated profile are varied according to some optimisation procedure and the best coefficients are those which minimise χ^2.

A more practical merit function is the reduced chi–squared value [29]. If we estimate the variance in the experimental data as,

$$\sigma^2 \;=\; \frac{1}{M-1} \sum_{i=1}^{M} (x_i - \overline{x})^2, \tag{3.48}$$

where $\overline{x}$ is the average of x over the same M points in the sum (typically $M = 50$ along the baseline of the composite profile). The reduced chi–squared is then,

$$\chi^2 \;=\; \frac{1}{\sigma^2 (N-L)} \sum_{x=1}^{N} \Big[D_0^K(k_1, k_2; v_p^x) \;-\; \mathcal{D}_0^K(k_1, k_2; v_p^x) \Big]^2 . \tag{3.49}$$

where N is the number of points and L is the total number of fitted parameters. This reduced chi–squared is preferred because it accounts for the noise in the experimental composite profiles which can be quite significant for the difference profiles. It therefore allows for easy comparison of chi–squared for low and high noise composite profiles.

3.9.2 Optimisation procedures

There are a number of numerical optimisation routines available [29]. Since the equations are linear, it is possible to employ inversion or decomposition procedures such as *Singular Value Decomposition* (SVD). In practice, however, it was found that χ^2 was reduced to the point of returning unphysical parameter distributions; the a_{lm} coefficients were able to stray beyond their allowed values. It is possible with most minimisation routines to apply *minor* constraints, such as fixing the value of certain a_{lm} coefficients. It is very difficult, however, to apply *major* restrictions to the coefficients, or, for that matter to relate restrictions on the returned distributions to constraints on the coefficients.

One minimisation algorithm which is able to outperform many others in its ability to find the global minimum, particularly in highly constrained problems, is the method of *Simulated Annealing*. This method combines a simple downhill method, such as the Simplex method, with random fluctuations during the optimisation procedure [29]. The magnitude of these fluctuations is controlled by an external parameter analogous to temperature. The temperature is controlled according to the *annealing schedule* during the minimisation. The net result is a method which contains some element of random sampling, but retains a desire to follow downhill paths (*via* the simplex). Constraints may be added very simply by including them as a variable penalty function in χ^2:

$$\chi^2_{\text{total}} \;=\; \chi^2 \;+\; \lambda\chi_{\text{penalty}}, \tag{3.50}$$

In this equation χ_{penalty} is a variable penalty function which is proportional to the deviation of the solution from its constraints and λ is a user defined scaling parameter. Alternatively, during the fitting, we may choose to discard solutions which do not fulfill some criteria, e.g. solutions which return unphysical parameter distributions.

Simulated Annealing programs employing the above methods were developed from the routines given in ref. [29]. The constraints were enforced by employing the variable penalty method.

3.10 Error estimation using Monte Carlo methods

Estimates of the uncertainties in the fitted distributions were obtained by following a "brute force" Monte Carlo procedure [29, 30]. The fit coefficients were randomly sampled over a wide range and the returned χ^2 was used as the criterion for rejection of a particular set of coefficients. In this way the statistical variance of a particular coefficient can be found. This in turn is used to calculate confidence limits for the fitted distributions.

3.11 Quasiclassical trajectory calculations

A full review of the quasiclassical trajectory (QCT) method is outwith the scope of this thesis and so the reader is directed elsewhere for a general discussion of the method [31, 32, 33, 34].

Hamilton's equations of motion were integrated using a fixed timestep Predictor–Corrector method[1] which was seeded by a fourth order Runge–Kutta integration for the initial steps [29]. The fixed timestep is convenient for calculating the trajectory time–delays (see below) and for following individual trajectories as a function of time.

Initial conditions, e.g. impact parameter and target molecule orientation, were selected

[1] I am indebted to Professor F. J. Aoiz and co–workers for supplying the trajectory programs, and to Professor R. Schinke for supplying the code of the SL surface.

by Monte Carlo random sampling using a seeded random number generator [29, 34]. This produces a unique sequence of random numbers given an integer parameter and allows the retrieval of the initial conditions for any trajectory without the need to store the random number sequence.

3.11.1 The Schinke and Lester Potential

The potential energy surface (PES) is the foundation of any scattering calculation, since in theory it contains the dynamical information for a particular system. The PES specifies the potential energy, and therefore the forces (the gradient of potential) as a function of the position of the interacting nuclei. By carrying out theoretical dynamical calculations and performing novel experiments, we hope to refine the potential energy surface as a model of the interaction between molecules.

The present calculations for the $O(^1D_2) + H_2/HD$ reaction were carried out using a slightly modified version of the potential by Schinke and Lester (SL) [35] and on the recent K PES of Schatz and co–workers [36]. Of all of the presently available surfaces, the SL1 surface has been the most widely studied in dynamical calculations, and so has been used in the present work. The SL surface is a fit to *ab initio* calculations by Howard, McLean and Lester [37] at the first order configuration interaction (FOCI) level. The *ab initio* calculations for the K PES are at a much higher level (see [36] for details).

There are a number of papers in the literature which deal with the topology of the reactive ground state potential (see section 1.9), and so only brief details will be given here. A schematic correlation diagram (not to scale) is shown in figure (3.6) for reaction correlating *via* the collinear ($C_{\infty v}$,$D_{\infty h}$) symmetries (abstraction) and the planar (C_s, C_{2v}) symmetries (insertion).

In the C_{2v} configuration, water in its $^1A_1$ state has a potential well with an experimentally

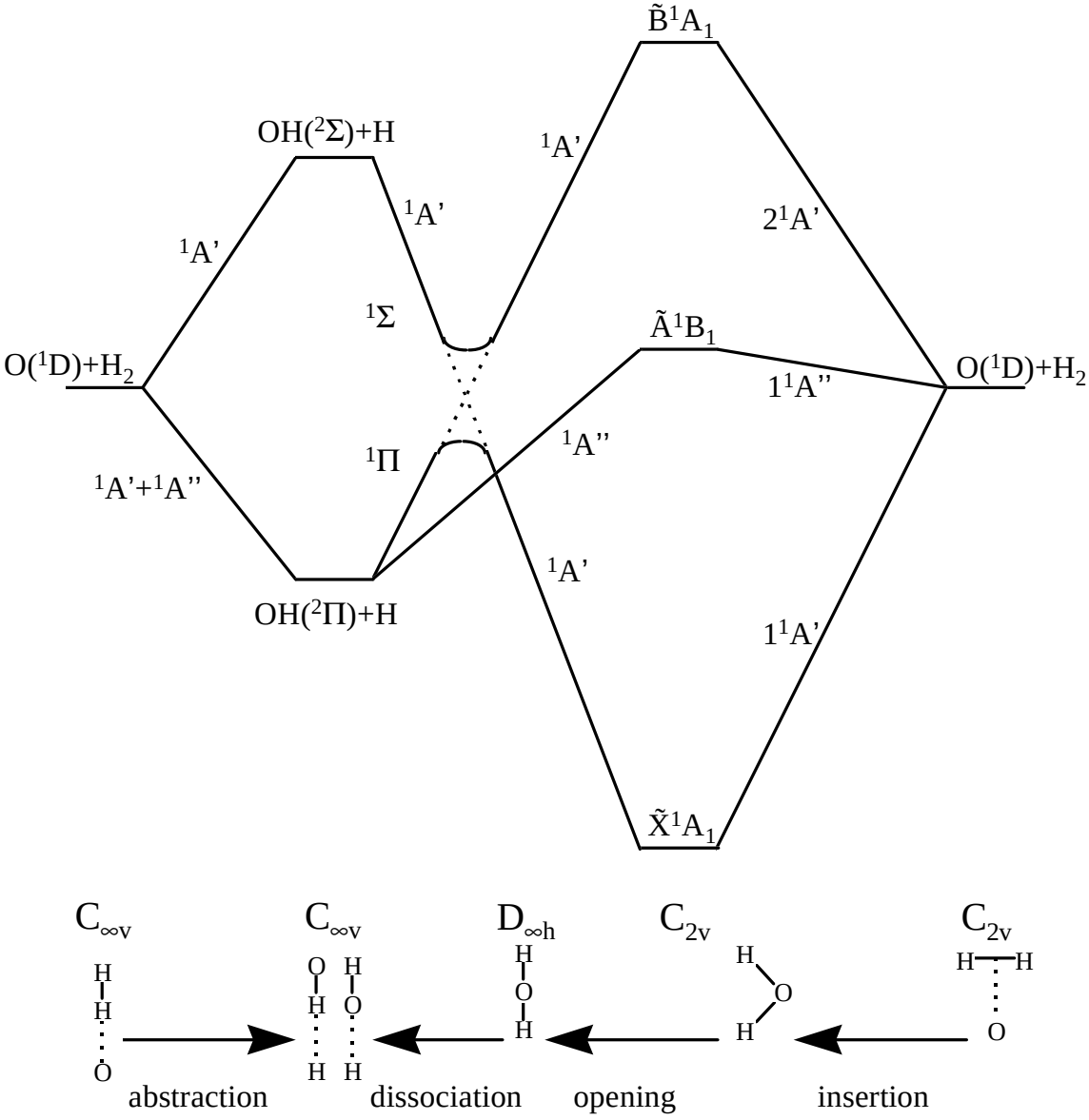

Figure 3.6 Schematic correlation diagram (not to scale) adapted from figures 1 and 21 of ref.[38]. Only the three lowest singlet states are shown.

measured depth of -10.08 eV relative to the $O(^3P) + 2H(^2S)$ dissociation limit, and this is reproduced quite acceptably in the SL surface (-8.95 eV) [35] and the K PES (-9.80) [36]. In the linear configuration there is a crossing between the $^1\Sigma$ and $^1\Pi$ states which becomes an avoided crossing for deviations away from linearity. This "conical intersection" occurs as a unidimensional seam, although it is smoothed out in the fitted surfaces with only a remnant "bump".

In the original work of Schinke and Lester it was recognised that the entrance channel is a key element in defining the dynamics of the surface. The SL surface exists in 3 versions: SL1, SL2 and SL3, which all differ in the degree of attractiveness in the entrance channel region and represent fits within the magnitude of the errors of the *ab initio* calculations. SL2 may be discounted immediately due to the presence of barriers in the both the insertion and collinear entrance channels; these barriers are at variance with the observed zero activation energy [35]. The K PES lies between the SL1 and SL3 in terms of attractiveness: see figure (3.7).

The Schinke–Lester surface as used in the present work has been modified in two ways from the original. The exoergicity of the original surface is somewhat larger than the experimental value and the surface has been modified (hereafter SL1M) by artificially lowering the entire entrance channel region relative to the exit channel [39]. The result of this procedure is an improvement in the overall energetics of the reaction without a significant alteration in the dynamics compared to the original surface. The calculated absolute cross sections and reaction rates are significantly deviated from experimental observations, however [40].

A further complication arises in the SL surface from a triplet–singlet crossing which results in a discontinuity in the first derivative of the fitted potential (see refs. [35, 41] for details). The cusp exists quite high into the H_2 diatomic potential where it was assumed to have little effect. It is now known, however, that OH_2 intermediates which last for several vibrational

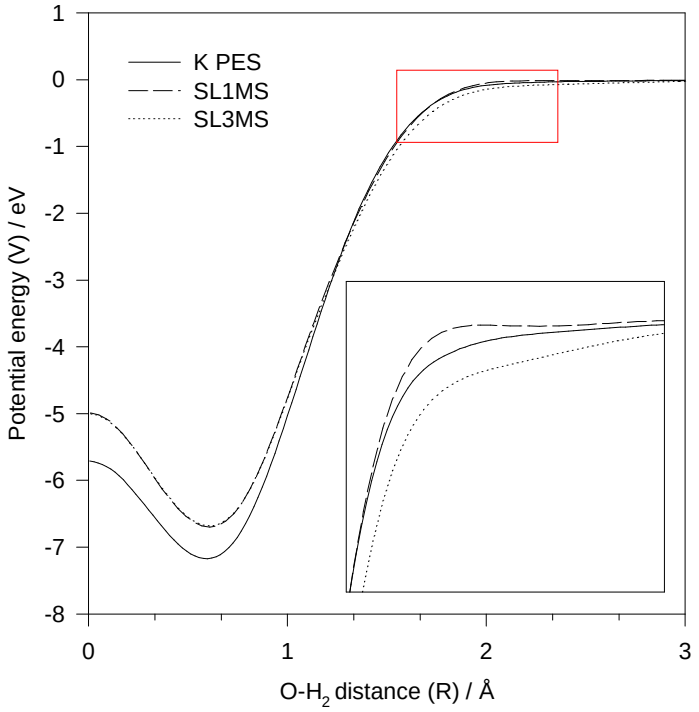

Figure 3.7 The Schinke & Lester and K potential energy surfaces following the minimum energy path for insertion: the oxygen approaches at right angles to the H_2 which is allowed to relax for each point in the plot. The insert shows the difference in entrance channel features. The zero of the minimum energy path is set to the asymptotic $O(^1D_2)$ + H_2 limit.

periods are often highly excited in the bending motion, and the cusp is presumably accessed a number of times [41, 42]. This is evident from the trajectory calculations whose energy conservation is adversely affected by the discontinuity. A seventh order spline polynomial by Goldfield and Wiesenfeld greatly improved the energy conservation [41]. The final SL1 surface used in the present work incorporates both modification (M) of the entrance channel and spline smoothing (S), and shall be referred to as SL1MS.

3.11.2 Quantisation

Rovibrational quantisation may be carried out in a number of ways. If the PES is an accurate representation of the true potential, it may be possible to use spectroscopically determined term values. In general this will not be the case and rovibrational energies can be tailored to the PES using the semiclassical action integral at the asymptotes of the potential energy surface [33].

Taking the reagent diatomic as an example, the following implicit equation is solved numerically to yield the energy levels $E_{v,j}$, the turning points $r_{\pm}$, and the vibrational period, $\tau_{v,j}$ [31, 33].

$$\frac{1}{2}J_v \; - \; \pi\hbar\left(v+\frac{1}{2}\right) \; = \; 0, \tag{3.51}$$

where,

$$J_v \; = \; 2\int_{r+}^{r-}\left\{2\mu_{\mathrm{BC}}\left[E_{v,j} \; - \; V_{\mathrm{BC}}(r) \; - \; \frac{J_r^2}{2r^2\mu_{\mathrm{BC}}}\right]\right\}^{1/2}\mathrm{d}r. \tag{3.52}$$

In this equation μ_{BC} is the diatomic reduced mass, J_r is the angular momentum $[j(j+1)]^{1/2}\hbar$, and V_{BC} represents the asymptotic diatomic potential energy. For a given (v,j) an initial trial energy is estimated. From this trial energy, the equations are iteratively solved for the turning points and the energy levels using, e.g. the Newton–Raphson method

[29, 33].

Once a ladder of energy levels have been obtained, it is possible to fit them to a Dunham expansion [43],

$$E_{v,j} \;=\; \sum_{lj} Y_{lj}(v+\frac{1}{2})^l j^l (j+1)^l, \tag{3.53}$$

The energies may then be retrieved trivially from the Dunham coefficients, Y_{lj}. Product rovibrational quantisation was carried out by equating the classical rotational angular momentum of the diatomic to the quantum expression $[j'(j'+1)]^{1/2}\hbar$. This (real) quantum number is then used in equating the internal energy of the diatomic molecule to the Dunham expansion to retrieve the (real) vibrational quantum number. The real quantum numbers are then rounded to the nearest integer. In the remainder of this thesis j and j' are reserved for the QCT nuclear rotational angular momentum quantum numbers, N' is reserved for the experimental (spectroscopic) angular momentum quantum number (see appendix A).

3.11.3 Trajectory time delays

Classical trajectory time delays, τ_d, were calculated following the method of Muga and Levine [34, 44]:

$$\tau_d \;=\; T - \frac{R_f}{v_f} - \frac{R_i}{v_i}, \tag{3.54}$$

where T is the total duration of the trajectory from state i to state f, R is the position co–ordinate and v is the relative velocity at the initial and final times of the trajectory. Put another way, this is the difference between the real time taken for a trajectory and the times of flights of the reagents and products at the constant initial and final relative velocities

(*i.e.,* to and from the centre of the reaction sphere). Although this is not to be regarded as a lifetime in a conventional sense, it is convenient to use as an estimate of the amount of time spent in the interaction. Also τ_d may be negative, particularly for direct and sudden interactions, although the majority of time delays for the O + H_2 reaction were positive, as will be discussed in the following chapters.

3.11.4 Reaction probabilities and methods of moment expansion

The probability of an outcome, P_r, is given simply by the ratio of the number of trajectories with a given outcome to the total number of trajectories, N_r/N; although using the Monte Carlo sampling method this is only correct in the limit $N \rightarrow \infty$. The absolute cross section is given by $\sigma_r = \pi b_{\max}^2 (N_r/N)$ and the variance is given by [33],

$$\mathsf{var}[\sigma_r] \;=\; \sigma_r^2 \;\left(\frac{N - N_r}{N_r N}\right). \tag{3.55}$$

It is clear from this equation that quite a considerable number of trajectories are required to ensure statistical confidence, particularly for outcomes with a low probability.

Product distributions were calculated by means of moment expansion as a numerical series. This method has the advantage of producing numerically smooth distributions which may be described by a few coefficients making them numerically easy to handle. Fourier series are a traditional and flexible method of fitting a random variable, but in the present case expansion in Legendre polynomials (also spherical harmonics) is preferred where possible for a number of reasons. The polynomials form an orthonormal set, and so the calculation of the Legendre moments as a Monte Carlo average is very straightforward – see equation (3.57) below. Another major reason for employing the Legendre polynomials is their direct physical interpretation as moments of the full CM $\boldsymbol{k}$,$\boldsymbol{k'}$,$\boldsymbol{j'}$ distribution as has been discussed by Herschbach and co–workers [45] (see also chapter 2). A general account of the method

is given here, although the reader is directed elsewhere for a full discussion of the method [33, 34].

The continuous variable to be expressed as a series must first be mapped from the range $u \in [u_{\min}, u_{\max}]$ to $x \in [-1, 1]$, where x is the so–called *reduced* variable. An approximation, $g(x)$, to the unit normalised probability distribution, is written as a sum in Legendre polynomials truncated at the M^{th} term,

$$g(x) \;=\; \frac{1}{2} \sum_{n=0}^{M} [n] a_n \mathrm{P}_n(x). \tag{3.56}$$

where a_n is the n^{th} Legendre moment, $\mathrm{P}_n(x)$ is the n^{th} degree Legendre polynomial, and $[n] = 2n + 1$. The a_n coefficients are calculated as the Monte Carlo average,

$$a_n \;=\; \langle \mathrm{P}_n(x) \rangle \;=\; \frac{1}{S_{N_\alpha}} \sum_{\ell=1}^{N_R} w_\ell \mathrm{P}_n(x_\ell), \tag{3.57}$$

where α denotes a specific quantum state. The sum runs over all N_R reactive trajectories, where w_ℓ is the weight of each individual trajectory. S_{N_α} is the total weight of the state α,

$$S_{N_\alpha} \;=\; \sum_{\ell=1}^{N_R} w_\ell. \tag{3.58}$$

In the case of an unbiased sampling system w_ℓ will take the value of either 1 or 0 depending on whether the trajectory ends in α or not; in this case $S_{N_\alpha} = N_\alpha$, the number of reactive trajectories ending in final state α. The uncertainty in this series is obtained from the variance,

$$\mathsf{var}[g(x)] \;=\; \frac{1}{4} \sum_{n=1}^{M} [n]^2 \, s_n^2 \mathrm{P}_n^2(x), \tag{3.59}$$

where s_n^2 is the estimate of variance in the coefficients, $s_n^2 \equiv \mathsf{var}[a_n]$,

$$s_n^2 \;=\; \frac{1}{S_{N_\alpha}} \left(\langle \mathrm{P}_n^2(x) \rangle \;-\; \langle \mathrm{P}_n(x) \rangle^2 \right). \tag{3.60}$$

The angle brackets in this equation represent an average over all the trajectories leading to the given product state, α. As an example, the product $\boldsymbol{k}$,$\boldsymbol{k'}$ differential cross section may be written as:

$$\frac{\mathrm{d}\sigma}{\mathrm{d}\omega_t} \;=\; \frac{\sigma}{2\pi} g(x), \tag{3.61}$$

where $x = \cos\theta_t$, the CM scattering angle. The variance is given by [34]:

$$\mathsf{var}\left[\frac{\mathrm{d}\sigma}{\mathrm{d}\omega_t}\right] \;=\; \left(\frac{N - S_{N_\alpha}}{S_{N_\alpha} N}\right) \left(\frac{\mathrm{d}\sigma}{\mathrm{d}\omega_t}\right)^2 \;+\; \left(\frac{\sigma}{2\pi}\right)^2 \mathsf{var}[g(x)]. \tag{3.62}$$

Analogous expressions may be used to expand any of the polar angles including θ_r ($\boldsymbol{k}$,$\boldsymbol{j'}$) and θ_{tr} ($\boldsymbol{k'}$,$\boldsymbol{j'}$). For the dihedral angle (triple vector) distributions of $\boldsymbol{l}$, $\boldsymbol{l'}$ or $\boldsymbol{j'}$ with respect to the $\boldsymbol{k}$–$\boldsymbol{k'}$ scattering plane, expansion in Fourier series was employed (see section 2.4.4). For example, the ϕ_r distribution may be written as [28]:

$$P(\phi_r) \;=\; \frac{1}{2} \left(1 \;+\; \sum_{\text{even } n \geq 2} a_n \cos n\phi_r \;+\; \sum_{\text{odd } n \geq 1} b_n \sin n\phi_r \right), \tag{3.63}$$

with a_n and b_n given by,

$$a_n \;=\; 2\langle \cos n\phi_r \rangle \tag{3.64}$$

$$b_n \;=\; 2\langle \sin n\phi_r \rangle. \tag{3.65}$$

Similar expressions were used for ϕ_l and $\phi_{l'}$, the dihedral angles of the orbital angular momenta.

Polarisation dependent differential cross sections (PDDCS) were calculated as an expansion in modified spherical harmonics, equation (2.35) repeated here [28],

$$\frac{1}{\sigma}\frac{\mathrm{d}\sigma_{kq}}{\mathrm{d}\omega_t} = \sum_{k_1} \frac{[k_1]}{4\pi}\, s^{k_1}_{kq\pm}\, \mathrm{C}_{k_1\,-q}(\theta_t, 0) \tag{3.66}$$

The coefficients of the expansion, $s^{k_1}_{kq\pm}$, are calculated as,

$$\begin{aligned} s^{k_1}_{kq\pm} &= (-1)^q\, 2i\, \langle \mathrm{C}_{k_1 q}(\theta_t, 0)\, \mathrm{C}_{kq}(\theta_r, 0)\, \sin q\phi_r \rangle \qquad k \ \text{odd} \\ &= (-1)^q\, 2\, \langle \mathrm{C}_{k_1 q}(\theta_t, 0)\, \mathrm{C}_{kq}(\theta_r, 0)\, \cos q\phi_r \rangle \qquad k \ \text{even} \end{aligned} \tag{3.67}$$

The $s^{k_1}_{kq\pm}$ coefficients follow the same symmetry constraints (resulting from the distribution of product OH internuclear axes) as the $a^k_{q\pm}$ polarisation parameters. These are calculated as,

$$\begin{aligned} a^k_{q\pm} &= 2i\, \langle \mathrm{C}_{kq}(\theta_r, 0)\, \cos q\phi_r \rangle \qquad k \ \text{odd} \\ &= 2\, \langle \mathrm{C}_{kq}(\theta_r, 0)\, \sin q\phi_r \rangle \qquad k \ \text{even} \end{aligned} \tag{3.68}$$

For $q = 0$, this reduces to $a^k_0 = \langle \mathrm{P}_k(\cos\theta_r) \rangle$. The above expectation values may be expanded as [46]:

$$a^1_{1+} = -i\sqrt{2}\, \langle \sin\theta_r\, \sin\phi_r \rangle = -i\sqrt{2}\, \left\langle j'_y / j' \right\rangle$$

$$\begin{aligned} a_0^2 &= \langle \mathrm{P}_2(\cos\theta_r)\rangle = \left\langle (3\,j_z'^2 - j'^2)/2\,j'^2 \right\rangle \\ a_{1-}^2 &= -\sqrt{6}\,\langle \sin\theta_r\,\cos\theta_r\,\cos\phi_r\rangle = -\sqrt{6}\,\left\langle j_x' j_z'/j'^2 \right\rangle \\ a_{2+}^2 &= \sqrt{3/2}\left\langle \sin^2\theta_r\,\cos 2\phi_r \right\rangle = \sqrt{3/2}\left\langle (j_x'^2 - j_y'^2)/j'^2 \right\rangle \end{aligned} \tag{3.69}$$

where j_x', j_y' and j_z' are the components of $\boldsymbol{j'}$ along the x, y and z axes respectively. It is clear from equations (3.69) that the polarisation parameters are simply expectation values of the multipole moments of the expansion of $\boldsymbol{j'}$: the renormalised PDDCS are conditional expectation values (see section 2.5). It should be noted that, as a result of the symmetry constraints for an achiral system, $a_0^1 \propto \langle j_z'/j'\rangle$ and $a_{1-}^1 \propto \langle j_x'/j'\rangle$ are necessarily zero; the system can be *aligned* but not *oriented* along the CM x and z axes [28, 47].

The truncation point of the fitted series was determined by performing Smirnov–Kolmogorov statistical testing [29, 48]. The number of coefficients is changed until the deviation between the observed and fitted cumulative probability distributions is small enough with a significance level of 70%–95%.

References

[1] M. P. Docker, *Chem. Phys.*, **135** (1989) 405.

[2] G. S. Selwyn and H. S. Johnston, *J. Chem. Phys.*, **74** (1981) 3791.

[3] K. F. Preston and R. F. Barr, *J. Chem. Phys.*, **54** (1971) 3347.

[4] T. F. Hanisco and A. C. Kummel, *J. Phys. Chem.*, **97** (1993) 7242.

[5] P. Felder, B. -M. Haas and J. R. Huber, *Chem. Phys. Lett.*, **186** (1991) 177.

[6] A. Heck, D. Neyer and D. W. Chandler, *personal communication.*

[7] J. M. Teule, *Ph. D. Thesis*, Vrije Universiteit, Netherlands, 1997.

[8] R. N. Zare, *Mol. Photochem.*, **4** (1972) 1.

[9] N. Shafer, K. Tonokura, Y. Matsumi, S. Tasaki and M. Kawasaki, *J. Chem. Phys.*, **95** (1991) 6218.

[10] L. L. Springsteen, S. Satyapal, Y. Matsumi, L. M. Dobeck and P. L. Houston, *J. Phys. Chem.*, **97** (1993) 7239.

[11] T. Suzuki, H. Katayanagi, Y. Mo and K. Tonokura, *Chem. Phys. Lett.*, **256** (1996) 90.

[12] see, for example, P. L. Houston, *J. Phys. Chem.*, **91** (1987) 5388.

[13] D. G. Hopper, *J. Chem. Phys.*, **80** (1984) 4290.

[14] A. J. Alexander, F. J. Aoiz, M. Brouard and J. P. Simons, *Chem. Phys. Lett.*, **256** (1996) 561.

[15] J. Short, *D. Phil. Thesis*, University of Oxford, 1997.

[16] G. K. Smith and J. E. Butler, *J. Chem. Phys.*, **73** (1980) 2243.

[17] G. H. Dieke and H. M. Crosswhite, *J. Quant. Spectrosc. Radiat. Transfer*, **2** (1961) 97.

[18] J. L. Chidsey and D. R. Crosley, *J. Quant. Spectrosc. Radiat. Transfer*, **23** (1980) 187.

[19] C. H. Greene and R. N. Zare, *J. Chem. Phys.*, **78** (1983) 6741.

[20] R. N. Dixon, *J. Chem. Phys.*, **85** (1986) 1866.

[21] F. J. Aoiz, M. Brouard, P. A. Enriquez and R. Sayos, *J. Chem. Soc. Faraday Trans.*, **89** (1993) 1427.

[22] W. Demtröder, *Laser Spectroscopy*, Springer–Verlag, 1988.

[23] P. A. Enriquez, *Ph. D. Thesis*, University of Nottingham, 1993.

[24] M. Brouard, H. M. Lambert, J. Short and J. P. Simons, *J. Phys. Chem.*, **99** (1995) 13571.

[25] M. Brouard, S. P. Duxon and J. P. Simons, *Isr. J. Chem.*, **34** (1994) 67.

[26] H. L. Kim, M. A. Wickramaaratchi, X. N. Zheng and G. E. Hall, *J. Chem. Phys.*, **101** (1994) 2033.

[27] M. Brouard and C. Vallance, *unpublished results.*

[28] F. J. Aoiz, M. Brouard and P. A. Enriquez, *J. Chem. Phys.*, **105** (1996) 4964.

[29] W. H. Press, S. A. Teukolsky, W. T. Vetterling and B. P. Flannery, *Numerical Recipes: the art of scientific computing*, 2nd. edn. Cambridge University Press, 1992.

[30] S. P. Rayner, *D. Phil. Thesis*, University of Oxford, 1997.

[31] M. Karplus, R. N. Porter and R. D. Sharma, *J. Chem. Phys.*, **43** (1965) 3259.

[32] J. N. Murrell and S. D. Bosanac, *Introduction to the theory of atomic and molecular collisions*, John Wiley and sons, 1989.

[33] D. G. Truhlar and J. T. Muckerman, in *Atom molecule collision theory: A guide for the experimentalist*, ed. R. B. Bernstein, 1979 Plenum, New York, p. 505.

[34] F. J. Aoiz, V. J. Herrero and V. Sáez Rábanos, *J. Chem. Phys.*, **97** (1992) 7423, and references therein.

[35] R. Schinke and W. A. Lester Jr., *J. Chem. Phys.*, **72** (1980) 3754.

[36] T-. S. Ho, T. Hollebeek, H. Rabitz, L. B. Harding and G. C. Schatz, *J. Chem. Phys.*, **105** (1996) 10472.

[37] R. E. Howard, A. D. McLean and W. A. Lester Jr., *J. Chem. Phys.*, **71** (1979) 2412.

[38] G. Durand and X. Chapuisat, *Chem. Phys.*, **96** (1985) 381.

[39] R. Schinke, *J. Chem. Phys.*, **80** (1984) 5510.

[40] A. J. Alexander, F. J. Aoiz, L. Bañares, M. Brouard, V. J. Herrero and J. P. Simons, *Chem. Phys. Lett.*, *in press.*

[41] E. M. Goldfield and J. R. Wiesenfeld, *J. Chem. Phys.*, **93** (1990) 1030.

[42] P. A. Berg, J. J. Sloan and P. J. Kuntz, *J. Chem. Phys.*, **95** (1991) 8038.

[43] *Molecular Spectra and Molecular Structure vol. 1*, G. Herzberg, 2nd ed. Krieger, Florida 1989.

[44] J. G. Muga and R. D. Levine, *Chem. Phys. Lett.*, **162** (1989) 7.

[45] J. D. Barnwell, J. G. Loeser and D. R. Herschbach, *J. Phys. Chem*, **87** (1983) 2781, and references therein.

[46] A. J. Alexander, F. J. Aoiz, L. Bañares, M. Brouard, J. Short and J. P. Simons, *J. Phys. Chem. A*, **101** (1997) 7544.

[47] F. J. Aoiz, M. Brouard, V. J. Herrero, V. Sáez Rábanos and K. Stark, *Chem. Phys. Lett.*, **264** (1997) 487.

[48] F. J. Aoiz, V. J. Herrero and V. Sáez Rábanos, *J. Chem. Phys.*, **94** (1991) 7991.

Chapter 4 $O(^1D_2)$ + HD: Product angular and energy distributions

4.1 Introduction

Despite numerous theoretical and experimental studies over the past decade, the detailed dynamics of the title reaction have remained hazy (see chapter 1). Until now, much of the work has involved the determination of the scalar properties. More recently, experimental studies have moved to a larger arena: that of the vectorial and angular properties of the $O(^1D_2)$ + H_2/HD/D_2 reaction. Since the crossed beam study of Lee *et al.* [1] very little work has been done towards unravelling the vectorial scattering properties, in contrast to the kinematically similar (but direct abstractive) reaction, F + H_2. More recently interest in the reaction has been revived and a number of studies are ongoing or underway (see the Introduction for details).

The present work aims to explore some of the vectorial properties of the $O(^1D_2)$/H_2(HD) reaction. A laser photolysis technique is used, coupled with polarised Doppler resolved laser spectroscopy. This technique allows product rovibrational states to be selected and the method is sensitive to both the linear *and* angular momentum CM distributions of the product. These product distributions are compared directly with extensive quasi-classical trajectory (QCT) calculations on an *ab–initio* potential energy surface, and the calculations are also employed to further the understanding of this benchmark bimolecular reaction.

The present chapter deals with the linear momentum and energy distributions of the $O(^1D_2)$/HD reaction from a quasi-classical trajectory study employing the Schinke–Lester

surface (SL1MS)[2]. Experimental measurements of the OH($v' = 0, N' = 14, f$) product angular distribution and excitation function from the reaction of $O(^1D_2)$+H_2 are presented in chapter 5, as are QCT calculations using the SL1MS surface and the K PES of Schatz and co–workers [3]. In chapter 6 experimental measurements of the state resolved product alignment in the CM frame are presented and are discussed in the light of state–resolved QCT calculations of the $\boldsymbol{l}$, $\boldsymbol{l'}$ and $\boldsymbol{j'}$ angular momentum distributions.

4.2 Trajectory calculations

A batch of 2×10^5 trajectories was run at a collision energy of 0.197 eV (19 kJ mol^{-1}) with HD in ($v = 0,\ j = 0$) on the SL1MS PES. This collision energy was used in order to form a comparison with a recent molecular beam study by Che and Liu. Additionally 10^5 trajectories were run with HD in ($v = 0,\ j = 1$) to allow for the rotational population of the experimental HD molecular beam.

Trajectories were started from an oxygen–HD distance of 600 pm and the equations of motion were integrated with a timestep of 0.01 to 0.02 fs. This ensured an energy conservation to better than 1 in 10^5, and an angular momentum conservation of better than 1 in 10^7.

4.3 Energy disposal and Total cross sections

Vibrationally v' product state resolved integral cross sections, $\sigma_R(v')$ for the two isotopic channels, as well as the average rotational quantum number, $\langle j' \rangle_{v'}$, are shown in table 4.1. As can be seen, the most populated vibrational state is $v' = 0$, and no vibrational inversion is apparent, in agreement with previous studies on this surface for the O + H_2 reaction. As discussed in chapter 1, this result stems mainly from the attractiveness of the surface in the entrance channel, and we can see that the present mass combination does not affect this overall result. The form of the rotational distribution also agrees well with previous

	OH Channel		OD Channel	
	$\sigma_R(v')/\text{Å}^2$	$\langle j' \rangle_{v'}$	$\sigma_R(v')/\text{Å}^2$	$\langle j' \rangle_{v'}$
all v'	6.144	17	9.482	22
$v' = 0$	1.636	22	1.805	29
$v' = 1$	1.550	19	1.687	26
$v' = 2$	1.286	16	1.663	23
$v' = 3$	1.026	13	1.555	20
$v' = 4$	0.569	9	1.301	17
$v' = 5$	0.077	5	0.963	13
$v' = 6$	–	–	0.463	10
$v' = 7$	–	–	0.045	7

Table 4.1 Product state–resolved integral cross sections and average rotational quantum numbers, $\langle j' \rangle_{v'}$ for the O + HD reaction on the SL1MS surface at a collision energy of 0.197 eV. With the exception of the highest populated vibrational states, the uncertainties are less than 1%.

studies, extending out to the maximum product j' for both OH and OD, see figure 4.1.

Average fractional values of energy going into vibration, rotation and translation are shown in table 4.2. The available energy is essentially distributed equally amongst the three modes. The values for $\langle f_t' \rangle$ are comparable to those measured experimentally by Laurent *et al.* [4] and Matsumi *et al.* [5]. Both experiments were carried out at slightly lower collision energy (13.5 kJ mol^{-1}) and assume an isotropic product atom angular distribution in the laboratory frame to extract moments from the Doppler lineshapes. The ratio $\langle f_t'(\text{OD} + \text{H}) \rangle / \langle f_t'(\text{OH} + \text{D}) \rangle = 1.16$ is also comparable to the previous measurements of Laurent *et al.* (1.28) [4] and more recently Che and Liu (1.36) [6], although there seems

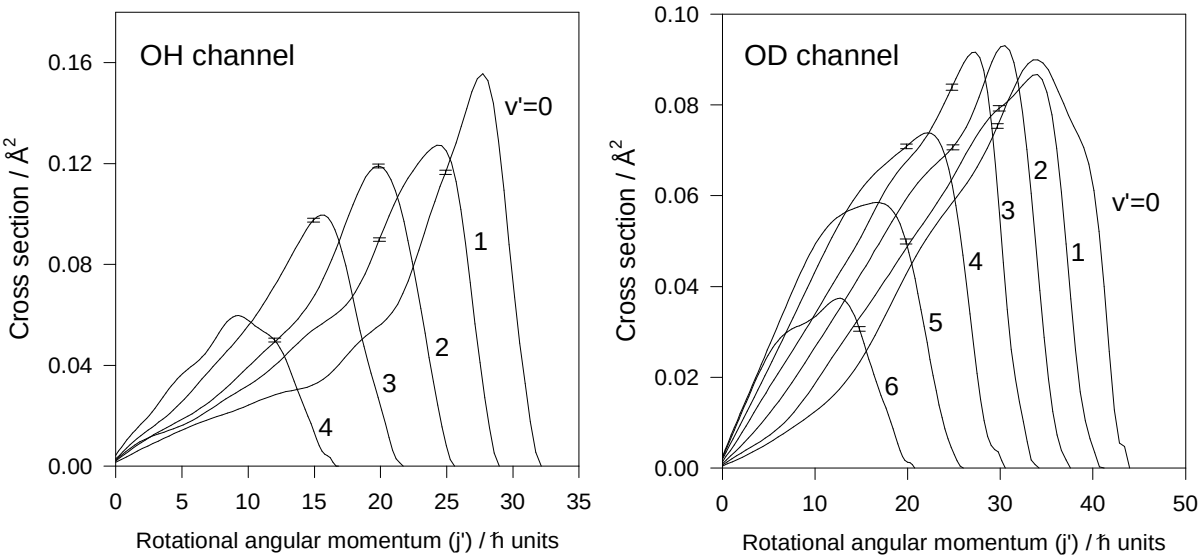

Figure 4.1 OH and OD product rotational distributions, resolved by product vibration, as a function of semiclassical rotational angular momentum.

to be larger discrepancy with the results of Matsumi *et al.* (2.15) [5]. The value for the average fractional vibrational energy $\langle f_v' \rangle$ is very close to the measurement for the O/H_2 reaction as measured by Park *et al.* ($\langle f_v' \rangle$=0.40) – see table 1.3. This should be compared with the value of $\langle f_v' \rangle = 0.66$ for the kinematically similar, but direct abstractive F + H_2 reaction.

The fractional translational energy release distribution, $P(f_t')$, is shown in figure 4.2. There is quite a large spread of values, and the range is larger for the OD channel, in very good agreement with recent experimental measurements [6].

The calculated branching ratio, $\Gamma_{H/D} = 1.56 \pm 0.02$ is in good agreement with recent measurements made by Laurent *et al.*, who obtained a value of $\Gamma_{H/D} = 1.35 \pm 0.2$, and with the value of $\Gamma_{H/D} = 1.4 \pm 0.2$ from Matsumi *et al.*, although the present result agrees less convincingly with Tsukiyama *et al.* [7] who measured a value of 1.13 ± 0.08. It should be noted that these three experimental studies were performed at a slightly lower collision energies, (see also table 1.5). It is clear that the result is higher than that expected from

	OH channel	OD channel
translation $\langle f'_t \rangle$	0.28	0.33
ref. [4] $\langle f'_t \rangle$	0.32 ± 0.05	0.41 ± 0.07
ref. [5] $\langle f'_t \rangle$	0.19 ± 0.04	0.41 ± 0.09
vibration $\langle f'_v \rangle$	0.39	0.40
rotation $\langle f'_r \rangle$	0.32	0.28

Table 4.2 Average fractional values of energy going into vibration, rotation and translation. Uncertainties for the QCT data are less than the last significant figure.

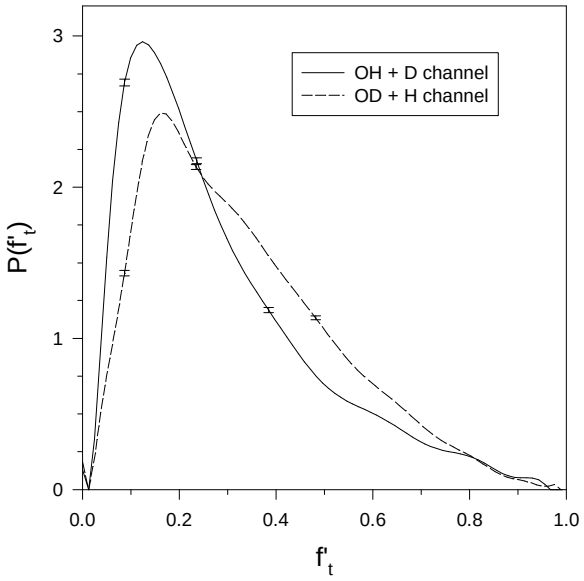

Figure 4.2 Product translational energy probability distribution function, $P(f'_t)$, normalised to unit area, for the OH and OD channels.

a statistical prior distribution ($\Gamma_{H/D} = 1.00$) and is greater than the value obtained for the F/HD reaction (see table 1.4 and the surrounding discussion).

The above data highlight many similarities between the O+H_2 and O+HD reactions, perhaps more similarities than would be expected from kinematic arguments: the leaving D atom from O/HD is twice the mass of the corresponding H atom in O/H_2. It is clear though, that these observations are highly state averaged. In the next section we show differential cross sections for the O/HD reaction obtained from the ground state SL1MS PES. As will be discussed, the state selection of products is a key indicator of the microscopic dynamics of this reaction, and that the measurement of state averaged properties may be quite misleading.

4.4 Differential cross sections

Figure 4.3 shows the total (summed over all final states) differential cross sections (DCS) for the OH and OD product channels. These are in reasonable agreement with the experimental work of Che and Liu [6], although it is evident that the calculations underestimate the amount of backward scattering (note that in fig. 2 of ref. [6] the curves are scaled to the same area).

Velocity–angle polar contour maps, $d^2\sigma/d\omega dw_C$ (where C is the product atom) for the OH and OD reaction channels are displayed in figures 4.4 and 4.5. In order to be directly comparable to experimental results of ref. [6] the velocity scale shown corresponds to the CM velocity of the outgoing atom (w_C), whereas the angular variables (ω) refer to the product OH: zero degrees (forward) corresponds to the direction of the incoming $O(^1D_2)$ atom. The contour maps include equal contributions from trajectories with HD($j = 0$) HD ($j = 1$), roughly corresponding to an HD rotational temperature of *ca.* 100 K. The plots include a full coupling between angle and velocity and were found to be significantly different

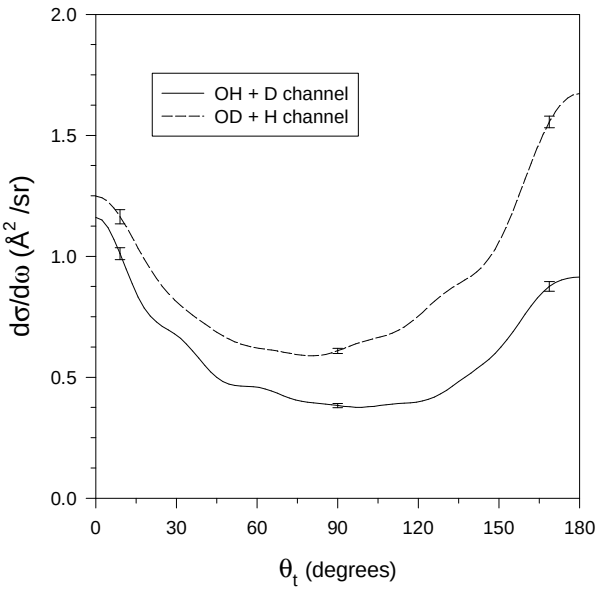

Figure 4.3 Total (summed over all final states) solid angle OH and OD product differential cross–sections.

from maps created assuming a separable function of the form $F(\theta_t, w_C) = I(\theta_t)\, G(w_{\rm C})$. The non–separable maps are less circular than their separable counterparts, and the ridge in the forward hemisphere is only apparent if a non–separable expansion in Legendre moments is used. The presence of the ridges was confirmed by two dimensional velocity plots of the forward angular region.

Non–separability between angular and velocity co–ordinates was encountered experimentally by Che and Liu in ref. [6]. The fact that no ridges were observed in their work may result from the limiting experimental resolution, and blurring from averaging over a spread of collision energies and initial j states. The non–separability could be attributed to reaction over higher surfaces which produce different angular distributions from reaction over the ground state surface. However, the results are also consistent with a picture in which trajectories associated with different product internal states result in different angular distributions; we shall develop this finding below.

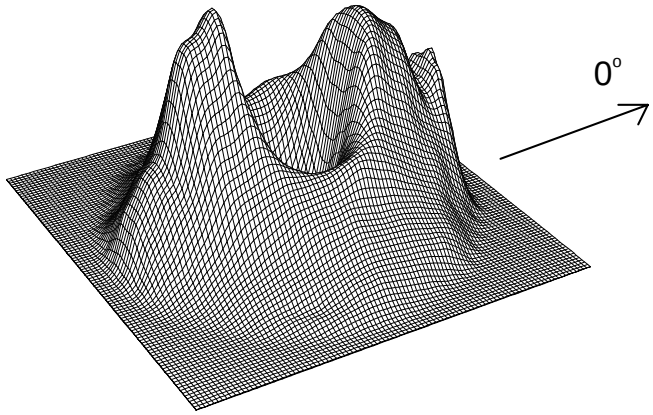

Figure 4.4 Velocity–angular (triple) differential cross section $d\sigma/d\omega dw_C$ for the OH + D isotopic channel. The scale of velocities corresponds to the product D atom and the angular variables are those of the OH molecule. Forward corresponds to the direction of the incoming $O(^1D_2)$ atom: see text for details.

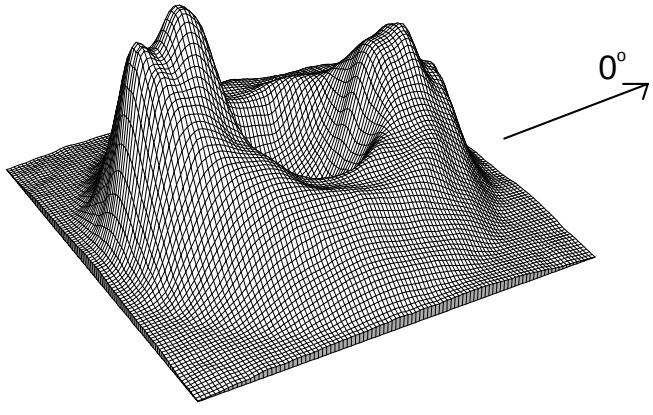

Figure 4.5 As for fig. 4.4, but for the OD + H isotopic channel.

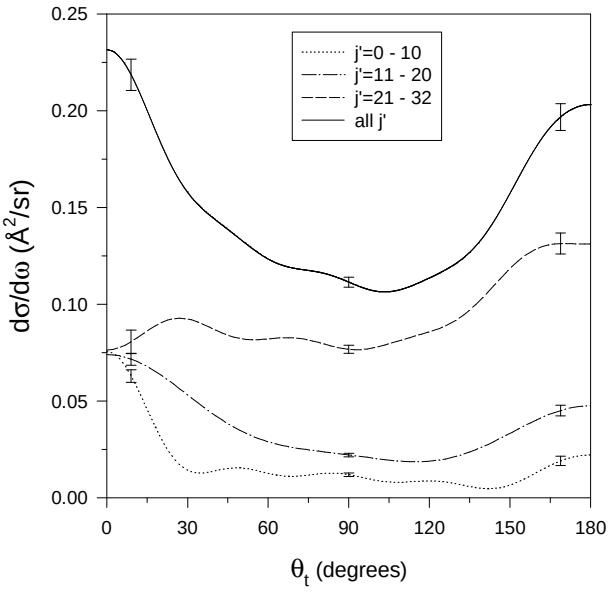

Figure 4.6 OH product rovibrationally resolved differential cross–sections for $v' = 0$ resulting from the reaction of O + HD. The corresponding opacity distribution is shown in fig. 4.8.

Figure 4.6 shows the OH product vibrationally resolved $v' = 0$ DCS which has been further resolved by product rotational state. A similar plot for $v' = 4$ is shown in figure 4.7. Each of the differential cross–sections when resolved solely in v' appear to be forward–backward symmetric. Other vibrational levels are intermediate in nature between these two cases, and similar behaviour is found for the OD product differential cross sections. Forward–backward symmetry has often been taken as evidence for the existence of intermediate 'complexes' with lifetimes longer than that of their mean rotational period. The symmetry in these plots, however, belies the marked deviations from forward–backward symmetry visible in the $v' = 0$ rotationally resolved DCS, which range from strongly forward (low j') to more backward (high j'). The rotationally resolved plots for $v' = 4$ are both nearly symmetric, however, and do not show such a marked trend as for $v' = 0$.

In order to understand the origin of the trends of scattering in the differential cross sections, it is instructive to look the nature of the intermediates formed, particularly the mean

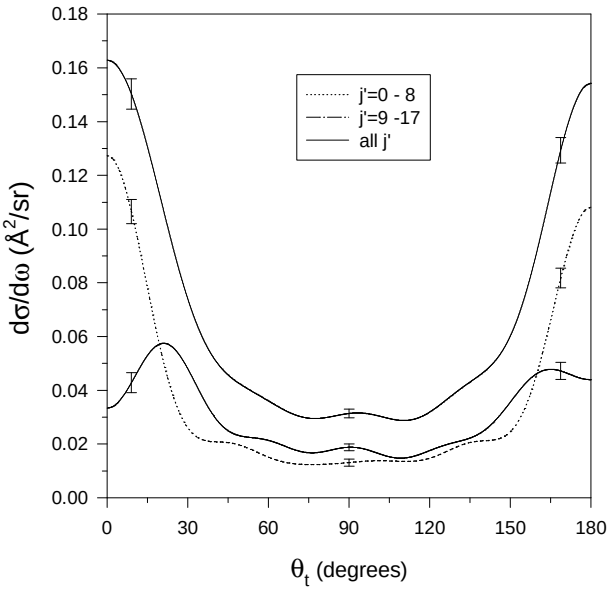

Figure 4.7 OH product rovibrationally resolved differential cross–sections for $v' = 4$ resulting from the reaction of O + HD. The corresponding opacity distribution is shown in fig. 4.9.

lifetimes and rotational periods, as will be discussed in the following section.

4.5 Opacity functions and mean lifetimes

Plots of the OH $v' = 0$ product rotationally state-resolved orbital angular momentum opacity function, $P(l)$, are shown shown in figure 4.8. The corresponding plot for $v' = 4$ is shown in figure 4.9. The reagent orbital angular momentum was calculated by equating the classical angular momentum with the quantum expression, $\sqrt{l(l+1)}\hbar$. It is immediately obvious that the opacity functions for $v' = 4$ are skewed in favour of higher impact parameters, whereas the impact parameters for $v' = 0$ lie over a broad range. It is also noticeable that the opacity function for $v' = 0$, low j' has a small bump at around $l = 33\,\hbar$.

The 'complex lifetime' of intermediates was estimated using the trajectory time delay method of Muga *et al.* [8] as described in section 3.11.3. The rotational period was estimated from the initial angular momentum using the following expression,

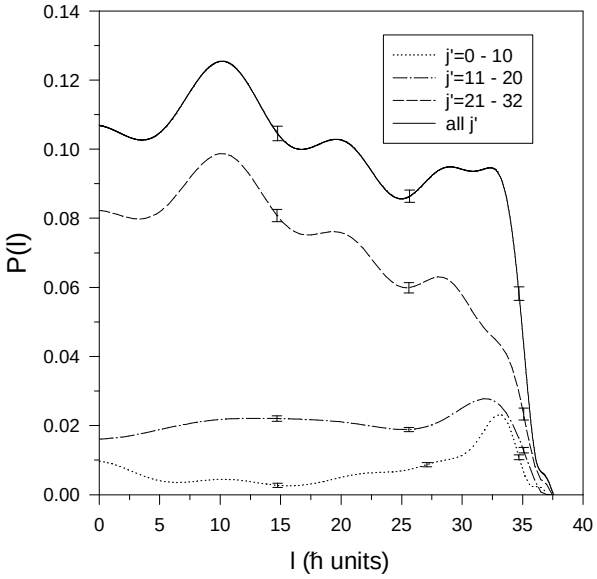

Figure 4.8 $OH(v' = 0)$ reagent orbital angular momentum opacity distribution $P(l)$. The corresponding DCS is shown in fig. 4.6.

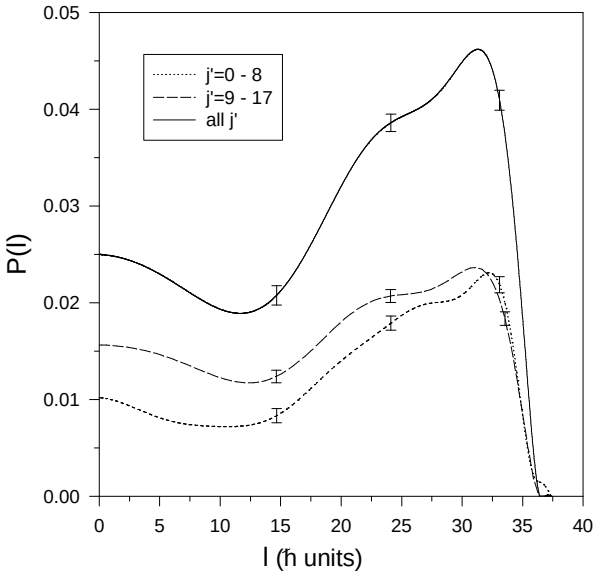

Figure 4.9 As for fig. 4.8, but for products in $v' = 4$. The corresponding DCS is shown in fig. 4.7.

Product states	$\langle b \rangle \pm \Delta b$ (Å)	$\langle \tau_d \rangle \pm \Delta\tau_d$ (fs)	$\langle \tau_r \rangle \pm \Delta\tau_{\mathrm{R}}$ (fs)
$v' = 0$, $j' = 0 - 10$	1.8 ± 0.3	45 ± 51	79 ± 25
$v' = 0$, $j' = 11 - 20$	1.6 ± 0.9	74 ± 93	97 ± 81
$v' = 0$, $j' = 21 - 32$	1.4 ± 0.6	80 ± 81	114 ± 33
$v' = 0$, all j'	1.5 ± 0.8	75 ± 94	106 ± 73
$v' = 4$, $j' = 0 - 8$	1.7 ± 0.4	110 ± 18	84 ± 27
$v' = 4$, $j' = 9 - 17$	1.6 ± 0.5	98 ± 57	91 ± 34
$v' = 4$, all j'	1.7 ± 0.4	104 ± 62	88 ± 31

Table 4.3 Average impact parameters $\langle b \rangle$, mean time delays $\langle \tau_d \rangle$, with corresponding mean (estimated) rotational periods, $\langle \tau_r \rangle$, for state resolved OH products. The corresponding dispersions, Δb, $\Delta\tau_d$ and $\Delta\tau_r$ represent one standard deviation

$$\tau_r \;=\; \frac{2\pi I}{(2\mu E_t)^{1/2} b}, \tag{4.1}$$

where μ is the reduced mass of the reagents, E_t is the reagent translational energy, b is the impact parameter and I is the moment of inertia of the intermediate. The moment of inertia is taken as the average of the principal moments of (appropriately deuterated) water (3.06 kg m^2). Table 4.3 shows average impact parameters $\langle b \rangle$, mean time delays $\langle \tau_d \rangle$, and mean rotational periods $\langle \tau_r \rangle$ for the set of OH trajectories in the range of states corresponding to figures 4.6—4.9. The angle brackets $\langle \ldots \rangle$ imply an average over all trajectories leading to a specific final state. Table 4.3 also shows the range of each variable contributing to each state (calculated as one single standard deviation).

From table 4.3 one can see an increase in trajectory time delay with vibrational state: a

trend which is shown over the full vibrational range (not shown). In contrast there is an apparent *decrease* in the estimated mean rotational period, which to some extent mirrors the structure of the state–resolved opacity functions shown in figures 4.8 and 4.9. Notice also from table 4.3, that there is a larger spread around the mean impact parameter for $v' = 0$ – this is also clear in figures 4.8 and 4.9.

From the data it would appear that for OH products in $v' = 4$, the combination of longer lifetime, combined with a shorter rotational period stemming from collision at predominantly higher impact parameters, conspire to produce the near–symmetric DCS. In contrast, the $v' = 0$ trajectories yield time delays shorter than the mean rotational period. One can also see a slight increase in the $v' = 0$ mean time delay with increasing j' which may possibly account for the change from forward scattering (low j') to slightly more backward (high j'). Similar trends to those described above were observed for the OD channel: although the variation of DCS with product rotation was not quite as marked.

It is suggested that, for OH products born in $v' = 0$, many of the intermediate 'complexes' last on average for a shorter time than their rotational period, in contrast with the observed behaviour for $v' = 4$. As one might intuitively expect, the forward scattered products (low j') may be associated with predominantly higher impact parameter collisions, whilst backward scattering (higher j') comes mainly from lower impact parameter collisions, see figure 4.8.

4.6 Viewing the trajectories

It is possible to gain some insight into the dynamics by viewing individual trajectories, and trying to identify common or typical reaction mechanisms. Of course this is a procedure which must be undertaken with care, since the sample size is necessarily small and the results are arguably subjective.

As has been previously observed for this surface [9, 10], no trajectories viewed could be described as abstractive: the O atom was observed to insert into the HD bond. For trajectories yielding OH products in $v' = 4$ it was observed that the majority of collisions yield HOD collision "complexes". These complexes were found to be highly vibrationally excited (both bend and stretch) and lasted on average for longer than one rotational period, lending support to the results above.

On viewing trajectories for OH products born in $v' = 0$, with low product j', it was possible to identify rapidly rotating HOD intermediates which originate from predominantly higher impact parameters. These intermediates promptly dissociate and the products are scattered in the forward hemisphere. Another common type of trajectory was a simple 'straight–through' mechanism where the O atom was observed to pass through the HD bond largely without rotation or hindrance, picking up an H atom on its exit. In contrast, trajectories resulting in OH ($v' = 0$, high j') favour lower impact parameters, although with a broader range of orbital angular momenta (figure 4.8). Many trajectories were observed to rotate very little with products scattered in the backward hemisphere.

The trajectories analysed clearly indicate the dominance of an insertion mechanism, as would be expected for reaction over the ground state with a deep intermediate potential well. There was no evidence, however, for the existence of "long lived" persistent collision complexes: intermediates survived on average for less than or on the order of their rotational period. This result is in excellent agreement with the previous QCT studies and with the recent QM time–dependent wavepacket study on the SL1 surface by Peng *et al.* [11] who noted that insertion dynamics were dominant, but found no evidence for scattering resonances.

4.7 Conclusions

QCT trajectories were carried out for the $O(^1D_2)$ + HD ($v = 0$, $j = 0, 1$) using a slightly modified Schinke–Lester surface (SL1MS) [2, 12] at the collision energy of a recent molecular beam studies [6, 13]. The total differential cross sections for OH and OD were found to be in reasonable agreement with the experimental work, although the calculations fail to account fully for the magnitude of backward scattering.

Strong non–separability between velocity and angular variables was found in the present study, despite the deceptive forward–backward symmetry of the OH total differential cross section, and this is in good agreement with the beam experiments. State–resolved analysis of the OH product channel revealed different identifiable characteristics of the insertion mechanism for low product v' and high product v'. Intermediates which lead to OH ($v' = 4$, all j') were observed to survive on average for longer than the estimated mean rotational period, and provide the major contribution to the observed forward–backward symmetry of the $v' = 4$ DCS. In contrast, for $v' = 0$, a range of observed intermediate lifetimes and rotational periods result in a trend moving from forward scattering (low j') to backward scattering (high j').

References

[1] R. J. Buss, P. Casavecchia, T. Hirooka, S. J. Sibener and Y. T. Lee, *Chem. Phys. Lett.*, **82** (1981) 386.

[2] R. Schinke, *J. Chem. Phys.*, **80** (1984) 5510.

[3] T-. S. Ho, T. Hollebeek, H. Rabitz, L. B. Harding and G. C. Schatz, *J. Chem. Phys.*, **105** (1996) 10472.

[4] T. Laurent, P. D. Naik, H.-R. Volpp, J. Wolfrum, T. Arusi-Parpar, I. Bar and S. Rosenwaks, *Chem. Phys. Lett.*, **236** (1995) 336.

[5] Y. Matsumi, K. Tonokura, M. Kawasaki and H. L. Kim, *J. Phys. Chem.*, **96** (1992) 10622.

[6] K. Liu and D-. C. Che, *J. Chem. Phys.*, **103** (1995) 5164.

[7] K. Tsukiyama, B. Katz and R. Bersohn, *J. Chem. Phys.*, **83** (1985) 2889.

[8] J. G. Muga and R. D. Levine, *Chem. Phys. Lett.*, **162** (1989) 7.

[9] S. W. Ransome and J.S. Wright, *J. Chem. Phys.*, **77** (1982) 6346.

[10] M. S. Fitzcharles and G. C. Schatz, *J. Phys. Chem.*, **90** (1986) 3634.

[11] T. Peng, D. H. Zhang, J. Z. H. Zhang and R. Schinke, *Chem. Phys. Lett.*, **248** (1996) 37.

[12] A. J. Alexander, F. J. Aoiz, M. Brouard and J. P. Simons, *Chem. Phys. Lett.*, **256** (1996) 561.

[13] Y. -T. Hsu and K. Liu, *J. Chem. Phys.*, **107** (1997) 1664.

Chapter 5 $O(^1D_2) + H_2$: Product angular and energy distributions

5.1 Trajectory calculations

6×10^5 trajectories were run at a collision energy of 0.1 eV (9.65 kJ mol^{-1}) with H_2 ($v = 0,\ j = 1$) on the SL1MS [1] and the K [2] ground state surfaces. The experimental mean collision energy is 0.12 eV (11.6 kJ mol^{-1}) with a standard deviation of 0.07 eV (6.8 kJ mol^{-1}). Thus, calculations at 0.1 eV and initial $j = 1$ roughly correspond to the mean collision energy and the most populated H_2 rotational level (300 K) of the present experiments.

Trajectories were integrated from an initial distance of 800 pm using a time step of 0.02 fs to ensure conservation of energy and momentum. The large number of trajectories calculated was essential to allow a significant "population" of the $j' = 14$ rovibrational state.

As commented on in section (3.8.2), the analysis of the Doppler profiles required a state–specific excitation function to be taken into account, *i.e.,* a collisional energy dependence of the reaction cross section, $\sigma(E_t)$. Quasiclassical excitation functions and energy dependent differential cross sections were calculated by Aoiz and Bañares following the method of Aoiz *et al.* [3, 4]. These calculations include sampling of reagent j from a thermal (300 K) H_2 rotational distribution. The reader is directed to ref. [5] for the details.

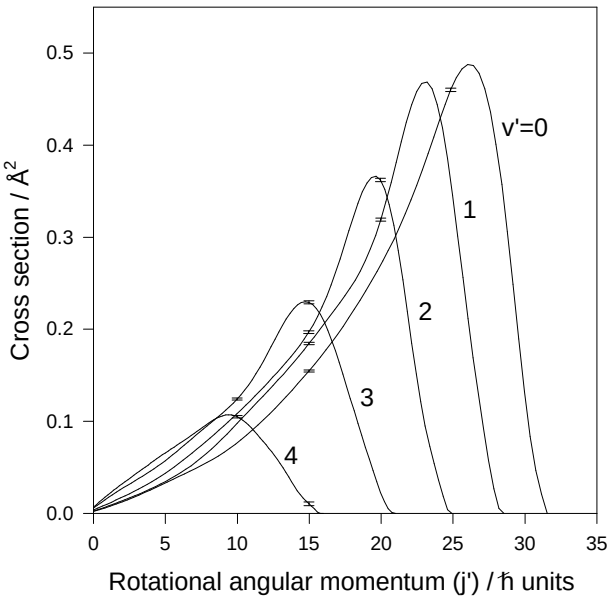

Figure 5.1 OH product rotational distributions, resolved by product vibration, as a function of semiclassical rotational angular momentum for the SL1MS PES.

5.2 Total integral and differential cross sections

As for the reaction of $O(^1D_2)$ with HD (chapter 4), the vibrational distribution was found to be monotonically decreasing – see table (5.1). The product rotational distribution is hot, see figure (5.1).

The total integral cross section[1], 3.48 Å^2 for the SL1MS and 4.03 Å^2 for the K, are nearly half the recent experimental value of Koppe *et al.* (7.6 ± 1.5 Å) [6]. Their experimental measurement of the rate constant appears to be twice the recommended value of DeMore *et al.*[7], however, and this may be due to the superthermal collision energy used (0.12 eV).

Total differential cross sections for the SL1MS and K surfaces are compared in figure (5.2). The SL1MS DCS is much more prominently backward scattered, and the K DCS is forward

[1]Absolute cross sections in the literature are often divided by 5 to represent a surface degeneracy factor. This has been applied to the results quoted in the text but not to the results in table (5.1).

	SL1MS PES		K PES	
OH quantum state	N_R	σ_R (Å^2)	N_R	σ_R (Å^2)
v'=0	170924	5.819	129658	6.153
v'=1	142967	4.868	113028	5.364
v'=2	102810	3.500	42332	4.381
v'=3	65120	2.217	61039	2.897
v'=4	27836	0.948	27145	1.288
v'=5	1663	0.056	1775	0.084
all v'	511320	17.41	424977	20.16
v'=0, j'=14	4100	0.1396	2494	0.1183

Table 5.1 Number of successful trajectories, N_R and reactive cross sections, σ_R, for specific product quantum states. Error bounds are typically less than 1%. The cross sections have not been divided by the surface degeneracy factor of 5.

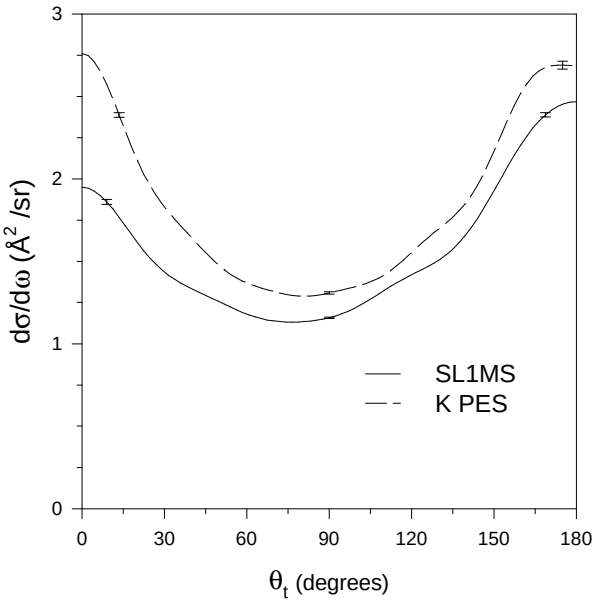

Figure 5.2 Product OH total (summed over all final states) solid angle differential cross section for the SL1MS and K surfaces.

backward symmetric. One possible reason for increased forward scattering is the degree of attraction in the entrance channel, since the more attractive SL3 surface is also observed to produce more forward scattering [1, 8] (see figure 3.7). Both the SL1MS and the K PES total differential cross sections are in good agreement with a recent crossed molecular beam study by Casavecchia and co–workers [9] who observed a DCS with slightly more backward than forward scattering.

5.3 Quasiclassical product state resolved differential cross sections

Product OH vibrationally resolved differential cross sections obtained using the SL1MS surface are shown in fig. (5.3). The appearance of the total differential cross section belies the variation of the state–resolved DCSs which move from predominantly backward ($v' = 0$) to almost symmetric ($v' = 4$), in general agreement with results reported in chapter (4) for O + HD (using the SL1MS surface). The state resolved differential cross sections for OH(v') also show a strong dependence on product rotation: see figures (5.4) and (5.5).

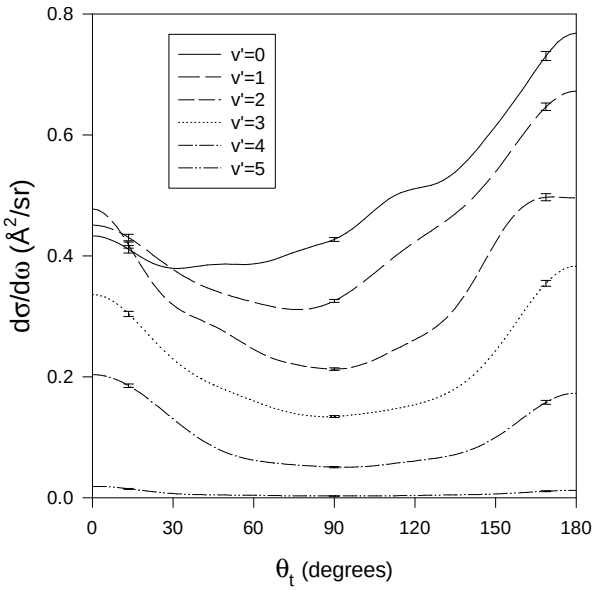

Figure 5.3 Quasiclassical OH product vibrationally resolved differential cross sections calculated for O+H_2 using the SL1MS surface.

The corresponding reagent orbital angular momentum opacity functions, $P(\boldsymbol{l})$, are shown in figures (5.6) and (5.7).

OH products in ($v' = 0$, low j') show a strong preference for *backward* scattering and the opacity function is quite flat, with a slight preference for low reagent orbital angular momenta (lower impact parameters). This is in stark contrast to the preference for *forward* scattering found for O + HD $\rightarrow$ OH($v' = 0$, low j') with an opacity function peaking at large ($\sim 33\hbar$) reagent orbital angular momentum. For OH($v' = 0$, high j') the amount of sideways scattering increases, although there is still a preference for backward scattering. The increase in sideways scattering is due to the high product angular momentum (j') which can tilt the reagent $\boldsymbol{l}$ and product $\boldsymbol{l'}$ orbital angular momenta away from each other [10, 11] (see section 6.3). The opacity function extends out to $l = 24$ and displays a broad maximum at $l = 12$. OH products in $v' = 4$ show differential cross sections which are nearly forward–backward symmetric, with a slight preference for forward scattering. The corresponding state specific opacity functions are bimodal, peaking at both high and low

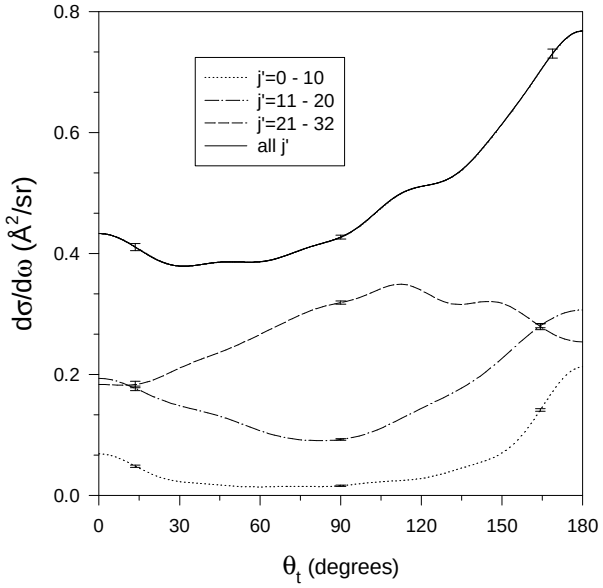

Figure 5.4 QCT calculated OH product rovibrationally resolved differential cross sections for $v' = 0$ (SL1MS surface). The corresponding opacity function is shown in fig. (5.6).

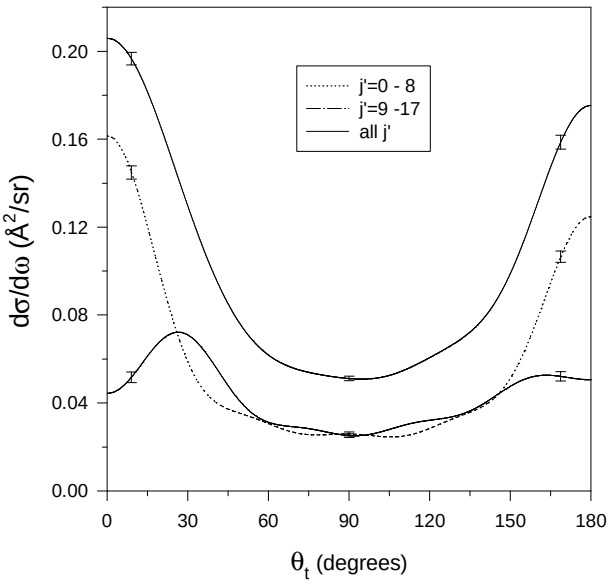

Figure 5.5 QCT calculated OH product rovibrationally resolved differential cross sections for $v' = 4$ (SL1MS surface). The corresponding opacity function is shown in fig. (5.7).

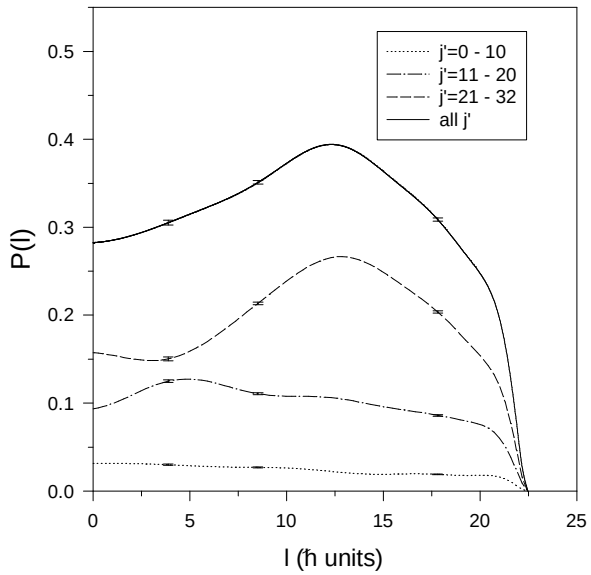

Figure 5.6 QCT calculated OH($v' = 0$) reagent orbital angular momentum opacity distribution P(l) (SL1MS surface). The corresponding DCS is shown in fig. (5.4).

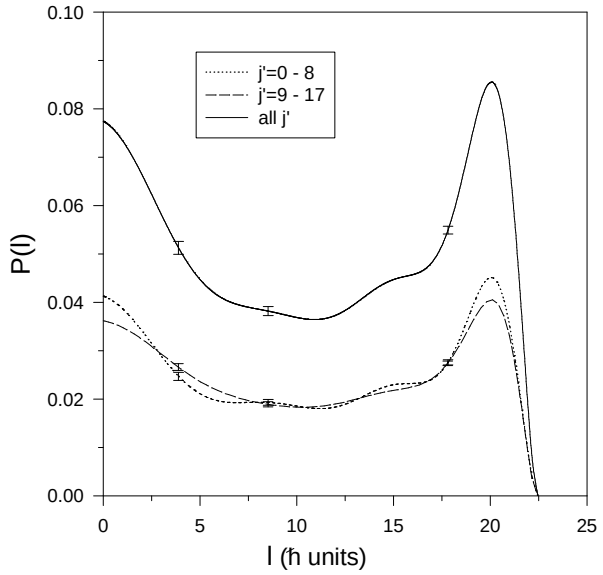

Figure 5.7 QCT calculated OH($v' = 4$) reagent orbital angular momentum opacity distribution P(l) (SL1MS surface). The corresponding DCS is shown in fig. (5.5).

reagent l.

In the study of the O/HD reaction, the change in DCS from $v' = 0$ to $v' = 4$ was accompanied by an increase in the mean trajectory time delay $\langle\tau_d\rangle$, and a shift in the state specific opacity function towards collisions favouring high orbital angular momenta, l. In the present case the increase in $\langle\tau_d\rangle$ is even more pronounced: as v' increases from 0 to 5 there is a four–fold increase in $\langle\tau_d\rangle$, see table (5.2). Approximate estimates of the mean rotational periods of the collision complexes $\langle\tau_r\rangle$ (see section 4.5) indicate an increase in the ratio $\langle\tau_d\rangle/\langle\tau_r\rangle$ from $\sim 1/3$ for OH($v' = 0$) to $\langle\tau_d\rangle/\langle\tau_r\rangle \sim 1$ for OH($v' = 5$). Despite the increase, the trajectory time delay is still comparable to the rotational period (*i.e.*, the rotational "clock rate").

5.4 State resolved differential cross sections and excitation functions

The LAB "speed–dependent", $D_0^0(0,0;v_p)$, and "angular–dependent", $D_0^2(2,0;v_p)$, Doppler profiles for OH($v' = 0, N' = 14$) are shown in figures (5.8) for the $\Pi(A'')$ Λ–doublet and (5.9) for the $\Pi(A')$ Λ–doublet. The state resolved angular distributions and excitation functions obtained by following the data analysis procedures detailed in chapter 3 are shown in figure (5.10). The quality of the fits can be gauged by comparing the overlap of the analytical and experimental contours. The resolution of the fits were limited by the truncation point of the Legendre moment expansion given in equation (3.36). It was found that 7 moments in the angular distribution and 5 moments in the excitation function were required to fit the data using a separable functional form (see section 3.8.5). In the absence of data for the exact form of the the $O(^1D_2)$ atom angular distribution, the fitting was initially restricted to the LAB speed dependent contour which is independent of the O atom reagent anisotropy, β_O. The contour reflecting the OH product angular distribution, $D_0^2(2,0;v_p)$, could only be simulated assuming an average $\overline{\beta}_O \approx 0.15$–$0.2$ over the effective collision energy range

Product states	$\langle$b$\rangle \pm \Delta$b / Å	$\langle\tau_d\rangle \pm \Delta\tau_d$ / fs	$\langle\tau_\mathrm{r}\rangle \pm \Delta\tau_\mathrm{r}$ / fs
$v' = 0$	1.54 ± 0.53	30 ± 77	106 ± 140
$v' = 1$	1.56 ± 0.58	35 ± 80	105 ± 155
$v' = 2$	1.63 ± 0.56	46 ± 88	102 ± 125
$v' = 3$	1.64 ± 0.59	58 ± 98	109 ± 204
$v' = 4$	1.70 ± 0.59	83 ± 115	104 ± 220
$v' = 5$	1.62 ± 0.59	129 ± 132	116 ± 205
$v' = 0$, $j' = 0 - 10$	1.49 ± 0.59	32 ± 72	121 ± 232
$v' = 0$, $j' = 11 - 20$	1.50 ± 0.56	31 ± 74	113 ± 140
$v' = 0$, $j' = 21 - 32$	1.56 ± 0.51	30 ± 78	101 ± 126
$v' = 4$, $j' = 0 - 8$	1.72 ± 0.58	88 ± 114	104 ± 224
$v' = 4$, $j' = 9 - 16$	1.69 ± 0.59	78 ± 114	105 ± 216

Table 5.2 QCT calculated average impact parameters $\langle b\rangle$, mean time delays $\langle\tau_d\rangle$, with corresponding mean (estimated) rotational periods, $\langle\tau_r\rangle$, for state resolved OH products (SL1MS surface). The corresponding dispersions, Δb, $\Delta\tau_d$ and $\Delta\tau_r$ represent one standard deviation.

– a result in good agreement with expectations based on recent photofragment imaging studies (see section 3.2). It should be noted that inclusion of an excitation function makes only a slight improvement to the quality of the fits in figures (5.8) and (5.9) and that the returned angular distributions are quite robust. The angular distributions, excitation functions, and the best fit anisotropy parameters were all used in the subsequent analysis of the polarisation data (chapter 6).

As can be seen from figures (5.8)–(5.10), the results for the A″ and A′ Λ–doublets are very similar, in excellent agreement with previous studies of $O(^1D_2)$+CH_4 [12, 13], $H(^2S)/CO_2$ [14, 15] and measurements of $OH(^2\Pi_{3/2}; v' = 0, N' = 5)$ for $O(^1D_2)/H_2$ [12, 5]. They display markedly different rotational polarisation, however – see chapter 6.

QCT energy–dependent differential cross sections, calculated by Aoiz and Bañares using a double expansion in Legendre moments, are presented in figure (5.11) [5]. Energy averaged differential cross sections were obtained by convoluting the double distribution with the experimental collisional energy distribution, $P(E_t)$. The comparison between the experimental and QCT calculated angular distributions and state specific excitation functions is shown in figure (5.12).

The double distributions plotted in figure (5.11) show almost flat excitation functions for both surfaces, with a slight increase in the cross section at lower collision energies. As can be seen, in both cases, the DCS does not change very much with collision energy, lending credence to the use of a separable distribution in the fitting of the experimental data. For the SL1MS results there is a slight preference in favour of backward scattering whereas the K DCS are mostly forward backward symmetric: the DCS calculated at fixed collision energy (not shown, but see ref. [5]) is very similar to the energy averaged DCS. A much stronger variation in the DCS with energy was found for $OH(v' = 0, j' = 5)$, for both surfaces [5].

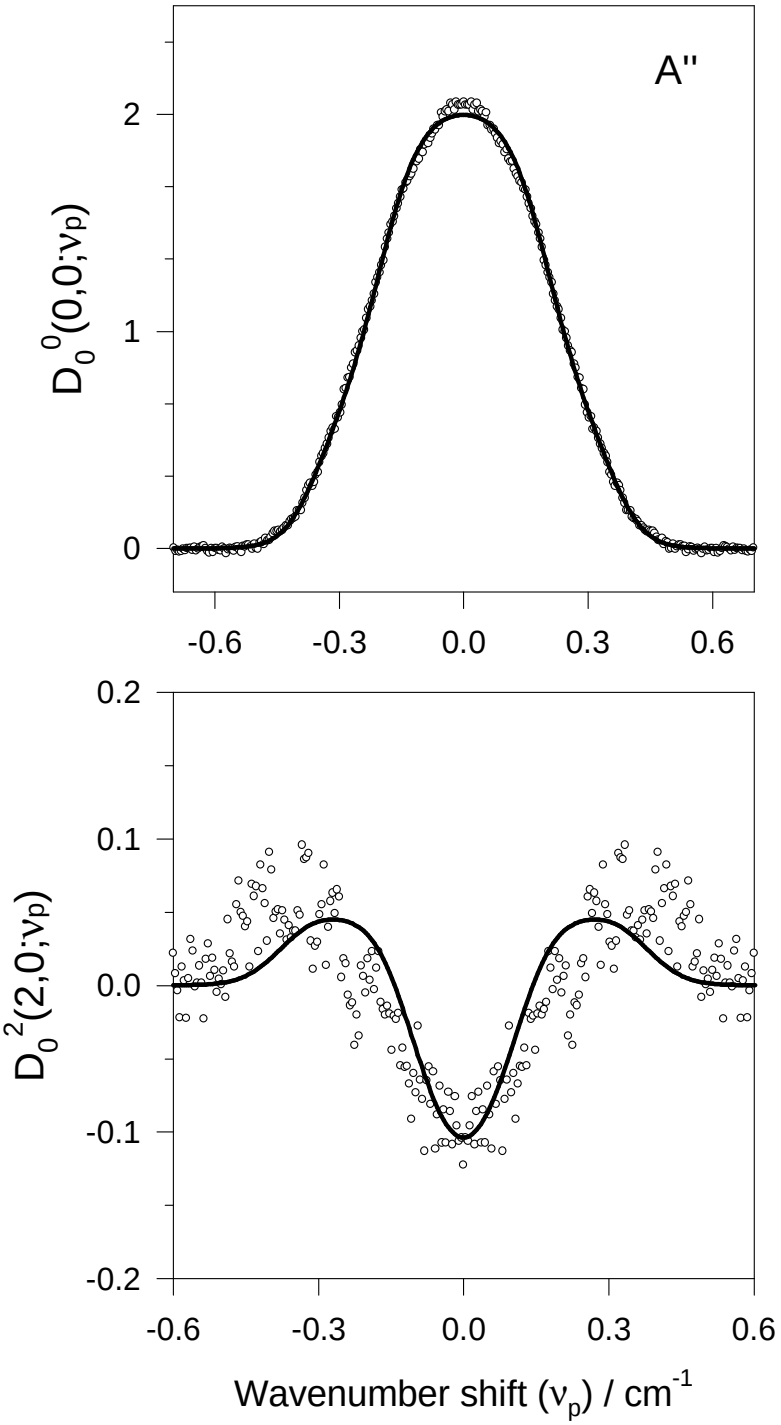

Figure 5.8 OH($v' = 0, N' = 14$) $\Pi(A'')$ Λ–doublet results: experimental composite profiles, $D_0^0(0,0;v_p)$ (top panel), and $D_0^2(2,0;v_p)$ (lower panel), which depend on the OH LAB speed and LAB translational anisotropy respectively. The experimental data are shown as points, and the solid lines represent fits as detailed in the text.

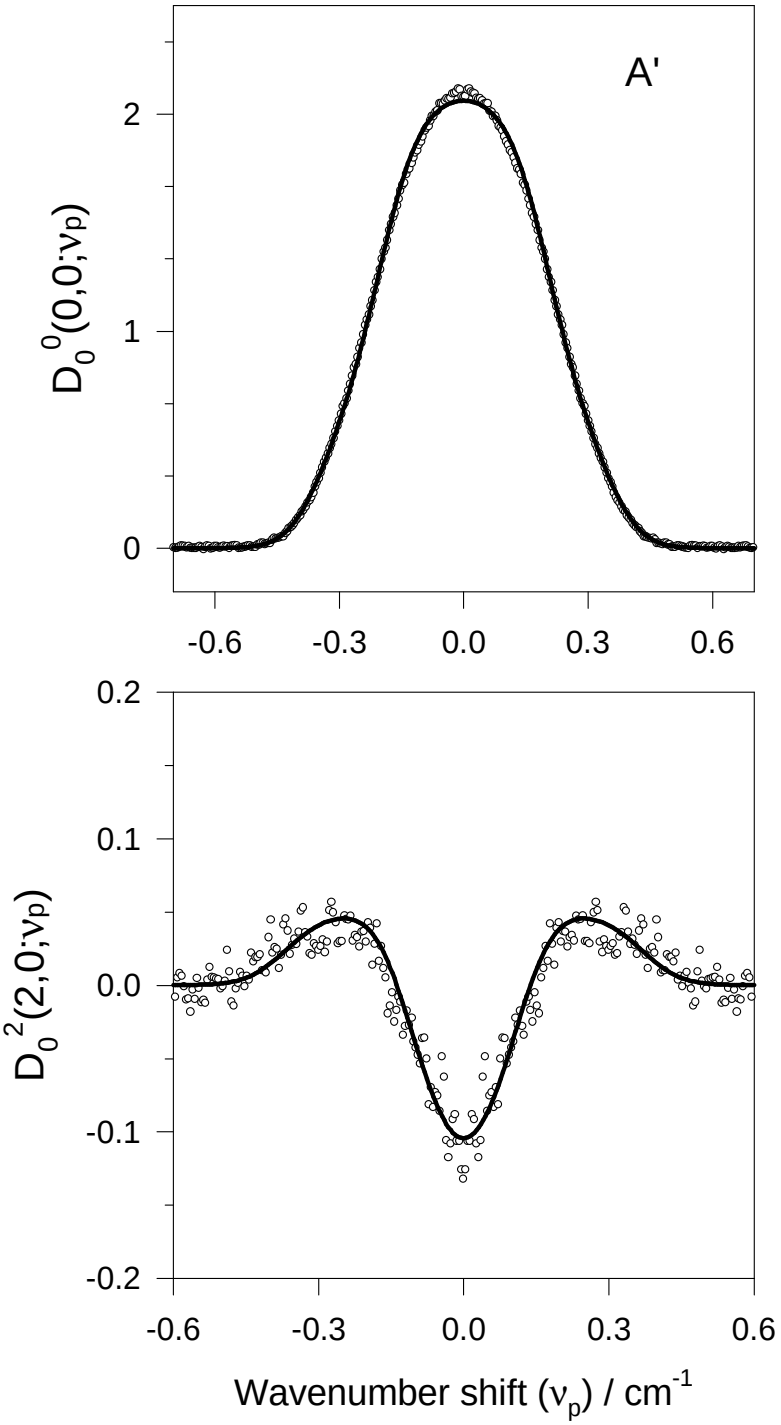

Figure 5.9 As for figure (5.8), but for the $\Pi(A')$ Λ–doublet.

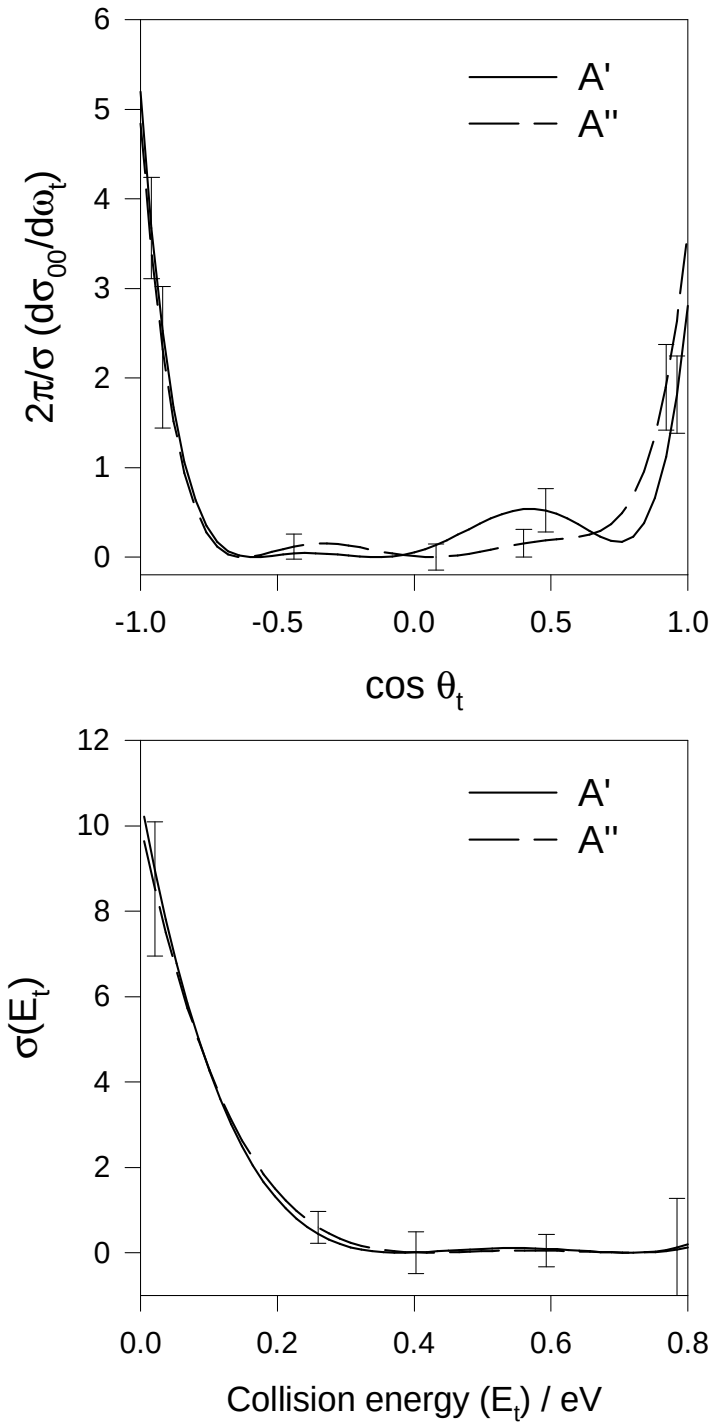

Figure 5.10 Product angular distributions (top panel) and excitation functions (bottom panel) for OH($v' = 0, N' = 14$, A″ and A′). The distributions are calculated as expansions in Legendre polynomials: see chapter 3. Error bars represent $\pm 1\sigma$ standard deviations. The corresponding experimental data are shown in figures (5.8) (A″) and (5.9) (A′).

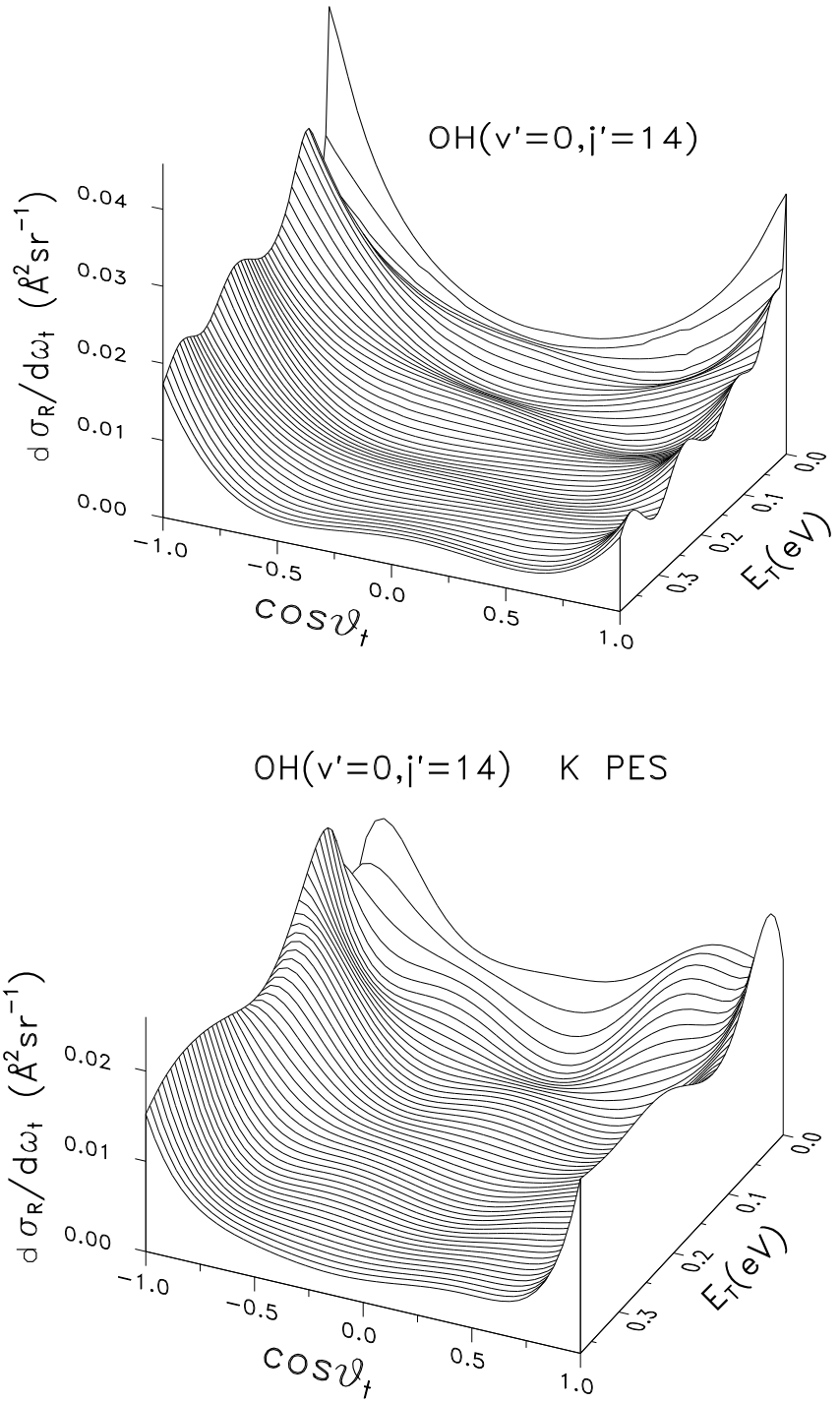

Figure 5.11 QCT collision energy dependence of the differential cross section for OH($v' = 0, j' = 14$) products calculated on the SL1MS (top) and K surfaces (bottom). The range of collision energies sampled was 0.01–0.4 eV and the reagent H_2 was sampled from a thermal (300 K) rotational distribution [5].

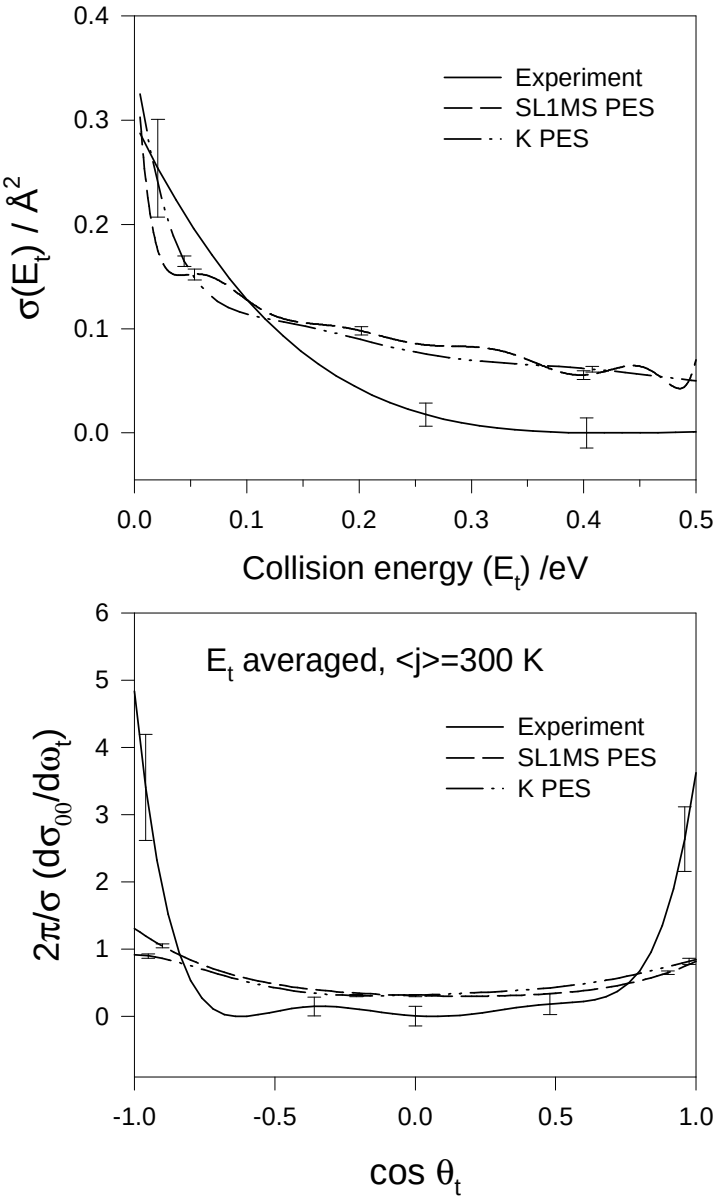

Figure 5.12 Comparison between experimental and quasiclassical state specific energy dependent reaction cross sections (top panel) and angular distributions (bottom panel) for OH($v' = 0, j' = 14$). The experimental data shown is for the A″ lambda doublet. The experimental excitation function has been scaled to agree with the SL1MS results at 0.1 eV. The experimental collisional energy distribution, $P(E_t)$, has been used to calculate the QCT energy averaged angular distributions – see text for details. Error bounds shown are all $\pm 1\sigma$.

The experimental results (figure 5.12) show a relative cross section which decreases with increasing energy, in qualitative agreement with the QCT results and consistent with an absence of any barrier in the entrance channel. The experimental angular distribution is very strongly polarised in backward and forward directions, with a slight preference for backward scattering. Although the relative amounts of backward to forward scattering are qualitatively in good accord with the QCT results, there is a clear discrepancy in the amount of sideways scattering.

5.5 Discussion

Although the dynamics of the reaction under investigation,

$$O(^1D_2) \; + \; H_2 \; (v = 0) \rightarrow \; OH(^2\Pi_{1/2}; v' = 0, N' = 14, f) + H \; , \tag{5.1}$$

have been studied under bulb conditions at 300 K, the experiments have been conducted under near state–to–state conditions: since the population of H_2 in levels $v > 0$ is negligible, and because of nuclear spin statistics, the rotational state population follows the ordering $(j = 1) \; > \; (j = 2) \; > \; (j = 0) \; \gg \; (j > 2)$. The translational exoergicity is quite large (138 kJ mol^{-1}), although the collision energies are small (12 ± 7 kJ mol^{-1}) due to the light H_2 target.

In principle, collisions between $O(^1D_2)$ and H_2 could access five different surfaces, the lowest of which is deeply bound and highly anisotropic, correlating with the ground ($\tilde{X}^1A'$) electronic state of H_2O. In contrast, the excited state surfaces, which would correspond in a linear configuration, to $^1\Pi$ and $^1\Delta$ states, are expected to display entrance channel barriers, with the $^1\Delta$ being strongly repulsive [16, 2].

Figure (5.13) shows the SL1MS PES for the $O(^1D_2)/H_2$ system, plotted in the same way

as the corresponding ground state *ab initio* PES for $O(^1D_2)/CH_4$ of Koda *et al.* [17]. The similarity between the two surfaces is striking. Each presents a deep well centred at the equilibrium geometry, corresponding to H_2O and CH_3OH. The detailed contours around the central well are remarkably alike, including the "humps" in the entrance and exit regions which are remnants of the conical intersections between the linear $^1\Sigma$ and $^1\Pi$ electronic states. Although the dynamics of the reaction,

$$O(^1D_2) \; + \; CH_4 \rightarrow \; OH \; + \; CH_3, \tag{5.2}$$

will undoubtedly be influenced by the polyatomic nature of the coproduct, the similarities in the two surfaces suggest that the two reactions may bear some dynamical resemblances. In each case the absence of exit barriers and the exoergicity of the reactions will limit the lifetime of the the collision intermediate, despite the deep potential energy well.

The favourable kinematics of the $O(^1D_2)/CH_4$ system [13] allow the angular distribution of excited $OH(v' = 4)$ products to be determined with a greater confidence than would be possible for $O(^1D_2)/H_2$. Experimental scattering maps for $OH(v' = 0, N' = 5)$ and $OH(v' = 4, N' = 8)$ from the reaction of $O(^1D_2)$ with CH_4 are shown in figure (5.14). These may be compared with corresponding maps generated from the QCT results of the $O(^1D_2)/H_2$ reaction using the SL1MS surface (figure 5.15). The similarities are remarkable. The two scattering maps for $OH(v' = 0)$ each display a sharp backward peak and a weak forward peak; those for $OH(v' = 4)$ approach forward–backward symmetry. For these particular product channels, the $\boldsymbol{k}$,$\boldsymbol{k'}$ vector correlations appear to be almost identical for the two reactions. The scalar distributions in the strongly exoergic channels leading to $OH(v' = 0)$ are very different, however, since the kinetic energy released to the $OH(v' = 0, N' = 5)$ from the reaction of $O(^1D_2)$ with CH_4 is low: most of the exoergicity appears as internal excitation in the (unobserved) polyatomic CH_3 fragment, implying considerable IVR within

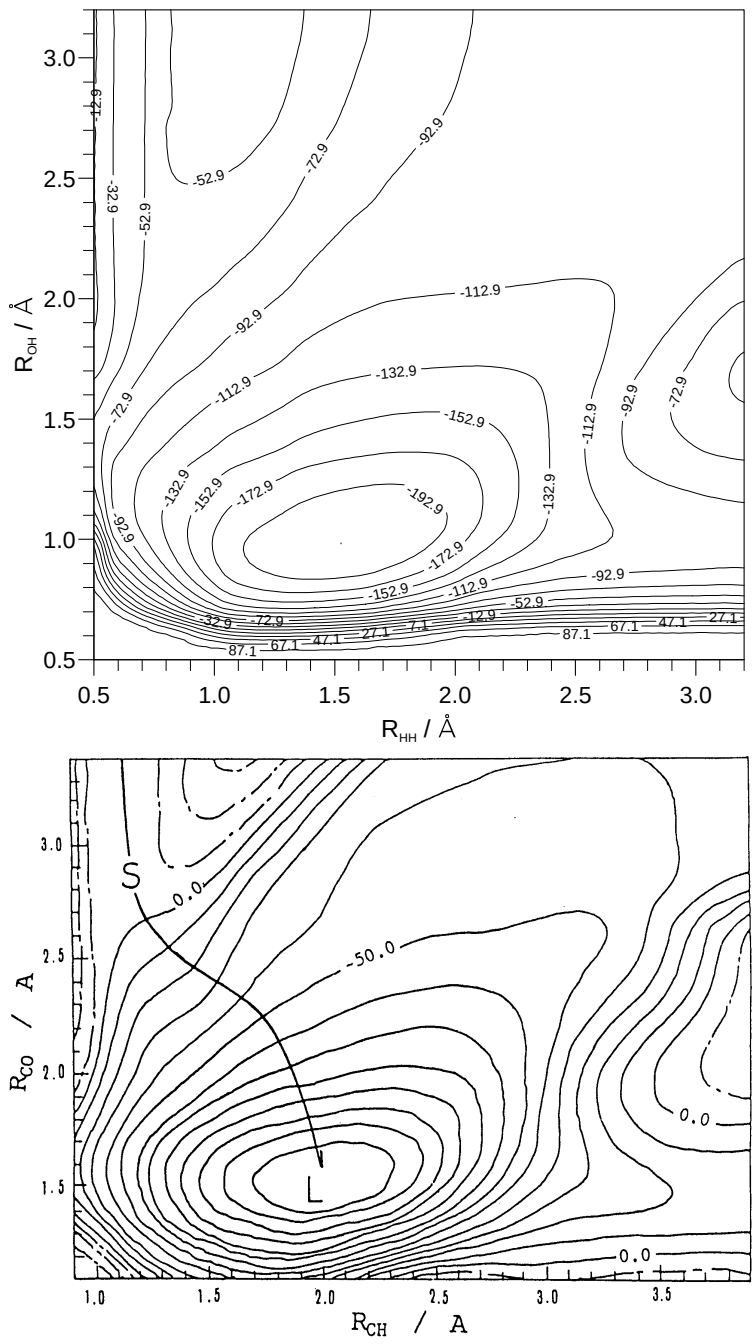

Figure 5.13 Contour plot of the ground state Schinke–Lester (SL1MS) PES for the reaction $O(^1D_2)$ + H_2 reaction (top), and of the Koda PES for the $O(^1D_2)$ + CH_4 reaction (bottom) (figure 5 of ref. [17]). The surfaces are plotted as functions of the OH (CO) and HH (CH) bond lengths, the remaining OH bond length has been optimised to minimise the energy. The contours are labelled in kcal mol^{-1} (1 kcal $mol^{-1} \equiv 4.184$ kJ mol^{-1}).

a (CH_3OH) complex [18].

The state–resolved DCS displayed in figure (5.14) were interpreted in terms of different state–resolved opacity functions for $OH(v' = 0)$ and $OH(v' = 4)$, with the former peaked at low impact parameters and leading to collision complexes with rotational periods $\langle \tau_r \rangle \leq 2$ ps [18]. Stevenson and van Zee made a "real–time" experimental measurement of the rate of decomposition of the (CH_3OH) complex into the $OH(v' = 0, N')$ channels *via* photodissociation of an $O_3 \cdots CH_4$ van der Waals complex and using ultrafast laser pulses [19]. They determined a complex lifetime $\langle \tau_d \rangle \simeq 3$ ps. The QCT estimates of the mean lifetime of the (H_2O) complex show much shorter lifetimes, in the range $\langle \tau_d \rangle \sim 30 - 100$ fs. The real–time and rotational "clocks" used to analyse the results for $O(^1D_2)/CH_4$ suggest time scales an order of magnitude longer in duration [18] – time enough for extensive IVR – associated, no doubt, with the increased moment of inertia and the polyatomic nature of the collision complex. Nevertheless, the remarkable similarity between the two sets of scattering data (figures 5.14 and 5.15) suggests that the *relative* timescales, $\langle \tau_d \rangle$ / $\langle \tau_r \rangle$, in the two channels $v' = 0$ and $v' = 4$, are little changed when CH_4 is substituted for H_2. For OH scattered into the higher vibrational levels, $\langle \tau_d \rangle \sim \langle \tau_r \rangle$, and the DCS displays strong forward and backward peaks. OH produced in the lower quantum states ($v' = 0$, low j'), $\langle \tau_d \rangle < \langle \tau_r \rangle$, and the fragments are scattered predominantly into the backward hemisphere, resulting perhaps from predominantly low impact parameter collisions (see figure 5.6).

5.6 Conclusions and Future work

Extensive QCT calculations for the reaction of $O(^1D_2)$ + H_2 using two *ab initio* ground state potential energy surfaces have been presented. Experimental measurements of the product linear momentum distribution have been carried out for the reaction using Doppler resolved LIF probing of $OH(v' = 0, N' = 14)$ fragments.

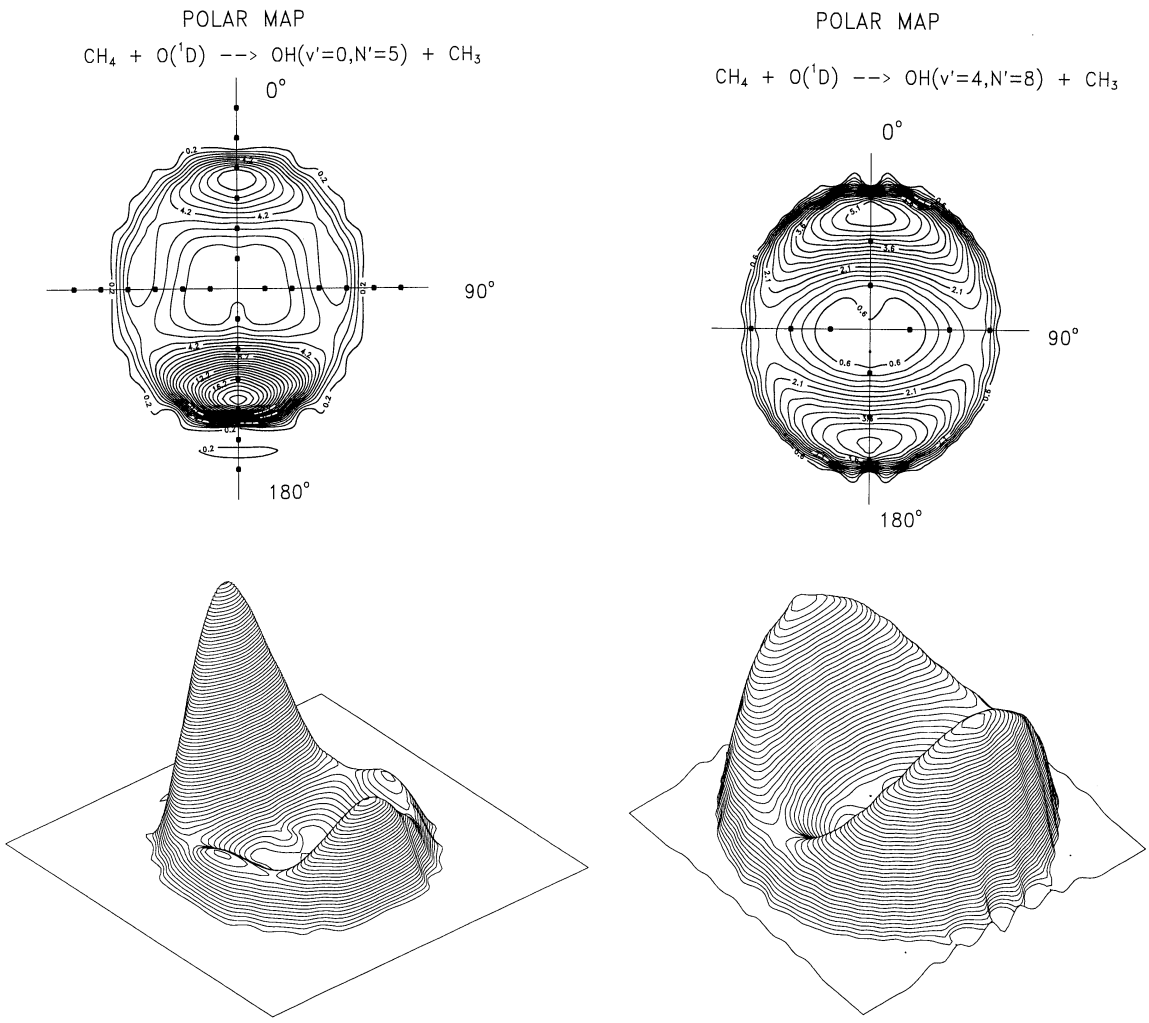

Figure 5.14 Experimentally derived, velocity–scattering angle polar maps for the reaction $O(^1D_2) + CH_4$ [13, 5]. Product state $OH(v' = 0, N' = 5)$ is shown on the left, $OH(v' = 4, N' = 8)$ is shown on the right. Forward scattering (0°) corresponds to the direction of the scattered OH with respect to the direction of the incoming atom.

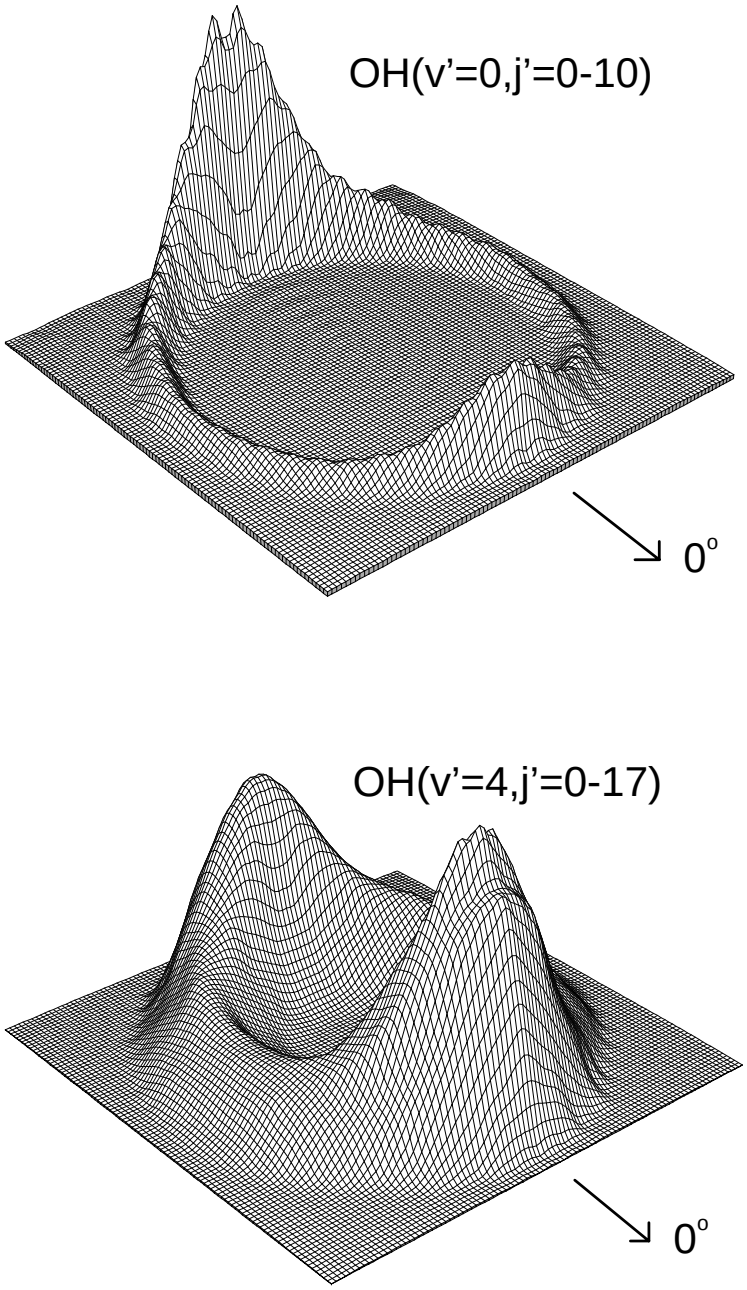

Figure 5.15 As in figure (4.4), but showing quasiclassical velocity–angular scattering maps for OH products from the reaction of $O(^1D_2)$ with H_2 on the SL1MS PES. Forward scattering (0°) corresponds to the direction of the scattered OH with respect to the direction of the incoming atom. Top panel: $OH(v' = 0, j' = 0 - 10)$, bottom panel: $OH(v' = 4, j' = 0 - 17)$.

The results visibly demonstrate the importance of *state–resolved* experiments coupled with detailed scattering calculations in probing and interpreting the dynamics of bimolecular reactions. The product state–resolved differential cross sections for the insertion reaction of $O(^1D_2)$ with H_2 are highly sensitive to the product quantum state; the near symmetry of the state averaged DCS for the reaction of $O(^1D_2)$ with H_2 belies its underlying complexity.

The experimental results for the presented here, along with those of previous studies of the $O(^1D_2)/H_2$ reaction [20, 5, 9] are quite well reproduced by the QCT calculations assuming reaction over the ground state ($1^1A'$) potential energy surface (see also chapter 6). The results are consistent with preferential reaction of $O(^1D_2)$ atoms with $|m_J| = 0$ in the molecular frame, *i.e.*, the component oriented with its empty p–orbital lobe directed toward the molecular reagent to access directly the highly attractive $^1A'$ PES: the reaction dynamics do not appear to be influenced by the production of atoms with $|m_J| \neq 0$ [21] (referenced to their recoil velocity) – (see section 3.2). This could be ascribed to their reorientation during collision or to their inelastic scattering from excited $^1\Pi$ or $^1\Delta$ surfaces.

Experiments similar to the one presented here are presently underway to measure the reaction of $O(^1D_2)$ with H_2 probing fragments in $OH(v' = 4, N' = 1)$ [22]. Simulations indicate that it may be possible to extract the product angular distribution despite the "unfriendly" kinematics. This will, hopefully, help to identify the role of excited state surfaces, since recent QCT calculations using a newly developed *ab initio* ($1^1A''$) surface indicate a preferential population of the $v' = 4$ channel, with a strongly backward scattered DCS [23]. The reaction of $O(^1D_2)$ with HD is also being studied, probing fragments in $OH(v' = 0, N' = 11)$ [24]. The QCT calculations predict predominantly *forward* scattering for this channel, in strong contrast to the *backward* scattering for similar product channels in $O(^1D_2)/H_2$. This may prove to be a fundamental test of the surface and the calculations.

References

[1] R. Schinke and W. A. Lester Jr., *J. Chem. Phys.*, **72** (1980) 3754.

[2] T-. S. Ho, T. Hollebeek, H. Rabitz, L. B. Harding and G. C. Schatz, *J. Chem. Phys.*, **105** (1996) 10472.

[3] F. J. Aoiz, L. Bañares, T. Díez–Rojo and V. J. Herrero, V. Saez Rábanos, *J. Phys. Chem.*, **100** 4071.

[4] F. J. Aoiz, L. Bañares, *J. Phys. Chem.*, **100** 18108.

[5] A. J. Alexander, F. J. Aoiz, L. Bañares, M. Brouard, J. Short and J. P. Simons, *J. Phys. Chem. A*, **101** (1997) 7544.

[6] S. Koppe, T. Laurent, P. D. Naik, H.-R. Volpp, J. Wolfrum, T. Arusi-Parpar, I. Bar and S. Rosenwaks, *Chem. Phys. Lett.*, **214** (1993) 546.

[7] W. B. DeMore, S. P. Sander, D. M. Sander, D. M. Golden, R. F. Hampson, M. J. Kurylo, C. J. Howard, A. R. Ravishankara, C. E. Kolb and M. J. Molina, *Chemical kinetics and photochemical data for use in stratospheric modeling*, JPL publication 94–26 (Jet Propulsion Laboratory, 1994).

[8] A. J. Alexander, F. J. Aoiz, M. Brouard and J. P. Simons, *unpublished results.*

[9] M. Alagia, N. Balucani, L. Cartechini, P. Casavecchia, E. H. van Kleef, G. G. Volpi, P. J. Kuntz and J. J. Sloan, *J. Chem. Phys.*, *submitted.*

[10] R. D. Levine and R. B. Bernstein, *Molecular Reaction Dynamics and Chemical Reactivity*, Oxford University Press, 1987.

[11] S. K. Kim and D. R. Herschbach, *Faraday Discuss. Chem. Soc.* **84** (1987) 159.

[12] J. Short, *D. Phil. Thesis*, University of Oxford, 1997.

[13] M. Brouard, H. M. Lambert, J. Short and J. P. Simons, *J. Phys. Chem.*, **99** (1995) 13571.

[14] S. P. Rayner, *D. Phil. Thesis*, University of Oxford, 1997.

[15] M. Brouard, H. M. Lambert, S. P. Rayner and J. P. Simons, *Mol. Phys.*, **89** (1996) 403.

[16] S. P. Walch and L. B. Harding, *J. Chem. Phys.*, **88** (1988) 7653.

[17] H. Arai, S. Kato, S. Koda, *J. Phys. Chem.*, **98** (1994) 12.

[18] M. Brouard, H. M. Lambert, C. L. Russell, J. Short and J. P. Simons, *Faraday Discuss. Chem. Soc.*, **102** (1995) 179.

[19] R. D. van Zee and J. C. Stevenson, *J. Chem. Phys.*, **102** (1995) 6946.

[20] A. J. Alexander, F. J. Aoiz, M. Brouard, I. Burak, Y. Fujimura, J. Short and J. P. Simons, *Chem. Phys. Lett.*, **262** (1996) 589.

[21] J. M. Teule, *Ph. D. Thesis*, Vrije Universiteit, Netherlands, 1997.

[22] A. J. Alexander, F. J. Aoiz, L. Bañares, D. Blunt, M. Brouard, Y. Fujimura, M. Tsubouchi and J. P. Simons, *in progress.*

[23] G. C. Schatz, A. Papaioannou, L. A. Pederson, L. B. Harding, T. Hollebeek, T. -S. Ho, and H. Rabitz, *J. Chem. Phys.*, **107** (1997) 2340.

[24] D. A. Blunt, M. Brouard and J. P. Simons, *in progress.*

Chapter 6 $O(^1D_2) + H_2$: Product state–resolved polarisation

6.1 Introduction

In this chapter the product state resolved polarisation in the reaction of $O(^1D_2)$ + H_2 is discussed. Experimental estimates of the scattering angle ($\cos\theta_t$) dependent rotational alignment in the centre of mass frame for product OH in ($v' = 0, N' = 14, f$) are presented and the results are discussed by reference to QCT calculations on the ground state ($1^1A'$) SL1MS and K potential energy surfaces.

6.2 Experimental and quasiclassical rotational alignment

The laboratory (LAB) frame alignment parameters, $\langle A_0^{(2)} \rangle$ for the two Λ–doublet levels of OH($v' = 0, N' = 14$) are given in table (6.1). The result for the A′ level is opposite in sign to the alignment for the A″ level, and this is reflected in the CM frame alignment, as will be shown below.

Composite Doppler profiles, $D_0^2(0, 2; v)$, $D_0^0(2, 2; v)$, $D_0^2(2, 2; v)$, which are sensitive to the LAB frame rotational alignment, are shown for OH($v' = 0, N' = 14$) in the Π(A″) Λ–doublet level in figure (6.1). The corresponding plots for the Π(A′) level are shown in figure (6.2). The fits obtained following the procedures outlined in section (3.8) are shown as solid lines. The derived PDDCS, which reflect the variation in the CM rotational polarisation with scattering angle are shown in figures (6.3) and (6.4) and the experimental state–resolved polarisation parameters, obtained by integrating the PDDCS over $\cos\theta_t$, are given in table (6.2), along with the QCT results (see later). The coefficients for the expansion of the

Level	LAB frame alignment $\langle A_0^{(2)} \rangle$
A″	$+0.023 \pm 0.015$
A′	-0.028 ± 0.012

Table 6.1 Experimental laboratory (LAB) frame alignment parameters for OH($v' = 0, N' = 14$,A″/A′).

renormalised PDDCS in modified spherical harmonics, $m^{k'}_{k_2 q\pm}$, are given in table (6.2). Nine coefficients were determined for the A′ data and only the six lowest order coefficients were required to fit the A″ data.

Despite the somewhat lower signal–to–noise in the composite profiles, compared to those of chapter 5, it was found that the general structure of the returned PDDCS were quite robust. The overall magnitude of the PDDCS was sensitive to the value of $\overline{\beta}$ employed; use of a velocity–dependent $\beta(v_O)$ tending to low values at low atom speeds [1] was found to improve the fits, particularly to the $D^2_0(0, 2; v)$ and $D^2_0(2, 2; v)$ profiles which explicitly involve β. The polarisation parameters returned by such an analysis were not significantly changed from those in table (6.2), however.

As can be seen from figures (6.3) and (6.4), the composite profiles for the A′ and A″ levels differ in sign, as do the polarisation parameters (table 6.2), in good agreement with results from a previous study of $O(^1D_2) + H_2 \rightarrow OH(v' = 0, N' = 5, f) + H$ [2], and with results of studies on $O(^1D_2)/CH_4$ [3, 4] and $H(^2S)/O_2$ [5]. Kim et al. found that a strong rotational alignment of the A′ OH products were required to fit their data. In contrast, a recent state resolved study of $H + CO_2$ probing $OH(v' = 0, N' = 5, f)$ products showed strong alignment of the A″ product [6, 7]. The present data indicate a marginally stronger alignment of the A′ products.

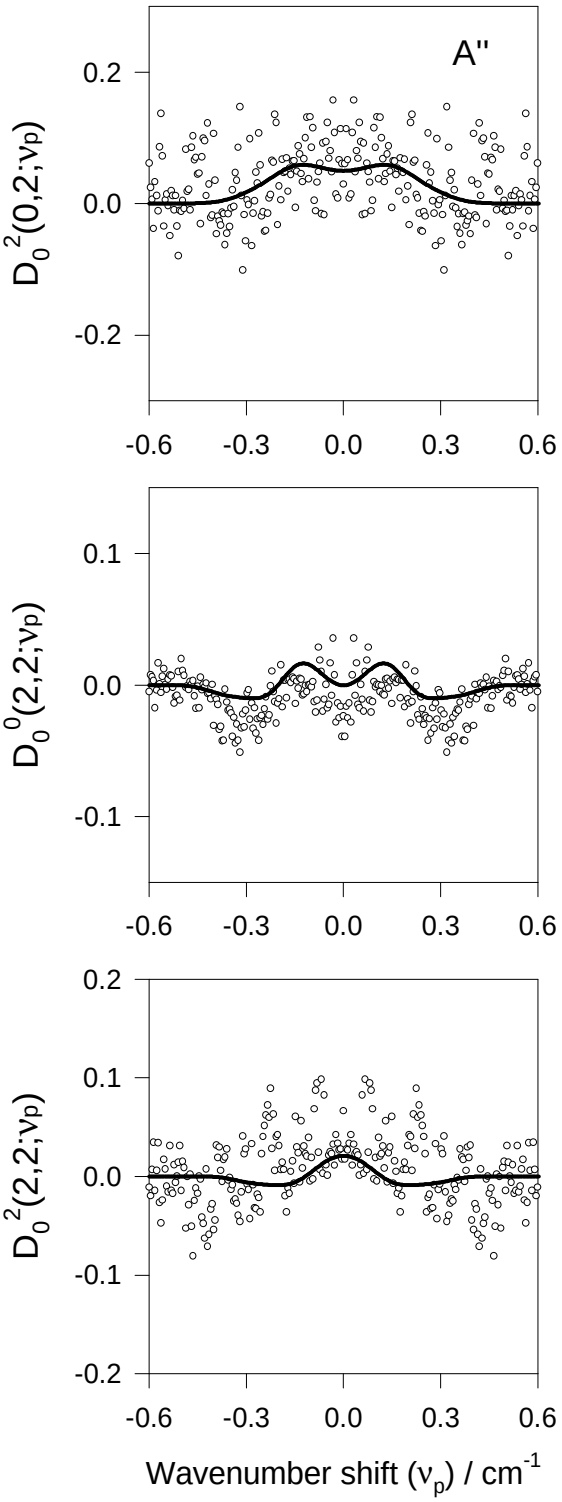

Figure 6.1 Experimental composite profiles $D_0^2(0,2;v)$ (top panel), $D_0^0(2,2;v)$ (middle panel) and $D_0^2(2,2;v)$ (lower panel) for the $\Pi(A'')$ Λ–doublet level of $OH(v'=0, N'=14)$ from the reaction of $O(^1D_2)$ with H_2. The experimental data are shown as points and the solid lines are fits to the data – see text for details. The derived PDDCS are shown in figure (6.3).

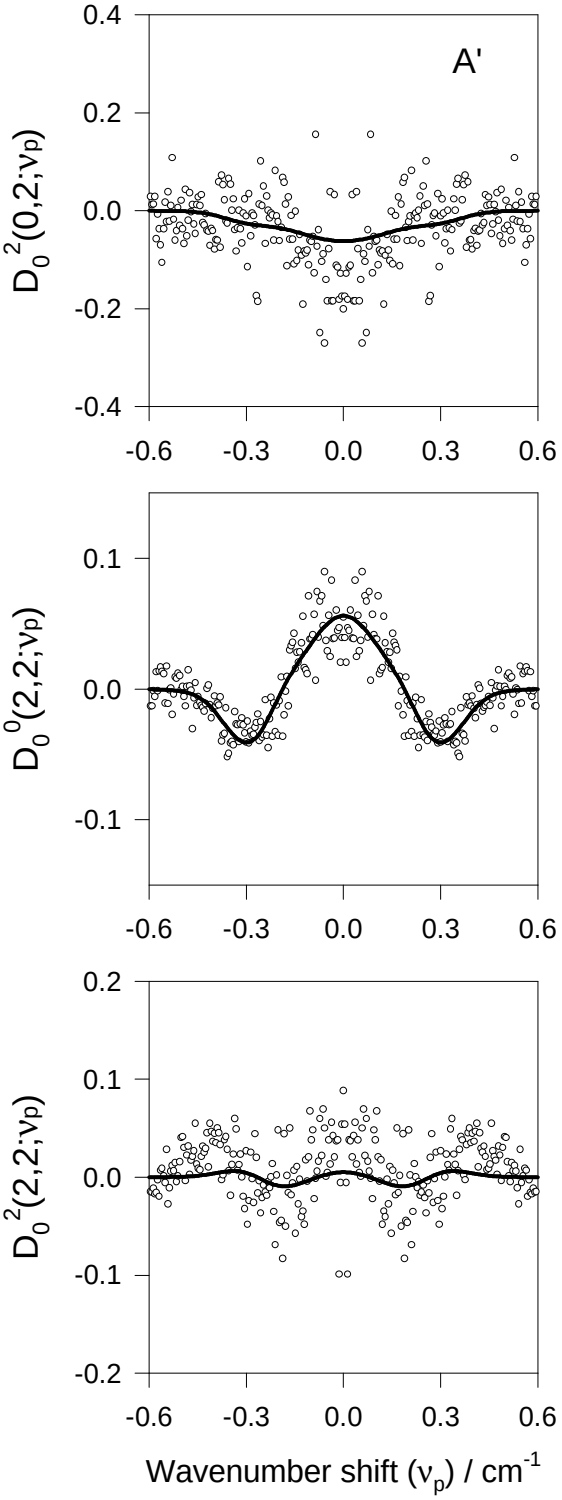

Figure 6.2 As for figure (6.1) but for the OH $\Pi(A')$ Λ–doublet level. The derived PDDCS are shown in figure (6.4).

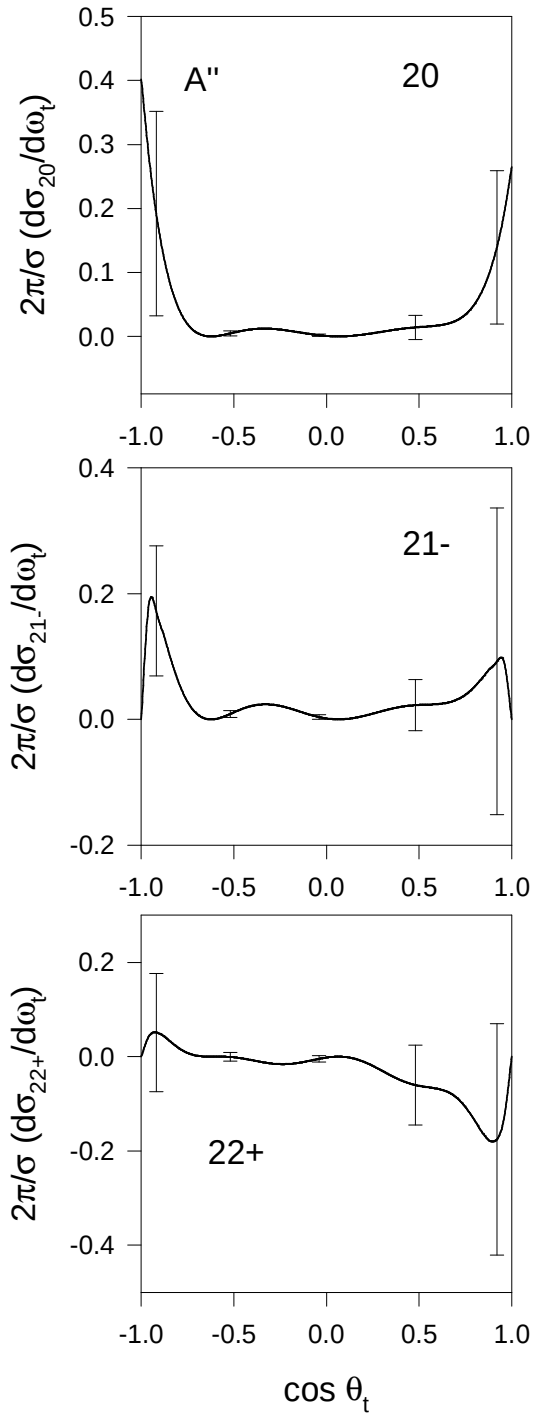

Figure 6.3 Three PDDCS $\frac{2\pi}{\sigma}\frac{\mathrm{d}\sigma_{20}}{\mathrm{d}\omega_t}$ (top panel), $\frac{2\pi}{\sigma}\frac{\mathrm{d}\sigma_{21-}}{\mathrm{d}\omega_t}$ (middle panel) and $\frac{2\pi}{\sigma}\frac{\mathrm{d}\sigma_{22+}}{\mathrm{d}\omega_t}$ (bottom panel) derived from the data for the $\Pi(\mathrm{A}'')$ Λ–doublet level of $\mathrm{OH}(v'=0, N'=14)$ shown in figure (6.1). The error bars represent two standard deviations ($\pm 2\sigma$).

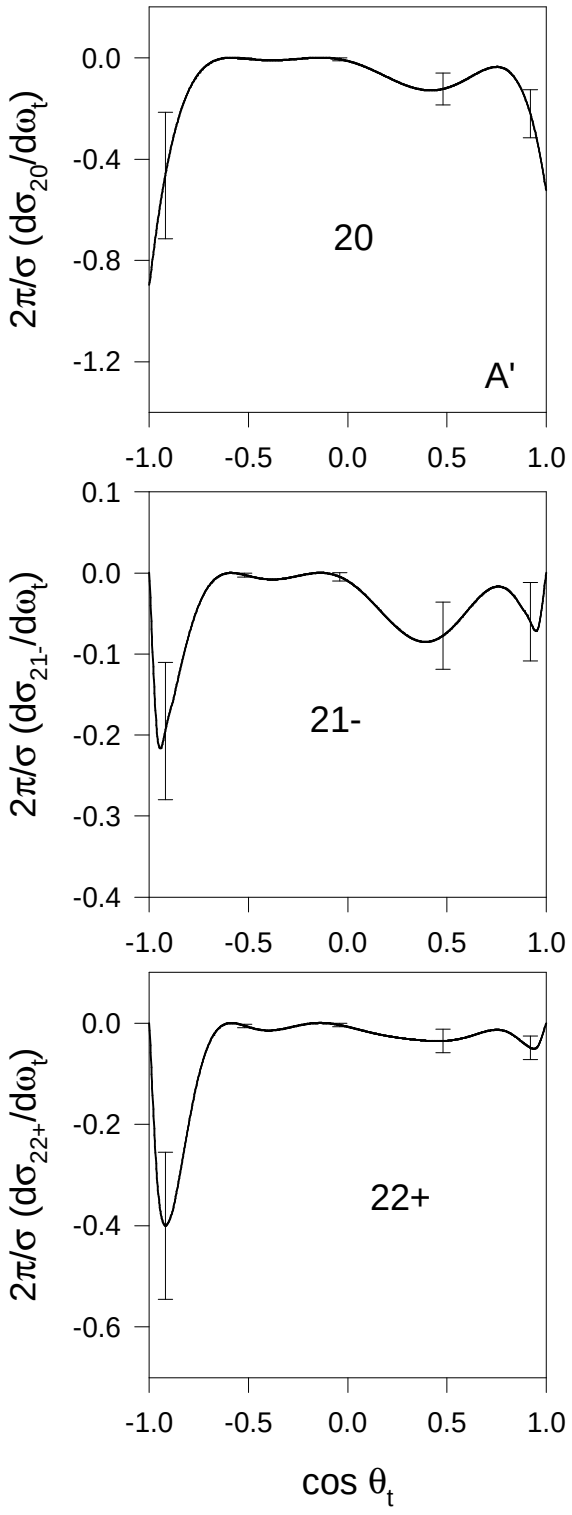

Figure 6.4 As for figure (6.3) but for the OH Π(A′) Λ–doublet level. The experimental data are shown in figure (6.2). Error bars represent two standard deviations ($\pm 2\sigma$).

OH state	a_0^2	a_{1-}^2	a_{2+}^2
		Experimental	
$N' = 14, \Pi(A'')$	$+0.18 \pm 0.01$	0.13 ± 0.01	-0.12 ± 0.02
$N' = 14, \Pi(A')$	-0.45 ± 0.10	-0.17 ± 0.01	-0.19 ± 0.01
		Theoretical	
$j' = 14$, SL1MS surface	-0.120 ± 0.003	-0.086 ± 0.003	-0.260 ± 0.006
$j' = 14$, K surface	-0.080 ± 0.003	$+0.021 \pm 0.004$	-0.290 ± 0.005

Table 6.2 State resolved, experimental and QCT calculated polarisation parameters with $k = 2$ for the $OH(v' = 0, N' = 14, f)$ products from the reaction of $O(^1D_2)$ with H_2. The uncertainties in the experimental data represent two standard deviations (2σ) and the QCT error bounds are single standard deviations (1σ).

The QCT calculated PDDCS for both the SL1MS and K surfaces are shown in figure (6.5), and the corresponding alignment parameters $a_{q\pm}^k$ are given in table (6.2). The results for the two surfaces are very similar. The $a_{q\pm}^k$ are somewhat smaller than the experimental results and are more similar to the experimental A' results; the QCT can not distinguish Λ–doublets.

The results for the experimental A' and the QCT derived PDDCS 20 indicate strong alignment for extreme forward and backward scattering, which corresponds to the limit of $\boldsymbol{j'}$ perpendicular to $\boldsymbol{k}$ as required by angular momentum conservation in the limit of $j = 0$ in H_2. The PDDCS 20 becomes nearly isotropic, however, for sideways scattering. Inspection of the PDDCS 22+, which is negative for all scattering angles, reveals a noticeable preference for an alignment of $\boldsymbol{j'}$ along the CM y axis as opposed to the x axis.

A more convenient way of visualising the angular momentum polarisation is in the form of

$m^{k'}_{k_2q\pm}$	A″	A′
m^0_{20}	0.16 ± 0.01	-0.45 ± 0.11
m^1_{20}	-0.44 ± 0.11	0.52 ± 0.12
m^2_{20}	—	-0.75 ± 0.13
m^1_{21-}	-0.75 ± 0.62	-0.014 ± 0.001
m^2_{21-}	0.010 ± 0.002	-0.053 ± 0.031
m^3_{21-}	—	0.59 ± 0.09
m^2_{22+}	0.058 ± 0.048	0.091 ± 0.010
m^3_{22+}	-0.59 ± 0.37	-0.026 ± 0.017
m^4_{22+}	—	-0.44 ± 0.05

Table 6.3 OH($v' = 0, N' = 14, f$) experimentally determined $m^{k'}_{k_2q\pm}$ coefficients for the expansion of the renormalised PDDCS in spherical harmonics: see equation (3.46). Coefficients are given for both A″ and A′ lambda doublets. The uncertainties are quoted as $\pm 2\sigma$.

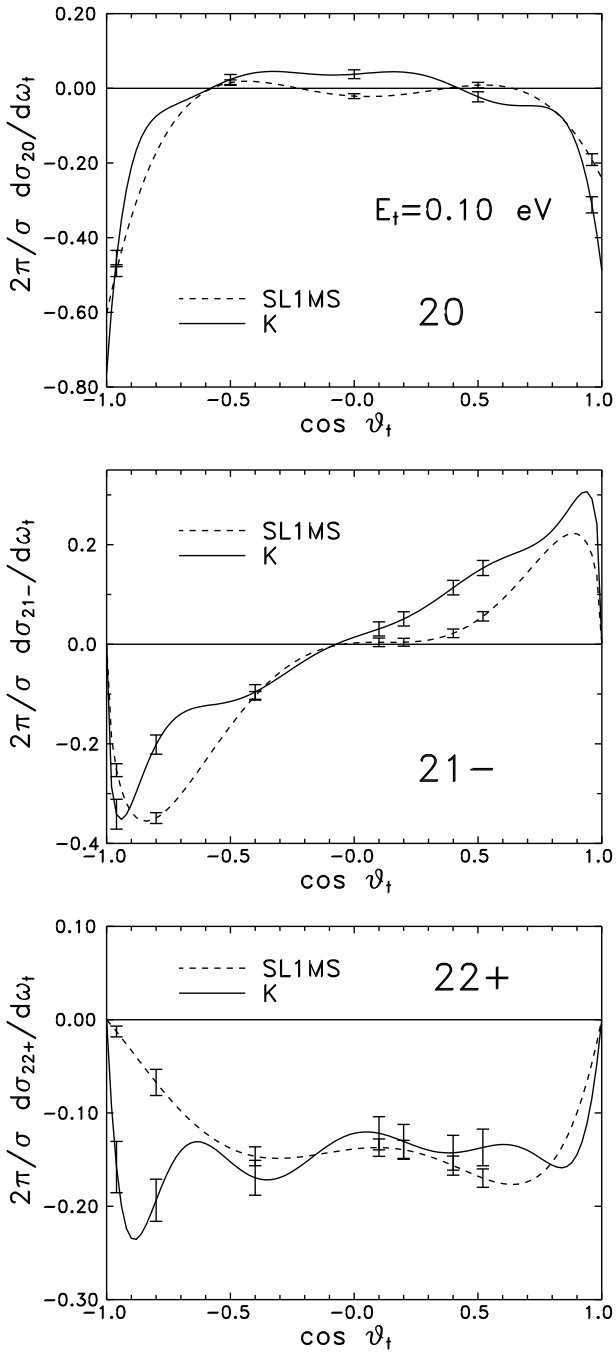

Figure 6.5 OH($v' = 0, j' = 14$) QCT derived PDDCS 20 (top panel), 21− (middle panel) and 22+ (bottom panel). Error bars represent one standard deviation. The calculations were performed at a fixed collision energy of 0.1 eV on the SL1MS and K surfaces.

a polar plot, displaying the probability of finding the angular momentum vector at angles (θ_r, ϕ_r) with respect to the CM (xz) scattering plane. These are obtained by employing the $a^k_{q\pm}$ parameters which are simply the coefficients of the total (summed over all $\cos\theta_t$) rotational differential cross section, expanded in terms of modified spherical harmonic functions (equation 2.47 repeated here):

$$\begin{aligned}\frac{1}{\sigma}\frac{\mathrm{d}\sigma}{\mathrm{d}\omega_r} &= \frac{1}{4\pi}\sum_k\sum_q\ [k]\, a^k_q\, C_{kq}(\theta_r,\phi_r)^* \\ &= \sum_k\sum_{q\geq 0}\ [k]\,[a^k_{q\pm}\cos q\phi_r\ -\ ia^k_{q\mp}\sin q\phi_r]\, C_{kq}(\theta_r,0)\end{aligned}$$

The reconstruction of the probability distribution from the present experimental data is necessarily incomplete, however, since the latter are restricted to the first two even k moments of the expansion ($k = 0, 2$). Figure (6.6) displays the experimentally derived rotational polar distributions for the A″ and A′ Λ–doublet levels, which may be compared with those predicted *via* QCT calculation and employing even moments with $k \leq 2$ only, shown in figure (6.7).

Both the experimental data for the A′ level and the QCT results display a preferential alignment along the CM frame y axis (*i.e.*, perpendicular to the scattering plane): for the A″ level the experimentally derived alignment is, in contrast, preferentially in the xz scattering plane. A more subtle feature of these plots however, is the tilting of the angular momentum alignment in the CM xz plane. Although not particularly clear from the 3D plots, the experimental A″ and QCT (SL1MS) alignment is tilted towards the positive x axis, the QCT (K) alignment is tilted towards the $-x$ axis. This is a result of the different signs in the a^2_{1-} (see table 6.2) and ultimately the $21-$ PDDCS. Looking at the QCT $21-$ PDDCS we see that they are negative for backward scattering and positive for forward scattering. Integrating this over the range of $\cos\theta_t$ gives an overall positive value for the SL1MS results, and an overall negative value for the K PES results. The origin of this effect might be traced back to a preferential alignment of $\boldsymbol{j'}$ perpendicular to $\boldsymbol{k'}$: the QCT

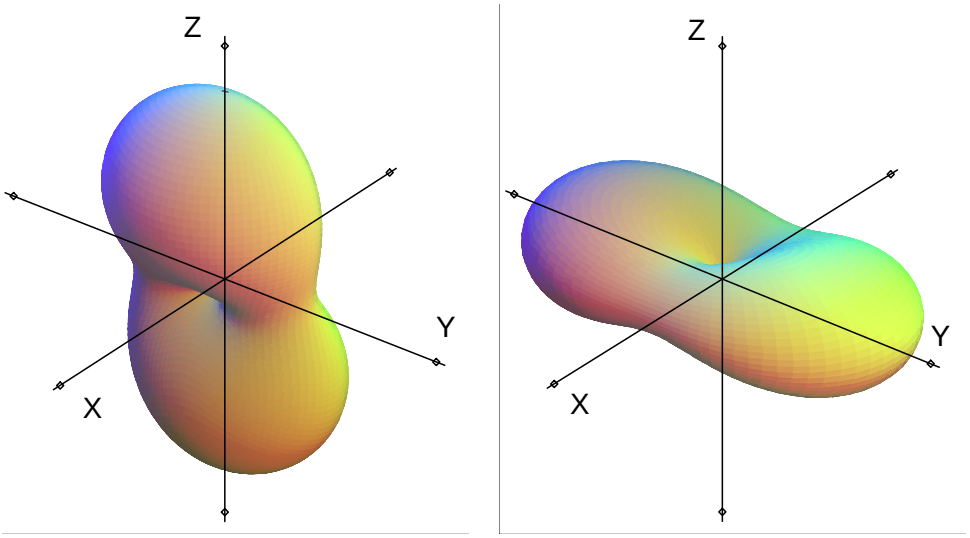

Figure 6.6 Experimentally derived polar plots of the ($\cos\theta_t$ averaged) rotational polarisation, $P(\theta_r, \phi_r)$, for OH($v' = 0, N' = 14, f$). Note that only even moments with $k \leq 2$ are included. Left panel: $\Pi(A'')$ Λ–doublet, right panel: $\Pi(A')$ level.

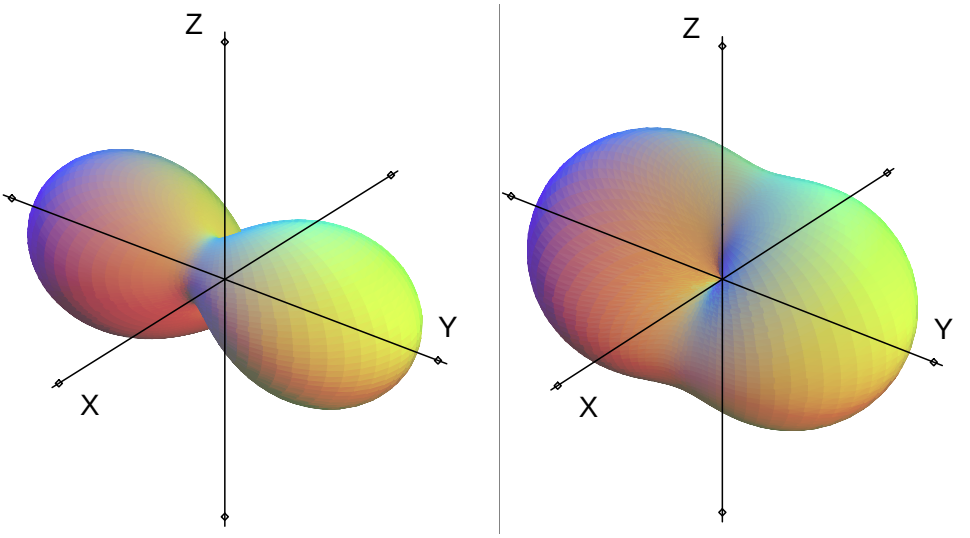

Figure 6.7 As in figure (6.6), but showing the QCT results using the SL1MS (left panel) and K surfaces (right panel) at a fixed collision energy of 0.1 eV. Note that only even moments with $k \leq 2$ are included, .

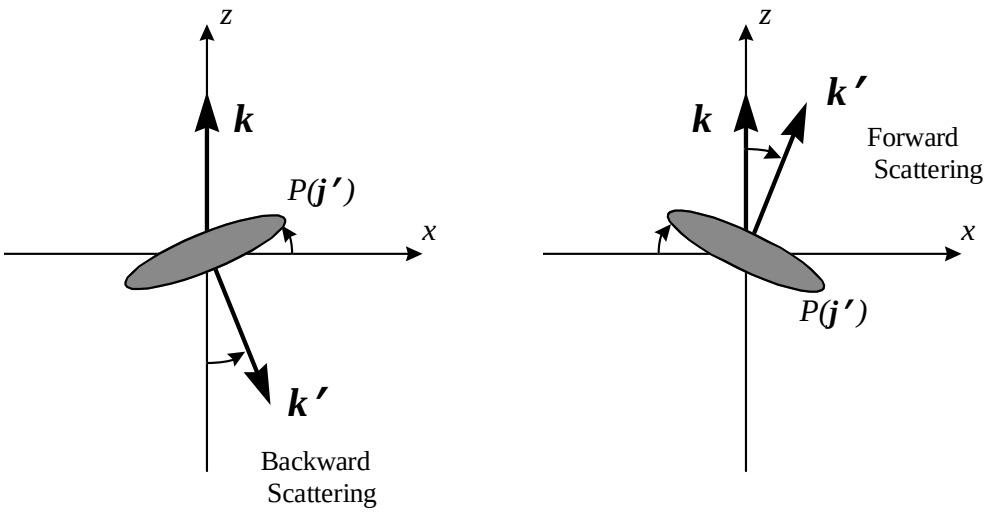

Figure 6.8 Schematic diagram showing the tilting of the CM $\boldsymbol{j'}$ angular distribution in the xz plane following the change in the sign of the PDDCS 21− from negative (backward scattering) to positive (forward scattering).

calculations suggest significantly greater polarisation of $\boldsymbol{k'} \perp \boldsymbol{j'}$ compared with that evident in the $\boldsymbol{k}$–$\boldsymbol{j'}$ correlation, see figure (6.9). For reaction with rotationless reactant molecules, in the limit of extreme backward scattering, corresponding to $\boldsymbol{k'}$ lying along the $-z$ axis, $\boldsymbol{j'}$ must lie in the CM xy plane as a result of angular momentum conservation ($\boldsymbol{l}$ must be perpendicular to z). In reality, the *mean* scattering angle is less than 180°, and on average both $\boldsymbol{k'}$ and $\boldsymbol{j'}$ will be titled away from the $-z$ direction and $\boldsymbol{j'}$ from the $+x$ direction, see figure (6.8). For *forward* scattering, $\boldsymbol{k'}$ and $\boldsymbol{j'}$ will be tilted away from the $+z$ and $-x$ axes respectively, resulting in the positive value for $(\mathrm{d}\sigma_{21-}/\mathrm{d}\omega_t)$.

6.3 Vector pair correlations: k-k', k-j' and k'-j'.

The agreement between the experimental (A′) and the quasi-classical PDDCS in the preceding section is marked, although the experiments are presently limited to measuring only low order even moments of the $\boldsymbol{j'}$ distribution. The quasi-classical method, however, allows a full investigation of the state–resolved vector correlations [8] including all moments of the

classical angular distribution.

Of all of the possible vector correlations, the most familiar are the pair correlations, $\boldsymbol{k}$–$\boldsymbol{k'}$, $\boldsymbol{k}$–$\boldsymbol{j'}$ and $\boldsymbol{k'}$–$\boldsymbol{j'}$ characterised by the angular distributions $P(\theta_t)$, $P(\theta_r)$ and $P(\theta_{tr})$. The first of these is given simply by the differential cross section, as discussed in preceeding chapters, and has been widely used as an indicator of the dynamics of a reaction. We concentrate now on the distributions involving $\boldsymbol{j'}$. The distributions $P(\theta_r)$ and $P(\theta_{tr})$, resolved by OH v', are shown in figure (6.9). To fully characterise the correlation between three vectors, however, we require three angles [9]. The third angle gives the *azimuthal* angular distribution of $\boldsymbol{j'}$ with respect to the $\boldsymbol{k}$–$\boldsymbol{k'}$ plane, $P(\phi_r)$ and this distribution is plotted in figure (6.10).

Of the vector pair distributions, both $P(\theta_r)$ and $P(\theta_{tr})$ are symmetrical about $\theta = 90^\circ$ as required by symmetry considerations (see section 2.4.3). $P(\theta_r)$ appears quite flat, slightly peaking at 90° ($\boldsymbol{j'} \perp \boldsymbol{k}$), and there appears to be very little variation with OH product vibration. $P(\theta_{tr})$ is also peaked at 90° (split in the case of $v' = 0 - 2$) although it becomes increasingly broadened with product vibration indicating a move away from $\boldsymbol{j'} \perp \boldsymbol{k'}$. The most striking of the three distributions, however, is $P(\phi_r)$ which is not only polarised, but *oriented* for OH($v' = 0 - 2$): there is a preference for $\boldsymbol{j'}$ to lie either above or below the scattering plane. This may appear somewhat counter–intuitive at first, but the simultaneous observation of the three vectors results in a breaking of the azimuthal symmetry of the collision event [10]. The orientation is strongest for the $v' = 0$ products, and the distribution appears almost symmetric for $v' = 4$.

Kim and Herschbach have derived limiting forms of the θ_t, θ_r and ϕ_r distributions for a statistical complex in the kinematic limits $\boldsymbol{l} \rightarrow \boldsymbol{j'}$ (case I) and $\boldsymbol{l} \rightarrow \boldsymbol{l'}$ (case II). These are reproduced in figure (6.11). A common feature of these distributions is the symmetry about 90° for the polar distributions and about 180° for the azimuthal distribution. Perhaps the most familiar of these forms is the forward–backward symmetry of the DCS expected in the

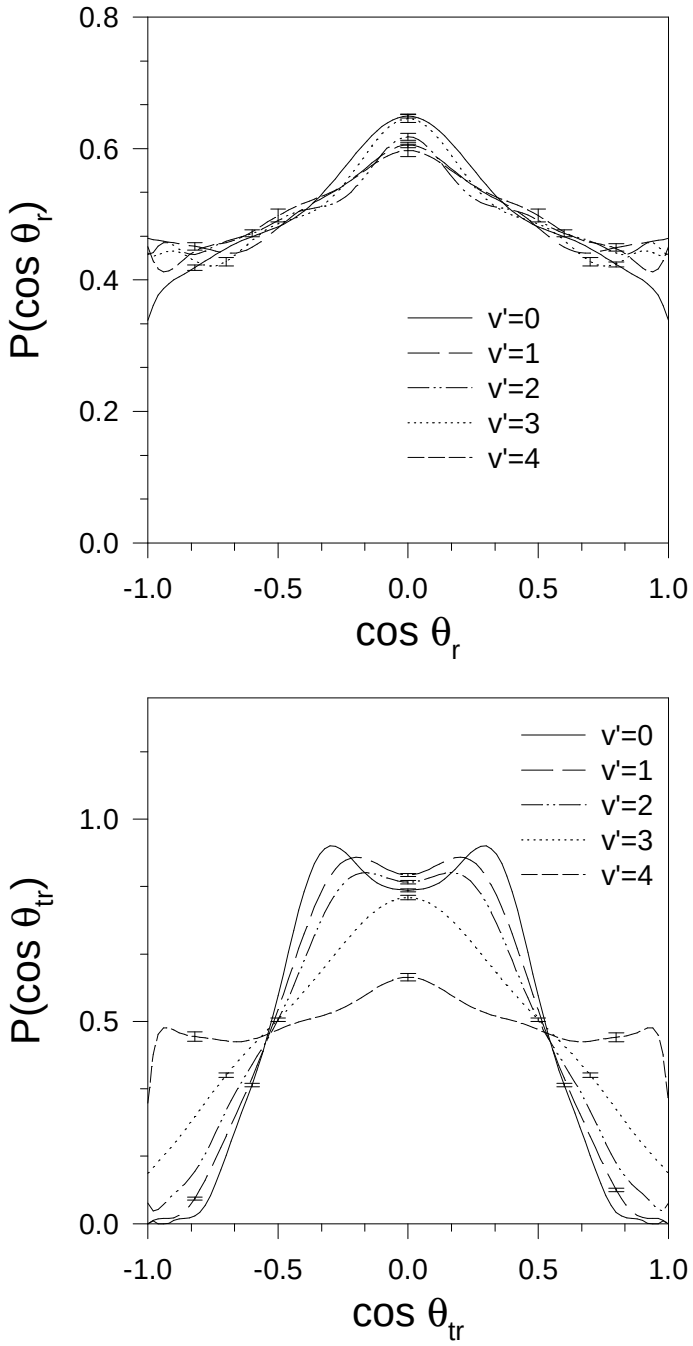

Figure 6.9 OH product vibrationally resolved vector pair angular distributions $P(\theta_r)$ (top panel) and $P(\theta_{tr})$ (bottom panel) reflecting the $\boldsymbol{k}$–$\boldsymbol{j'}$ and $\boldsymbol{k'}$–$\boldsymbol{j'}$ vector correlations respectively. Calculations made using the SL1MS surface. Note that all plots are normalised to unit area, and do not contain information about vibrational cross sections.

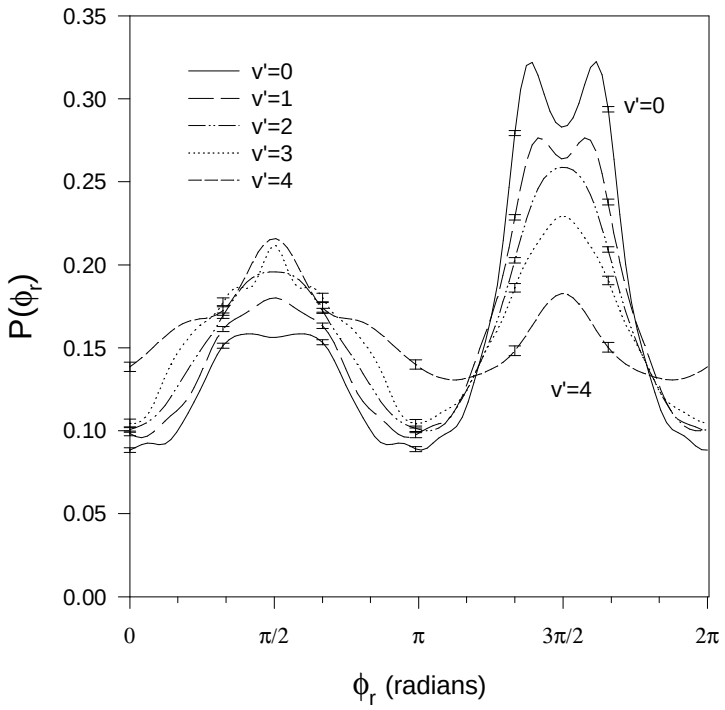

Figure 6.10 OH product vibrationally resolved azimuthal angular distribution of $\boldsymbol{j'}$ vector with respect to the $\boldsymbol{k}$–$\boldsymbol{k'}$ scattering plane (SL1MS PES).

limit of a long–lived complex [10].

It is clear that the present results, both experimental and QCT, do not correlate directly with either of the cases. The form of $P(\theta_t)$ is perhaps closest in form to case II, but the $P(\theta_r)$ results are in better agreement with case I. Neither of the limiting forms of $P(\phi_r)$ match the experimental and quasi-classical dihedral angular distributions which are peaked at 90° and 270°. This is in agreement from the analysis of the DCS alone from which it was inferred that a statistical model was inappropriate for this system.

The limiting forms are closest in structure to the results for OH($v' = 4$) which are *almost* forward–backward in θ_t, peaked at 90° for θ_r and isotropic in ϕ_r. These seem to be somewhat mixed between cases I and II, however. Case and Herschbach quantified the angular momentum of a separable complex in terms of two scalar parameters [12]: $\Lambda = \langle l/(l+j)\rangle$ and $\Lambda' = \langle l'/(l'+j')\rangle$. In the present case, $l \gg j$ and so $\Lambda \to 1$. The product parameter

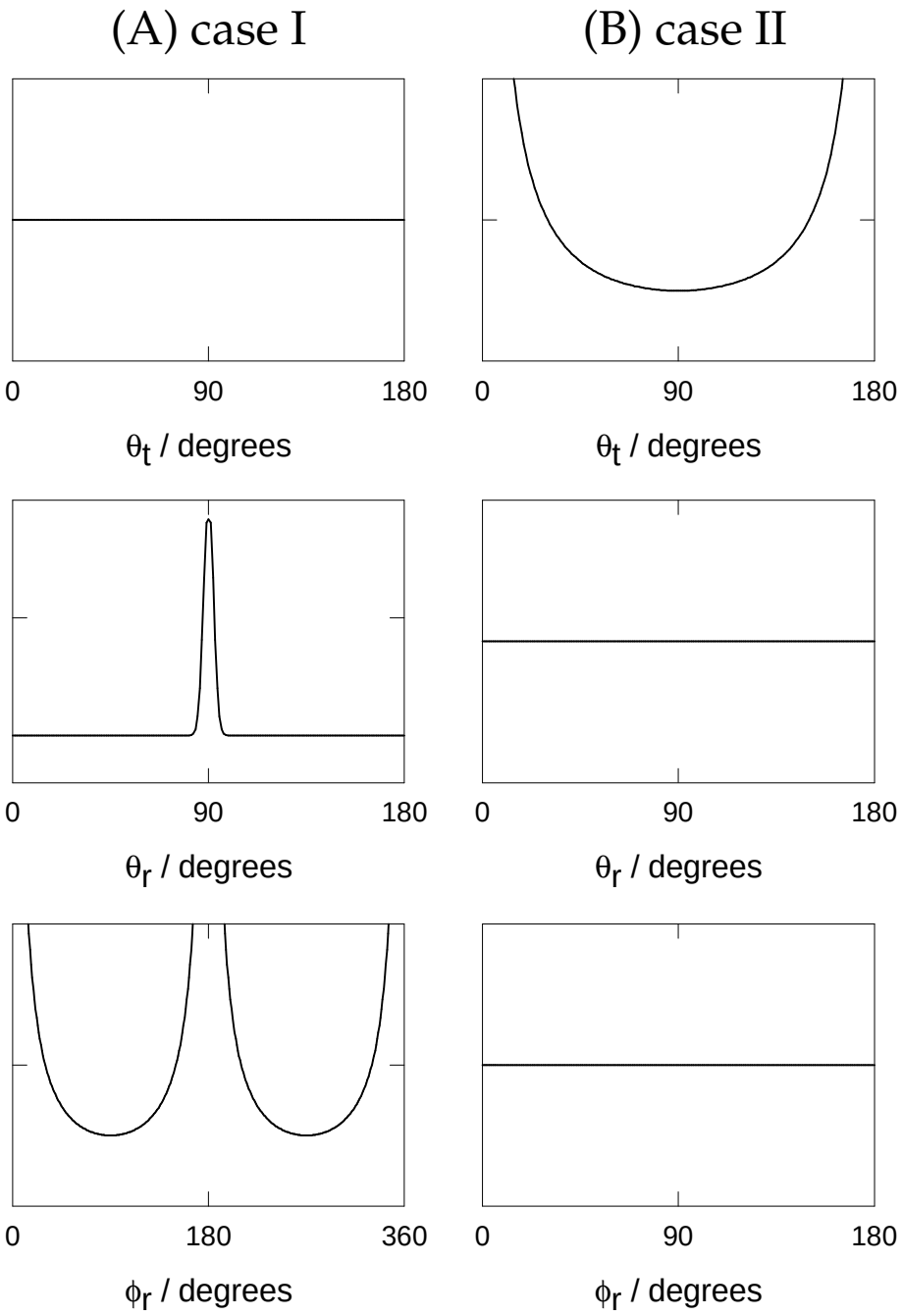

Figure 6.11 Limiting forms of the distributions of θ_t, θ_r and ϕ_r for a statistical complex model as derived by Kim and Herschbach [11]. (A) case I, $\boldsymbol{l} \approx \boldsymbol{J} \approx \boldsymbol{j'}$; (B) case II, $\boldsymbol{l} \approx \boldsymbol{J} \approx \boldsymbol{l'}$.

Product states	$\Lambda' = \langle l'/(l'+j') \rangle$
all v'	0.54
$v' = 0$	0.50
$v' = 2$	0.54
$v' = 4$	0.65
$v' = 0$, $j' = 0 - 10$	0.64
$j' = 11 - 20$	0.53
$j' = 21 - 32$	0.48

Table 6.4 Product angular momentum dominance given by scalar parameter Λ' calculated for the O + H_2 trajectories on the SL1MS surface. Uncertainties (not shown) are less than the last significant figure.

limits are:

$$l' \ll j' \quad \Rightarrow \quad \Lambda' \rightarrow 0 \quad \text{(case I)} \tag{6.1}$$

$$l' \gg j' \quad \Rightarrow \quad \Lambda' \rightarrow 1 \quad \text{(case II)} \tag{6.2}$$

The product parameter Λ' may be quantified from the trajectories and are shown in table (6.4). From this table it can be seen that the reaction is in general not dominated by either $\boldsymbol{l'}$ or $\boldsymbol{j'}$ and it is clear that neither kinematic limit, case I or II, is appropriate. Products in $v' = 4$ show somewhat more statistical behaviour, in accord with the results presented in chapters 4 and 5, although the kinematic case is still not well defined ($\Lambda' = 0.65$).

6.4 Reagent and product angular momentum distributions

In the previous section the most commonly encountered two-vector correlations, $\boldsymbol{k}$–$\boldsymbol{k}$, $\boldsymbol{k}$–$\boldsymbol{j'}$ and $\boldsymbol{k'}$–$\boldsymbol{j'}$, were characterised for the O + H_2 reaction. The present section aims to establish

the link between the vectors $\boldsymbol{l}$, $\boldsymbol{l'}$ and $\boldsymbol{j'}$ and their relative distributions with respect to the $\boldsymbol{k}$–$\boldsymbol{k'}$ scattering plane. In chapter 5 different characteristic behaviour of product *state–resolved* distributions was found, and we continue to use these as examples of behaviour within the O + H_2 reaction, and with particular reference to the product state–resolved experiments.

As has been discussed, the O + H_2 reaction is of the form H + LL $\rightarrow$ HL + L, where the reagent atom is heavy compared to the light target molecule. The rotation of the target molecule may be neglected (see above) and in the preceding chapters it was shown that the reagent orbital angular momentum extends out to large $l \approx J$, where J is the total angular momentum of the system. In the previous section it was shown that the scalar parameter $\Lambda' \sim 0.5$ implying that $l' \sim j'$. Product OH vibrationally resolved orbital angular momentum distributions are shown in figure (6.12) as is the corresponding data for $v' = 0$ resolved by j'. Comparing this figure with the distributions $P(l)$ and $P(j')$, given in chapter 5, we see that the magnitudes of the product orbital angular momenta are of the same order as the other momenta.

Full orbital angular momentum distributions of $\boldsymbol{l}$, $\boldsymbol{l'}$ and $\boldsymbol{j'}$ with respect to the CM ($\boldsymbol{k}$,$\boldsymbol{k'}$) scattering frame are shown for $v' = 0$, low and high j', and $v' = 4$ in figures (6.13) to (6.15) respectively. These plots contain all moments, both odd and even for $k \leq 10$. Inclusion of extra moments ($k > 10$) was found to result in little alteration to these plots.

The variation in the angular momenta shown in these plots is quite striking. In one of a number of prescient papers on the subject of vector correlations Herschbach wrote:

> "In effect, a potential energy surface acts as a polarising lens which induces anisotropies and correlations among the relative velocity and rotational momentum vectors."

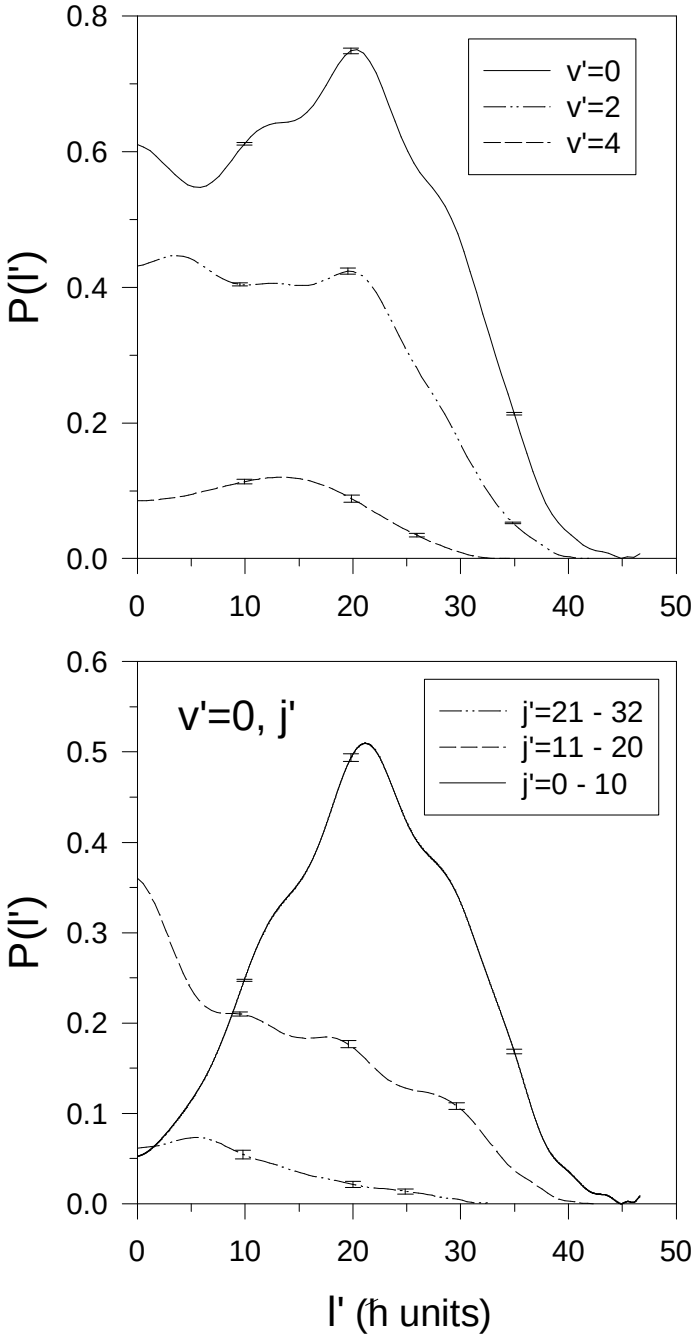

Figure 6.12 OH vibrationally resolved product orbital angular momentum distribution, $P(l')$ (SL1NS PES). Only $v' = 0, 2$ and 4 are shown for clarity. Bottom panel shows the $v' = 0$ distribution resolved by product j'.

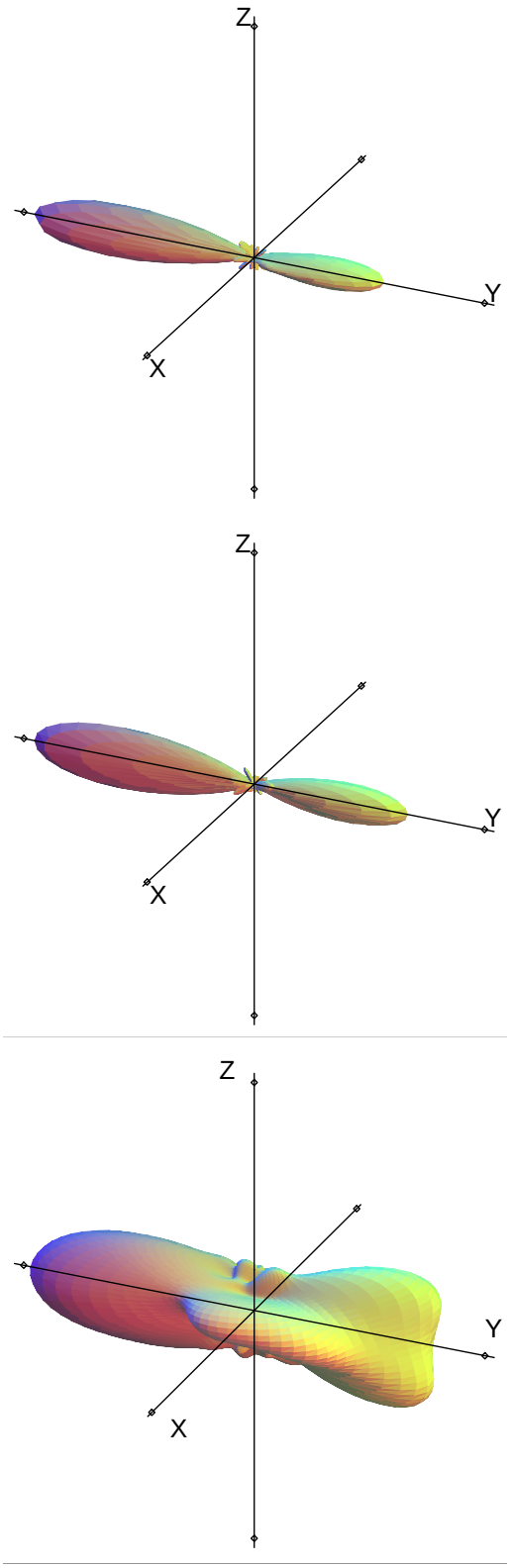

Figure 6.13 Product OH($v' = 0$, $j' = 0 - 10$) angular momentum distributions: $P(\boldsymbol{l})$ (top panel), $P(\boldsymbol{l'})$ (middle panel), and $P(\boldsymbol{j'})$ (bottom panel) (SL1MS surface). Each plot includes both odd and even moments (see text for details).

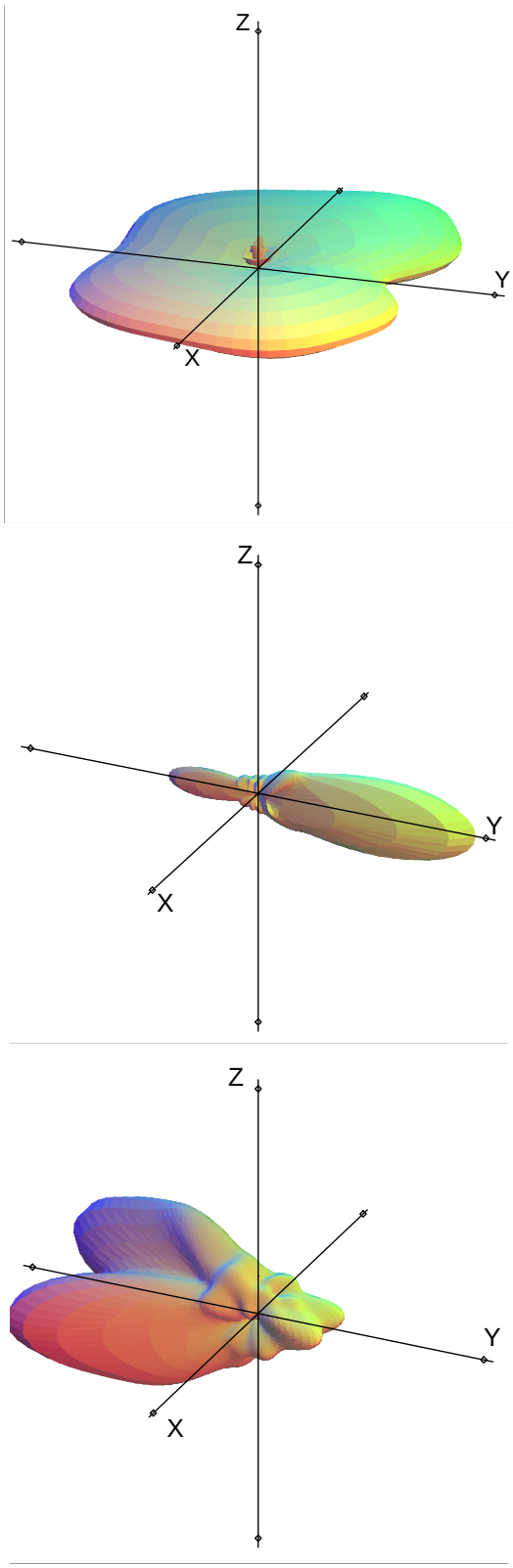

Figure 6.14 As for figure (6.13), but for OH($v' = 0$, $j' = 21 - 32$). $P(\boldsymbol{l})$ (top panel), $P(\boldsymbol{l'})$ (middle panel), and $P(\boldsymbol{j'})$ (bottom panel) (SL1MS surface).

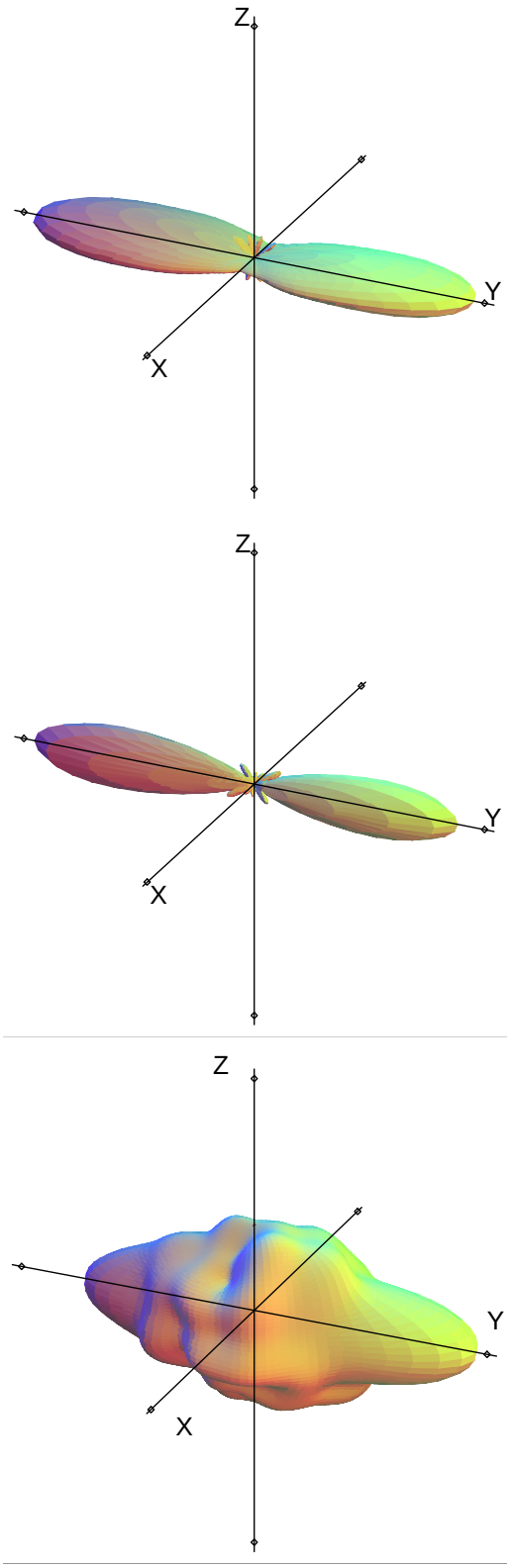

Figure 6.15 As for figure (6.13), but for OH($v' = 4$). $P(\boldsymbol{l})$ (top panel), $P(\boldsymbol{l'})$ (middle panel), and $P(\boldsymbol{j'})$ (bottom panel) (SL1MS surface).

One need only look at the 3D plots of angular momenta for justification of this statement.

For OH($v' = 0, j' = 0 - 10$) both $\boldsymbol{l}$ and $\boldsymbol{l'}$ are strongly polarised along the $-y$ axis, with a preference to lie below the scattering plane. In contrast, $\boldsymbol{j'}$ is aligned along the y axis, but not strongly oriented. Since j' is small, $\boldsymbol{l}$ and $\boldsymbol{l'}$ are nearly parallel. For OH products in $v' = 4$ both $\boldsymbol{l}$ and $\boldsymbol{l'}$ are aligned, but not oriented, along the CM y axis. In contrast, the $\boldsymbol{j'}$ distribution is relatively unpolarised, although somewhat aligned along the y axis. Figures (6.13) and (6.15) suggest that channels populating OH($v' = 0, j' = 0 - 10$) and OH($v' = 4$) are both very selective: P($\boldsymbol{l}$) is very strongly polarised with respect to the CM frame.

Products in OH($v' = 0, j' = 21 - 32$) form the major channel for the reaction of $O(^1D_2)$ with H_2 at 300 K. Figure (6.14) shows an isotropic distribution of $\boldsymbol{l}$ which, since $\boldsymbol{k}$ defines the z axis, results in a disk of $\boldsymbol{l}$ in the xy plane. This suggests that OH($v' = 0, j' = 21 - 32$) is populated by rather unselective collisions, which is not surprising considering that this is the most populated state with a large total cross section. In spite of the relatively unpolarised $P(\boldsymbol{l})$ both $P(\boldsymbol{l'})$ and $P(\boldsymbol{j'})$ are strongly oriented: the product orbital angular momentum, $\boldsymbol{l'}$, is strongly oriented along the CM $+y$ axis, with $\boldsymbol{j'}$ strongly oriented in the opposite direction showing a distinct V shaped splitting (as is evident in figure 6.10). Looking at the magnitudes of the angular momenta involved (figures 5.6, 6.12 and 5.1), it is clear that the *magnitude* of the product angular momentum l', is greater than j' and about twice the magnitude of l. As a result $\boldsymbol{j'}$ and $\boldsymbol{l'}$ are nearly antiparallel. To be more precise $\langle l \rangle = 15$, $\langle l' \rangle = 25$ and $\langle j' \rangle = 26$; in this particular case, all of these averages are quite well defined because the distributions have low standard deviations. A simple use of the cosine rule yields the corresponding tilt between $\boldsymbol{j'}$ and $\boldsymbol{l'}$ as being $\approx \pm 34°$ which almost exactly matches the splitting observed in figure (6.14). A similar effect of splitting in the product $\boldsymbol{j'}$ azimuthal angular distribution has also been observed for QCT calculations on the F + H_2 system [13] where the splitting is dependent on the reagent rotational quantum state, j. In

the present case no dependence on $j \leq 3$ was found, and no correlation with the direction of $\boldsymbol{j}$ could be determined.

The strong anti–parallel correlation of $\boldsymbol{j'}$ and $\boldsymbol{l'}$ has been observed previously in quasi-classical calculations by Hijazi and Polanyi [14] who studied both attractive and repulsive potential energy surfaces for a range of reagent mass combinations (H + HL, L + LL and L+HH). They highlighted two dominant sources of product rotation:

1. Reagent orbital angular momentum: when a Heavy attacking atom reacts with a HL molecule giving a HH molecule, much of the final product angular momentum will appear as motion of H about H. Also, HH diatomics generally have closely spaced rotational energy levels. The result is $l \rightarrow j'$. This is a kinematic effect.
2. A substantial torque applied to the product diatomic on formation will also result in large j'. This may happen in the case of repulsive energy release *via* a bent intermediate, particularly for reactions ejecting an atom with a significant mass. This is a dynamic effect.

When $\boldsymbol{l}\rightarrow\boldsymbol{j'}$ one might expect a random polarisation of $\boldsymbol{j'}$ with respect to $\boldsymbol{l'}$. A repulsive energy release, however, will give rise to rotational motion in the product molecule that is coplanar with, but opposed to the orbital motion of the product atom [15]. Hijazi and Polanyi concluded that, in general, repulsive energy release will show the greatest tendency for $\boldsymbol{j'}$ to lie anti–parallel to $\boldsymbol{l'}$. The situation of repulsive energy release was encountered in the reaction of F + H_2 by Polanyi and Schreiber [15] and more recently by Aoiz *et al.* [8] on an improved *ab–initio* surface which is known to possess a bent transition state.

The present reaction proceeds preferentially *via* insertion: an attractive process, and has a mass combination of Heavy + Light–Light. At 300 K H_2 mostly populates j=1 due to the large rotational constant and nuclear spin statistics. The reagent reduced mass is $\mu_{O,H_2} = 1.8$ amu, the product reduced mass $\mu_{OH,H} = 0.94$. The product diatomic also

has a reduced mass $\mu_{\mathrm{OH}} = 0.94$. From kinematic considerations alone, it is no surprise that product rotational angular momentum and orbital angular momenta may both be large; this appears as a kinematic effect. What is striking though, is the strong correlation between $\boldsymbol{j'}$ and $\boldsymbol{l'}$. The insertion of the oxygen atoms to produce intermediates which are highly excited in the bending vibration has been remarked upon a number of times (see section 1.9): the light hydrogen atoms may possess a significant fraction of the initial orbital angular momentum as angular momentum around the oxygen. Despite having a deep intermediate well, there is quite a sizeable exoergicity (*ca.* 1.78 eV=172 kJ mol^{-1}) available to the products. Since the products are in $v' = 0$, this must be partitioned between rotation and translation. The light hydrogen atom may be thrown clear with a large exit impact parameter, see figure (6.16). This could happen preferentially as the HOH bond is opening, perhaps as a result of collision of the two H atoms, as has been observed both by Whitlock *et al.* [16] and in the present work. In any case, it is clear that the anisotropy of the PES plays a significant role. The preferential anti-parallel alignment of $\boldsymbol{l'}$ and $\boldsymbol{j'}$ is similar to the behaviour found in the photodissociation of water *via* the *linear* $\tilde{\mathrm{B}}^1A_1$ state [17].

6.5 Orientation of angular momentum in the CM frame

As was discussed previously (section 6.2), the present experiments are limited to the determination of low order *even* moments of the product rotational angular momentum distribution. In the preceeding section, the importance of *orientation* as an indicator of the reaction (stereo–) dynamics has been highlighted. In particular, for the channel presently under consideration, it would appear that orientation of $\boldsymbol{j'}$ is a distinct possibility. Polar plots of $P(\boldsymbol{j'})$, including moments $k \leq 10$ for the OH($v' = 0, j' = 14$) channel on the SL1MS and K ground state surfaces are compared in figure (6.17).

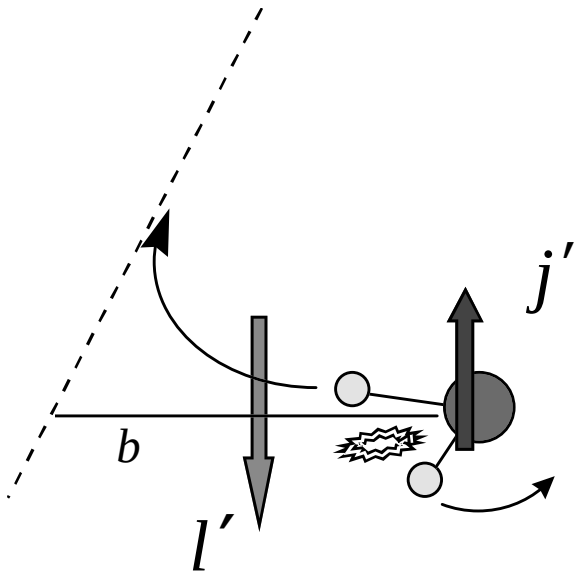

Figure 6.16 Schematic figure illustrating the ejection of an H atom with large exit orbital angular momentum, perhaps after some repulsive energy release, and showing antiparallel correlation of $\boldsymbol{l}'$ and $\boldsymbol{j}'$.

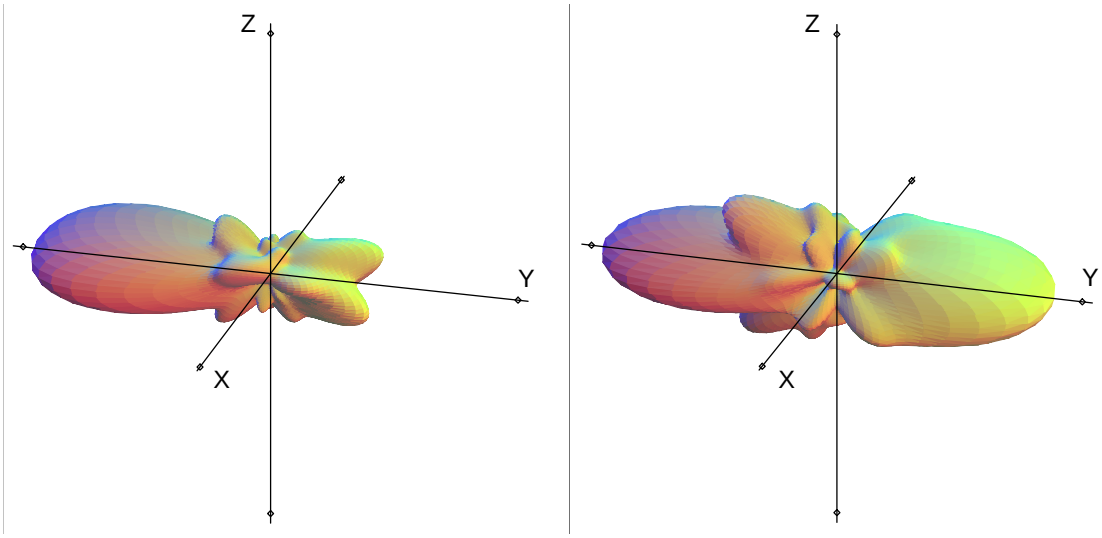

Figure 6.17 As in figure (6.7), but showing the QCT results from the SL1MS (left panel) and K surfaces (right panel) and including both even *and* odd moments $k \leq 10$.

It is clear from figure (6.17) that the two surfaces differ somewhat in the degree of rotational orientation produced. In fact it has been found that the K PES shows very little product angular momentum orientation [18], and much less variation of vector correlations between product quantum states. In contrast, the F + H_2 system shows strong orientation effects, and these are notably reagent j dependent [8, 13].

The mechanism for orientation in the present reaction is still unclear. Results for the F + H_2 system have been interpreted in terms of a reorienting of collisions by the PES [8]. The same could be said of the present surface, which is attractive but strongly anisotropic. The distribution of scattering angles and lifetimes in the present reaction make it difficult to generalise about the mechanism for orientation. It is clear, however, that measurement of orientation effects offers a possible method of distinguishing between similar surfaces.

6.6 Conclusions and Look forward

In this chapter the product state–resolved polarisation of angular momenta in the reaction of $O(^1D_2)$ + H_2 has been discussed. Experimental estimates of the scattering angle (θ_t) dependent rotational alignment in the centre of mass (CM) frame for product OH in ($v' = 0, N' = 14$) have been presented. The results indicate a preferential rotational alignment *in* the CM ($\boldsymbol{k}$,$\boldsymbol{k'}$) scattering plane for products in OH $\Pi(A'')$, and perpendicular to the scattering plane for products populating OH $\Pi(A')$.

The experiments are reasonably well reproduced by quasiclassical trajectory calculations using only the ground ($1^1A'$) state potential energy surface. Variations in $\boldsymbol{l}$, $\boldsymbol{l'}$ and $\boldsymbol{j'}$ CM angular momentum distributions with product quantum state were found to be quite marked, with no evidence for the existence of a long lived collision complex: the product angular momentum distributions generally do not resemble the limiting statistical forms defined by Herschbach and co–workers [11].

Examination of the (scattering angle averaged) angular momentum distributions for the most populated channel producing OH($v' = 0$, high j') indicated the occurrence of *orientation* with respect to the $\boldsymbol{k}$,$\boldsymbol{k'}$ scattering plane. In particular a strong correlation of $\boldsymbol{j'}$ anti–parallel to $\boldsymbol{l'}$ was found and implicates the involvement of dynamical surface effects.

The O + H_2 system when viewed from a state averaged approach, appears quite broad and perhaps dynamically uninteresting. Product state resolution has revealed that the reaction is, in truth, dynamically rich. One of the major limitations of the present experiment lies with the reagent atom source. The $O(^1D_2)$ reagent distribution from the photolysis of N_2O is too broad, both in energy and in anisotropy, resulting in unfavourable kinematics. The absorption cross section for photolysis of N_2O is so low that intense 193 ArF laser radiation is required, and this interferes with the LIF detection scheme. A more convenient source of $O(^1D_2)$ is the 157 nm photolysis of O_2 which has a much higher absorption cross section, and a well defined anisotropy ($\overline{\beta} \approx -1$) [19].

Measurements of rotational angular momentum orientation should be possible using circularly polarised probe laser radiation to gain insight into the otherwise unobserved correlations between $\boldsymbol{j'}$ and the reagent and product orbital angular momenta, $\boldsymbol{l}$ and $\boldsymbol{l'}$ [20]. These measurements may prove a stringent test for theoretical calculations, adding a powerful diagnostic capable of distinguishing perhaps otherwise apparently similar potential energy surfaces.

References

[1] A. Heck, D. Neyer and D. W. Chandler, *personal communication.*

[2] A. J. Alexander, F. J. Aoiz, L. Bañares, M. Brouard, J. Short and J. P. Simons, *J. Phys. Chem. A*, **101** (1997) 7544.

[3] M. Brouard, H. M. Lambert, J. Short and J. P. Simons, *J. Phys. Chem.*, **99** (1995) 13571.

[4] J. Short, *D. Phil. Thesis*, University of Oxford, 1997.

[5] H. L. Kim, M. A. Wickramaaratchi, X. Zheng and G. E. Hall, *J. Chem. Phys.*, **101** (1994) 2033.

[6] M. Brouard, H. M. Lambert, S. P. Rayner and J. P. Simons, *Mol. Phys.*, **89** (1996) 403.

[7] S. P. Rayner, *D. Phil. Thesis*, University of Oxford, 1997.

[8] F. J. Aoiz, M. Brouard, V. J. Herrero, V. Sáez Rábanos and K. Stark, *Chem. Phys. Lett.*, **264** (1997) 487.

[9] J. D. Barnwell, J. G. Loeser and D. R. Herschbach, *J. Phys. Chem*, **87** (1983) 2781.

[10] G. M. McClelland and D. R. Herschbach, *J. Phys. Chem.*, **83** (1979) 1445.

[11] S. K. Kim and D. R. Herschbach, *Faraday Discuss. Chem. Soc.*, **84** (1987) 159.

[12] D. A. Case and D. R. Herschbach, *Mol. Phys.*, **30** (1975) 1537.

[13] F. J. Aoiz, M. Brouard, *personal communications.*

[14] (a) N. H. Hijazi and J. C. Polanyi, *J. Chem. Phys.*, **63** (1975) 2249.

(b) N. H. Hijazi and J. C. Polanyi, *Chem. Phys.*, **11** (1975) 1.

[15] J. C. Polanyi and J. L. Schreiber, *Faraday Discuss. Chem. Soc.*, **62** (1977) 267.

[16] (a) P. A. Whitlock, J. T. Muckerman and P. M. Kroger, in *Potential Energy Surfaces and Dynamics Calculations*, ed. D. G. Truhlar, (Plenum, New York, 1981), pp 551–586.

(b) P. A. Whitlock, J. T. Muckerman and E. R. Fisher, *J. Chem. Phys.*, **76** (1982) 4468.

[17] (a) T. J. Carrington, *J. Chem. Phys.*, **41** (1964) 2012.

(b) J. P. Simons and P. W. Tasker, *Mol. Phys.*, **27** (1974) 1691.

[18] A. J. Alexander, F. J. Aoiz, L. Bañares, M. Brouard and J. P. Simons, *unpublished results.*

[19] D. H. Parker, *personal communication.*

[20] M. Brouard and S. Gatenby, *in progress.*

[21] D. A. Case and D. R. Herschbach, *J. Chem. Phys.*, **64** (1976) 4212.

Appendix A Spectroscopy of the OH radical

The OH radical appears in an number of important processes, including combustion and stratospheric chemistry. For this reason it has been widely studied, experimentally and theoretically, and the spectroscopy of the lower electronic states is largely well determined.

We deal here with the spectroscopy of the ($A^2\Sigma^+$-$X^2\Pi$) transition, particularly to be clear about the nomenclature used in this thesis. The reader is directed to figure (A.1) for the following discussion, and to Herzberg [1] for a more thorough discussion of diatomic spectroscopy.

A.1 The X state

The ground electronic state of the OH radical has the electronic configuration

$$(1\mathrm{sn})^2(2\mathrm{s}\sigma)^2(2\mathrm{s}\sigma^*)^2(2p\sigma)^2(2p\pi)^1$$

and so there is one unpaired electron in the outer shell with spin angular momentum of $\frac{1}{2}$ and orbital angular momentum of 1. In the limit that the molecule has low rotational angular momentum, the electronic angular momenta couple independently to the internuclear axis and their projections on this axis are $\Sigma = \pm\frac{1}{2}$ (spin) and $\Lambda = \pm 1$ (orbital). The total angular momentum along the axis is then well defined, $\Omega = |\Lambda \pm \Sigma|$ giving two spin-orbit components, $\Omega = \frac{3}{2}$ and $\Omega = \frac{1}{2}$. This total $\boldsymbol{\Omega}$ and the rotational angular momentum, $\boldsymbol{N}$ then couple to give the resultant total angular momentum, $\boldsymbol{J}$. The two spin-orbit states correspond to two states split by an energy difference of 1.67 kJ mol^{-1}. The lower of these

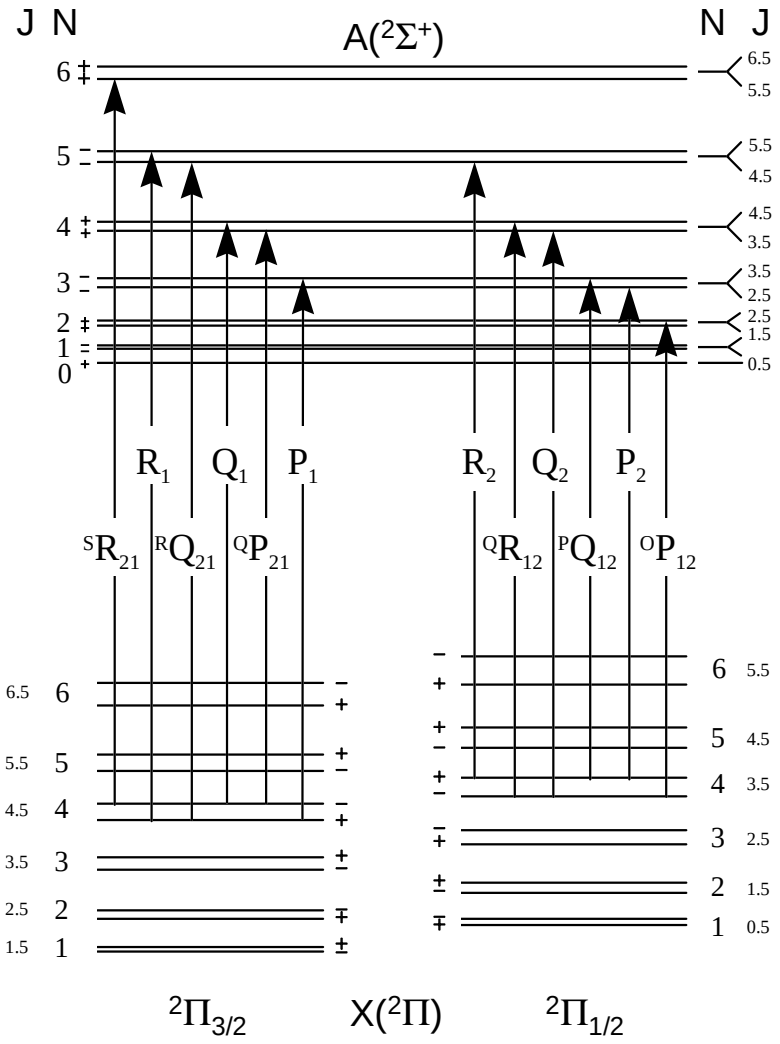

Figure A.1 Diagram illustrating the A-X LIF transitions used in the present work. Undispersed fluorescence is measured: see text for details.

two states ($^2\Pi_{3/2}$) is labelled F_1 and the higher ($^2\Pi_{1/2}$) is labelled F_2. This is an example of **Hund's case (a)** coupling.

As the rotation of the nuclei increases, there are two effects which become important. Firstly there is an increasing coupling between rotation and the electronic orbital angular momentum. This results in a splitting into two components for each $\boldsymbol{J}$ value. This splitting is known as Λ-*type doubling* and the splitting increases with increasing $\boldsymbol{J}$. The two states can be distinguished by their parity with respect to the plane of rotation, one is symmetric: $\Pi(A')$, whilst the other is antisymmetric: $\Pi(A'')$. These symmetries are visualised in figure A.2. In addition to this, the spin becomes decoupled from the nuclear axis and Ω is no longer a good quantum number. This process is called *spin uncoupling* and is an example of **Hunds case (b)**.

A.2 The A state

The $A(^2\Sigma^+)$ excited state of OH possesses no orbital angular momentum. The rotational angular momentum, $\boldsymbol{N}$, and the spin angular momentum, $\boldsymbol{S}$ couple directly to give the total angular momentum $\boldsymbol{J}$. This causes a splitting into two components for each N level in the rotational stack. The two components are labelled f_1 and f_2, where $J = N + \frac{1}{2}$ for f_1 and $J = N - \frac{1}{2}$ for f_2. This is another example of **Hund's case (b)**.

A.3 Selection rules

The dipole-allowed selection rules are:

$$\Delta J = 0, \pm 1$$

$$+ \rightarrow - \quad \text{and} \quad - \rightarrow +$$

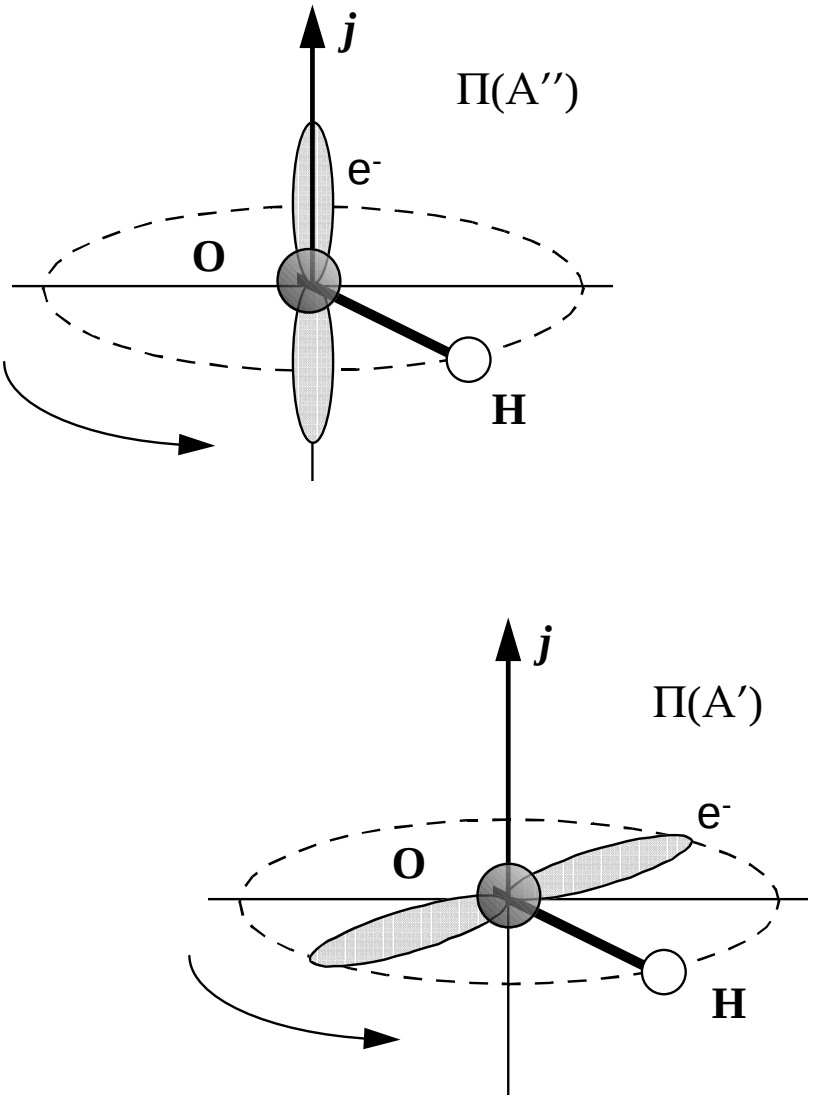

Figure A.2 Λ-doublet symmetries probed by the rotational branches. The e/f describe the rotation-independent parity of the Λ-doublet wavefunction.

ΔJ	${}^{\Delta N}\Delta J$	ΔN	DC$^{(a)}$	ΔJ	ΔN
P_{12}	${}^{O}P_{12}$	O_{12}	O_{12}	-1	-2
P_{11}			P_1	-1	-1
P_{22}			P_2	-1	-1
P_{21}	${}^{Q}P_{21}$	Q_{21}	Q'_1	-1	0
Q_{12}	${}^{P}Q_{12}$	P_{12}	P'_2	0	-1
Q_{11}			Q_1	0	0
Q_{22}			Q_2	0	0
Q_{21}	${}^{R}Q_{21}$	R_{21}	R'_1	0	$+1$
R_{12}	${}^{Q}R_{12}$	Q_{12}	Q'_2	$+1$	0
R_{11}			R_1	$+1$	$+1$
R_{22}			R_2	$+1$	$+1$
R_{21}	${}^{S}R_{21}$	S_{21}	S_{21}	$+1$	$+2$

$^{(a)}$ Dieke and Crosswhite, ref. [2].

Table A.1 Rotational branches for a $A^2\Sigma^+ \leftarrow X^2\Pi$ transition showing alternative forms of notation.

Transitions are generally labelled according to the ΔJ branch in the regular way, P_{kq}, Q_{kq}, or R_{kq} with k and q denoting the numbers of the components involved in the upper and lower states respectively, e.g. P_{21} is a transition with $\Delta J = -1$ and from the F_1 stack to the f_2 stack. Unfortunately, however, this is not the only notation in the literature. There are 12 possible rotational branches and these are listed in table A.1 along with other notation commonly found in the literature. Transitions between F_1 and f_1 levels and the transitions between F_2 and f_2 levels are known as "main" branch transitions. there are also six transitions which cross between the $f_1 \leftarrow F_2$ and $f_2 \leftarrow F_1$ manifolds, and these correspond to "satellite" branch transitions.

The passage, in the X state, from Hund's case (a) at low N to Hund's case (b) at higher N causes the satellite branch intensity to tend to zero with increasing N. The satellite transitions are essential for the retrieval of Λ-doublet specific vector correlations, and as a result this creates some difficulty for larger N.

The P/R and Q branches (ΔJ) probe different Λ-doublet levels in the ground state, see figure A.2.

References

[1] G. Herzberg, *Molecular Spectra and Molecular Structure vol. 1*, 2nd edn., Krieger, Florida 1989.

[2] G. H. Dieke and H. M. Crosswhite, *J. Quant. Spectrosc. Radiat. Transfer*, **2** (1961) 97.